MECHANICS OF HETEROGENEOUS METALLIC MATERIALS

A Dissertation
Presented to
The Academic Faculty

by

Yin Zhang

In Partial Fulfillment
of the Requirements for the Degree
Doctoral Degree in the
George W. Woodruff School of Mechanical Engineering

Georgia Institute of Technology
August 2021

MECHANICS OF HETEROGENEOUS METALLIC MATERIALS

Approved by:

Dr. Ting Zhu, Advisor
School of Mechanical Engineering
Georgia Institute of Technology

Dr. Aaron Stebner
School of Mechanical Engineering
Georgia Institute of Technology

Dr. David McDowell
School of Mechanical Engineering
Georgia Institute of Technology

Dr. Min Zhou
School of Mechanical Engineering
Georgia Institute of Technology

Dr. Olivier Pierron
School of Mechanical Engineering
Georgia Institute of Technology

Dr. Morris Wang
Department of Materials Science and Engineering
University of California, Los Angeles

Date Approved: June 29, 2021

ACKNOWLEDGEMENTS

I would like to first express my sincere gratitude to my advisor, Dr. Ting Zhu, for his invaluable mentorship and support during the past years. I have learned much from Dr. Zhu on how to conduct research with the highest standard. His teaching will continue to inspire me throughout my career.

I would like to acknowledge the collaborators for their work covered in this thesis, Jie Ren and Dr. Wen Chen from University of Massachusetts, Amherst, Dr. Zan Li from Shanghai Jiao Tong University, China, Dr. Morris Wang from University of California, Los Angeles, Dr. David McDowell, Sandra Stangebye, Dr. Joshua Kacher and Dr. Olivier Pierron from Georgia Tech, Zhao Cheng, Linfeng Bu and Dr. Lei Lu from Institute of Metal Research, Shenyang, China.

I would like to acknowledge my thesis committee members: Dr. David McDowell, Dr. Olivier Pierron, Dr. Aaron Stebner, Dr. Min Zhou and Dr. Morris Wang for their guidance and patient support on this thesis work.

I would like to thank my colleagues Dr. Zhi Zeng, Dr. Dengke Chen, Baolin Wang, Kunqing Ding and Yiping Si for their insightful discussion and collaboration.

I would like to thank my parents and my wife for their wise counsel and wholehearted support.

TABLE OF CONTENTS

LIST OF TABLES

LIST OF FIGURES

LIST OF SYMBOLS AND ABBREVIATIONS

RVE	representative volume element
AM	additively manufactured
SLM	selective laser melting
L-PBF	lase powder-bed-fusion
SS	stainless steel
EBSD	electron backscatter diffraction
SEM	scanning electron microscope
TEM	transmission electron microscopy
HAADF STEM	high-angle annular dark-field scanning transmission electron microscopy
EDS/EDX	energy dispersive X-ray spectroscopy
DEC	diffraction elastic constant
SXRD	synchrotron X-ray diffraction
CPFE	crystal plasticity finite element
FCC	face-centered cubic
BCC	body-centered cubic
DC	diamond cubic
LD	loading direction
TD	transverse direction
ND	normal direction
BD	build direction
HEA	high-entropy alloy
DP-CPFE	dual-phase crystal plasticity finite element

GNT	gradient nanotwinned
GND	geometrically necessary dislocation
SSD	statistically stored dislocation
GPFE	gradient plasticity finite element
HNT	homogeneous nanotwinned
TB	twin boundary
BCD	bundle of concentrated dislocations
nc	nanocrystalline
ufg	ultrafine-grained
GB	grain boundary
MD	molecular dynamics
EAM	embedded atom method
TST	transition state theory
NEB	nudged elastic band
FENEB	free-end nudged elastic band
PES	potential energy landscape
MEP	minimum energy path
$\boldsymbol{\sigma}$	stress tensor
$\boldsymbol{\varepsilon}$	strain tensor
$\mathbf{L}$	elastic stiffness tensor
$\mathbf{M}$	elastic compliance tensor
$\mathbf{U}$	constrained compliance tensor
E_{LD}^{hkl}	diffraction elastic constant of grain family $\{hkl\}$ along LD
E_{TD}^{hkl}	diffraction elastic constant of grain family $\{hkl\}$ along TD

$\mathbf{F}$	deformation gradient tensor
$\mathbf{F}^e$	elastic deformation gradient
$\mathbf{F}^p$	plastic deformation gradient
$\mathbf{E}^*$	eigen-strain tensor reflecting the Type II internal stresses
$\mathbf{T}$	Cauchy stress
$\mathbf{T}^*$	second Piola–Kirchhoff stress
$\mathbf{B}$	back-stress tensor representing the Type III internal stresses
m	strain rate sensitivity
$\dot{\gamma}_i^p$	plastic shear rate on each slip system
s^α	slip resistance
s_0	initial value of slip resistance
h_0	hardening parameter
$\bar{\sigma}$	von Mises stress
α	scalar measure of plastic strain gradient
V_a	apparent activation volume
V^*	true activation volume

SUMMARY

Overcoming the strength-ductility tradeoff is a widely pursued goal in the materials community. In recent years, design, fabrication, and optimization of heterogeneous microstructures have been extensively explored to achieve exceptional combinations of strength and ductility. However, there is currently a critical lack of the mechanics understanding of heterogeneous microstructures. In general, structural heterogeneities generate mechanical heterogeneities that are manifested as spatially non-uniform back stresses and forward stresses. These long-range, directional internal stresses can result in enhanced yield strength, work hardening, and tensile ductility. To understand the effects of heterogeneous microstructures and associated internal stresses on mechanical properties, this thesis is focused on development of novel constitutive and atomistic models for several emergent heterogeneous material systems, including additively manufactured metal alloys, gradient nanotwinned metals, nanocrystalline thin films, and nanodispersion-strengthened composites. Overall, the thesis research provides a new framework to bridge the structural heterogeneities and mechanical heterogeneities in several heterogeneous material systems through new constitutive models of strain gradient plasticity, internal-stress-dependent crystal plasticity, and dual-phase crystal plasticity. Atomistic simulations uncover the critical deformation processes that are strength/rate-controlling. Coupled with novel material processing, characterization, and testing, the modeling and simulation results offer quantitative predictions and mechanistic insights toward the design of heterogeneous metallic materials with improved combinations of strength and ductility.

CHAPTER 1. INTRODUCTION

1.1 Heterogeneous Metallic Materials

Metals and alloys are the most commonly used class of engineering materials. This is mainly because they have either high strength or high ductility. However, a superior combination of strength and ductility is rarely achieved: high-strength metals and alloys usually suffer from poor ductility. For example, nanocrystalline metals exhibit strength near 1 GPa but only less than 5% tensile ductility [1]. Pre-worked metals have high strength due to high dislocation density from severe plastic deformation, but their diminishing strain hardening capability leads to limited ductility [2]. Therefore, it is a great challenge to develop stronger and tougher materials.

In recent years, there have been many explorations of structural heterogeneity designs, including bimodal, lamellar, gradient and hierarchical nanostructures as shown in Figure 1.1, in order to achieve high strength with good ductility. This route of heterogeneity engineering shows promising combinations of strength and ductility. However, there is currently a critical lack of fundamental understanding of heterogeneous microstructures. Therefore, the focus of this thesis is to understand the mechanics and physics of these heterogeneous metallic systems, thereby facilitating and inspiring better design of structural heterogeneities to achieve exceptional combinations of high strength and ductility.

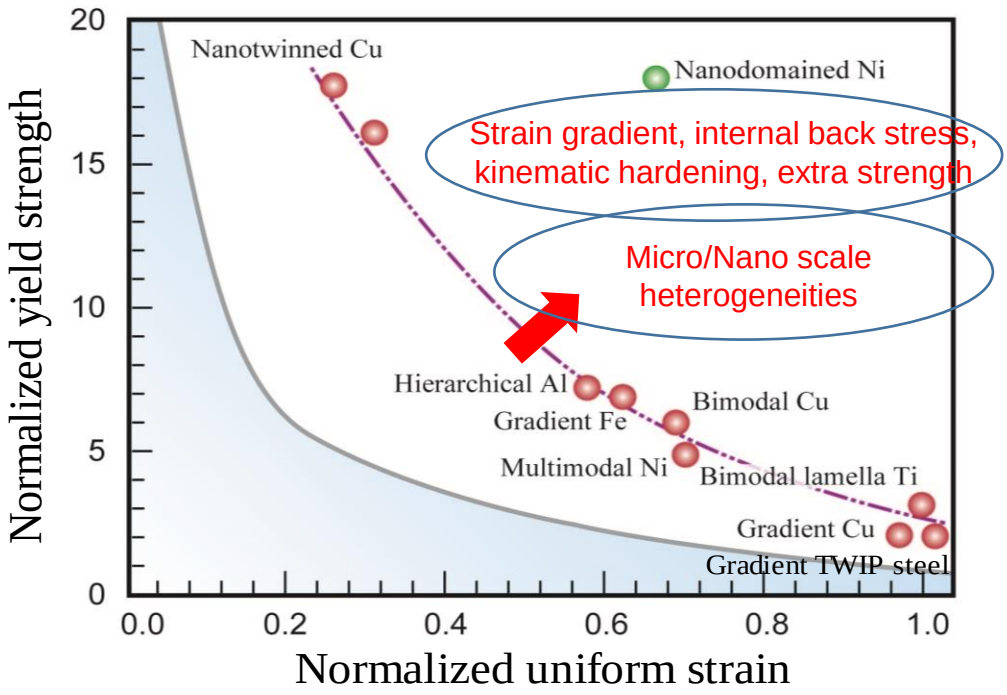

Figure 1.1 Yield strength versus uniform elongation of metals adapted from [3]. The shaded area under the banana-shaped curve covers the strength-ductility data of conventional metals with homogeneous microstructures.

1.2 Mechanical Heterogeneities and Internal Stresses

Metals and alloys usually contain different microstructural heterogeneities across many length scales, for example, (i) short-range ordering and clustering in high-entropy alloys, (ii) grain boundaries in nanocrystalline metals, (iii) reinforced particle in nanocrystals, (iv) chemical segregation and dislocation cells in additively manufactured alloys, (v) gradient nanotwinned metals. These heterogeneities with different mechanical properties produce heterogeneous stress distributions inside materials when external loading is applied. We define the differences between the local stress and the average macroscopic stress as

internal stresses. These internal stresses (also called residual stresses upon unloading) strongly influence the strength, ductility, fracture and fatigue properties of the materials. The internal stresses are usually categorized into three types based on their length scales as shown in Figure 1.2: (i) macrostresses or type-I internal stresses that occurs over a distance comparable to the size of the component, (ii) intergranular internal stresses or type-II internal stresses at the scale of grain size and (iii) intragranular internal stresses or type-III internal stresses at the level of sub-grain microstructures. Such internal stresses are long-range, directional and self-equilibrating, producing the Bauschinger effect and kinematic hardening.

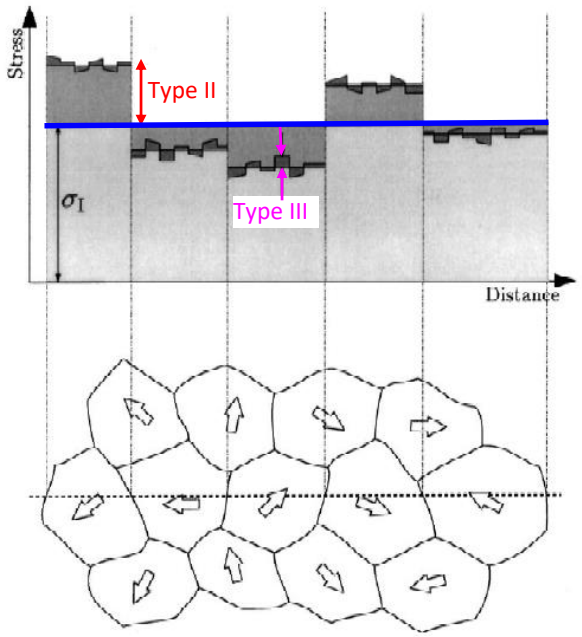

Figure 1.2 Schematic illustration of the distribution of macro internal stresses, intergranular internal stresses and intragranular internal stresses in a randomly orientated polycrystalline material, adapted from [4].

Figure 1.3 presents a general framework for understanding the mechanics of different types of heterogeneous nanostructures (shown in upper-row images). Let us consider gradient nanotwinned (GNT) Cu as an example. It is important to take into consideration the size of a selected representative volume element (RVE) relative to the characteristic length scales of GNT Cu, which feature the wavelength of periodically varying twin thickness (on the order of hundreds of micrometers) as well as the nanotwin thickness (on the order of tens of nanometers). As shown in the red panel of Figure 1.3, when the entire sample of GNT Cu is taken as a "large" RVE, the strengthening effect of structural gradient inside the RVE can be characterized by partitioning the overall stress into the back and effective stresses based on the plasticity model of kinematic hardening [5-7]. The back stress reflects the strengthening contribution from the directional, long-range internal stress arising from plastically inhomogeneous deformation in gradient structures, while the effective stress represents the strengthening contribution from the non-directional, short-range resistance to gliding dislocations from lattice friction and local pinning obstacles. In contrast, the blue panel of Figure 1.3 shows an alternative approach of choosing a "small" RVE that contains twin lamellae with a uniform thickness. Suppose a "small" RVE represents a "soft" region containing uniformly-thick twin lamellae, while another adjacent "small" RVE represents a "hard" region containing uniformly-thin twin lamellae. A structural gradient across the two RVEs results in a gradient of plastic strain, whose strengthening effect can be characterized by the constitutive model of strain gradient plasticity. Therefore, the strengthening effects of nanotwin gradients and uniform nanotwins are separated in the "small-RVE" approach, while these two strengthening effects are combined in the "large-RVE" approach. Note that the "small" RVEs with

uniform twin thickness also contain structural heterogeneity due to the presence of twin boundaries (TBs) and twin lamellae with different orientations. The strengthening effect of such kind of structural heterogeneity at the "small" RVE level can be characterized by the corresponding back and effective stresses. Hence, the multiple types of back stress in GNT Cu originate from structural heterogeneities at different length scales and thus illustrate the complexity of back stresses arising from highly heterogeneous microstructures.

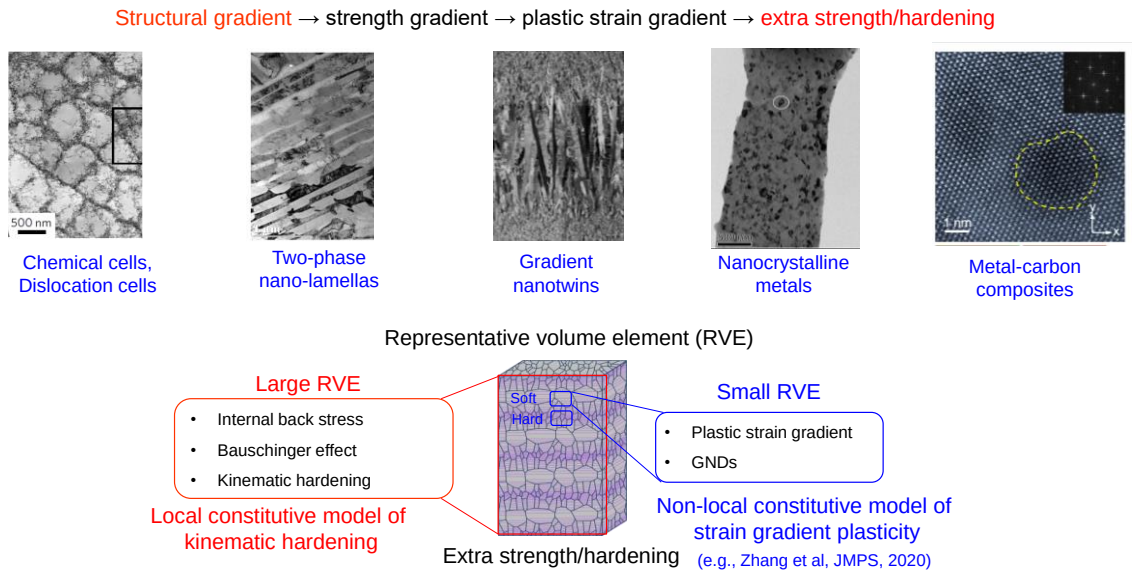

Figure 1.3 Unified mechanics framework of heterogeneous microstructures. The mechanical heterogeneities induce plastic strain gradient leading to extra strengthening and hardening.

In summary, structural heterogeneities generate mechanical heterogeneities that are manifested as spatially non-uniform back stresses and forward stresses. These long-range, directional internal stresses can result in enhanced yield strength, work hardening, and tensile ductility. To understand the effects of heterogeneous microstructures and associated internal stresses on mechanical properties, this thesis research is focused on development

of novel constitutive and atomistic models for several emergent heterogeneous material systems, including additively manufactured metal alloys, gradient nanotwinned metals, nanocrystalline thin films, and nanodispersion-strengthened metal composites.

1.2.1 Microscale Heterogeneities in Additively Manufactured Alloys

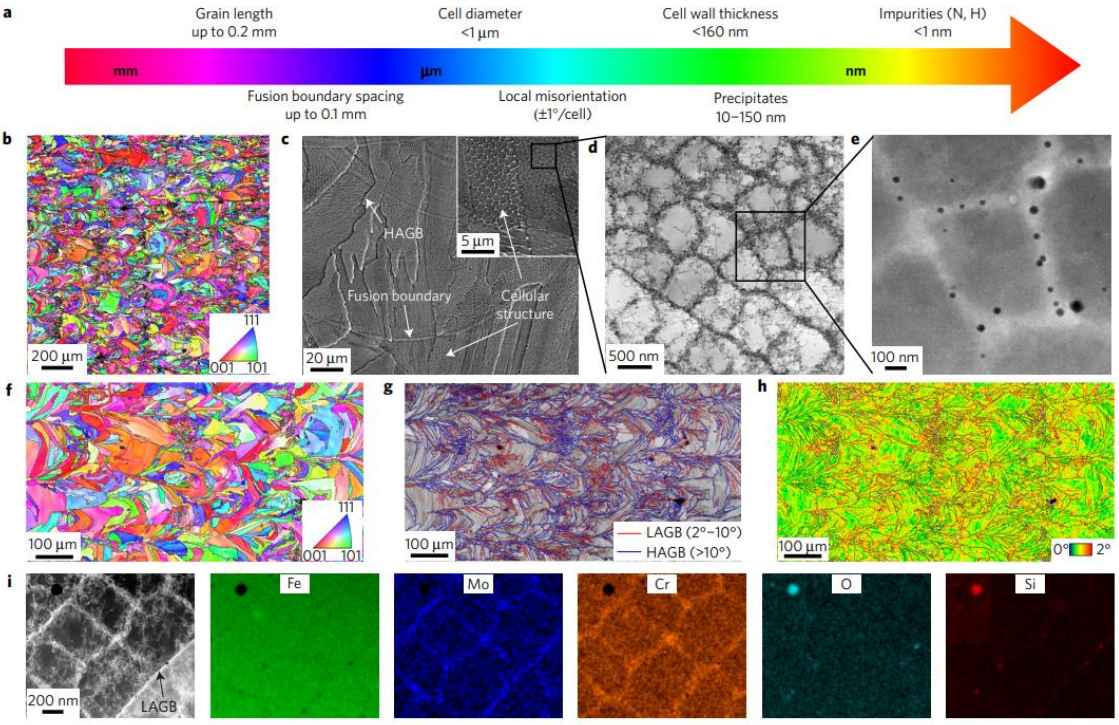

Figure 1.4 Typical microstructures of laser powder-bed-fusion (L-PBF) produced 316 stainless steels (SS) adapted from [8]. **a**, A schematic of various length scales uncovered in L-PBF 316L SS. **b**, A cross-sectional electron backscatter diffraction (EBSD) inverse-pole figure. **c**, A cross-sectional scanning electron microscopy (SEM) image, revealing fusion boundaries, high-angle grain boundaries (HAGBs), and solidification cellular structures. **d**, A bright-field transmission electron microscopy (TEM) image of solidification cells. **e**, A high-angle annular dark-field (HAADF) scanning TEM (STEM) image of the solidification cells shown in d. The nanoparticles segregated to the cell walls were identified as transition-metal-rich silicates formed during L-PBF processing. **f,** EBSD IPF map acquired with a 1-µm step size. **g**, EBSD image quality (IQ) map with HAGBs and low-angle grain boundaries (LAGBs) superimposed. **h**, A map of the kernel average misorientation (KAM), measured in degrees, to illustrate the local misorientation across individual grain. **i**, A HAADF STEM (Z contrast) image showing segregation of Mo and

Cr to the solidification cellular walls and a LAGB, with corresponding Fe, Mo, and Cr energy-dispersive spectroscopy (EDS) maps that confirm this segregation.

AM materials produced by laser powder-bed-fusion (L-PBF) feature highly non-equilibrium microstructures such as high dislocation density, irregular and tortuous grain morphologies, cellular structures, and chemical segregation. These unique microstructural characteristics result in mechanical properties that significantly differ from traditional materials. The L-PBF technology shares many common roots with welding as both processes melt and bond materials by utilizing a localized heat source. The highly localized heating and rapid cooling associated with a melt pool, in conjunction with the repetition of this thermomechanical process layer-by-layer, give rise to large thermal gradients and therefore large residual stresses within highly non-equilibrium microstructures as shown in Figure 1.4. The thermal gradients are affected by many processing parameters, including build plate/powder bed temperature, laser power, powder thermophysical characteristics, melt pool size, etc. The convolution of these processing parameters often leads to a complex residual stress field within the build part. It remains a great challenge to understand the origin and impact of complex residual stresses correlated to the heterogeneities. While recent studies on the macroscale residual stresses in AM materials have revealed various deleterious effects such as loss of net shape, detachment from support structures, or even failure of the build parts, the influences of the microscale residual stress on the mechanical performance of AM materials remain elusive, due largely to the difficulty of measurements of their spatial-temporal evolution at the micrometer length scales.

In the first part of this thesis, we develop a crystal plasticity finite element (CPFE) model to quantitatively characterize the effects of both intragranular and intergranular internal stresses on AM stainless steels. This CPFE model is further extended to investigate an AM high-entropy alloy with a dual-phase microstructure; the dual-phase CPFE model is used to inversely determine the elastic-plastic properties of individual phases based on in situ neutron diffraction experiments. The CPFE simulations are applied to interpret experimental results and provide guidance for improving the mechanical properties of AM materials through tuning the printing conditions and heterogeneous microstructures.

1.2.2 Macroscale Heterogeneities in Gradient Nanotwinned Cu

In addition to microscale heterogeneities in AM materials, macroscale heterogeneities can lead to an exceptional combination of high strength and ductility, for example, in gradient nanotwinned Cu (GNT-Cu) [9]. The extraordinary strengthening effect of GNT-Cu results from plastic strain gradients arising in plastically deformed gradient structures. As shown in Figure 1.5, an increase in nanostructure gradient causes a marked increase of the sample-level yield strength, and a large nanostructure gradient produces a high yield strength exceeding that of the strongest component of the gradient nanostructure. The extra strength is measured as a function of structure and strength gradients. These results call for a fundamental understanding of the strengthening effects of plastic strain gradients originating from gradient nanostructures. In addition, given the high tunability of its gradient structures, GNT Cu can serve as an effective model system for benchmarking the gradient theories of plasticity.

In the second part of this thesis, we develop a gradient theory of plasticity by incorporating the strengthening effect of plastic strain gradient into the J_2 flow theory. Motivated by the simple gradient theory of plasticity by Bassani [10], a scalar measure of plastic strain gradient is introduced into a hardening rate relation, so that higher-order stresses and additional boundary conditions are not needed. This approach enables a quantitative analysis of strain gradient plasticity without much mathematical complexity. To study the gradient plastic responses of GNT Cu under uniaxial tension, we reduce the general three-dimensional (3D) gradient theory into a one-dimensional (1D) theory, and numerically implement this 1D theory with the finite-difference method. Numerical simulations reveal the primary effects of strain gradient plasticity on GNT Cu with different structure gradients. Also, we numerically implement the 3D gradient theory into the general finite element package ABAQUS/Explicit by writing user subroutines and simulate the 3D stress-strain responses in GNT Cu by accounting for the effects of strain gradient plasticity. Based on insights gained from both 1D and 3D gradient plasticity simulations, we explore the optimization of structure and strength gradients toward achieving the maximum strength of GNT Cu.

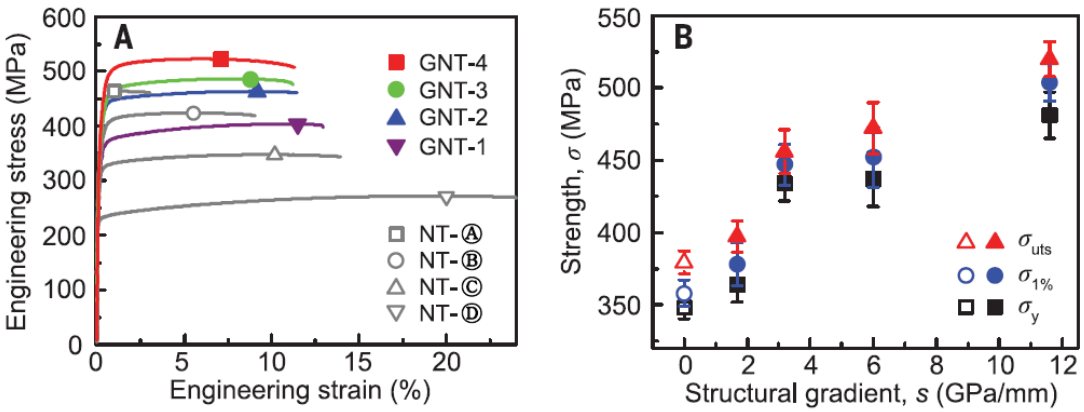

Figure 1.5 Mechanical properties of GNT structures adapted from [11], (A) Tensile engineering stress-strain relations of GNT samples in comparison with those of homogeneous nanotwinned components. (B) Yield strength, stress at 1% strain, and ultimate tensile strength of GNT samples with various structural gradients.

Heterogeneous materials often exhibit significant back stress upon unloading. Based on the experimentally measured back stress, a mechanistically-based gradient plasticity finite element (GPFE) model is further developed to directly elucidate the origin of extra strengths arising from strain gradient plasticity, so as to connect the back stresses with underlying gradient microstructures. These GPFE models allow us to design GNT materials with higher strengths by optimizing the structural gradient distributions.

1.2.3 Nanoscale Heterogeneities in Nanocrystalline Metals and Composites

Beyond the constitutive modeling of micro- and macro-scale heterogeneities in Part I and II, we investigate the mechanics of nanoscale heterogeneities including interfaces using atomistic simulations. Strengthening in structural metals and alloys is often built upon a fundamental principle of hindering dislocation glide through the rational deployment of different types of obstacles, e.g., precipitates and grain boundaries. Incorporation of second phases with high hardness and stiffness into a metal matrix, forming metal matrix composites, provides an effective approach for strengthening and stabilizing metal nanostructures. For nanocrystalline and ultrafine-grained metals, grain boundaries impede further dislocation glide, raising plastic deformation resistance. Our atomistic simulations are coupled with experiments to provide an in-depth understanding of the strengthening effects of those nanoscale heterogeneities.

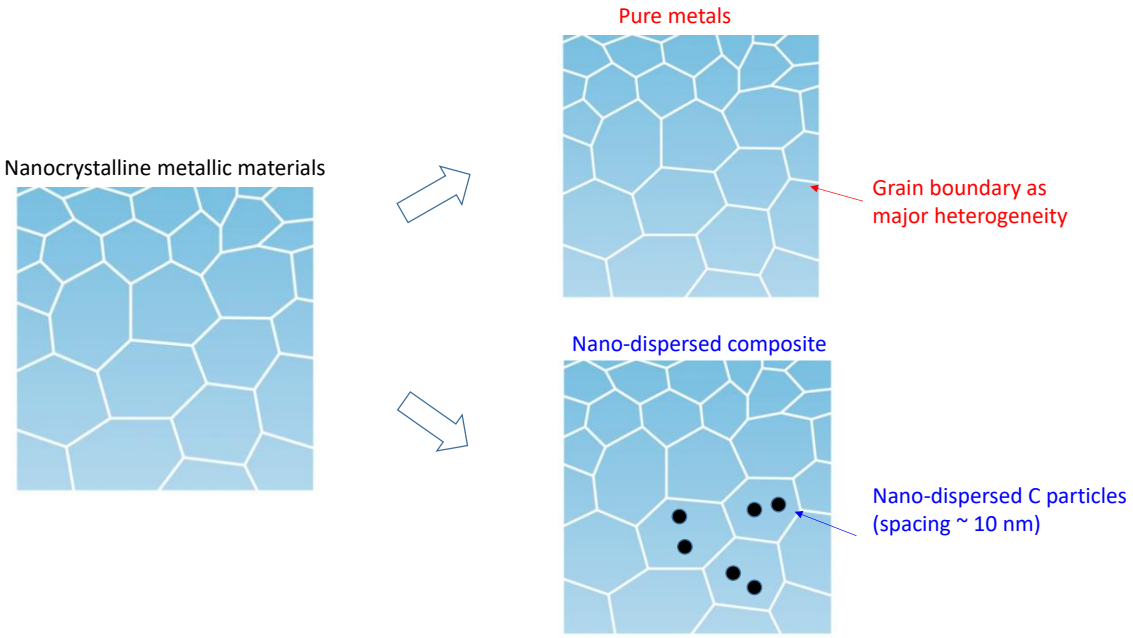

Figure 1.6 Two major heterogeneities in nanocrystalline metals and alloys. (Top right) Grain boundaries in nanocrystalline metals Au and Al. (Bottom right) Nano-dispersed carbon particles in Cu

We perform molecular dynamics (MD) simulations using LAMMPS [12] to study the interaction between dislocations and nano-C particles. The atomic interactions in the Cu-C system are modeled by combining the embedded atom method (EAM) potential for Cu-Cu interaction, the Tersoff potential for C-C interaction, and the Lennard-Jones potential for Cu-C interaction. Our MD simulations and theoretical analyses enable a fundamental understanding of the underlying mechanisms responsible for the ultrahigh strength and high hardening of the nanocomposites with nano-C embedded in a nanocrystalline Cu matrix. In addition to nano-C reinforced metal matrix composites, we investigate the atomic-scale plastic deformation mechanisms in ultrafine-grained/nanocrystalline thin films of Al and Au, in order to understand the effects of nanoscale heterogeneities on the evolution of deformed nanocrystalline structures. Recently, our experimental collaborators

observed pronounced grain growth in ultrafine-grained thin films of Al and Au by in situ transmission electron microscopy (TEM) straining experiments. To understand these experimental results, we conduct MD simulations of nanocrystalline Al films and use a newly-developed coloring scheme to track GB migration over time. The combined in situ TEM observation and MD simulation results can reveal the important role of grain growth in plastically deforming nanocrystalline Al. Moreover, our experimental collaborators used a MEMS-based nanomechanical testing platform to measure the stress relaxation responses and associated activation volumes in ultrafine-grained Au and Al thin films. To interpret their experimental results and further guide experimental design, we investigate the thermal activation of dislocation nucleation by atomistic reaction pathway calculations using the nudged elastic band (NEB) method. The NEB method allows us to overcome the timescale limitation of MD simulations. As such, we directly compare the atomistically calculated activation volumes with the corresponding experimental measurements. The combined in situ activation volume measurement and atomistic simulation enable us to understand the rate-limiting plastic deformation mechanisms in ultrafine-grained metallic materials.

Part I: Microscale Heterogeneities in Additively Manufactured Alloys

CHAPTER 2. LATTICE STRAINS AND DIFFRACTION EXPERIMENTS

2.1 Introduction

In situ synchrotron X-ray diffraction (SXRD) and neutron diffraction experiments are widely used in a broad range of disciplines, including materials science, geophysics, environmental science, biophysics and others [13, 14]. They can provide measurements of the average lattice strains in different families of grains with specific orientations in polycrystalline materials [4, 15]. In the elastic regime, the lattice strain of individual grains increases linearly with the macroscopically applied stress, as demonstrated, for example, by neutron diffraction of copper [15], steel [16-20], nickel-based alloys [21, 22], and SXRD of austenitic stainless steel [23, 24]. The linear relationship also holds for the average lattice strains in each grain family and is usually characterized by the so-called diffraction elastic constants [25-28], which vary with the orientation of the grain family. The lattice strains and diffraction elastic constants have many possible uses in the analysis of microscale residual stresses [29] and progressive yielding [23, 24]. However, it is hard to find solutions for lattice strains and diffraction elastic constants of many materials in the literature. The demand for these solutions is expected to grow in the coming years, as *in situ* diffraction experiments can be used for high-throughput and data-analytics studies of the mechanical behavior of polycrystalline materials with varying compositions and microstructures, such as high-entropy alloys [30], additively manufactured alloys [23, 24], heterogeneous nanostructured metals and alloys [3, 31], and others.

In this Chapter, we make a combined use of the classical Eshelby inclusion solution [32] and the self-consistent method of microstructure homogenization [33] to derive a general analytic solution of the grain-level lattice strains and diffraction elastic constants. This solution is applicable to a broad class of elastically isotropic polycrystals with cubic crystal symmetry, including face-centered cubic (FCC), body-centered cubic (BCC) and diamond cubic (DC) crystals. Bollenrath, Hauk and Müller [25] derived an analytic solution of diffraction elastic constants of a cubic polycrystal using Kröner's self-consistent method [34]. De Wit obtained alternative solutions of diffraction elastic constants [27]. But they did not provide the general analytic solution of lattice strains, and their derivations of the diffraction elastic constant solutions were not completely presented. The diffraction elastic constants can be also calculated using different numerical methods. One is based on the self-consistent polycrystal model that requires a numerical average of lattice strains in grains within the same family [15]. Another is based on the finite element polycrystal model that relies on a full numerical calculation of lattice strains in a polycrystalline aggregate [35]. Nonetheless, the analytic solutions are highly desired to facilitate the clear understanding and robust parametric study of the lattice strain effects. Here we adopt a modern micromechanics notation [33] to derive a general analytic solution of the lattice strains and diffraction elastic constants for cubic polycrystals. This solution can be readily understood and applied. It only requires an input of the three independent elastic constants of a cubic crystal. The associated numerical results are validated by literature data as well as polycrystal elasticity finite element simulations. Since the present solution requires only simple algebraic calculations, one can pursue straightforward numerical calculations to

determine lattice strains and diffraction elastic constants for any cubic polycrystals using a MATLAB code.

2.2 Lattice Strains and Diffraction Elastic Constants

Figure 2.1a shows the schematic diagram of *in situ* SXRD measurement of lattice strains in a polycrystalline specimen under uniaxial tension. An incident X-ray beam into the specimen is diffracted to generate a series of Debye-Scherrer rings [36]. Each diffracted spot (i.e., red segment) on a ring corresponds to a family of grains with a common crystallographic plane, such as a {111} plane, oriented along a specific spatial direction, for example, the loading direction (denoted as LD), transverse direction (TD), or normal direction (ND) of the specimen. By tracking the change of lattice spacings during tensile testing, one can obtain the average lattice strains in different grain families as a function of applied load, and further calculate the stresses in these grain families using single-crystal elastic constants. Figure 2.1b shows a two-dimensional cross section of a representative volume element (RVE) in the tensile specimen. In a typical grain (highlighted in red) in this RVE, the unit normal vector $\mathbf{n}$ of a set of lattice planes is oriented along LD, and the unit normal vector $\mathbf{m}$ of another set of lattice planes is oriented along TD. Each grain is associated with a set of the orthonormal crystal basis vectors $\left\{\mathbf{e}_1^c, \mathbf{e}_2^c, \mathbf{e}_3^c\right\}$. Also plotted are the representative grains in different {*hkl*} grain families oriented along LD. Different grain families usually exhibit different lattice strains and diffraction elastic constants, due to the elastic anisotropy of grain crystals.

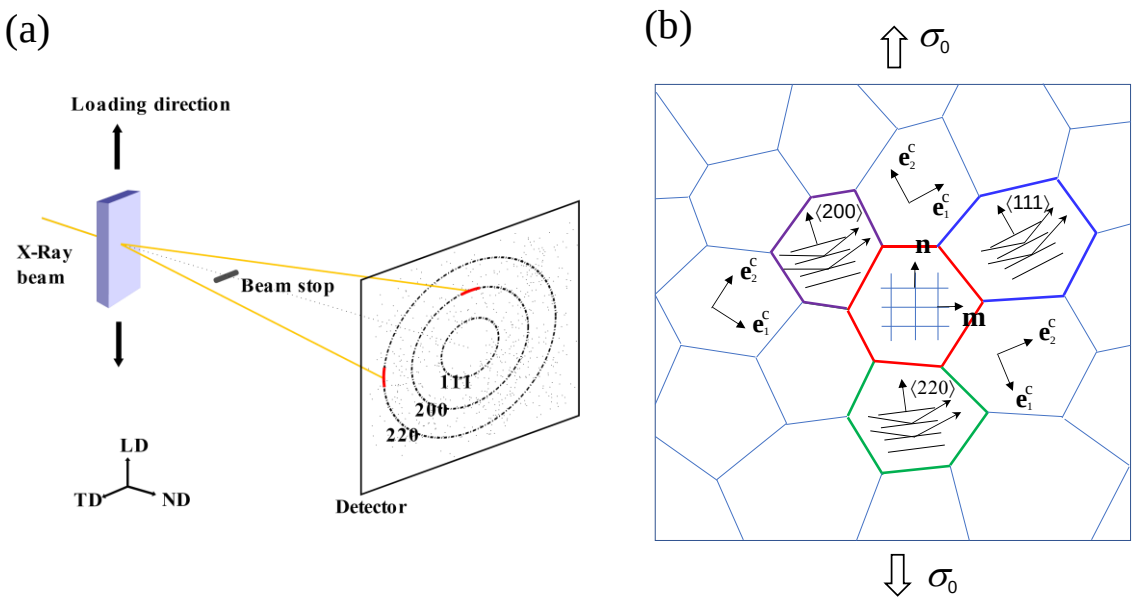

Figure 2.1 Schematic diagrams of *in situ* SXRD measurements of lattice strains in a polycrystalline material. (a) Schematic of SXRD experiment, showing an incident X-ray beam into a polycrystalline specimen diffracted to generate a series of Debye-Scherrer rings. The loading direction (denoted as LD), transverse direction (TD), and normal direction (ND) of the specimen are marked. (b) Schematic of a cross section of a representative volume element (RVE) of a polycrystalline aggregate in the tensile specimen in (a), subject to an uniaxial tensile stress σ_0. The unit normal vector $\mathbf{n}$ is oriented along LD and $\mathbf{m}$ along TD. Each grain is associated with a set of local orthonormal crystal basis vectors $\mathbf{e}_1^c, \mathbf{e}_2^c$, and $\mathbf{e}_3^c$ (not shown). Representative grains in respective {200}, {220} and {111} families oriented along LD are marked.

Consider a {*hkl*} grain family consisting of *N* grains in an RVE (Figure 2.1b). These grains are numbered by 1,… α,…, *N*. To predict the average lattice strains and diffraction elastic constants in this grain family, one needs to derive a linear tensorial relation between the macroscopic stress $\overline{\sigma}_{ij}$ and the strain $\varepsilon_{ij}^{(\alpha)}$ in the grain α, i.e.,

$$\varepsilon_{ij}^{(\alpha)} = U_{ijkl}^{(\alpha)} \overline{\sigma}_{kl} \tag{2.1}$$

where $U_{ijkl}^{(\alpha)}$ is the constrained compliance tensor of the grain α embedded in the polycrystal. It should be noted that under a macroscopically applied load, the strain response of the grain α in a polycrystal is not merely determined by single-crystal elastic constants, since elastic anisotropic grains interact with each other to adjust local strains for accommodating their deformation incompatibility. Hence, $U_{ijkl}^{(\alpha)}$ is different from the single-crystal compliance tensor $M_{ijkl}^{(\alpha)}$ and will be derived in Section 2.3. Also note that throughout this paper, all the components of vectors and tensors expressed with the index notation are resolved in the local orthonormal basis of the grain crystal, e.g., $\left\{\mathbf{e}_1^{c,(\alpha)}, \mathbf{e}_2^{c,(\alpha)}, \mathbf{e}_3^{c,(\alpha)}\right\}$ in grain α; the Einstein summation convention is used for repeated indices, except for repeated α and β.

Under an applied uniaxial tensile stress σ_0 (Figure 2.1b), the macroscopic stress tensor $\overline{\sigma}_{ij}$ acting on the polycrystalline RVE can be expressed as

$$\overline{\sigma}_{ij} = \sigma_0 n_i^{(\alpha)} n_j^{(\alpha)} \tag{2.2}$$

where $n_i^{(\alpha)}$ denotes the components of the unit vector along LD resolved in terms of the local cubic basis of the single-crystal grain α. The lattice strain $\varepsilon_{\mathrm{LD}}^{(\alpha)}$ along LD can be similarly resolved in terms of the local cubic basis as

$$\varepsilon_{\mathrm{LD}}^{(\alpha)} = \varepsilon_{ij}^{(\alpha)} n_i^{(\alpha)} n_j^{(\alpha)} \tag{2.3}$$

Substitution of Eqs. (2.1) and (2.2) into Eq. (2.3) yields

$$\varepsilon_{\mathrm{LD}}^{(\alpha)} = \sigma_0 U_{ijkl}^{(\alpha)} n_i^{(\alpha)} n_j^{(\alpha)} n_k^{(\alpha)} n_l^{(\alpha)} \tag{2.4}$$

The average lattice strain $\bar{\varepsilon}_{\mathrm{LD}}$ in the {*hkl*} grain family along LD is, therefore, given by

$$\bar{\varepsilon}_{\mathrm{LD}} = \frac{1}{N} \sum_{\alpha=1}^{N} \varepsilon_{\mathrm{LD}}^{(\alpha)} \tag{2.5}$$

The corresponding diffraction elastic constant is defined as

$$\frac{1}{E_{\mathrm{LD}}^{hkl}} = \frac{\bar{\varepsilon}_{\mathrm{LD}}}{\sigma_0} \tag{2.6}$$

Combining Eqs. (2.4-2.6), one can express E_{LD}^{hkl} as

$$\frac{1}{E_{\mathrm{LD}}^{hkl}} = \frac{1}{N} \sum_{\alpha=1}^{N} U_{ijkl}^{(\alpha)} n_i^{(\alpha)} n_j^{(\alpha)} n_k^{(\alpha)} n_l^{(\alpha)} \tag{2.7}$$

once $U_{ijkl}^{(\alpha)}$ is specified.

2.3 General Solution for the Constrained Compliance Tensor **U**

As shown in section 2.2, the constrained compliance tensor $U_{ijkl}^{(\alpha)}$ is key to determining the lattice strains and diffraction elastic constants for a cubic polycrystal. In this section, a general solution of this compliance tensor is derived using the direct notation. We consider a polycrystalline RVE with a specific distribution of grain orientations. The anisotropic elasticity tensor of the grain α is denoted as $\mathbf{L}^{(\alpha)}$. As discussed earlier, the lattice strain response of this grain is not merely determined by $\mathbf{L}^{(\alpha)}$, since elastic anisotropic grains

interact with each other to adjust local strains. To account for such grain interactions, we consider a single-crystal grain in an RVE as a spherical inclusion embedded in a homogeneous matrix. As shown by Eshelby [32], the stress and strain fields are uniform in the spherical inclusion and can be determined using the Eshelby inclusion solution. We determine the effective elastic stiffness tensor of the homogeneous matrix $\bar{\mathbf{L}}$ using the self-consistent method [33]. The macroscopic stress $\bar{\boldsymbol{\sigma}}$ and strain $\bar{\boldsymbol{\varepsilon}}$ applied to the RVE are taken to be the volume averages of the stress and strain in all the grains, respectively. They are related by

$$\bar{\boldsymbol{\sigma}} = \bar{\mathbf{L}}\bar{\boldsymbol{\varepsilon}}, \ \bar{\boldsymbol{\varepsilon}} = \bar{\mathbf{M}}\bar{\boldsymbol{\sigma}} \tag{2.8}$$

where $\bar{\mathbf{M}}$ is the effective elastic compliance tensor of the RVE, i.e., $\bar{\mathbf{M}} = \bar{\mathbf{L}}^{-1}$. When the RVE is subjected to macroscopic applied strain, $\bar{\boldsymbol{\varepsilon}}$, the Eshelby inclusion solution [33] shows that the uniform strain $\boldsymbol{\varepsilon}^{(\alpha)}$ in the spherical grain inclusion is given by

$$\boldsymbol{\varepsilon}^{(\alpha)} = \mathbf{T}^{(\alpha)}\bar{\boldsymbol{\varepsilon}} \tag{2.9}$$

where the global strain concentration tensor $\mathbf{T}^{(\alpha)}$ [33] is given by

$$\mathbf{T}^{(\alpha)} = \left[\mathbf{I} + \mathbf{S}^{(\alpha)}\bar{\mathbf{L}}^{-1}\left(\mathbf{L}^{(\alpha)} - \bar{\mathbf{L}}\right)\right]^{-1} \tag{2.10}$$

In Eq. (2.10), $\mathbf{I}$ is the fourth rank identify tensor and $\mathbf{S}^{(\alpha)}$ is the Eshelby inclusion tensor of a spherical grain inclusion embedded in a matrix with the elastic stiffness tensor of $\bar{\mathbf{L}}$. From Eqs. (2.8) & (2.9), the strain $\boldsymbol{\varepsilon}^{(\alpha)}$ in the grain α can be expressed in terms of the macroscopic stress $\bar{\boldsymbol{\sigma}}$ as

$$\boldsymbol{\varepsilon}^{(\alpha)} = \mathbf{U}^{(\alpha)}\overline{\boldsymbol{\sigma}} \tag{2.11}$$

where the grain compliance tensor $\mathbf{U}^{(\alpha)}$ is given by

$$\mathbf{U}^{(\alpha)} = \mathbf{T}^{(\alpha)}\overline{\mathbf{M}} \tag{2.12}$$

2.4 Constrained Compliance Tensor $\mathbf{U}$ in a Cubic Polycrystal

From the grain compliance tensor $\mathbf{U}^{(\alpha)}$ given in Section 3, we derive a general solution of the diffraction elastic constants for an elastically isotropic polycrystal with cubic crystal symmetry. Using the index notation, the components of $\mathbf{L}^{(\alpha)}$ can be expressed in terms of the local crystal basis as [33]

$$L_{ijkl}^{(\alpha)} = C_{12}\delta_{ij}\delta_{kl} + C_{44}\left(\delta_{ik}\delta_{jl} + \delta_{il}\delta_{jk}\right) + \left(C_{11} - C_{12} - 2C_{44}\right)d_{ijkl} \tag{2.13}$$

where C_{11}, C_{12} and C_{44} are the single-crystal elastic constants, δ_{ij} is the Kronecker delta and the non-zero components of d_{ijkl} are $d_{1111} = d_{2222} = d_{3333} = 1$. As shown by Qu and Cherkaoui [33], it is helpful to introduce the symbolic representations for the fourth-order tensors involved, so as to facilitate a convenient algebraic operation for these tensors, including addition, subtraction, multiplication, and inverse. To this end, the components of $\mathbf{L}^{(\alpha)}$ can be equivalently written as

$$L_{ijkl}^{(\alpha)} = \left(3\eta_1 - 2\eta_2\right)\frac{1}{3}\delta_{ij}\delta_{kl} + 2\eta_3\frac{1}{2}\left(\delta_{ik}\delta_{jl} + \delta_{il}\delta_{jk}\right) + \left(2\eta_2 - 2\eta_3\right)d_{ijkl} \tag{2.14}$$

where $3\eta_1 = C_{11} + 2C_{12}, 2\eta_2 = C_{11} - C_{12}$ and $2\eta_3 = 2C_{44}$. Then the fourth-order tensor $\mathbf{L}^{(\alpha)}$ in Eq. (2.14) can be written symbolically as [37]

$$\mathbf{L}^{(\alpha)} = \left(3\eta_1, 2\eta_2, 2\eta_3\right) \tag{2.15}$$

We consider a polycrystal having random grain orientations and thus an isotropic elasticity tensor $\overline{\mathbf{L}}$. With the same symbolic notation, $\overline{\mathbf{L}}$ and its corresponding compliance tensor $\overline{\mathbf{M}}$ are respectively written as

$$\overline{\mathbf{L}} = \left(3\overline{K}, 2\overline{\mu}, 2\overline{\mu}\right) \text{ and } \overline{\mathbf{M}} = \left(\frac{1}{3\overline{K}}, \frac{1}{2\overline{\mu}}, \frac{1}{2\overline{\mu}}\right) \tag{2.16}$$

where $\overline{K}$ is the effective bulk modulus and $\overline{\mu}$ is the effective shear modulus of the elastically isotropic polycrystal. The equations for $\overline{K}$ and $\overline{\mu}$ from the self-consistent solution [37] are given by

$$\overline{K} = \frac{1}{3}\left(C_{11} + 2C_{12}\right) \tag{2.17}$$

$$8\overline{\mu}^3 + \left(5C_{11} + 4C_{12}\right)\overline{\mu}^2 - C_{44}\left(7C_{11} - 4C_{12}\right)\overline{\mu} - C_{44}\left(C_{11} - C_{12}\right)\left(C_{11} + 2C_{12}\right) = 0 \tag{2.18}$$

Given the single-crystal elastic constants, one can calculate $\overline{K}$ from Eq. (2.17) and $\overline{\mu}$ by solving Eq. (2.18). On the other hand, the Eshelby inclusion tensor for a spherical inclusion in an elastically isotropic matrix can be written symbolically as [33]

$$\mathbf{S}^{(\alpha)} = \left(3\overline{\gamma}, 2\overline{\delta}, 2\overline{\delta}\right) \tag{2.19}$$

where

$$\bar{\gamma} = \frac{\overline{K}}{3\overline{K} + 4\overline{\mu}} \text{ and } \bar{\delta} = \frac{3\overline{K} + 6\overline{\mu}}{15\overline{K} + 20\overline{\mu}} \tag{2.20}$$

In addition, the fourth-order identity tensor is $\mathbf{I} = (1,1,1)$. Our symbolic calculations of $\mathbf{T}^{(\alpha)}$ based on Eq. (2.10) and $\mathbf{U}^{(\alpha)}$ based on Eq. (2.12) yield

$$\mathbf{U}^{(\alpha)} = \left(\frac{1}{3\left[\overline{K} + \bar{\gamma}(3\eta_1 - 3\overline{K})\right]}, \frac{1}{2\left[\overline{\mu} + \bar{\delta}(2\eta_2 - 2\overline{\mu})\right]}, \frac{1}{2\left[\overline{\mu} + \bar{\delta}(2\eta_3 - 2\overline{\mu})\right]} \right) \tag{2.21}$$

To proceed further, we represent $\mathbf{U}^{(\alpha)}$ symbolically as

$$\mathbf{U}^{(\alpha)} = (3a, 2b, 2c) \tag{2.22}$$

where $3a$, $2b$ and $2c$ correspond to the respective component of $\mathbf{U}^{(\alpha)}$ in Eq. (2.21). By comparing Eqs. (2.14) and (2.15), we rewrite $\mathbf{U}^{(\alpha)}$ in Eq. (2.22) as

$$U_{ijkl}^{(\alpha)} = (3a - 2b)\frac{1}{3}\delta_{ij}\delta_{kl} + 2c\frac{1}{2}\left(\delta_{ik}\delta_{jl} + \delta_{il}\delta_{jk}\right) + (2b - 2c)\, d_{ijkl} \tag{2.23}$$

The solution of $U_{ijkl}^{(\alpha)}$ in Eq. (2.23) enables numerical calculations of the lattice strains and diffraction elastic constants in Sections 5 and 6, as well as the grain-level stresses for the study of progressive yielding in different grain families [24]. It should be emphasized that this solution applies to a random orientation of grains. Consideration of crystallographic textured polycrystals is beyond the scope of this work.

2.5 Diffraction Elastic Constants along LD

Consider the grain α in a {*hkl*} grain family along LD. In the crystal basis of this grain, the component of the unit vector $\mathbf{n}^{(\alpha)}$ along the [*hkl*] direction can be expressed as

$$\mathbf{n}^{(\alpha)} = \left(n_1^{(\alpha)}, n_2^{(\alpha)}, n_3^{(\alpha)}\right) = \left(h,k,l\right)/\sqrt{h^2+k^2+l^2} \tag{2.24}$$

From Eqs. (2.7) and (2.23), the diffraction elastic constant for the {*hkl*} grain family along LD is derived as

$$\frac{1}{E_{\mathrm{LD}}^{hkl}} = \frac{1}{N}\sum_{\alpha=1}^{N}\left[\frac{3a-2b}{3}n_i^{(\alpha)}n_i^{(\alpha)}n_k^{(\alpha)}n_k^{(\alpha)} + 2cn_i^{(\alpha)}n_i^{(\alpha)}n_j^{(\alpha)}n_j^{(\alpha)} + 2\left(b-c\right)\sum_{i}^{3}\left(n_i^{(\alpha)}\right)^4\right] \tag{2.25}$$

With $n_i^{(\alpha)}n_i^{(\alpha)} = 1$, substitution of Eq. (2.24) into Eq. (2.25) yields

$$\frac{1}{E_{\mathrm{LD}}^{hkl}} = \frac{3a+4b}{3} - 4\left(b-c\right)\Gamma \tag{2.26}$$

where the orientation index parameter Γ is defined as

$$\Gamma = \frac{h^2k^2+l^2k^2+h^2l^2}{\left(h^2+k^2+l^2\right)^2} \tag{2.27}$$

This orientation parameter varies between 0 and 1/3 to cover all the grain families with random orientations, and they are 0, 19/121, 1/4 and 1/3 for the representative grain families of {200}, {311}, {220} and {111}, respectively. Equation (2.26) reveals a linear dependence of $1/E_{\mathrm{LD}}^{hkl}$ on Γ, which is modulated by $b-c$. Since $4\left(b-c\right) = \overline{\delta}(\eta_3-\eta_2)/\left\{\left[\overline{\mu}+\overline{\delta}(2\eta_2-2\overline{\mu})\right]\left[\overline{\mu}+\overline{\delta}(2\eta_3-2\overline{\mu})\right]\right\}$, the sign of $4\left(b-c\right)$ is

determined by the anisotropy ratio $A = 2C_{44}/(C_{11}-C_{12}) = \eta_3/\eta_2$. Hence, Eq. (2.26) indicates that if $A > 1$, then $b - c > 0$ and thus E_{LD}^{hkl} increases for increasing Γ, and vice versa. For example, $E_{\mathrm{LD}}^{111} > E_{\mathrm{LD}}^{200}$ for FCC Cu, because of A = 3.21, while $E_{\mathrm{LD}}^{111} < E_{\mathrm{LD}}^{200}$ for BCC Nb, due to A = 0.49. This analysis relates the anisotropy ratio A with the relative magnitude of E_{LD}^{111} and E_{LD}^{200}, a factor that strongly influences the progressive yielding responses during loading and the residual stresses after unloading in different grain families [4].

Using the analytic solution of Eq. (2.26), we calculated the diffraction elastic constants for various cubic polycrystals, with the experimental values of single-crystal elastic constants [38] (as also provided in the Appendix). Table 1 lists the numerical results of the diffraction elastic constants along LD for 26 representative elastically isotropic polycrystals with FCC, BCC and DC crystal symmetries (as indicated in the Appendix).

Table 2.1 Diffraction elastic constants E^{hkl} along LD (in GPa)

	E^{200}	E^{220}	E^{111}	E^{311}
Ag	65.30	88.43	100.27	78.14
Al	67.09	71.29	72.80	69.67
Au	63.55	84.69	95.25	75.36
Cu	101.15	139.06	158.91	122.05
Ir	491.12	554.66	579.65	529.19
Ni	183.74	237.86	263.76	214.38

Table 2.1 continued

Pb	18.59	26.97	31.74	23.10
Pd	107.11	142.53	160.18	126.92
Pt	159.41	182.98	192.47	173.45
Cr	298.59	267.89	259.02	278.54
Fe	175.18	224.29	247.40	203.11
K	2.50	3.96	4.92	3.25
Li	7.43	12.4	15.97	9.93
Mo	335.10	325.04	321.81	328.71
Na	4.41	7.56	9.92	5.98
Nb	127.25	100.46	93.87	109
Ta	166.76	190.41	199.86	180.87
V	136.79	126.33	123.19	130.03
W	408.65	410.07	410.55	409.54
C	963.66	1037.68	1064.95	1008.86
Ge	117.23	135.63	143.12	128.15
Si	147.69	168.02	176.10	159.84
CuZn	70.13	116.95	150.42	93.69
Cu_3Au	103.15	133.9	148.67	120.54
NiAl	144.94	200.23	229.4	175.35
SS 316L	149.25	212.69	247.81	183.66

To validate the present analytic solution and associated calculations of diffraction elastic constants, we compared our numerical results of FCC Cu and stainless steel (SS)

316L with literature data. Table 2.2 shows that our results of diffraction elastic constants along LD closely match those by Clausen *et al*. [15], who used the Kröner self-consistent solution and the same sets of single-crystal elastic constants as ours. In addition, Table 2.2 shows that our results for diffraction elastic constants along LD for SS 316L reasonably agree with SXRD measurements [24].

Table 2.2 Comparison the present model predictions of diffraction elastic constants E^{hkl} (in GPa) along LD with those by Clausen *et al*. [15] for Cu and SS 316L and with SXRD measurements for SS 316L [24].

	E^{200}	E^{220}	E^{111}	E^{311}
Cu (this work)	101.2	139.1	158.9	122.1
Cu [15]	101.5	138.7	158.0	121.8
SS 316L (this work)	149.3	212.7	247.8	183.7
SS 316L [15]	149.8	212.0	246.2	183.2
SS 316L [24]	139.1	219.1	264.1	179.6

2.6 Diffraction Elastic Constants along TD

Consider a {*hkl*} grain family along TD in an RVE (Figure 2.1b). The grains in this family are numbered as 1,… β ,…, *N*. In the local crystal basis of the grain β, the component of the unit vector $\mathbf{m}^{(\beta)}$ along the [*hkl*] direction can be expressed as

$$\mathbf{m}^{(\beta)} = \left(m_1^{(\beta)}, m_2^{(\beta)}, m_3^{(\beta)}\right) = \left(h,k,l\right) / \sqrt{h^2 + k^2 + l^2} \tag{2.28}$$

It should be emphasized that in this $\{hkl\}$ grain family, the unit vector along LD, $\mathbf{n}^{(\beta)}$, can be any vector perpendicular to $\mathbf{m}^{(\beta)}$. Without loss of generality, we can express $\mathbf{n}^{(\beta)}$ using a single variable θ. Specifically, we introduce the orthonormal basis vectors $\mathbf{p}^{(\beta)}$ and $\mathbf{q}^{(\beta)}$ in the plane perpendicular to $\mathbf{m}^{(\beta)}$

$$\begin{aligned}\mathbf{p}^{(\beta)} &= \left(p_1^{(\beta)}, p_2^{(\beta)}, p_3^{(\beta)}\right) = \left(-k, h, 0\right) / \sqrt{h^2 + k^2} \\ \mathbf{q}^{(\beta)} &= \left(q_1^{(\beta)}, q_2^{(\beta)}, q_3^{(\beta)}\right) = \left(hl, kl, -h^2 - k^2\right) / \sqrt{\left(h^2 + k^2\right)\left(h^2 + k^2 + l^2\right)}\end{aligned} \tag{2.29}$$

Then, $\mathbf{n}^{(\beta)}$ can be expressed as

$$\mathbf{n}^{(\beta)} = \mathbf{p}^{(\beta)} \cos\theta + \mathbf{q}^{(\beta)} \sin\theta \tag{2.30}$$

with θ as the angle between $\mathbf{n}^{(\beta)}$ and $\mathbf{p}^{(\beta)}$. By this construction, $\mathbf{n}^{(\beta)}$ is perpendicular to $\mathbf{m}^{(\beta)}$ automatically.

Similar to $\varepsilon_{\mathrm{LD}}^{(\alpha)}$ in Eq. (2.3), the lattice strain $\varepsilon_{\mathrm{TD}}^{(\beta)}$ along TD can be calculated as

$$\varepsilon_{\mathrm{TD}}^{(\beta)} = \varepsilon_{ij}^{(\beta)} m_i^{(\beta)} m_j^{(\beta)} \tag{2.31}$$

Substitution of Eq. (2.1) (replacing α by β) into Eq. (2.31) yields

$$\varepsilon_{\mathrm{TD}}^{(\beta)} = \sigma_0 U_{ijkl}^{(\beta)} m_i^{(\beta)} m_j^{(\beta)} n_k^{(\beta)} n_l^{(\beta)} \tag{2.32}$$

The average lattice strain $\bar{\varepsilon}_{\mathrm{TD}}$ in the {*hkl*} grain family along TD is given by

$$\bar{\varepsilon}_{\mathrm{TD}} = \frac{1}{N}\sum_{\beta=1}^{N} \varepsilon_{\mathrm{TD}}^{(\beta)} \tag{2.33}$$

The corresponding diffraction elastic constant E_{TD}^{hkl} is defined as

$$\frac{1}{E_{\mathrm{TD}}^{hkl}} = -\frac{\bar{\varepsilon}_{\mathrm{TD}}}{\sigma_0} \tag{2.34}$$

Since σ_0 and $\bar{\varepsilon}_{\mathrm{TD}}$ have opposite signs by virtue of Poisson's effect, E_{TD}^{hkl} defined in Eq. (2.34) is positive. From Eqs. (2.32) to (2.34), E_{TD}^{hkl} can be expressed as

$$\frac{1}{E_{\mathrm{TD}}^{hkl}} = -\frac{1}{N}\sum_{\beta=1}^{N} U_{ijkl}^{(\beta)} n_i^{(\beta)} n_j^{(\beta)} m_k^{(\beta)} m_l^{(\beta)} \tag{2.35}$$

Substitution of Eq. (2.23) into Eq. (2.35) yields

$$\frac{1}{E_{\mathrm{TD}}^{hkl}} = -\frac{1}{N}\sum_{\beta=1}^{N}\left[\frac{3a-2b}{3} + 2\left(b-c\right)\sum_{i=1}^{3}\left(n_i^{(\beta)}\right)^2\left(m_i^{(\beta)}\right)^2\right] \tag{2.36}$$

For a sufficiently large RVE, the {*hkl*} grain family along TD should contain a sufficient number of grains with random orientations in the plane spanned by $\mathbf{p}^{(\beta)}$ and $\mathbf{q}^{(\beta)}$. Hence, one can change the summation over β grains in Eq. (2.36) to the integration over θ from 0 to 2π, and then use Eq. (2.30) to obtain

$$\begin{aligned}\frac{1}{E_{\mathrm{TD}}^{hkl}} &= -\frac{3a-2b}{3} - 2(b-c)\frac{1}{2\pi}\int_0^{2\pi}\sum_{i=1}^{3}\left(p_i^{(\beta)}\cos\theta + q_i^{(\beta)}\sin\theta\right)^2\left(m_i^{(\beta)}\right)^2 \mathrm{d}\theta \\ &= -\frac{3a-2b}{3} - (b-c)\sum_{i=1}^{3}\left[\left(p_i^{(\beta)}\right)^2 + \left(q_i^{(\beta)}\right)^2\right]\left(m_i^{(\beta)}\right)^2\end{aligned} \tag{2.37}$$

Substituting Eqs. (2.28) and (2.29) into Eq. (2.37), we obtain

$$\frac{1}{E_{\mathrm{TD}}^{hkl}} = -\frac{3a-2b}{3} - 2(b-c)\Gamma \tag{2.38}$$

where the orientation index parameter Γ is defined in Eq. (2.27).

Similar to E_{LD}^{hkl}, we calculated the numerical values of E_{TD}^{hkl} using Eq. (2.38) and single-crystal elastic constants in the Appendix. Table 3 lists the numerical results of E_{TD}^{hkl} for 26 representative elastically isotropic polycrystals with FCC, BCC and DC crystal symmetries.

Table 2.3 Diffraction elastic constants E^{hkl} along TD (in GPa).

	E^{200}	E^{220}	E^{111}	E^{311}
Ag	165.35	247.21	296.06	208.77
Al	189.76	206.98	213.44	200.22
Au	144.77	202.29	233.17	176.24
Cu	268.3	420.22	517.98	347.12
Ir	1824.28	2317.3	2546.73	2105.67
Ni	556.41	848.88	1029.22	710.07
Pb	43.16	67.52	83.16	55.81
Pd	262.84	378.12	442.87	325.09

Table 2.3 continued

Pt	392.63	466.65	497.94	436.08
Cr	1722.85	1294.79	1195.75	1426.61
Fe	538.86	812.42	977.91	683.39
K	6.50	12.52	18.11	9.31
Li	18.67	37.64	56.92	27.32
Mo	1168.72	1108.85	1090.23	1130.38
Na	12.17	28.57	51.86	19.03
Nb	343.44	252.56	232.08	280.12
Ta	471.74	572.27	616.03	530.25
V	387.47	346.78	335.06	360.88
W	1456.48	1465.52	1468.55	1462.14
C	8391.01	12171.11	14321.73	10424.59
Ge	489.97	683.84	787.73	596.12
Si	590.51	778.95	871.67	696.31
CuZn	175.65	352.21	529.7	256.37
Cu_3Au	264.74	375.35	436.09	324.87
NiAl	408.88	669.73	850.62	541.3
SS 316L	433.18	763.86	1024.57	594.95

2.7 Diffraction Elastic Constants along any Q direction

Consider a {*hkl*} grain family along the direction of a diffraction vector **Q** in an RVE. The grains in this family are numbered as 1,… γ ,…, *N*. The orientation of grains in this

family can be represented by a single variable $\theta^{(\gamma)}$ and three orthogonal unit vectors as shown in Figure 2,

$$\begin{aligned}\mathbf{Q} &= \left(Q_1, Q_2, Q_3\right) = \left(h, k, l\right) / \sqrt{h^2 + k^2 + l^2} \\ \mathbf{p} &= \left(p_1, p_2, p_3\right) = \left(-k, h, 0\right) / \sqrt{h^2 + k^2} \\ \mathbf{q} &= \left(q_1, q_2, q_3\right) = \left(hl, kl, -h^2 - k^2\right) / \sqrt{\left(h^2 + k^2\right)\left(h^2 + k^2 + l^2\right)}\end{aligned} \tag{2.39}$$

Here, the components of **Q**, **p** and **q** are all expressed in the local crystal basis of grain γ.

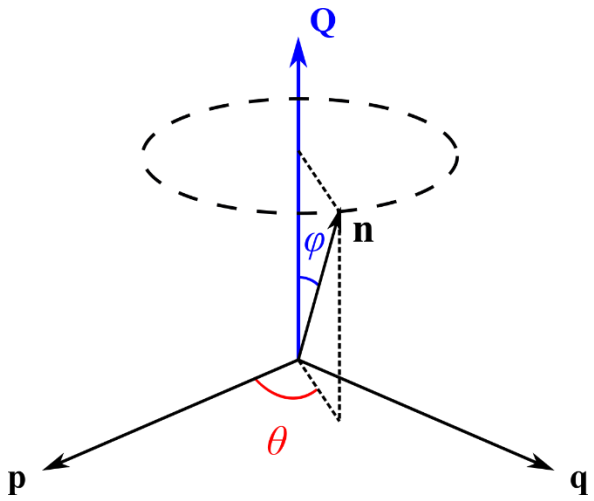

Figure 2.2 Schematic to calculate DECs along TD. In the coordinate system spanned by the orthonormal vectors {Q, p, q}, the dashed line circle represents all the unit vectors n that form a constant angle φ with the diffraction vector Q.

For the {*hkl*} grain family along the **Q** direction, the angle between **Q** and the loading direction **n** must be a constant, such that $\mathbf{n}^{(\gamma)}$ associated with grain γ can be expressed as

$$\mathbf{n}^{(\gamma)} = \mathbf{Q}\cos\varphi + \left(\mathbf{p}\cos\theta^{(\gamma)} + \mathbf{q}\sin\theta^{(\gamma)}\right)\sin\varphi \tag{2.40}$$

where φ denotes the angle between **Q** and $\mathbf{n}^{(\gamma)}$, and $\theta^{(\gamma)}$ denotes the angle between **p** and the vector component of $\mathbf{n}^{(\gamma)}$ resolved in the plane of **p** and **q**.

The normal strain along **Q** for each grain $\varepsilon_Q^{(\gamma)}$ is given by

$$\varepsilon_Q^{(\gamma)} = \sigma_0 U_{ijkl}^{(\gamma)} Q_i Q_j n_k^{(\gamma)} n_l^{(\gamma)} \tag{2.41}$$

Substitution of Eqs. (2.22), (2.39) and (2.40) into Eq. (2.41) yields

$$\begin{aligned}\frac{\varepsilon_Q^{(\gamma)}}{\sigma_0} &= \frac{3a-2b}{3} + 2c\cos^2\varphi + 2(b-c)(1-2\Gamma)\cos^2\varphi \\ &\quad +2(b-c)\sum_{i=1}^{3} Q_i^2 \left[2Q_i \left(p_i \cos\theta^{(\gamma)} + q_i \sin\theta^{(\gamma)} \right) \sin\varphi\cos\varphi + \left(p_i \cos\theta^{(\gamma)} + q_i \sin\theta^{(\gamma)} \right)^2 \sin^2\varphi \right]\end{aligned}$$

(2.42)

The corresponding diffraction elastic constant E_Q^{hkl} is defined as

$$\frac{1}{E_Q^{hkl}} = \frac{1}{N} \sum_{\gamma=1}^{N} \frac{\varepsilon_Q^{(\gamma)}}{\sigma_0} \tag{2.43}$$

With a sufficient number of grains, we can change the summation over γ grains in Eq. (2.43) to the integration over θ from 0 to 2π. Substituting Eq. (2.42) into Eq. (2.43), we obtain the general solution of diffraction elastic constant E_Q^{hkl} for any diffraction vector **Q**,

$$\frac{1}{E_Q^{hkl}} = \frac{1}{2\pi}\int_0^{2\pi}\frac{\varepsilon_Q(\theta)\,d\theta}{\sigma_0}$$
$$= \frac{3a-2b}{3} + 2c\cos^2\varphi + 2(b-c)(1-2\Gamma)\cos^2\varphi + (b-c)\sum_{i=1}^{3}Q_i^2\left(p_i^2+q_i^2\right)\sin^2\varphi$$
$$= \frac{3a-2b}{3} + 2b\cos^2\varphi + 2(b-c)\left(\sin^2\varphi - 2\cos^2\varphi\right)\Gamma$$

(2.44)

This expression is consistent with Eq. (2.26) when $\varphi = 0^\circ$ and Eq. (2.38) when $\varphi = 90^\circ$.

2.8 Validation by Finite Element Simulations

To further validate our micromechanics solutions, we performed polycrystal elasticity finite element simulations for FCC Cu, Ni, and BCC Nb using the commercial finite element program ABAQUS [39]. The constitutive model of the anisotropic linear elasticity of single-crystal grains was implemented via a user material subroutine [24]. For finite element simulations, we constructed a "texture-free" polycrystal model consisting of 8000 cubic elements, where each element represents a cubic-symmetry grain with random orientation. During a finite simulation of uniaxial tensile deformation, the lattice strain in each {*hkl*} grain family was determined by averaging the elastic strain of grains with their respective [*hkl*] direction along LD or TD (within a deviation of ±5°). Then we calculated the diffraction elastic constant E^{hkl} by the ratio of the applied tensile stress and corresponding lattice strain.

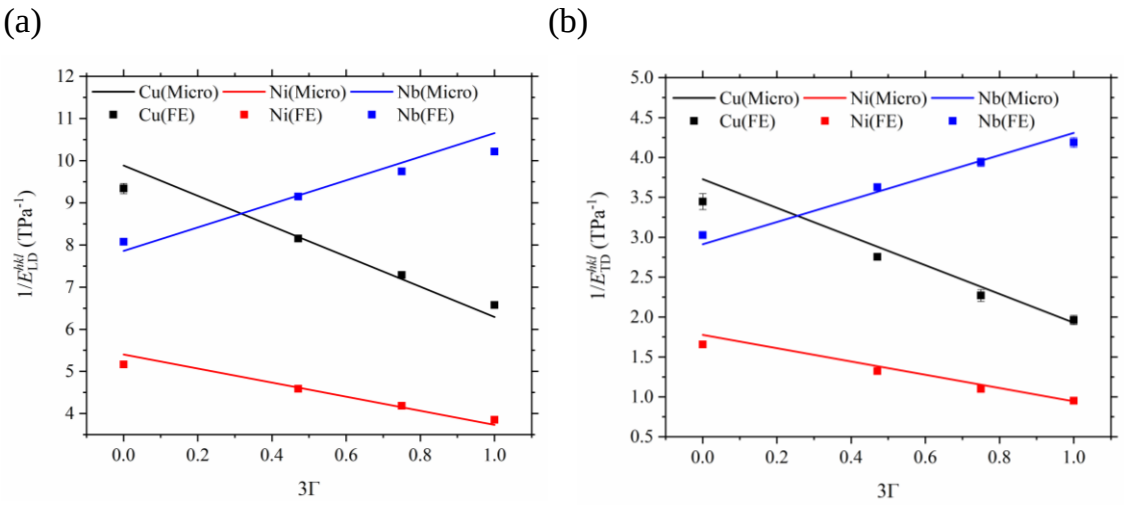

Figure 2.3 Plot of the reciprocal of diffraction elastic constant $1/E^{hkl}$ as a function of orientation parameter Γ along (a) LD and (b) TD for FCC Cu, Ni and BCC Nb. The solid lines represent the micromechanics (Micro) solutions, and the squares the finite element (FE) simulation results for the representative grain families of {200}, {311}, {220} and {111}, with their respective 3Γ values of 0, 57/121, 3/4 and 1. The small error bars of FE results represent the negligible standard deviations calculated from 10 FE polycrystal models with different random grain orientations.

Figure 2.3 shows the diffraction elastic constants of Cu, Ni, and Nb along LD (Figure 2.3a) and TD (Figure 2.3b) calculated from the micromechanics solutions (i.e., Eq. (2.26) for LD and Eq. (2.38) for TD) as well as from the polycrystal elasticity finite element simulations. The micromechanics solutions (solid lines) are plotted as a function of the orientation index parameter 3Γ covering all the possible $\{hkl\}$ grain families for a polycrystal with random orientation distribution of grains. The polycrystal elasticity finite element simulation results (squares) are given for the {200}, {311}, {220} and {111} grain families. For each family, we used 10 finite element polycrystal models with different random grain orientations, so as to obtain the mean value and standard deviation of $1/E^{hkl}$

. It is seen that the finite element results are in good agreement with the micromechanics solution, despite small differences in the numerical results of $1/E^{hkl}$ between the two methods. These differences may arise from several approximations used in the micromechanics solution, including the self-consistent method of polycrystal homogenization and the spherical grain shape, as well as the use of a single element to represent each grain in the finite element simulations.

As shown in Figure 2.3, $1/E^{hkl}$ is linearly dependent on 3Γ. This is predicted by the micromechanics solutions, i.e., Eq. (2.26) for LD and Eq. (2.38) for TD. As discussed earlier, the slope of the $1/E^{hkl}$ versus 3Γ curve is dictated by the sign of $b-c$, which is further controlled by the anisotropy ratio *A*, with *A* = 1.0 for isotropic elasticity, 3.21 for Cu, 2.57 for Ni and 0.49 for Nb. As listed in the Appendix, the *A* values are greater than 1 for most cubic polycrystals, so that $b-c<0$. As a result, the slopes of both the $1/E_{\mathrm{LD}}^{hkl}$ versus 3Γ and the $1/E_{\mathrm{TD}}^{hkl}$ versus 3Γ curves are negative. In contrast, the positive slopes for Nb is a result of $b-c>0$. Among 26 cubic polycrystals in the Appendix, Cr, Mo, and V also have *A* < 1 and thus should have positive slopes for their respective $1/E^{hkl}$ versus 3Γ curves. In addition, the slopes of the $1/E_{\mathrm{LD}}^{hkl}$ versus 3Γ and the $1/E_{\mathrm{TD}}^{hkl}$ versus 3Γ curves for Cu are larger than the corresponding ones for Ni because of the higher elastic anisotropy *A* of Cu.

2.9 Summary

We have derived a general analytic solution of grain-level lattice strains and diffraction elastic constants for an elastically isotropic polycrystal using a self-consistent micromechanics model. This solution is applicable to a broad class of "texture-free" polycrystals with cubic crystal symmetry and only requires an input of the three independent elastic constants of a cubic crystal. It establishes direct linear relations between the reciprocal of the elastic diffraction constant and the orientation index parameter, as given by Eq. (2.26) for the tensile loading direction and by Eq. (2.38) for the transverse direction. While these analytic relations are equivalent to those by Bollenrath, Hauk and Müller [25], our derivation is facilitated by the use of the components of related vectors and tensors resolved in the local crystal basis, such that it can be readily understood and applied. This approach can be taken to further obtain the related results such as resolved shear stresses for the study of progressive yielding in different grain families [24]. From a straightforward numerical implementation of this solution by MATLAB, we have calculated diffraction elastic constants for 26 representative cubic polycrystals. The results agree closely with modeling and experimental results in the literature as well as with our polycrystal elasticity finite element simulations.

Theoretical predictions of grain-level lattice strains and diffraction elastic constants complement *in situ* synchrotron X-ray and neutron diffraction experiments. They can be directly compared with experimental measurement of diffraction elastic constants, and also can be used for analysis of microscale residual stresses [29] and progressive yielding [23, 24]. We expect these solutions will facilitate high-throughput and data-analytics studies of the mechanical behavior of polycrystalline materials with varying compositions and

microstructures, such as high-entropy alloys [30], additively manufactured alloys [23, 24], heterogeneous nanostructured metals and alloys [3, 31], and others.

CHAPTER 3. INTERNAL STRESSES IN ADDITIVELY MANUFACTURED STEELS

3.1 Introduction

Residual stress is one of the most critical issues for additively manufactured (AM) metallic materials [8, 40-43]. Its presence can markedly influence the mechanical behavior of AM parts. This issue is especially significant for AM materials processed by selective laser melting (SLM), which inevitably results in substantial residual stresses. The build-up of high residual stresses during SLM processing can readily induce the damage and eventual failure of AM parts in service. As such, mitigation of residual stresses is considered as one of the most outstanding challenges in the AM field. To mitigate the deleterious effects of residual stresses, a fundamental understanding of their impact on the mechanical behavior of AM materials is needed.

The residual stresses in polycrystalline materials can be categorized according to two major classes [4, 44]: macroscale and microscale residual stresses. The so-called Type I macroscale residual stresses are distributed across the overall dimension of a part and contribute to its distortion. They arise due to long range gradients of plastic deformation in the part, for example. By contrast, the microscale residual stresses manifest at the scale of microstructure and are categorized into two types: Type II intergranular residual stresses and Type III intragranular residual stresses. Type II self-equilibrates over a length scale of grains and results from strain incompatibility between grains. Type III is associated with the heterogeneous microstructure such as dislocation cells inside grains and also satisfies

the self-equilibrium condition. Generally, microscale residual stresses develop after material processing and subsequently evolve during deformation due to applied loading. Following the literature [15], we use the terms ‘residual stress’ and ‘internal stress’ interchangeably with regard to these microscale residual stresses. To understand and control the microscale residual stresses, it is necessary to track their spatiotemporal evolution in real time at high resolution. This has been often pursued by means of *in situ* X-ray or neutron diffraction methods [15, 18, 29, 35, 36, 45-49].

Additive manufacturing of metallic materials via laser powder-bed-fusion (L-PBF) results in highly non-equilibrium microstructures with a high density of dislocations, irregular and tortuous grain morphologies, cellular structures and chemical segregation [40, 43]. These microstructural characteristics can result in mechanical properties that significantly differ from materials conventionally processed by wrought and cast [8, 50, 51]. L-PBF shares many common roots with welding as both processes involve the melting and bonding of materials via motion of a local heat source. The highly localized heating and rapid cooling of a melt pool, in conjunction with the layer-by-layer repetition of such a thermomechanical process, give rise to large thermal gradients and heterogeneous residual stresses within a non-equilibrium microstructure [52-55]. The thermal gradients are affected by many processing parameters [56], including build plate/powder bed temperature, laser power, powder thermophysical characteristics, melt pool size, etc. The convolution of these parameters often leads to a complex residual stress field. While studies of the macroscale residual stresses in AM materials have revealed various deleterious effects such as loss of net shape, detachment from support structures, or even failure of the build parts [57], the ways in which microscale residual stresses influence the mechanical

performance of AM materials remain elusive. This is due to the difficulty in measurement and understanding of the spatial-temporal evolution of residual stresses at the scale of individual grains or phases [4].

Here we present a combined experimental and modeling study of the microscale residual stresses in AM 316L austenitic stainless steel. We performed *in situ* synchrotron X-ray diffraction (SXRD) measurements of lattice strains in AM stainless steel under uniaxial tension. Micromechanics and crystal plasticity finite element (CPFE) models were developed to understand the impact of elastic anisotropy, progressive yielding and hardening on the extent and evolution of lattice strains and associated Type II intergranular residual stresses. We observed pronounced tension-compression asymmetries in yield strength and strain hardening for AM stainless steel. Combining the experimental and CPFE modeling results, we show that such tension-compression asymmetries are associated with the back stresses that originate from heterogeneous dislocation distributions and resultant Type III intragranular residual stresses. Our work not only demonstrates an effective approach to quantitatively evaluate the microscale residual stresses of both intergranular and intragranular character, but also conveys the practical ramification that the microscale residual stress effects should be carefully considered when using AM to design and build complex components for structural applications.

3.2 Microstructure Characterization of AM 316L Steels

The 316L stainless steel sample fabricated via L-PBF possesses a complex microstructure that is sensitive to laser processing parameters, as shown in previous studies [8, 58-60]. Here we use an open architecture Fraunhofer L37 L-PBF machine to build 316L

stainless steel plates. The electron backscatter diffraction (EBSD) image in Figure 3.1a shows that grains in the as-built sample are equiaxed from the top view and slightly elongated from the side view. The average grain size is 18 ± 9 μm, as measured from the top view. A rather weak texture is revealed in the build plane, as indicated by the pole figures in Figure 3.1b for stainless steel with the face-centered cubic structure. The high-angle annular dark-field (HAADF) scanning transmission electron microscopy (STEM) images in Figures 3.1c and 1d reveal insignificant chemical segregation in the as-built sample. In the HAADF STEM image of Figure 3.1d, the dislocation structures do not appear to be well defined, as they consist of tangled dislocations and are decorated with some visible precipitates.

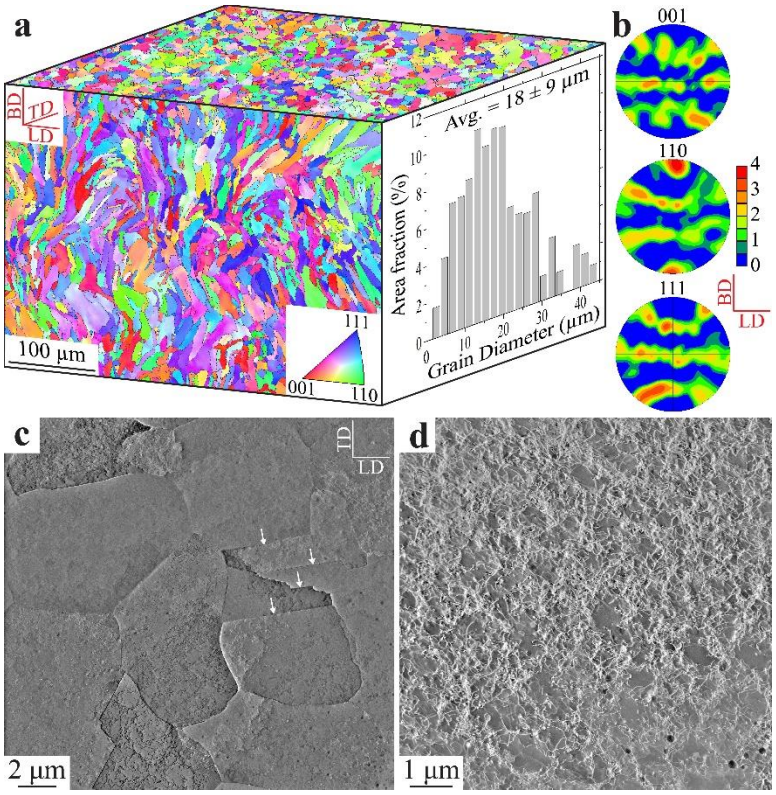

Figure 3.1 Microstructure of as-printed 316L stainless steel. (**a**) EBSD image along the build direction (BD) and transverse direction (TD), respectively. The EBSD image along the loading direction (LD) is similar to that along TD. The grain size distribution is obtained

from the top surface (the TD-LD plane) in the image. (**b**) 001, 110, 111 pole figures corresponding to the EBSD image taken along the BD. (**c**) Top-view HAADF STEM image of the same sample in (**a**). Tangled dislocations and a few twin boundaries (marked with white arrows) are visible; cellular structures are poorly defined. (**d**) A higher resolution HAADF STEM image of cellular structures compared to (**c**). Some precipitates are visible.

3.3 Diffraction Experiments and Intergranular Internal Stresses

To investigate the microscale residual stresses in AM 316L stainless steel, we performed *in situ* SXRD measurements of lattice strains for the as-built sample subjected to uniaxial tension (as schematically illustrated in Figure 3.2a). Figure 3.2b shows the engineering and true stress-strain (σ-ε) curves up to the onset of necking. The 0.2%-offset yield strength σ_Y is 541 ± 11 MPa, which is consistent with the earlier results for AM 316L stainless steel [8, 50]. Such high strength is 2-3 times those of coarse-grained counterparts, and has been attributed to printing-induced sub-grain microstructures such as dislocation cells [8]. Figure 3.2b also shows that further increase of the applied stress beyond σ_Y results in significant strain hardening, which is due to the deformation-induced evolution of heterogeneous microstructures [8]. For polycrystalline materials, the {hkl} grain family refers to a set of grains having the normal vector of {hkl} planes in a common direction. The so-called lattice strain for the {hkl} grain family is defined as $\varepsilon^{hkl} = (d^{hkl}-d_0^{hkl})/d_0^{hkl}$, where d^{hkl} and $d_0{}^{hkl}$ denote the interplanar spacing of {hkl} planes under loading and at the stress-free state, respectively [45]. The stress-free lattice spacing $d_0{}^{hkl}$ was determined by annealing an as-built sample at 1200 °C for 1 hr. In Figure 3.2c, we plot the *in situ* SXRD measurements of lattice strain along the loading direction (LD) against the macroscopic true stress for four representative grain families of {220}, {111}, {200} and

{311}. In addition, Figure 3.2d shows the lattice strain measured along the transverse direction (TD) against the macroscopic true stress for four grain families of {220}, {111}, {200} and {311}. The lattice spacing as a function of the azimuthal angle can be seen in Figure S3. Note that the constituent grains in the {hkl} grain family along LD are largely different from those in the {hkl} family along TD, and there is no clear relation between them [15].

It is seen from Figure 3.2c that prior to tensile loading, the {200} grain family exhibits the largest magnitude of residual lattice strain (being negative) in the LD. In comparison, the {111} and {220} families show negligibly small residual lattice strains, while the {311} family exhibits a residual lattice strain similar to that of the {200} family. These residual lattice strains originate from the complex thermomechanical history associated with L-PBF processing. Figure 3.2c also shows that upon tensile loading, each of the four grain families exhibits a near linear increase of lattice strain against applied stress when the macroscopic tensile stress-strain response is within the linear elastic regime. This is followed by a nonlinear behavior of lattice strain when the applied stress approaches and exceeds σ_{Y}. More specifically, in the elastic regime, the {200} family shows the highest rate of increase of lattice strain, which indicates the softest response. In contrast, the {111} family exhibits the stiffest response. The lattice strains of the other two families fall in between these two limits, with the {311} family having values close to those of the {200} family, and the values for the {220} family close to those of the {111} family. Such anisotropic lattice strain responses in different grain families can be quantitatively characterized in terms of the diffraction elastic constant E^{hkl}, which is given by the slope of the lattice strain versus applied stress curve for each {hkl} grain family [15]. The fitted values of E^{hkl} are listed in

Table 3.1, which reflects the strong elastic anisotropy of austenitic stainless steel single crystals and are consistent with the lattice strain measurements of stainless steel processed by conventional routes [15]. As the applied stress approaches σ_Y (as indicated by the vertical dashed line in Figure 3.2c), the {200} family shows a markedly nonlinear increase of lattice strain with increase of applied stress, while the {220} family shows a nonlinear decrease of lattice strain. The nonlinear lattice strain responses of the {311} and {111} families are less pronounced. A similar nonlinear behavior of lattice strain has been shown by the previous studies of stainless steel processed by conventional routes [15]. They were generally attributed to the elastic and plastic anisotropy in different grain families, which will be further studied for AM stainless steel by our computational modeling.

Figure 3.2d shows that prior to tensile loading, the {200} family exhibits the largest magnitude of residual lattice strain (being negative) along TD. In comparison, the {111} and {220} families show negligibly small residual lattice strains, while the {311} family shows a residual lattice strain similar to that of the {200} family. As noted earlier, the constituent grains in the {hkl} family along TD are largely different from those in the {hkl} family along LD, such that the lattice strains in the nominally identical {hkl} grain families along LD and TD cannot be simply related. Nonetheless, due to the effect of Poisson's contraction, an initial increase of tensile stress along LD results in a linear decrease of lattice strain along TD. Further loading gives rise to a nonlinear response of lattice strain along TD. Altogether, the *in situ* SXRD results in Figure 3.2c and 3.2d reveal the lattice strains in several representative grain families prior to and during tensile loading. We note that these lattice strains are elastic in nature and thus are proportional to Type II intergranular residual stresses, which will be quantitatively evaluated using

micromechanics and CPFE models later in this Chapter. Quantifying these Type II intergranular residual stresses provides a basis of further study of Type III intragranular residual stresses and their impact on the macroscopic mechanical behavior of AM stainless steel.

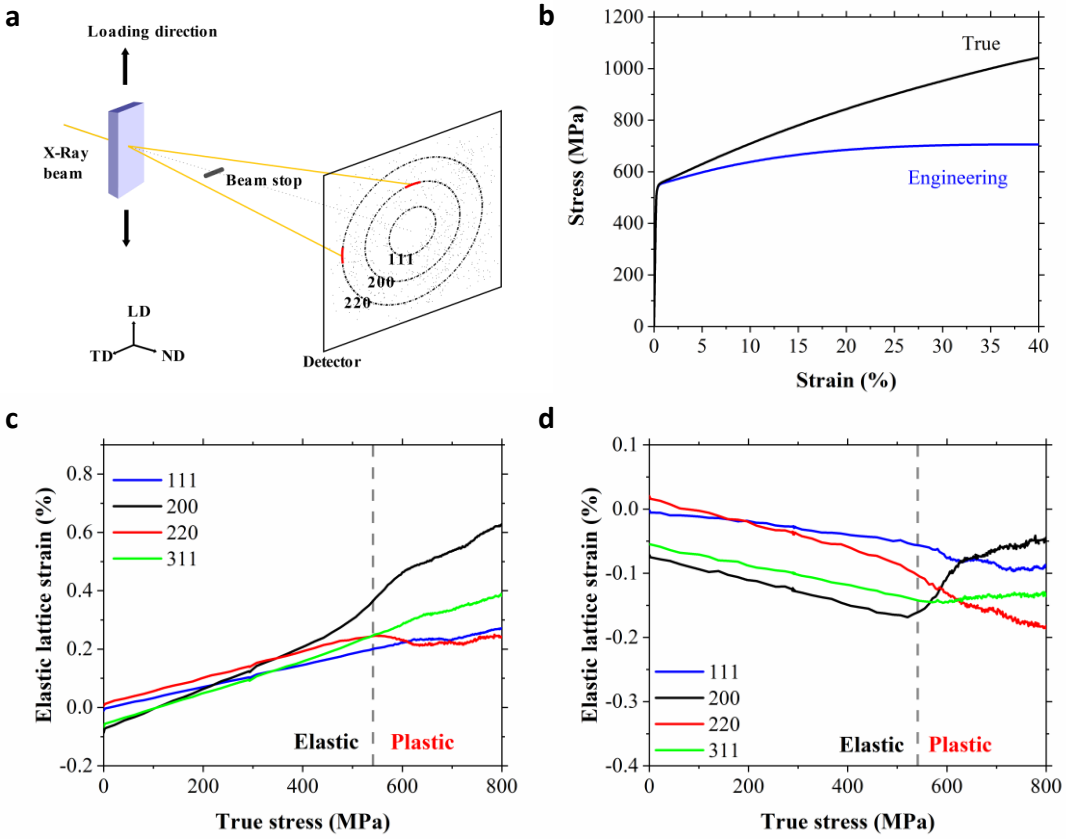

Figure 3.2 Lattice strain behaviour of an AM 316 stainless steel sample measured via *in situ* SXRD. (**a**) Schematic of *in situ* SXRD setup, where the loading direction (LD), transverse direction (TD) and normal direction (ND) are illustrated. (**b**) Engineering and true stress-strain curves of uniaxial tension, plotted up to the onset of necking. (**c**) *In situ* SXRD results of lattice strain (ε^{hkl}) along LD in four grain families of {111}, {200}, {220}, {311}, respectively, plotted against the macroscopic true stress of the sample. The 0.2%-offset yield strength (σ_Y) is marked with a dashed line, separating the elastic and plastic regimes. (**d**) Same as (c) except along TD.

3.4 Tension-Compression Asymmetry and Intragranular Internal Stresses

To investigate the impact of microscale residual stresses on the mechanical behavior of AM stainless steel, we compared the stress-strain responses from uniaxial tension and compression experiments. As shown in Figure 3.3a, the tensile and compressive stress-strain curves of the as-built samples exhibit pronounced asymmetries in yield strength and strain hardening. The 0.2%-offset yield strength from uniaxial compression is 600 ± 13 MPa, which is higher than that from uniaxial tension 541 ± 11 MPa by approximately 60 MPa. In addition, the normalized strain hardening rate, defined by $(d\sigma/d\varepsilon)/\sigma$, is appreciably higher under compression than tension (Figure 3.3b). To evaluate the influence of microscale residual stresses on the tension-compression asymmetries, we also measured the tensile and compressive stress-strain curves (Figure 3.3a) for samples after stress-relief annealing at 500 ºC for 4 hrs. In this case, the compressive yield strength decreases to 560 ± 14 MPa, and the tensile yield strength increases to 554 ± 10 MPa. These results indicate that thermal annealing can markedly reduce the tension-compression asymmetry. This can be reasonably attributed to the relaxation of printing-induced non-equilibrium microstructures and associated microscale residual stresses in as-built samples. If the asymmetry was primarily caused by printing-induced voids, the stress-release annealing experiment at a low temperature would be unlikely to remove those voids, and thus the tension-compression asymmetry would be little affected. In addition, since our AM samples have large grain sizes, the tension-compression asymmetry that is typically reported in nanocrystalline materials [61] can be excluded. Despite the similar yield strengths in tension and compression after annealing, Figure 3.3b shows that the strain hardening rate is still higher in compression than tension in annealed samples. Moreover,

thermal annealing leads to an increased strain hardening rate in annealed samples than as-printed samples for both tension and compression beyond the point of initial yielding.

The *in situ* SXRD experiments were further conducted to compare the lattice strain responses between as-printed and annealed samples under uniaxial tension. In Figure 3c, we plot the deviation of lattice strain $\varepsilon^{\mathrm{hkl}}$ from the linear response along LD, $\Delta\varepsilon^{\mathrm{hkl}} = \varepsilon^{\mathrm{hkl}} - \sigma_a/E^{\mathrm{hkl}}$, where σ_a is the applied tensile stress. $\Delta\varepsilon^{\mathrm{hkl}}$ has often been used to examine the progressive yielding and hardening behavior of different grain families. Figure 2c indicates that {200} and {220} families exhibit more pronounced deviation from the linear response. Hence, $\Delta\varepsilon^{200}$ and $\Delta\varepsilon^{220}$ are used for further analysis of the lattice strain [15, 62] in the nonlinear regime against applied stress. Figure 3c indicates that deviation from the linear response occurs well below the 0.2%-offset yield strength for both samples. In addition, the non-zero $\Delta\varepsilon^{\mathrm{hkl}}$ prior to loading of the as-printed sample shows a marked initial value of compressive lattice strain, particularly for the {200} family, and thus suggests the high magnitude of Type II residual stresses in the as-printed sample. After annealing, such compressive shift reduces substantially but is not completely removed (Figure 3.3c). The {220} family also demonstrates a qualitatively similar trend despite a much smaller initial value of tensile lattice strain prior to loading.

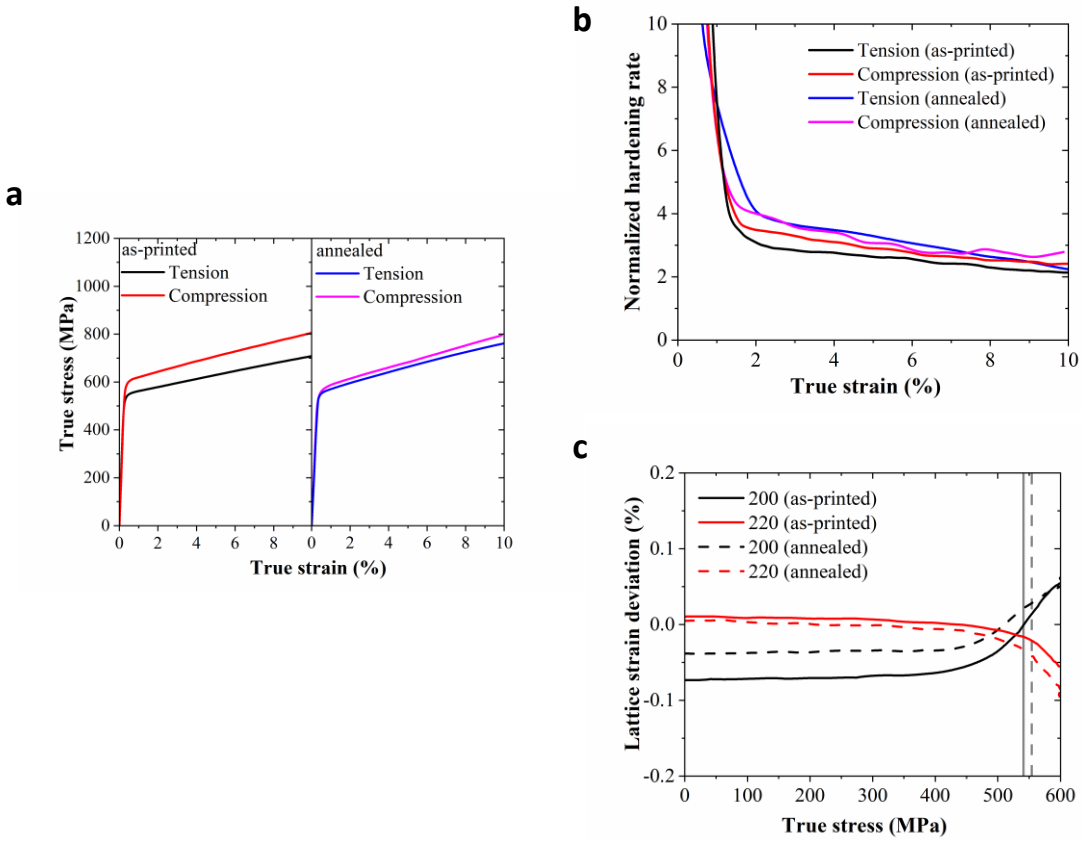

Figure 3.3 Experimental results of tension-compression asymmetry of AM 316L stainless steel. (**a**) True stress-strain curves of as-printed samples under tension and compression. Also plotted are the corresponding results of annealed samples. (**b**) Normalized hardening rate versus true strain corresponding to the four cases in (**a**). (**c**) *In situ* SXRD results for as-printed and annealed samples under unaixial tension, showing the lattice strain deviation ($\Delta\varepsilon^{\mathrm{hkl}}$) as a function of applied stress for {200} and {220} grain families.

3.5 Micromechanics Modeling of Lattice Strains

The above *in situ* SXRD results have revealed that in the linear elastic regime, the lattice strains in different grain families increase with applied stress, but at different rates. This orientation dependence of lattice strain response can be characterized by the diffraction elastic constant of each grain family for uniaxial loading [15]. The *in situ* SXRD

results have also shown that the different grain families begin to exhibit non-linear lattice strain responses at different applied stresses. This progressive yielding behavior can be understood by considering the maximum resolved shear stress or equivalently the maximum Schmid factor in each grain family. In this Chapter, we developed a micromechanics model to determine both the diffraction elastic constant and Schmid factor in different grain families. These micromechanics results facilitate our understanding of how the lattice strain and progressive yielding responses depend on the elastic anisotropy of individual grain families. They are also used to benchmark CPFE simulations for further studies of the non-linear lattice strain evolution with an increase of applied stress as well as the tension-compression asymmetries in AM stainless steel.

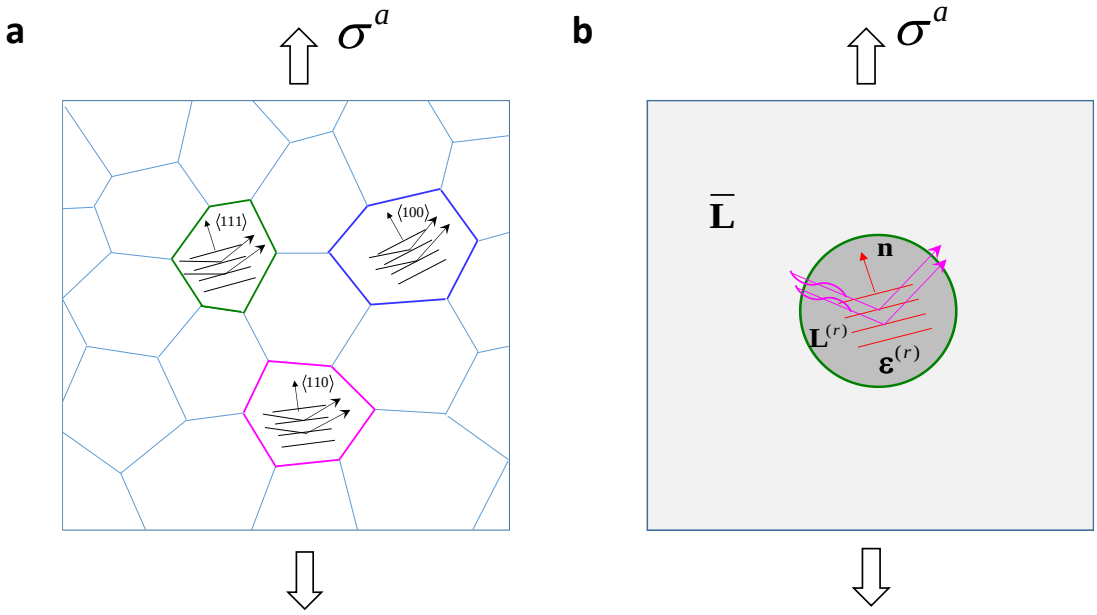

Figure 3.4 Illustration of the self-consistent micromechanics model of a polycrystalline aggregate. **(a)** A polycrystal consisting of different {hkl} grain families along the uniaxial loading direction. For example, the {111} grain family refers to a set of grains with the unit normal vector **n** of {111} planes along the loading direction. The X-rays reflected by the {hkl} planes are collected to track the average interplanar spacing of these {hkl} planes with deformation due to applied loading. **(b)** In the self-consistent polycrystal model, each single-crystal grain is approximated as a spherical inclusion with the anisotropic elastic

stiffness tensor $\mathbf{L}^{(r)}$ embedded in a homogeneous matrix with the effective isotropic stiffness tensor $\bar{\mathbf{L}}$.

The micromechanics model illustrated in Figure 3.4a is concerned only with the regime of linear elastic response of a polycrystalline aggregate. A random distribution of grain orientations is assumed. This assumption facilitates the derivation of an analytic micromechanics solution that enables an effective assessment of the diffraction elastic constant, tensile stress, and maximum resolved shear stress within different grain families. The residual stress is not included in the grains, since the diffraction elastic constant is known to be independent of residual stress [15]. For each grain, its anisotropic elastic stiffness tensor is denoted as $\mathbf{L}^{(r)}$, where *r* represents a family of grains with the same crystallographic orientation. Under a macroscopic applied load, the lattice strain and stress responses of individual grains in a polycrystalline aggregate are not simply determined by $\mathbf{L}^{(r)}$. This is because of the elastic anisotropy of individual grains that leads inevitably to deformation incompatibility between neighboring grains. To account for such incompatibility and resulting mutual constraints between grains, the concept of a representative volume element (RVE) is invoked to represent an infinite homogeneous matrix. Given the random distribution of grain orientations, this RVE has an effective isotropic elastic response that is characterized by the isotropic elastic stiffness tensor $\bar{\mathbf{L}}$. As shown in Figure 3.4b, a spherical inclusion is considered as a representative grain embedded in the RVE subjected to the macroscopic stress $\bar{\boldsymbol{\sigma}}$. According to the Eshelby inclusion solution, the stress $\boldsymbol{\sigma}^{(r)}$ and strain $\boldsymbol{\varepsilon}^{(r)}$ in the spherical inclusion are uniform [33]. The self-consistent micromechanics method [33] is used to determine the effective moduli

of polycrystalline stainless steel. These results are combined to derive the analytic formulas of stress and strain in the {hkl} grain family.

To understand the lattice strain and stress responses during *in situ* SXRD experiments, we considered an applied uniaxial tensile stress σ_a and used the above general solution to derive the corresponding lattice strain ε^{hkl} and stress σ^{hkl} along LD in the {hkl} grain family in the linear elastic regime. It follows that the diffraction elastic constant is given by $E^{hkl} = \sigma_a / \varepsilon^{hkl}$. We also calculated the normalized tensile stress $\alpha^{hkl} = \sigma^{hkl} / \sigma_a$, so as to compare the tensile stress along LD in different grain families, as well as the normalized maximum resolved shear stress $\beta^{hkl} = \tau^{hkl} / \sigma_a$ among the twelve $\{111\}\langle 110\rangle$ slip systems, so as to determine the sequence of onset of plastic yielding in different grain families. Using the anisotropic elastic constants of single-crystal stainless steel, we calculated the values of E^{hkl}, α^{hkl} and β^{hkl} for the four grain families, as listed in Table 3.1. The diffraction elastic constants from the micromechanics model confirm that the {200} and {111} families are respectively the softest and stiffest along LD, respectively, which are consistent with the SXRD results and closely match the modeling results by Clausen *et al*. [15]. It is also seen from Table 1 that the relative magnitudes of the tensile stress along LD (given by α^{hkl}) follow monotonically those of the diffraction elastic constant among different grain families. More interestingly, the relative magnitudes of the maximum resolved shear stress (given by β^{hkl}) and thus the maximum Schmid factor do not follow monotonically those of the diffraction elastic constant and tensile stress along LD. Due to the favored orientation between the most stressed $\{111\}\langle 110\rangle$ slip plane and

LD, the {220} family has the maximum resolved shear stress and thus the maximum Schmid factor, which implies the earliest onset of plastic yielding under uniaxial tension. The β^{hkl} values of both the {311} and {111} families are lower than that of the {220} family, indicating that yielding for these two families takes place at higher applied stresses than the {220} family. The {200} family still has the minimum resolved shear stress and thus minimum Schmid factor, which indicates the latest onset of plastic yielding among the four grain families. Finally, we note that while the diffraction elastic constants are independent of the printing-induced residual stresses that exist prior to loading, the stress and yielding responses in each grain family can be affected by these residual stresses, which will be further analyzed by CPFE modeling.

Table 3.1 Diffraction elastic constants E^{hkl} (in GPa) from the SXRD experiment (Exp), micromechanics (Micro) model and CPFE simulation, along with the normalized tensile stress α^{hkl} and normalized maximum resolved shear stress β^{hkl} from the micromechanics (Micro) model, in the {hkl} grain family of stainless steel.

	{200}	{311}	{220}	{111}
E^{hkl} (Exp)	139.1	179.6	219.1	264.1
E^{hkl} (Micro)	147.3	183.7	210.7	245.9
E^{hkl} (CPFE)	162.1	185.5	209.4	232.3
α^{hkl} (Micro)	0.74	0.94	1.07	1.18
β^{hkl} (Micro)	0.25	0.37	0.38	0.34

3.6 Crystal Plasticity Finite Element (CPFE) Framework

A CPFE model is developed to study the non-linear lattice strain behavior as well as the impact of Type II and Type III residual stresses on the mechanical behavior of AM stainless steel. The crystal plasticity constitutive equations are formulated within the rate-dependent, finite-strain framework of elastic-plastic deformation for individual grain crystals [63]. Here we present the major constitutive equations and highlight the new development that accounts for the Type II and Type III residual stresses in AM stainless steel through the residual lattice strain and back stress, respectively. Within each single-crystal grain, the deformation gradient tensor **F** is given in terms of the elastic deformation gradient tensor $\mathbf{F}^e$ and plastic deformation gradient tensor $\mathbf{F}^p$ using the multiplicative decomposition, $\mathbf{F} = \mathbf{F}^e\mathbf{F}^p$. The second Piola-Kirchhoff stress $\mathbf{T}^*$ is given by

$$\mathbf{T}^* = \mathbf{L}^{(r)}(\mathbf{E}^e - \mathbf{E}^*) \tag{3.1}$$

In Eq. (3.1), $\mathbf{L}^{(r)}$ is the elastic stiffness tensor of a single-crystal grain as defined in the micromechanics model; $\mathbf{E}^e$ is the elastic Green strain tensor given by

$$\mathbf{E}^e = 1/2(\mathbf{F}^{e\mathrm{T}}\mathbf{F}^e - \mathbf{I}) \tag{3.2}$$

where **I** is the 2nd rank identity tensor; and $\mathbf{E}^*$ is the eigen-strain tensor that reflects the residual lattice strain measured by *in situ* SXRD before loading and thus captures the effect of the Type II intergranular residual stress. The rate of change of $\mathbf{F}^p$ is given by $\dot{\mathbf{F}}^p = \mathbf{L}^p\mathbf{F}^p$ and $\mathbf{L}^p = \sum_{i=1}^{12} \dot{\gamma}_i^p \mathbf{m}_i \otimes \mathbf{n}_i$, where $\dot{\gamma}_i^p$ is the plastic shear rate on the *i*-th slip system, and $\mathbf{m}_i$

and $\mathbf{n}_i$ are unit vectors of the associated slip direction and slip plane normal, respectively. For austenitic stainless steel with the face-centered cubic structure, twelve $\{111\}\langle 110\rangle$ slip systems are considered. The plastic shearing rate $\dot{\gamma}_i^P$ is given by a power law

$$\dot{\gamma}_i^p = \dot{\gamma}_0^p \left| \frac{\tau_i - b_i}{s_i} \right|^{1/m} \operatorname{sgn}(\tau_i - b_i) \tag{3.3}$$

where τ_i is the resolved shear stress given by $\tau_i \approx \mathbf{T}^* : \operatorname{sym}(\mathbf{m}_i \otimes \mathbf{n}_i)$, $\dot{\gamma}_0^P$ is the reference plastic shear rate and m is the strain rate sensitivity. In Eq. (3.3), s_i is the slip resistance with an identical initial value of s_0 for all the slip systems, and it evolves according to $\dot{s}_i = \sum_j h_{ij} \left| \dot{\gamma}_j^p \right|$ and $h_{ij} = q_{ij} h_0 (1 - s_j / s_s)^a$, where q_{ij} is the latent hardening matrix; the diagonal elements of q_{ij} are 1.0 and off-diagonal elements are 1.4. The hardening parameters h_0, a and s_s are taken to be identical for all slip systems. Twinning shear is not accounted for in the crystal plasticity model, since *in situ* SXRD data and post-mortem TEM data indicate that deformation twinning plays a negligible role at low strain levels (<10%).

Following Hu *et al.* [29], we represent the effect of Type III residual stresses in terms of the back stress tensor **B** that gives rise to the tension-compression asymmetry. The so-called intergranular and intragranular back stresses in previous studies [64, 65] are collectively considered as the Type III residual stresses in this work, since both are associated with heterogeneous dislocation distributions within grains. The back stress tensor **B** is assumed to be deviatoric within the present pressure-independent crystal

plasticity model. The rate of change of **B** is taken as the sum of the rate of change of back stress in the twelve $\{111\}\langle 110\rangle$ slip systems that is respectively proportional to the corresponding plastic shear rate, i.e.,

$$\dot{\mathbf{B}} = \sum_{j=1}^{12} h_b e^{-k\gamma_j^p} \dot{\gamma}_j^p \mathrm{sym}(\mathbf{m}_j \otimes \mathbf{n}_j) \tag{3.4}$$

where h_b and k are the material constants and taken to be identical for all the slip systems. The back stress tensor **B** is calculated by time integration of Eq. (3.4) with the initial value of $\mathbf{B}_0$, giving a non-linear, rate-independent evolution of **B** with increase of plastic shear strain, which is extension of a similar scalar relationship between the back stress and plastic strain by Pham *et al*. [65] The determination of $\mathbf{B}_0$ for AM stainless steel is discussed in the main text. Then the back stress on the *i*-th slip system b_i is calculated by resolving **B** back onto individual slip systems, i.e.,

$$b_i = \mathbf{B} : \mathrm{sym}(\mathbf{m}_i \otimes \mathbf{n}_i) \tag{3.5}$$

The above constitutive model was implemented in the finite element simulation package ABAQUS/Explicit [39] by writing a user material subroutine VUMAT. The parameters of the crystal plasticity model used are listed in Table 3.2, while the evaluation of $\mathbf{E}^*$ and $\mathbf{B}_0$ will be discussed in detail later. In the finite element simulation, we constructed a three-dimensional cubic polycrystalline structure with 8000 cubic elements. Each element represents one single-crystal grain with an assigned orientation based on the EBSD data measured from the AM stainless steel sample. During CPFE simulations, the finite element polycrystal structure was first relaxed prior to applied loading, and then

subjected to uniaxial tensile or compressive deformation with the strain rate of 0.001/s. The lattice strain in different grain families was calculated from the elastic Green strain tensor $\mathbf{E}^e$ resolved in LD or TD. The lattice strain for each family of grains was determined by averaging the elastic strain of grains within a deviation of $\pm 5^o$ from the scattering vector direction with respect to LD or TD.

We stress that **E*** is the initial eigen-strain tensor arising from type II intergranular internal stresses, and $\mathbf{B}_0$ is the initial back-stress tensor arising from type III intragranular internal stresses. The grain-specific eigen-strain tensor **E*** was evaluated as follows. Based on the SXRD measurement of residual lattice strains in the {200}, {311}, {220} and {111} grain families, we assigned the initially estimated values to the eigen-strain tensor **E*** (i.e., normal components) for individual grains in the four grain families. Then we performed a CPFE simulation to relax the entire polycrystalline aggregate of 8000 grains without loading, so as to obtain the eigen-strain tensor **E*** for all grains in the simulated polycrystalline aggregate. More specifically, let us consider, as an example, one grain that belongs to both the {220} family along the loading direction (within a deviation of $\pm 5^o$) and the {100} grain family along the transverse direction (within a deviation of $\pm 5^o$). The corresponding **E*** for this grain is given by

$$\mathbf{E}^* = \varepsilon_{220}^{\mathrm{L}} \mathbf{n}_{220} \otimes \mathbf{n}_{220} + \varepsilon_{001}^{\mathrm{T}} \mathbf{n}_{001} \otimes \mathbf{n}_{001} \tag{3.6}$$

where $\varepsilon_{220}^{\mathrm{L}}$ and $\varepsilon_{001}^{\mathrm{T}}$ denote the lattice strain along the loading and transverse direction, respectively; $\mathbf{n}_{220}$ and $\mathbf{n}_{001}$ denote the unit vector along the [220] and [001] direction, respectively; and $\otimes$ denotes the tensor product between the two unit vectors. Supposing

the loading direction is along *x* axis and the transverse direction along *y* axis, the matrix components of **E*** can be written as

$$\mathbf{E}^{*}=\begin{pmatrix}\varepsilon_{220}^{\mathrm{L}} & 0 & 0\\ 0 & 0 & 0\\ 0 & 0 & 0\end{pmatrix}+\begin{pmatrix}0 & 0 & 0\\ 0 & \varepsilon_{001}^{\mathrm{T}} & 0\\ 0 & 0 & 0\end{pmatrix} \tag{3.7}$$

For individual grains in the {200}, {311}, {220} and {111} families, the initially estimated values of **E*** were chosen to be twice the corresponding residual lattice strains measured from the SXRD experiment. After the CPFE relaxation without loading, the residual lattice strains in the {220}, {111}, {200} and {311} grain families are changed from their initially assigned values to closely match the SXRD measurements; meanwhile, the residual lattice strains in other grain families are also obtained. The **E*** values do not change during subsequent deformation simulations.

Due to the lack of direct experimental characterization of type III intragranular internal stresses in individual grains, we assigned identical values to $\mathbf{B}_0$ for all grains in the simulated polycrystalline assembly, which approximately represent the average type III intragranular internal stresses in these grains. To match the asymmetry of tensile and compressive yield strengths between experiment and simulation, the initial back stress components along LD and TD within the build plane are both chose to be 30 MPa. As such, compared to the annealed sample without the initial back stresses, the compressive yield strength is elevated approximately by 30 MPa, since the initial back stress is directional and effectively increases the resistance to plastic yielding. On the other hand, the tensile yield strength is lowered approximately by 30 MPa, because the initial back

stress effectively reduces the resistance to plastic yielding. In addition, the initial back stress component along BD is chosen to be -60 MPa and the shear components of $\mathbf{B}_0$ are zero, so as to make $\mathbf{B}_0$ deviatoric. As a result, such initial back stresses lead to the asymmetry of tensile and compressive yield strengths by approximately 60 MPa in CPFE simulations.

Table 3.2 Parameters used for crystal plasticity finite element calculations.

	Parameter
$C_{11}\left(\mathrm{GPa}\right)$	204.6
$C_{12}\left(\mathrm{GPa}\right)$	137.7
$C_{44}\left(\mathrm{GPa}\right)$	126.2
$\dot{\gamma}_0\left(\mathrm{s}^{-1}\right)$	0.001
m	0.023
$s_0\left(\mathrm{MPa}\right)$	200
$h_0\left(\mathrm{MPa}\right)$	250
$s_s\left(\mathrm{MPa}\right)$	447
a	0.7
$h_b\left(\mathrm{GPa}\right)$	126.2
k	3000

3.7 CPFE Modeling of Non-linear Lattice Strains

While the micromechanics model provides analytic insights into the linear lattice strain behavior and the onset of plastic yielding in different grain families, we further developed a CPFE model to study the non-linear lattice strain behavior as well as the impact of Type II and Type III residual stresses on the mechanical behavior of AM stainless steel. The crystal plasticity constitutive equations are formulated within the rate-dependent, finite-strain framework of elastic-plastic deformation for individual grain crystals [63]. To account for the effects of Type II and Type III residual stresses, we introduced the eigen-strain tensor $\mathbf{E}^*$ and the back stress tensor **B** in the crystal plasticity model, respectively. More specifically, $\mathbf{E}^*$ represents the printing-induced residual lattice strains and thus reflects the impact of Type II residual stresses. The components of $\mathbf{E}^*$ for different grain families were estimated based on *in situ* SXRD measurements before loading, as described in the Methods section. On the other hand, the back stress tensor **B** represents the effective internal stresses within grains arising from heterogeneous dislocation distributions, thus reflecting the impact of Type III residual stresses [29]. As such, the so-called intergranular and intragranular back stresses in previous studies [64, 65] are collectively considered as the Type III residual stresses in this work. The back stress tensor **B** is assumed to be deviatoric within the present pressure-independent crystal plasticity model. The initial values of the back stress tensor, denoted as $\mathbf{B}_0$, were assigned to represent the internal stresses arising from printing-induced heterogeneous dislocation structures. These initial values are responsible for the tension-compression asymmetry of yield strength of the as-printed samples. Furthermore, the back stress tensor **B** in individual grains evolves with the local plastic shear on different $\{111\}\langle 110\rangle$ slip systems in a non-linear manner with an

increase of applied load. Such non-linear response reflects the rapid development of back stresses as measured with ~ 200 MPa at 3% strain under uniaxial tension and compression, which indicates a significant impact of deformation-induced back stresses on the plastic responses of AM stainless steel during loading. We implemented the crystal plasticity model in the finite element simulation package ABAQUS/Explicit [39] by writing a user material subroutine VUMAT. In finite element simulations, we constructed a three-dimensional cubic polycrystalline structure with 8000 cubic elements. Each element represents one single crystal grain with an assigned orientation based on the EBSD data measured from the AM stainless steel sample. The numerical simulations generated the macroscopic stress-strain curves and lattice strain responses in different grain families.

Figure 3.5(a) shows the true stress-strain curve from CPFE simulation of uniaxial tension, which closely matches the experimental result. Figure 5(b) shows the simulated lattice strains along LD for the four grain families of {220}, {111}, {200} and {311} against the macroscopic tensile stress. It is seen that the main features of the simulated lattice strain responses, including stages prior to loading and in the linear elastic and non-linear plastic regimes, are all in accordance with the experimental results. The fitted values of diffraction elastic constants E^{hkl} from CPFE simulations (as listed in Table 3.1) are close to the SXRD and micromechanics results. Further parametric studies indicate that the residual lattice strains prior to loading are directly correlated to the eigen-strain tensor $\mathbf{E}^{*}$ and thus are responsible for Type II intergranular residual stresses.

To reveal the progressive yielding behavior of different grain families and associated non-linear lattice strain responses, Figure 3.5(c) shows the volume fraction of plastically

yielded grains against the macroscopic tensile stress for the four grain families. Supposing that the 'mean' yield stress for each grain family is given by the macroscopic stress giving 50% yielded grains, we see from Figure 3.5(c) that the {220} family first yields, while the {200} family last yields; the mean yield stress of the {111} family is similar to the {200} family, and the {311} family is similar to the {200} family. This sequence of progressive yielding is mostly consistent the micromechanics model prediction, i.e., the relative magnitudes of the normalized maximum resolved shear stress β^{hkl} in Table 3.1. The only exception is the {311} family. This can be attributed to the large residual lattice strain in this grain family in the as-built sample (Figure 3.5(b)), which is accounted for in the CPFE model but not in the micromechanics model. In addition, we note that local deformation incompatibilities between neighboring grains can affect the stress state in individual grains, leading to the statistical variation of yield stresses of individual grains in each grain family and thus the gradual increase of volume fraction of yielded grains for each grain family in Figure 3.5(c). Comparison of Figure 3.5(b) and (c) also reveals that the highly non-linear response of the lattice strain versus applied stress for the {200} family begins at the macroscopic stress much lower than the mean yield stress of this grain family. This indicates that the non-linear lattice strain evolution for the {200} family is, in fact, initially associated with elastic deformation. That is, such non-linearity arises due to stress redistribution to this softest grain family (i.e., with the lowest diffraction elastic constant shown in Table 1); as other grain families progressively yield, they shed their loads onto the grains in the {200} family that remains elastic.

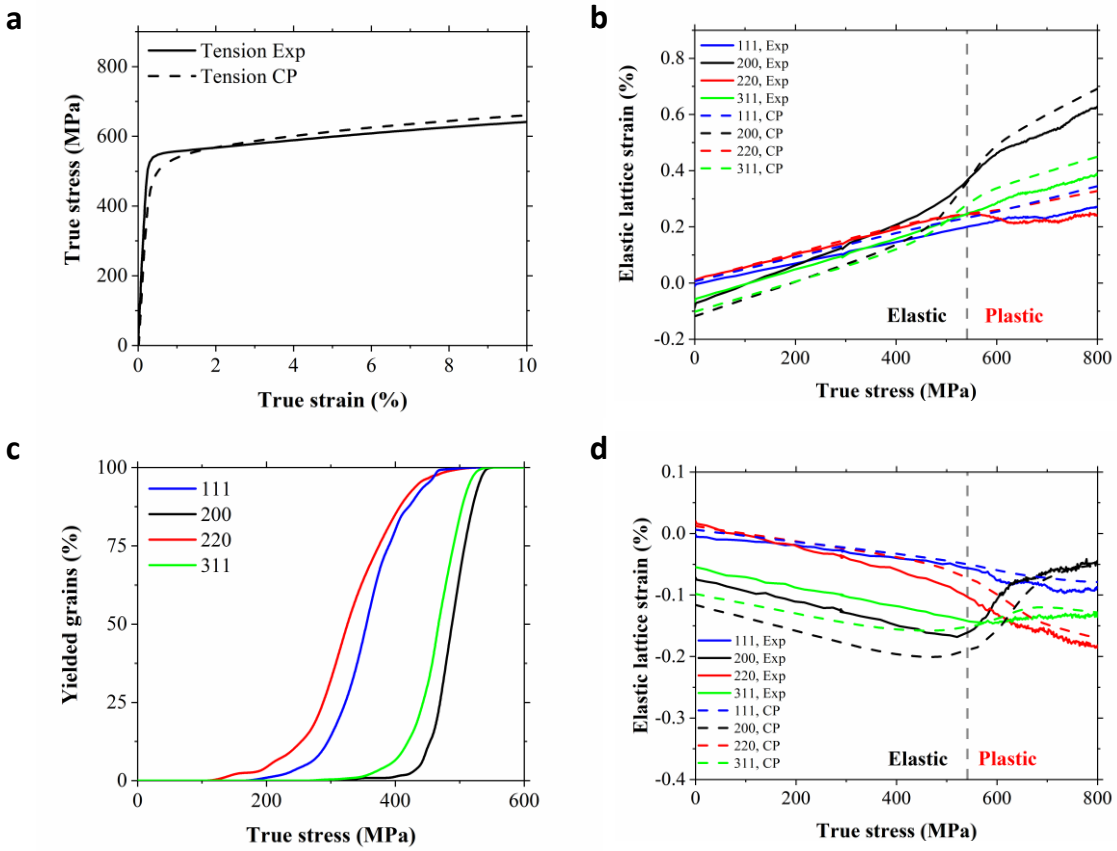

Figure 3.5 CPFE simulation results of the lattice strains in as-printed stainless steel under uniaxial tension. (**a**) Comparison of the true stress-strain curves of unaixial tension from experiment (Exp) and crystal plasticity (CP) finite element simulatoin. (**b**) Comparison of the lattice strains along LD against the macroscopic true stress for the {111}, {200}, {220}, {311} grain families from experiment and CPFE simulation. (**c**) Simulated volume fraction of plastically yielded grains within each family against the macrocopic true stress the as-printed sample, showing the progressive plastic yielding among different grian families. (**d**) Same as (b) except along TD.

In addition, Figure 3.5(d) shows the simulated lattice strain along TD for the four grain families of {220}, {111}, {200} and {311} against the macroscopic tensile stress. It is seen that the residual lattice strain responses before loading, in the linear elastic regime, and in the non-linear plastic regime are consistent with the experimental results. The non-linear lattice strain responses along TD in different grain families have similar origins as those along LD. However, the elastic lattice strain responses along TD are more complicated.

For example, the non-monotonic variation of lattice strain in the 200 family around the macroscopic yield stress suggests the highly non-linear interactions between this grain family and other families during load shedding and redistributions as other grain families become progressively yielded.

3.8 CPFE Modeling of Tension-Compression Asymmetry

To understand the effects of microscale residual stresses on the tension-compression asymmetry of AM stainless steel, we compared the CPFE simulations of uniaxial tension and compression. It is seen from Figure 3.6(a) that the simulated stress-strain curves of the as-printed sample agree with the experimental measurements. Further parametric studies indicate that the tension-compression asymmetry of the yield strength is predominantly controlled by the initial values of the back stress tensor $\mathbf{B}_0$. As described in the Section 3.6, we assigned identical values to $\mathbf{B}_0$ for all grains in the simulated polycrystalline aggregate, which approximately represent the average effect of type III intragranular internal stresses in these grains. That is, to match the simulation results of asymmetric tensile and compressive yield strengths with experimental ones, the initial back stress components along LD and TD within the build plane are both chosen to be 30 MPa, respectively; the initial back stress component along BD is chosen to be -60 MPa, so as to make $\mathbf{B}_0$ deviatoric; the shear components of $\mathbf{B}_0$ are chosen to be zero. It should be noted that the non-linear relation between the back stress and plastic strain adopted in the CPFE model is also important. This is because the deformation-induced back stresses increase quickly with applied stress, reaching ~200 MPa at the yield point for both tension and compression. As

such, the back stress component along LD in tension and compression at the respective yield point in CPFE simulations match the corresponding experimental measurements. These results demonstrate the different effects of printing-induced back stresses and deformation-induced back stresses in the CPFE model. Nonetheless, since the back stresses represent the effective long-range resistances to dislocation glide within grains, the CPFE simulation results indicate that the asymmetry of tensile and compressive yield strengths in as-printed samples is caused primarily by the printing-induced back stress and associated Type III intragranular residual stresses, which arise from heterogeneous dislocation structures in as-printed samples. In addition, the asymmetric strain hardening rate is also captured in CPFE simulations (Figure 3.6(b)) by fitting the constitutive parameters in the non-linear relation of back stress versus plastic shear strain. This indicates that both the printing- and deformation-induced microstructures and associated Type III intragranular residual stress affect the asymmetric evolution of strain hardening rate.

For comparison, Figure 3.6(a) and (b) also show the simulated stress-strain curves and strain hardening rate-true stress curves of the annealed sample by taking the eigen-strain tensor $\mathbf{E}^{*}$ and the initial values of the back stress tensor $\mathbf{B}_0$ as zero while keeping other model parameters unchanged. It is seen that the tension-compression asymmetries in yield strength and strain hardening are completely removed in CPFE simulations. Parametric studies indicate that zeroing the initial values of the back stress tensor $\mathbf{B}_0$ is essential to remove the tension-compression asymmetries in CPFE simulations of the annealed sample. In Figure 3.6(c), we plot the simulated lattice strain deviation ($\Delta\varepsilon^{\mathrm{hkl}}$) from the linear response for {200} and {220} grain families in the as-printed and annealed samples under unaixial tension. Their trends are similar to the correponding experimental results in Figure

3.2(c). However, the simulated initial values of $\Delta\varepsilon^{hkl}$ vanish and the non-linearity of lattice strain is reduced during loading. These responses arise from zeroing the eigen-strain tensor $\mathbf{E}^{*}$ in the CPFE simulations of the annealed sample. Altogether, these CPFE results also suggest that thermal annealing during experiment had not fully relaxed the printing-induced heterogeneous microstructures for completely removing back stresses and residual lattice strains in as-built samples. Finally, Figure 3.6(d) shows the simulated volume fraction of plastically yielded grains within the four grain families against the macrocopic tensile stress in the annealed sample. Compared to the correponding simulation results of the as-printed sample in Figure 3.5(c), the sequences of progressive yielding in different grain families are consistent between the two cases. However, the mean yield stressses of the {311} and {200} families in the annealed sample are markedly reduced due to the abscecne of the residual lattice strains (due to zeroing the eigen-strain tensor $\mathbf{E}^{*}$) in these two grain families. These results reinforce the notion that stress-relief heat treatment of AM samples can alter the footprints of microscale residual stresses through the experimentally measured lattice strain responses.

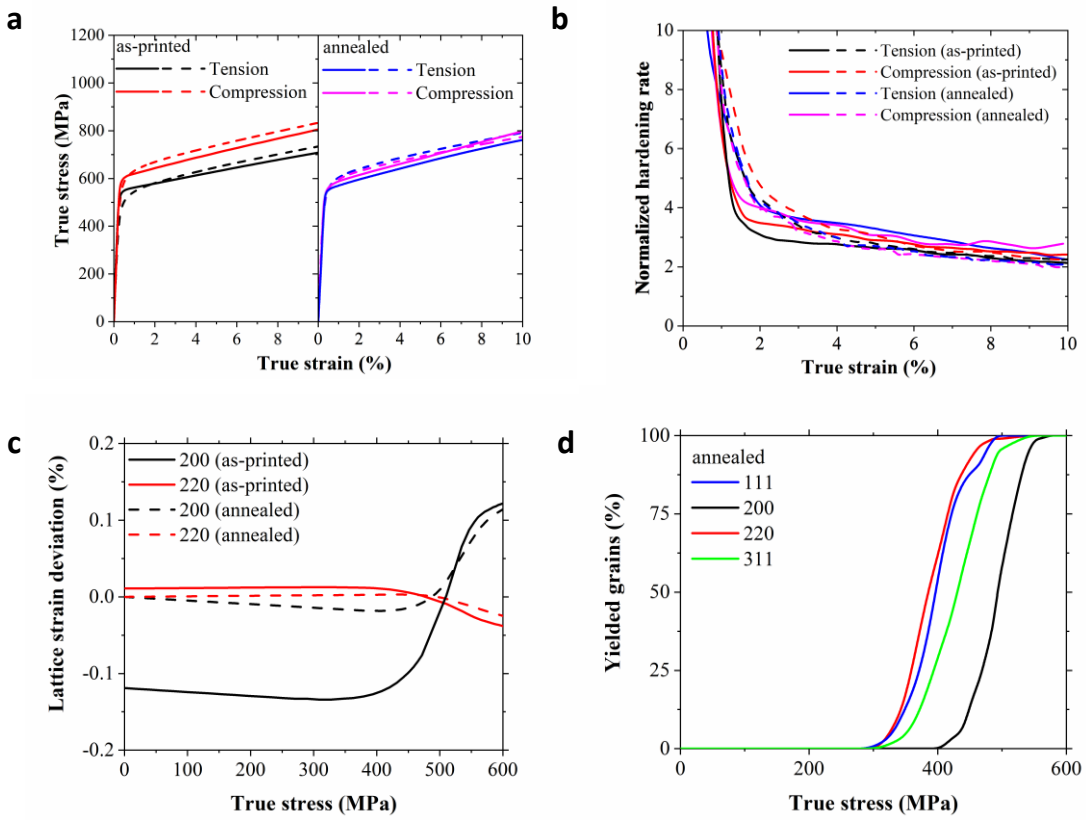

Figure 3.6 CPFE results of the tension-compression asymmetry of AM stainless steel. (**a**) Comparison of true stress-strain curves under uniaxial tension and compression from experiment (solid lines) and simulation (dashed lines) for as-printed and annealed samples. (**b**) Comparison of normalized strain hardening rate versus true strain under uniaxial tension and compression from experiment (solid lines) and simulation (dashed lines) for as-printed and annealed samples. (**c**) Simulated lattice strain deviation ($\Delta\varepsilon^{hkl}$) as a function of applied stress for {200} and {220} grain families for as-printed and annealed samples under unaixial tension. (**d**) Simulated volume fraction of plastically yielded grains within each family against the macrocopic true stress in the annealed sample, showing progressive plastic yielding among different grain families.

3.9 Summary

In summary, our combined experimental and modelling studies demonstrate that the microscale residual stresses have profound impacts on the yielding and strain hardening behavior of as-printed stainless steel. The *in situ* SXRD experiments provide a powerful

approach to unravel the residual lattice strains and associated Type II intergranular residual stresses for individual grain families in as-printed stainless steel as well as their evolution under applied loads. The combined SXRD and modeling results elucidate the effects of elastic anisotropy, progressive yielding and strain hardening on the extent and evolution of lattice strains and associated Type II intergranular residual stresses in different grain families. A pronounced tension-compression asymmetry of yield strength is observed, together with an asymmetric work hardening behavior. Such tension-compression asymmetries are shown to be governed by the back stresses and associated Type III intragranular residual stresses, which arise from heterogeneous dislocation distributions that can be strongly influenced by both L-PBF processing and mechanical loading. Hence, it is important to distinguish the printing and loading-induced back stresses. Our CPFE simulations show that the former dictates the tension-compression asymmetry of yield strength in as-printed samples, while the latter can quickly build up during loading and thereby affect both the yield strength and strain hardening responses. Hence, both L-PBF processing and subsequent mechanical loading can contribute substantially to the back stress evolution as measured from the loading-unloading experiment on as-printed samples, leading to the strong Bauschinger effect of AM stainless steel. Moreover, we show that thermal annealing of as-printed samples could mitigate both Type II and Type III residual stresses but is difficult to erase completely the footprints of these microscale residual stresses in the tension-compression asymmetries. Altogether, our results demonstrate the quantitative and mechanistic connections between the microscale residual stresses and mechanical behavior of AM stainless steel. Future studies on linking the printing parameters with the resultant microstructural heterogeneities and associated microscale

residual stresses are necessary to enable the control and mitigation of these residual stresses. We expect that our work has general implications for AM metallic materials, since multiscale residual stress is a critical issue for this rapidly developing technology.

CHAPTER 4. NEUTRON DIFFRACTION-INFORMED CONSTITUTIVE MODELING OF ADDITIVELY MANUFACTURED EUTECTIC HIGH-ENTROPY ALLOYS

4.1 Introduction

Nanolamellar metals exhibit high strength but come at the expense of hallmark ductility [66, 67]. Such strength-ductility tradeoff has been recently overcome by integrating the nanolamellar structure with a new composition design paradigm of multi-principal element alloys, also called high-entropy alloys (HEAs) [68-70]. However, nanolamellar materials have been often fabricated through thin-film deposition or (thermo-)mechanical processing with severe plastic deformation that is rather limited for practical applications. Additive manufacturing, also called three-dimensional (3D) printing, is an emerging technology for printing directly net-shaped components from digital models. In addition to the vast design freedom offered by this approach, the extreme printing conditions of metal alloys (e.g., via L-PBF) provide exciting opportunities for producing microstructures and mechanical properties beyond those achievable by conventional processing routes. For example, microstructures with highly heterogeneous grain geometries, sub-grain dislocation cells, chemical segregation at cell walls, and precipitates have been produced in a variety of AM metallic materials including stainless steels [8], cobalt- or nickel-based superalloys [71], aluminum alloys [72], and the novel HEAs. EHEA is a promising class of multi-principal element alloys with dual-phase lamellar structures that offer great potential for achieving excellent mechanical properties. Here, we use L-PBF to produce a unique type of far-from-equilibrium microstructure in the form of dual-phase nanolamellae in an $AlCoCrFeNi_{2.1}$

EHEA, which demonstrates an excellent combination of strength and ductility. Our work underscores the notion that additive manufacturing provides a powerful approach to engineer the heterogeneous nanostructured materials with superior mechanical performance.

4.2 Ultrahigh Strength and Ductility Achieved by Hierarchical Microstructures

The AM $AlCoCrFeNi_{2.1}$ EHEA is featured by eutectic colonies with nanolamellar structures (Figure 4.1b-d). Equiaxed colonies are observed predominantly on the top-view cross section of the sample, while elongated columnar colonies along the build direction (BD) are seen on the side-view cross section (Figure 4.1b). These colonies result from epitaxial growth across the hemispherical melt pool boundaries with further extension into the successive printed layers. Such epitaxial growth is common in alloys from L-PBF when the solidification microstructure is well-aligned along the maximum thermal gradient direction in parallel with BD. Since the laser scan direction was rotated by 90º between adjacent layers, the inter- and intra-layer laser remelting changed the direction of heat flux and thus promoted local side-branching. At the melt pool overlapping region, the direction of lamellar growth is ~45º inclined to the BD, and a subtle preferred orientation of FCC-<110>//BD is observed. No appreciable changes in chemical composition are observed between the $AlCoCrFeNi_{2.1}$ powders and as-printed samples.

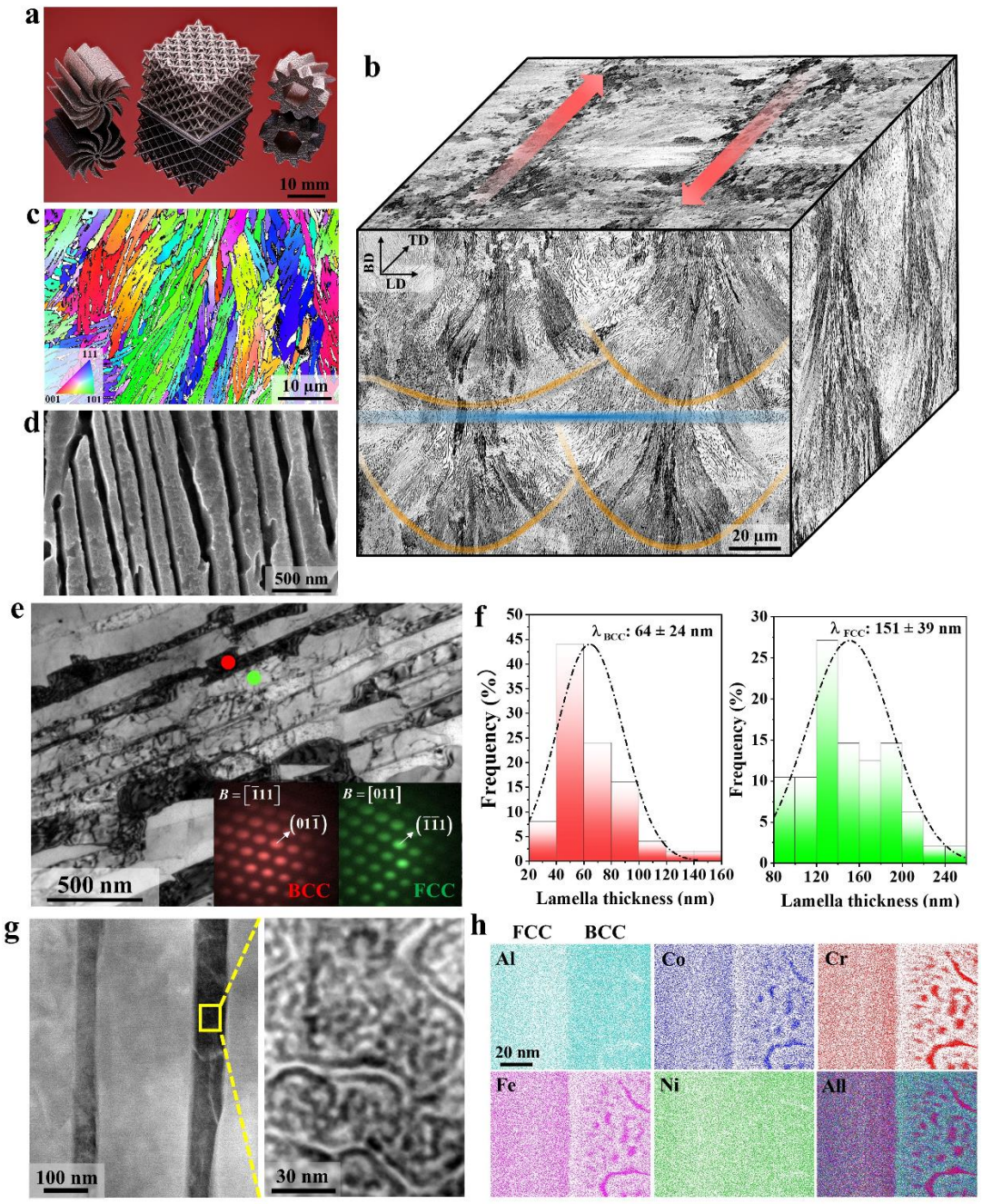

Figure 4.1 Microstructure of the AlCoCrFeNi$_{2.1}$ EHEA by L-PBF. **a**, Printed heatsink fan, octet lattice (strut size: ~300 μm), and gear (from left to right). **b**, 3D-reconstructed optical micrographs of as-printed AlCoCrFeNi$_{2.1}$ EHEA. The inter-layer boundary, melt pool boundaries, and laser scan tracks are illustrated by the blue line, orange lines, and red arrows, respectively. **c**, A cross-sectional electron backscatter diffraction (EBSD, Methods) inverse-pole figure (IPF) map of as-printed AlCoCrFeNi$_{2.1}$ EHEA with only FCC phase indexed, showing nanolamellar eutectic colonies. The build direction is vertical. The unindexed white regions are BCC phase. **d**, Secondary electron micrograph revealing the

typical nanolamellar structure. **e**, Bright field TEM image showing the nanolamellar structure. Insets show SAED patterns of BCC and FCC lamellae. **f**, Lamellar thickness distribution of BCC and FCC lamellae in as-printed $AlCoCrFeNi_{2.1}$ EHEA. **g**, HAADF-STEM image showing the modulated nanostructures within BCC lamella. **h,** APT maps of elemental distribution in a 100 × 78 × 5 nm section with an FCC/BCC interface in the center. Chemical fluctuations within BCC lamella are manifested by the nanoscale Ni-Al-rich and Co-Cr-Fe-rich regions.

The high cooling rate of ~10^5-10^7 K/s associated with L-PBF gave rise to highly refined eutectic microstructures in as-printed samples. Scanning electron microscopy (SEM) and transmission electron microscopy (TEM) characterizations reveal a dual-phase nanolamellar structure comprising alternating BCC and FCC nanolayers (Figure 4.1d, e), with the respective thickness of λ_{BCC} = 64 ± 24 nm and λ_{FCC} = 151 ± 39 nm (Figure 4.1f). Hence, the corresponding interlamellar spacing is $\lambda \approx 215$ nm, which is approximately half of that in the starting powder feedstock. Such dual-phase nanolamellar structures stand in contrast with the typical dual-phase micro-lamellar structures of $AlCoCrFeNi_{2.1}$ EHEA from casting ($\lambda \approx$ 0.77-2 μm) or thermomechanical processing ($\lambda \approx$ 1.5-5 μm). The much thinner nanolamellae in the AM EHEA are a result of rapid solidification in the extreme printing conditions from L-PBF.

Compared with conventional counterparts, the $AlCoCrFeNi_{2.1}$ EHEA from L-PBF shows distinct elemental distributions and phase structures. Both FCC and BCC phases in as-printed samples are solid solutions, as evidenced by the absence of superlattice reflections in neutron diffractions or extra super-lattice spots in the selected area electron diffraction (SAED) patterns (Figure 4.1e). A classical Kurdjumove-Sachs (K-S) orientation relationship was identified between the FCC and BCC solid solutions, giving

$\{111\}_{FCC} \parallel \{110\}_{BCC}$ and $<110>_{FCC} \parallel <111>_{BCC}$. Elemental mapping and compositional analysis by high angular annular dark-field scanning TEM (HAADF-STEM) energy dispersive X-ray spectroscopy (EDX) revealed nearly identical chemical compositions between the dual phases. Neutron diffraction measurements confirmed that the as-printed EHEA is composed of FCC and BCC phases, which have a weight fraction of 67% and 33%, respectively and show a lattice mismatch of 2.29%. No precipitates were detected in as-printed $AlCoCrFeNi_{2.1}$ EHEAs. In contrast, conventional $AlCoCrFeNi_{2.1}$ EHEAs consist of ordered $L1_2$ and B2 phases with different chemical compositions as well as copious nanoprecipitates; the B2/BCC lamellae are prominently rich in Ni and Al, whereas the $L1_2$/FCC lamellae are highly enriched by Co, Cr, and Fe. Altogether, the distinct lamellar thickness and elemental distributions between the AM and conventional $AlCoCrFeNi_{2.1}$ EHEAs indicate that atomic diffusion and chemical ordering are largely suppressed during rapid solidification of L-PBF processing. With increasing solidification rate, the conventional process of diffusion-mediated eutectic solidification is shifted toward diffusion-less (polymorphic) solidification. As such, diffusion of solute atoms at the lamellar interfaces lags behind solidification front growth, leading to nearly identical compositions in the eutectic nanolamellae from L-PBF.

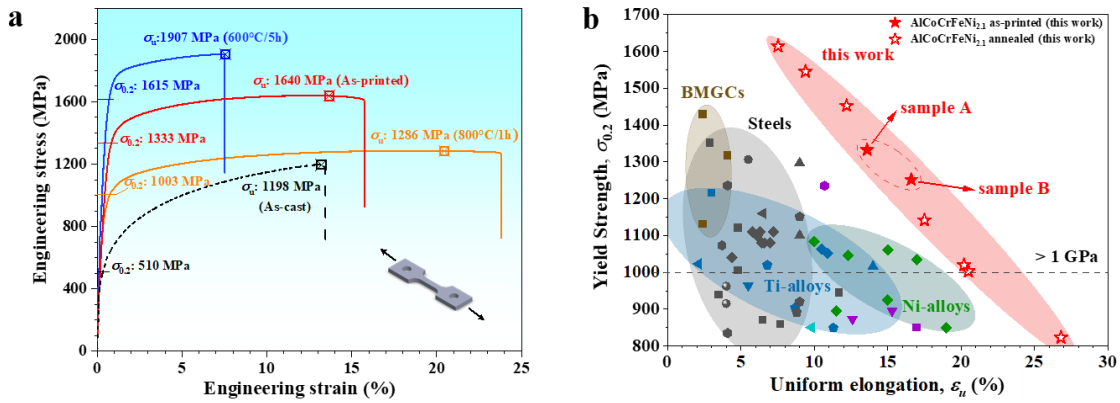

Figure 4.2 Tensile properties of AlCoCrFeNi$_{2.1}$ EHEAs from L-PBF. **a**, Representative tensile stress–strain curves for as-printed and annealed AlCoCrFeNi$_{2.1}$ EHEAs. The yield strength ($\sigma_{0.2}$) and ultimate tensile strength (σ_u) are marked on the curves. **b**, Tensile yield strength versus uniform elongation of AM AlCoCrFeNi$_{2.1}$ EHEAs in comparison with those of AM metal alloys with high strength ($\sigma_{0.2}$ > 800 MPa) in the literature.

4.3 Elastic Properties Extracted from Neutron Diffraction Experiments

Based on the neutron diffraction data of diffraction elastic constants, we developed a micromechanics model to inversely determine the anisotropic elastic constants of co-deforming FCC and BCC phases in our AM EHEAs, which enabled us to perform the stress partition analysis in the two phases. First, we derived an analytic micromechanics solution of diffraction elastic constants for co-deforming FCC and BCC phases by assuming their elastic properties are known. Then, we used the micromechanics solution to solve an optimization problem for determining the anisotropic elastic constants of both FCC and BCC phases in our AM EHEAs.

To derive the micromechanics solution, we considered a spherical FCC grain α in a $\{hkl\}$ grain family embedded in an elastically isotropic matrix comprising a mixture of FCC and BCC phases. Suppose the matrix has the effective bulk modulus $\bar{K}$ and shear

modulus $\bar{\mu}$. Based on the previous analytic solution [73], we used the constrained compliance tensor $\mathbf{U}_{(\alpha)}^{\mathrm{FCC}}$ to relate the applied average stress tensor $\bar{\boldsymbol{\sigma}}$ and local strain tensor $\boldsymbol{\varepsilon}_{(\alpha)}^{\mathrm{FCC}}$ in the FCC grain α according to

$$\boldsymbol{\varepsilon}_{(\alpha)}^{\mathrm{FCC}} = \mathbf{U}_{(\alpha)}^{\mathrm{FCC}} \bar{\boldsymbol{\sigma}}$$

Here the fourth-order tensor $\mathbf{U}_{(\alpha)}^{\mathrm{FCC}}$ can be expressed in a compact symbolic form

$$\mathbf{U}_{(\alpha)}^{\mathrm{FCC}} = \left(\frac{1}{3\left[\bar{K} + \bar{\gamma}\left(3\eta_1^{\mathrm{FCC}} - 3\bar{K}\right)\right]}, \frac{1}{2\left[\bar{\mu} + \bar{\delta}\left(2\eta_2^{\mathrm{FCC}} - 2\bar{\mu}\right)\right]}, \frac{1}{2\left[\bar{\mu} + \bar{\delta}\left(2\eta_3^{\mathrm{FCC}} - 2\bar{\mu}\right)\right]} \right)$$

where $\bar{\gamma} = \dfrac{\bar{K}}{3\bar{K} + 4\bar{\mu}}$ and $\bar{\delta} = \dfrac{3\bar{K} + 6\bar{\mu}}{15\bar{K} + 20\bar{\mu}}$ are the components of the Eshelby tensor for a spherical inclusion[58]; $3\eta_1^{\mathrm{FCC}} = C_{11}^{\mathrm{FCC}} + 2C_{12}^{\mathrm{FCC}}$, $2\eta_2^{\mathrm{FCC}} = C_{11}^{\mathrm{FCC}} - C_{12}^{\mathrm{FCC}}$, $2\eta_3^{\mathrm{FCC}} = 2C_{11}^{\mathrm{FCC}}$ are the combinations of FCC elastic constants. The above expression of $\mathbf{U}_{(\alpha)}^{\mathrm{FCC}}$ can be rewritten as

$$\mathbf{U}_{(\alpha)}^{\mathrm{FCC}} = \left(3a^{\mathrm{FCC}}, 2b^{\mathrm{FCC}}, 2c^{\mathrm{FCC}}\right)$$

where a^{FCC}, b^{FCC} and c^{FCC} are introduced to represent the corresponding terms in $\mathbf{U}_{(\alpha)}^{\mathrm{FCC}}$ and they are dependent on both the FCC elastic constants $C_{11}^{\mathrm{FCC}}, C_{12}^{\mathrm{FCC}}, C_{44}^{\mathrm{FCC}}$ and the effective elastic moduli of the isotropic matrix $\bar{K}, \bar{\mu}$. From $\mathbf{U}_{(\alpha)}^{\mathrm{FCC}}$, we obtained the analytic solution of diffraction elastic constants of grain α along the loading direction (LD)

$$\frac{1}{E_{\mathrm{LD}}^{\mathrm{FCC},hkl}} = \frac{\left\langle \mathbf{n} \cdot \boldsymbol{\varepsilon}^{\mathrm{FCC}} \cdot \mathbf{n} \right\rangle_{hkl}}{\mathbf{n} \cdot \bar{\boldsymbol{\sigma}} \cdot \mathbf{n}} = \frac{3a^{\mathrm{FCC}} + 4b^{\mathrm{FCC}}}{3} - 4\left(b^{\mathrm{FCC}} - c^{\mathrm{FCC}}\right)\Gamma$$

where $\mathbf{n}$ is the unit vector along the loading direction, $\langle \bullet \rangle_{hkl}$ represents the average over grains with their [hkl] directions aligned with $\mathbf{n}$, and $\Gamma = \frac{h^2k^2 + l^2k^2 + h^2l^2}{\left(h^2 + k^2 + l^2\right)^2}$ is the orientation index parameter. Following a similar procedure, we obtained the analytic solution of diffraction elastic constants of the BCC phase along LD,

$$\frac{1}{E_{\mathrm{LD}}^{\mathrm{BCC},hkl}} = \frac{\left\langle \mathbf{n} \cdot \boldsymbol{\varepsilon}^{\mathrm{BCC}} \cdot \mathbf{n} \right\rangle_{hkl}}{\mathbf{n} \cdot \bar{\boldsymbol{\sigma}} \cdot \mathbf{n}} = \frac{3a^{\mathrm{BCC}} + 4b^{\mathrm{BCC}}}{3} - 4\left(b^{\mathrm{BCC}} - c^{\mathrm{BCC}}\right)\Gamma$$

where $a^{\mathrm{BCC}}, b^{\mathrm{BCC}}$ and c^{BCC} are introduced to represent the constrained compliance tensor $\mathbf{U}_{(\alpha)}^{\mathrm{BCC}}$ and they are dependent on the elastic constants of the BCC phase $C_{11}^{\mathrm{BCC}}, C_{12}^{\mathrm{BCC}}, C_{44}^{\mathrm{BCC}}$ and the effective elastic moduli of the isotropic matrix $\bar{K}, \bar{\mu}$. We also obtained the similar analytic solution of diffraction elastic constants along the transverse direction (TD). We note that the elastic constants of $C_{11}^{\mathrm{FCC}}, C_{12}^{\mathrm{FCC}}, C_{44}^{\mathrm{FCC}}, C_{11}^{\mathrm{BCC}}, C_{12}^{\mathrm{BCC}}, C_{44}^{\mathrm{BCC}}, \bar{K}, \bar{\mu}$ completely determine the diffraction elastic constants of FCC and BCC phases, but they are not all independent of each other. Namely, we invoked the self-consistent method to evaluate the effective moduli $\bar{K}, \bar{\mu}$ for our dual-phase EHEAs. Hence, $\bar{K}, \bar{\mu}$ can be determined from the elastic constants of $C_{11}^{\mathrm{FCC}}, C_{12}^{\mathrm{FCC}}, C_{44}^{\mathrm{FCC}}, C_{11}^{\mathrm{BCC}}, C_{12}^{\mathrm{BCC}}, C_{44}^{\mathrm{BCC}}$ and the volume fractions of FCC and BCC phases. Specifically, the average strain for a dual-phase EHEA over all grain orientations is given by

$$
\begin{aligned}
\bar{\boldsymbol{\varepsilon}} &= \varphi^{\mathrm{FCC}} \left\langle \boldsymbol{\varepsilon}^{\mathrm{FCC}} \right\rangle_{all} + \varphi^{\mathrm{BCC}} \left\langle \boldsymbol{\varepsilon}^{\mathrm{BCC}} \right\rangle_{all} \\
&= \left[\varphi^{\mathrm{FCC}} \left\langle \mathbf{U}^{\mathrm{FCC}} \right\rangle_{all} + \varphi^{\mathrm{BCC}} \left\langle \mathbf{U}^{\mathrm{BCC}} \right\rangle_{all} \right] \bar{\boldsymbol{\sigma}} \\
&= \left(3\varphi^{\mathrm{FCC}} a^{\mathrm{FCC}} + 3\varphi^{\mathrm{BCC}} a^{\mathrm{BCC}}, \frac{4\varphi^{\mathrm{FCC}} b^{\mathrm{FCC}} + 4\varphi^{\mathrm{BCC}} b^{\mathrm{BCC}} + 6\varphi^{\mathrm{FCC}} c^{\mathrm{FCC}} + 6\varphi^{\mathrm{BCC}} c^{\mathrm{BCC}}}{5} \right) \bar{\boldsymbol{\sigma}} \\
&= \left(3\bar{a}, \frac{4\bar{b} + 6\bar{c}}{5} \right) \bar{\boldsymbol{\sigma}}
\end{aligned}
$$

where φ^{FCC} and φ^{BCC} are the volume fractions of FCC and BCC phases, respectively, and $\bar{a}, \bar{b}, \bar{c}$ are the phase average of previously defined a, b, c quantities. Recall that the average compliance tensor $\bar{\mathbf{M}}$ is given by

$$
\bar{\boldsymbol{\varepsilon}} = \bar{\mathbf{M}} \bar{\boldsymbol{\sigma}} = \left(\frac{1}{3\bar{K}}, \frac{1}{2\bar{\mu}} \right) \bar{\boldsymbol{\sigma}}
$$

As such, the above result expresses $\bar{K}, \bar{\mu}$ in terms of $C_{11}^{\mathrm{FCC}}, C_{12}^{\mathrm{FCC}}, C_{44}^{\mathrm{FCC}}, C_{11}^{\mathrm{BCC}}, C_{12}^{\mathrm{BCC}}, C_{44}^{\mathrm{BCC}}$. This self-consistent result is enforced by comparing the predicted values of $\bar{K}, \bar{\mu}$ with the corresponding experimental values.

Next, we used the above micromechanics solution to solve an optimization problem for determining the anisotropic elastic constants of FCC and BCC phases in our AM EHEAs. From the experimentally measured diffraction elastic constants and elastic moduli of AM EHEAs, we employed the gradient descent algorithm to minimize the error between predicted and measured values. We started with a random initial guess of $\mathbf{x} = \left[C_{11}^{\mathrm{FCC}}, C_{12}^{\mathrm{FCC}}, C_{44}^{\mathrm{FCC}}, C_{11}^{\mathrm{BCC}}, C_{12}^{\mathrm{BCC}}, C_{44}^{\mathrm{BCC}}, \bar{K}, \bar{\mu} \right]$. Then we computed the target elastic properties arranged in a linear array of $\mathbf{y}$, i.e.,

$$
\begin{aligned}
\mathbf{y} &= \mathbf{f}(\mathbf{x}) \\
&= [E_{\mathrm{LD}}^{\mathrm{FCC},200}, E_{\mathrm{LD}}^{\mathrm{FCC},220}, E_{\mathrm{LD}}^{\mathrm{FCC},111}, E_{\mathrm{LD}}^{\mathrm{FCC},311}, E_{\mathrm{LD}}^{\mathrm{FCC},331}, \\
&\quad E_{\mathrm{TD}}^{\mathrm{FCC},200}, E_{\mathrm{TD}}^{\mathrm{FCC},220}, E_{\mathrm{TD}}^{\mathrm{FCC},111}, E_{\mathrm{TD}}^{\mathrm{FCC},311}, E_{\mathrm{TD}}^{\mathrm{FCC},331}, \\
&\quad E_{\mathrm{LD}}^{\mathrm{BCC},200}, E_{\mathrm{LD}}^{\mathrm{BCC},110}, E_{\mathrm{LD}}^{\mathrm{BCC},211}, E_{\mathrm{LD}}^{\mathrm{BCC},321}, \\
&\quad E_{\mathrm{TD}}^{\mathrm{BCC},200}, E_{\mathrm{TD}}^{\mathrm{BCC},110}, E_{\mathrm{TD}}^{\mathrm{BCC},211}, E_{\mathrm{TD}}^{\mathrm{BCC},321}, \\
&\quad 3\bar{K} - \frac{1}{3\bar{a}}, 2\bar{\mu} - \frac{5}{4\bar{b} + 6\bar{c}}, \frac{9\bar{K}\bar{\mu}}{3\bar{K} + \bar{\mu}}]
\end{aligned}
$$

where the first 18 components in $\mathbf{y}$ are the diffraction elastic constants for different grain families along LD and TD, and the last 3 components serve to enforce the self-consistency for the dual-phase polycrystal, as discussed earlier. The target values of $\mathbf{y}$ are given as $\mathbf{y}_0$ taken from experimental measurements, i.e.,

$$
\begin{aligned}
\mathbf{y}_0 = [&136.53,\ 208.64,\ 238.72,\ 175.14,\ 222.78, \\
&399.34,\ 579.90,\ 784.18,\ 525.59,\ 646.36, \\
&107.75,\ 197.31,\ 192.44,\ 192.13, \\
&274.29,\ 542.89,\ 511.56,\ 491.94, \\
&0,\ 0,\ 171]\ \mathrm{GPa}
\end{aligned}
$$

To find the optimal solution for the elastic constants of FCC and BCC phases, the loss function L is defined as

$$
L = (\mathbf{y} - \mathbf{y}_0)\mathbf{g}(\mathbf{y} - \mathbf{y}_0)^{\mathrm{T}}
$$

where the weight matrix is $\mathbf{g} = \mathrm{diag}(4,4,4,4,4,1,1,1,1,1,4,4,4,4,1,1,1,1,3,5,3)$. This weight matrix was introduced to balance the relative importance of different diffraction elastic constants because their values along TD are usually two times higher than those

along LD. The gradient descent algorithm was used to minimize the loss function L by updating the components in $\mathbf{x}_i$ at the i-th iteration step along the gradient direction,

$$\mathbf{x}_{i+1} = \mathbf{x}_i - \lambda \frac{\partial L}{\partial \mathbf{x}}$$

The gradient $\frac{\partial L}{\partial \mathbf{x}}$ was calculated numerically by small perturbations near $\mathbf{x}_i$ and the iteration step size λ is 1×10^{-3}. The iteration process of optimization was terminated when the norm of $\frac{\partial L}{\partial \mathbf{x}}$ is less than 1×10^{-3}. Three different sets of initial values of $\mathbf{y}_0$ were tested and they all converged to the same result. The diffraction elastic constants are plot in the Figure 4.3 comparing to the experimental measured ones. The final optimized elastic constants of FCC and BCC phases for our AM HEAs are listed in Table 4.1.

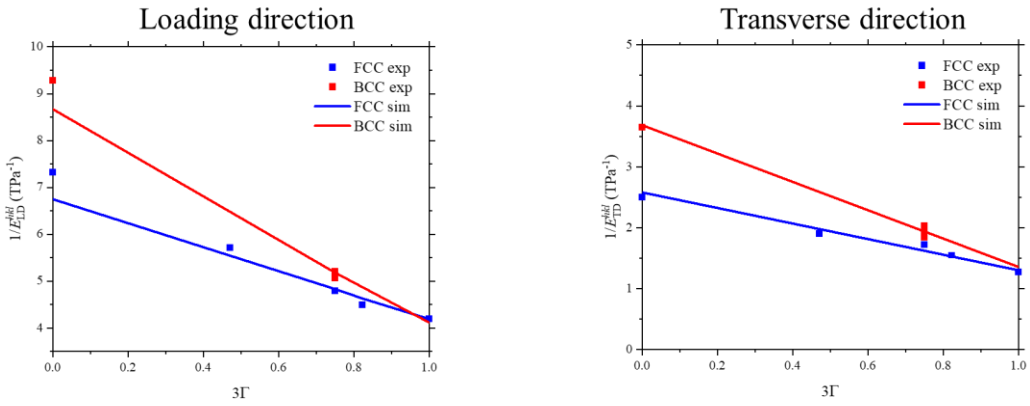

Figure 4.3 Plot of the reciprocal of diffraction elastic constant $1/E^{\mathrm{hkl}}$ as a function of orientation parameter Γ along (left) LD and (right) TD for Al-HEA. The solid lines represent the micromechanics (Micro) solutions, and the squares the experiment results from the neutron diffraction experiment.

Table 4.1 Elastic constants of FCC and BCC phases in the $AlCoCrFeNi_{2.1}$ EHEA determined from the micromechanics model (in GPa).

C_{11}^{FCC}	C_{12}^{FCC}	C_{44}^{FCC}	C_{11}^{BCC}	C_{12}^{BCC}	C_{44}^{BCC}	$\bar{K}$	$\bar{\mu}$
258.72	177.52	124.82	282.44	259.75	131.90	225.03	63.37

4.4 Dual-Phase Crystal Plasticity Finite Element Modeling

A DP-CPFE model was developed to evaluate both linear and non-linear lattice strain responses as well as to perform the stress partition analysis in the dual-phase EHEA. We used the rate-dependent, finite strain, crystal plasticity constitutive formulation [24] for both FCC and BCC phases. The deformation gradient $\mathbf{F}$ is decomposed into $\mathbf{F}=\mathbf{F}^e\mathbf{F}^p$, where $\mathbf{F}^e$ is the elastic deformation gradient and $\mathbf{F}^p$ is the plastic deformation gradient. The elastic Green strain tensor can be defined as $\mathbf{E}^e=1/2\left(\mathbf{F}^{e^{\mathrm{T}}}\mathbf{F}^e-\mathbf{I}\right)$, where $\mathbf{I}$ is second-order identity tensor. The second Piola-Kirchhoff stress $\mathbf{T}^*$ in the intermediate configuration can be determined as $\mathbf{T}^*=\mathbf{C}:\mathbf{E}^e$, and $\mathbf{C}$ is the forth-order single-crystal elastic tensor. The rate of plastic deformation gradient is given $\dot{\mathbf{F}}^p=\mathbf{L}^p\mathbf{F}^p$. Here, the plastic velocity gradient is expressed as $\mathbf{L}^p=\sum_{i=1}^{12}\dot{\gamma}_i^p\mathbf{m}_i\otimes\mathbf{n}_i$, where $\dot{\gamma}_i^p$ is the plastic shearing rate on *i*-th slip system, $\mathbf{m}_i$ and $\mathbf{n}_i$ are the slip direction and slip plane normal, respectively. We considered 12 $\{111\}\langle 110\rangle$ slip systems in the FCC phase and 12 $\{110\}\langle 111\rangle$ in the BCC phase. The plastic shearing rate $\dot{\gamma}_i^p$ is given by a power-law relation, $\dot{\gamma}_i^p=\dot{\gamma}_0^p\left|\tau_i/s_i\right|^{1/m}\operatorname{sgn}\left(\tau_i\right)$, where $\dot{\gamma}_0^p$ is the reference shearing rate, $\tau_i=\mathbf{m}_i\cdot\mathbf{T}\cdot\mathbf{n}_i$

is the resolved shear stress, m is the rate sensitivity and s_i is the slip resistance on the i-th slip system. The slip resistance on each slip system starts with an identical initial value s_0 and is hardened according to $\dot{s}_i = \sum_j h_{ij} \left| \dot{\gamma}_j^p \right|$; the hardening matrix is expressed as $h_{ij} = q_{ij} h_0 \left(1 - s_j / s_{\text{sat}}\right)^a$, where the diagonal components of q_{ij} are 1.0 and the off-diagonal components are 1.4. The parameters used in the above constitutive model are listed in Table 4.2.

Table 4.2 Parameters used in the DP-CPFE model

Phase	$\dot{\gamma}_0^p \left(\text{s}^{-1}\right)$	m	$s_0 \left(\text{MPa}\right)$	$h_0 \left(\text{MPa}\right)$	$s_{\text{sat}} \left(\text{MPa}\right)$	a
FCC	0.001	0.02	550	1000	600	0.7
BCC	0.001	0.02	475	4000	750	0.7

The above constitutive model was implemented in the general finite element package ABAQUS/Explicit by writing a user-defined material subroutine VUMAT. In finite element simulations, we constructed a polycrystalline cube comprising 8000 elements, where each element represents a single-crystal grain. The crystallographic orientation of each grain was randomly assigned to generate a texture-free sample. Each grain was also randomly assigned as an FCC or BCC phase, such that the corresponding volume fraction of each phase is consistent with experimental values. The polycrystal structure was subjected to uniaxial loading with a strain rate of 0.001s^{-1}. The lattice strain response was extracted from the elastic strain tensor in each grain by writing a Python script through the ABAQUS-Python interface.

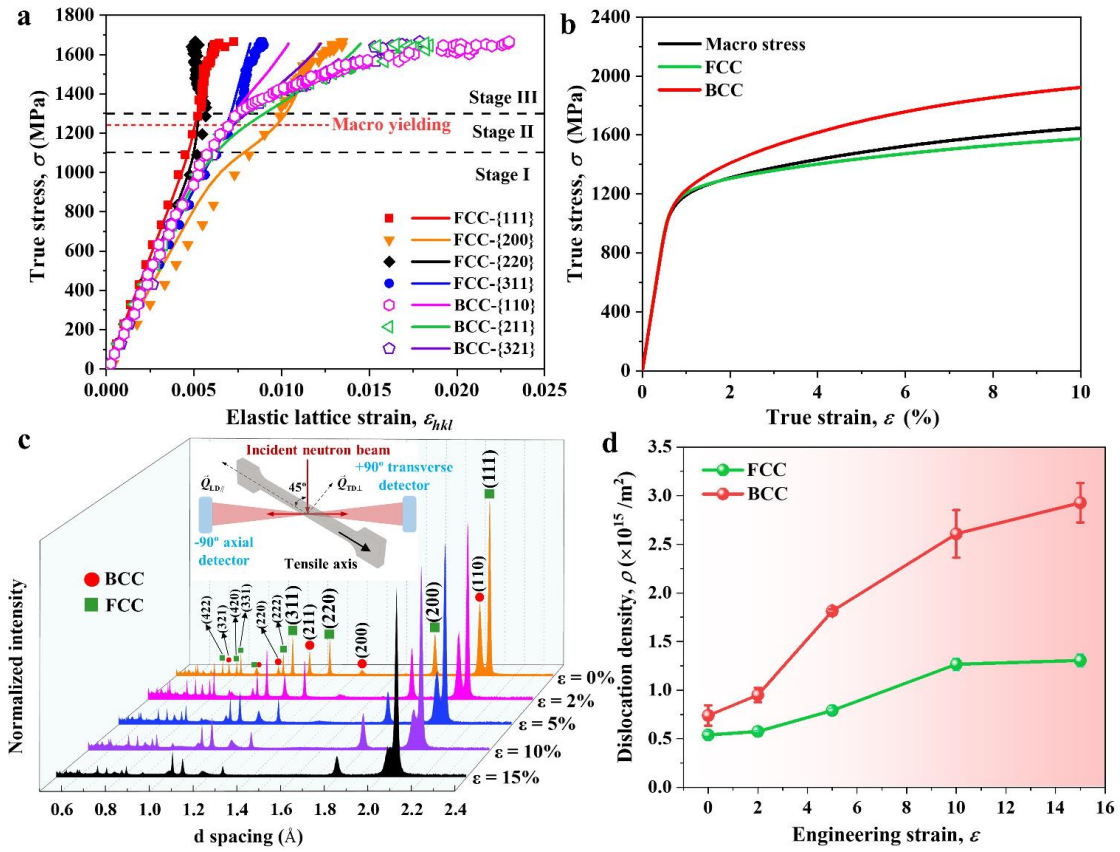

Figure 4.4 Lattice strain measurements and stress partitioning in FCC/BCC phases during uniaxial tension of AM $AlCoCrFeNi_{2.1}$ EHEA, from *in situ* neutron diffraction experiments and DP-CPFE modeling. **a**, Evolution of the lattice strain over macroscopic true stress for representative FCC (including {111}, {200}, {220}, {311}) and BCC (including {110}, {211} and {321}) grain families along the loading direction. The experimental and simulated results are depicted by symbols and solid lines, respectively. The macroscopic yield strength is marked with the red dashed line. **b**, DP-CPFE simulation results of the macroscopic stress-strain response with the corresponding stress partitioning in BCC and FCC phases. **c**, Selected neutron diffraction spectra along the loading direction during deformation. During the *in situ* neutron diffraction measurements, the sample was unloaded at 2%, 5%, and 10% engineering strains, respectively. **d**, Dislocation density evolution in BCC and FCC phases, derived from the diffraction spectra in **c** and the modified Williamson-Hall method.

It is important to note that DP-CPFE simulations further enable us to partition the bulk tensile stress into the corresponding tensile stress components in FCC and BCC phases, so

as to quantitatively evaluate the strain hardening behavior of co-deforming FCC and BCC nanolamellae. These simulations require a knowledge of anisotropic elastic constants of individual phases, which could not be readily obtained due to the non-equilibrium structures developed in as-printed EHEAs with the extremely small lamellar thicknesses and unique alloy compositions different from conventional counterparts. To address this issue, we used DP-CPFE simulations to solve an inverse problem to determine theses elastic constants, such that the predicted lattice strain responses (Figure 4.4a) and sample-level stress-strain curve (Figure 4.4b) from DP-CPFE simulations closely match the experimental measurements. After solving this inverse problem, our DP-CPFE simulations can provide the true stress-strain curves in co-deforming FCC and BCC phases, as shown in Figure 4.4b. It is seen that both BCC and FCC nanolamellae exhibit high strain hardening for a fairly large range of tensile strains, but BCC nanolamellae make greater contributions to the overall high strain hardening responses than FCC nanolamellae, thereby promoting the overall high tensile ductility of the present EHEA. Evidently, the AM EHEA enables the high strain hardening behavior in its constituent BCC nanolamellae that is hitherto difficult to achieve in single-phase BCC nanostructures.

4.5 Summary

In summary, we have harnessed additive manufacturing via L-PBF to develop a new class of dual-phase nanolamellar EHEAs that exhibits an exceptional combination of ultrahigh yield strength and large tensile ductility well surpassing other state-of-the-art 3D-printed metal alloys. In particular, rapid solidification inherent to L-PBF enables the

formation of far-from-equilibrium heterogeneous nanostructures with chemical modulations, which lead to the unusual work-hardening capability of nanoscale BCC phase that is greatly enhanced by the co-deforming nanoscale FCC phases and their semi-coherent interfaces. Additive manufacturing of multicomponent EHEAs not only offers a new means of pushing the limit of attainable microstructures and compositions for metal alloys, but also provides a general pathway for pursuing novel mechanical properties in many other metallic materials that can develop multi-phase lamellar structures such as aluminum alloys and titanium alloys.

Part II: Macroscale Heterogeneities in Gradient Nanotwinned Metals

CHAPTER 5. PHENOMENOLOGICAL THEORY OF STRAIN GRADIENT PLASTICITY

5.1 Introduction

Gradient structured metals have received considerable attention in recent years due to their enhanced strength, ductility and fatigue resistance compared to non-gradient counterparts [3, 74, 75]. Structure gradients can give rise to substantial extra strengths [9, 76, 77] that result from plastic strain gradients [10, 78-84] arising in plastically deformed gradient structures. However, the mechanics of gradient plasticity in gradient structures has not been clearly understood [85-88]. Recently, Cheng *et al*. [9] reported the fabrication of gradient nanotwinned (GNT) Cu having different gradient distributions of nanoscale twin thickness and thus different yield strength gradients. They showed that an increase in nanostructure gradient causes a marked increase of the sample-level yield strength, and a large nanostructure gradient produces a high yield strength exceeding that of the strongest component of the gradient nanostructure. In particular, they measured the extra strength as a function of structure and strength gradients. These results call for a fundamental understanding of the strengthening effects of plastic strain gradients originating from gradient nanostructures. In addition, given the high tunability of its gradient structures, GNT Cu can serve as an effective model system for benchmarking the gradient theories of plasticity.

In this Chapter, we develop a gradient theory of plasticity by incorporating the strengthening effect of plastic strain gradient into the J_2 flow theory. Motivated by the

simple gradient theory of plasticity by Bassani [10], we introduce a scalar measure of plastic strain gradient into a hardening rate relation, so that higher-order stresses and additional boundary conditions are not needed. This approach enables an effective analysis of strain gradient plasticity without much mathematical complexity. To study the gradient plastic responses of GNT Cu under uniaxial tension, we reduce the general three-dimensional (3D) gradient theory into a one-dimensional (1D) theory, and numerically implement this 1D theory with the finite-difference method. Numerical simulations reveal the primary effects of strain gradient plasticity on GNT Cu with different structure gradients. In addition, we numerically implement the 3D gradient theory into the general finite element package ABAQUS/Explicit [39]. Numerical results from 3D gradient plasticity finite element (GPFE) simulations confirm those from 1D finite-difference simulations, and further reveal the impact of stress components neglected in the 1D gradient theory and simulations. Based on insights gained from both 1D and 3D gradient plasticity simulations, we explore the optimization of structure and strength gradients toward achieving the maximum strength of GNT Cu.

5.2 Experiment

In this section, we provide a brief overview of the experimentally measured structure and strength gradients in GNT Cu. These results provide a basis for our development of gradient plasticity theories and associated computational models. As described in detail by Cheng *et al.* [9], direct-current electrodeposition was used to prepare GNT Cu samples with a controllable pattern of gradient nanotwinned structures. Figure 1a shows the schematic illustration of four types of GNT Cu samples, named GNT-1, GNT-2, GNT-3 and GNT-4, respectively. The corresponding electron microscopy images of

microstructures can be found in Cheng *et al.* [9]. These samples have similar thickness L around 400 μm, but different structure gradients through sample thickness. At each local region, preferentially oriented nanometer-scale twin lamellas are embedded within micrometer-scale columnar-shaped grains. As schematically illustrated in Figure 5.1a, GNT-1 exhibits approximately linear variations of twin thickness and grain size through sample thickness. The average twin thickness increases from 29 nm to 72 nm, with a concomitant increase of average grain size from 2.5 μm to 15.8 μm. Despite the dual gradient variations of twin thickness and grain size, the strengthening effects are mainly controlled by the gradient distributions of twin lamellas [9], due to their much smaller twin thicknesses than grain sizes. Hereafter, our description of structure gradients will focus on gradient distributions of nanotwinned structures. As also illustrated in Figure 1a, GNT-2, GNT-3 and GNT-4 exhibit periodic, piecewise linear, continuous variations of twin thickness [9], which can be approximately represented by triangle waves of twin thickness with different wavelengths, i.e., about L, $L/2$ and $L/3.5$, respectively. In fact, the linear profile of twin thickness in GNT-1 can be represented by the half period of a triangle wave with wavelength $2L$. For GNT-2 to GNT-4, the maximum and minimum twin thicknesses are close to those of GNT-1. As such, their twin thickness gradients are 2, 4 and 7 times that of GNT-1. We note that the control of the structural gradient becomes increasingly difficult with increasing structure gradient. As a result, GNT-4 has an actual sample thickness larger than 400 μm, such that its twin thickness gradient is not as ideal as 8 times that of GNT-1.

The gradient nanotwin structures lead to the gradient strengths in GNT Cu. Figure 5.1b shows the measured indentation hardness profiles of GNT-1 to GNT-4 through their

sample thickness, which can be also represented by triangle waves of hardness with different wavelengths (i.e., about 2*L*, *L*, *L*/2 and *L*/3.5, respectively). These triangle wave profiles have approximately identical maximum hardness 1.5 GPa and minimum hardness 0.8 GPa. The measured hardness gradient, denoted as *g*, for GNT-1 to GNT-4 are 1.75, 3.2, 6.0 and 11.6 GPa/mm, respectively. Most importantly, an increase of hardness gradient causes a marked increase in the sample-level yield strength [9]. These results will be presented along with the experimentally measured stress-strain curves of GNT Cu in section 5.4, where they will be compared with the corresponding gradient plasticity simulation results.

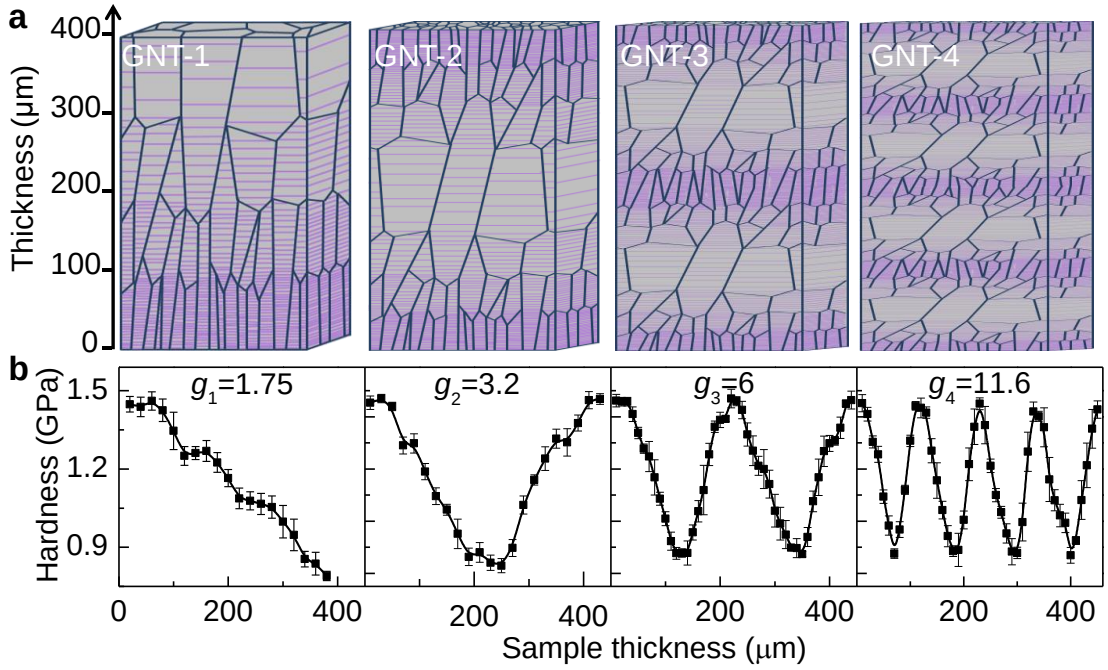

Figure 5.1 Schematic illustration of four types of GNT Cu samples, named GNT-1, GNT-2, GNT-3 and GNT-4, respectively [9]. (a) Through sample thickness, GNT-1 to GNT-4 exhibit gradient twin structures (with periodic, piecewise linear, continuous variations of twin thickness) as well as gradient grain sizes. Preferentially oriented nanometer-scale twin lamellas (with twin boundaries represented by purple lines) are embedded within micrometer-scale columnar-shaped grains (with grain boundaries represented by blue

lines). (b) Measured indentation hardness profiles through the sample thickness of GNT-1 to GNT-4. Each hardness curve is labeled with its corresponding hardness gradient *g*.

5.3 A Theory of Strain Gradient Plasticity

To study the mechanical behavior of GNT Cu, we developed a small-strain theory of strain gradient plasticity by incorporating the strengthening effect of plastic strain gradient into the classical J_2 flow theory. In the following, we present the gradient theory using index notation – a free index ranges over 1 to 3 and repeated indices mean summation. The total strain rate $\dot{\varepsilon}_{ij}$ is decomposed into

$$\dot{\varepsilon}_{ij} = \dot{\varepsilon}^{\mathrm{e}}_{ij} + \dot{\varepsilon}^{\mathrm{p}}_{ij} \tag{5.1}$$

In Eq. (5.1), the elastic strain rate $\dot{\varepsilon}^{\mathrm{e}}_{ij}$ is related to the stress rate $\dot{\sigma}_{ij}$ by the generalized Hooke's law

$$\dot{\varepsilon}^{\mathrm{e}}_{ij} = \frac{1}{E}\left[(1+\nu)\dot{\sigma}_{ij} - \nu\dot{\sigma}_{kk}\delta_{ij}\right] \tag{5.2}$$

where E is Young's modulus, ν is Poisson's ratio, $\delta_{ij} = 1$ when $i = j$ and $\delta_{ij} = 0$ otherwise. The plastic strain rate $\dot{\varepsilon}^{\mathrm{p}}_{ij}$ obeys the J_2-flow rule

$$\dot{\varepsilon}^{\mathrm{p}}_{ij} = \dot{\bar{\varepsilon}}^{\mathrm{p}}\frac{3\sigma'_{ij}}{2\bar{\sigma}} \tag{5.3}$$

In Eq. (5.3), σ'_{ij} is the deviatoric stress given by $\sigma'_{ij} = \sigma_{ij} - \sigma_{kk}\delta_{ij}/3$, $\bar{\sigma}$ is the equivalent stress

$$\bar{\sigma} = \sqrt{\frac{3}{2}\sigma'_{ij}\sigma'_{ij}} \tag{5.4}$$

and $\dot{\bar{\varepsilon}}^{\mathrm{p}}$ is the equivalent plastic strain rate given by a simple power-law relation

$$\dot{\bar{\varepsilon}}^{\mathrm{p}} = \dot{\bar{\varepsilon}}_0^{\mathrm{p}} \left(\frac{\bar{\sigma}}{s} \right)^{1/m} \tag{5.5}$$

where $\dot{\bar{\varepsilon}}_0^{\mathrm{p}}$ is the reference plastic strain rate, s is the plastic flow resistance, and m is the strain rate sensitivity parameter. The accumulated equivalent plastic strain is given by $\bar{\varepsilon}^{\mathrm{p}} = \int_0^t \dot{\bar{\varepsilon}}^{\mathrm{p}} dt'$.

To account for the hardening effect of the plastic strain gradient, an effective measure of plastic strain gradient is introduced into a hardening rate relation, as motivated by the gradient plasticity theory from Bassani [10]. That is, the instantaneous hardening rate is given by

$$\dot{s} = h\dot{\bar{\varepsilon}}^{\mathrm{p}} \tag{5.6}$$

where the hardening rate coefficient h is

$$h = \frac{h_0}{1+\left(\bar{\varepsilon}^{\mathrm{p}} / \varepsilon_1\right)^{n_1}} \left[1 + \frac{\kappa\sqrt{\alpha}}{1+\left(\bar{\varepsilon}^{\mathrm{p}} / \varepsilon_2\right)^{n_2}} \right] \tag{5.7}$$

In Eq. (5.7), the term outside the square bracket represents the conventional hardening effect due to plastic strain. In this term, h_0 is the hardening rate constant; ε_1 and n_1 control the nonlinear behavior of plastic strain hardening. Note that in Eq. (5.7), the second term

inside the square bracket reflects the extra hardening effect due to plastic strain gradient. Here α is defined as

$$\alpha = \sqrt{\bar{\varepsilon}^{\mathrm{p}}_{,i}\bar{\varepsilon}^{\mathrm{p}}_{,i}} \tag{5.8}$$

which is a scale measure of the spatial gradient of the accumulated equivalent plastic strain $\bar{\varepsilon}^{\mathrm{p}}_{,i} = \partial\bar{\varepsilon}^{\mathrm{p}} / \partial x_i$. As such, the hardening rate due to plastic strain gradient scales with $\kappa h_0\sqrt{\alpha}$, where κ is a constant. In addition, ε_2 and n_2 are used to control the range of $\bar{\varepsilon}^{\mathrm{p}}$ where the hardening effect of plastic strain gradient predominates. That is, this hardening effect is pronounced when $\bar{\varepsilon}^{\mathrm{p}}$ is less than ε_2, but it decays quickly as $\bar{\varepsilon}^{\mathrm{p}}$ increases above ε_2.

To capture the hardening behavior of GNT Cu, ε_2 is taken to be much smaller than ε_1; in addition, an appropriate κ is taken such that $\kappa h_0\sqrt{\alpha}$ is much larger than h_0. As a result, Eq. (5.7) represents a two-stage hardening response of GNT Cu. Specifically, a high hardening rate on the order of $\kappa h_0\sqrt{\alpha}$ predominates when $\bar{\varepsilon}^{\mathrm{p}}$ is less than ε_2, while a low high hardening rate on the order of h_0 takes over when $\bar{\varepsilon}^{\mathrm{p}}$ becomes greater than ε_2. The two-stage hardening is characteristic of the stress-strain response of GNT Cu [9] and implies the following dislocation strengthening effects in gradient structures. In the first stage of hardening, geometrically necessary dislocations [78] are quickly generated to accommodate plastic strain gradients resulting from built-in structure and strength gradients. Geometrically necessary dislocations give rise to a high hardening rate, thus reflecting a strong non-local strengthening effect of plastic strain gradients. In the second stage, hardening due to built-in structure and strength gradients becomes saturated, leading to a markedly reduced hardening effect.

5.4 Gradient Plasticity in GNT Cu

To study the gradient plastic responses of GNT Cu under uniaxial tension, we set up GNT-1 to GNT-4 models with different structures and strength gradients in section 5.4.1. Considering the dominant axial stresses in these GNT models, we reduced the general 3D gradient theory into a 1D gradient theory in section 5.4.2. This 1D theory was numerically implemented to simulate the tensile responses of GNT-1 to GNT-4 models, as described in section 5.4.3. Numerical results were compared with experimental measurements in terms of the overall stress-strain responses of GNT-1 to GNT-4. Detailed analysis of the numerical results for GNT-1 revealed the primary strengthening effects of gradient plasticity in GNT Cu.

5.4.1 GNT-1 to GNT-4 models

As shown in Figure 5.2a, we considered a rectangular block, with the dimensions of $L_x \times L_y \times L_z$, as a representative volume element of GNT-1 to GNT-4 samples. The *z*-axis of the block is oriented along the tensile loading direction, and the *y*-axis is along the sample thickness direction. A gradient distribution of initial plastic flow resistance $s(y, t=0)$ (equivalent to initial tensile yield strength) is prescribed in the *x*-*y* cross section and along the *y*-axis. Based on the experimentally measured hardness profiles of GNT-1 to GNT-4 samples (Figure 5.1), we used triangle waves with different wavelengths and gradients to represent $s(y, t=0)$ for GNT-1 to GNT-4 models. A typical triangle wave (Figure 5.2b) is prescribed by three parameters: the maximum resistance $s_{0,\max}$, minimum resistance $s_{0,\min}$ and wavelength λ. To facilitate comparison among different GNT

models, $s_{0,\max}$ is taken to be identical for GNT-1 to GNT-4 models and so is $s_{0,\min}$. Consider the GNT-1 model as an example. Its linear profile of $s^{\text{GNT-1}}(y, t=0)$ corresponds to the half period of a triangle wave, $\lambda^{\text{GNT-1}}/2 = L_y = 400\mu\text{m}$, and is expressed as

$$s^{\text{GNT-1}}(y, t=0) = s_{0,\max} - g_{\text{s}}^{\text{GNT-1}} \cdot y \tag{5.9}$$

where $g_{\text{s}}^{\text{GNT-1}}$ is the gradient of initial plastic flow resistance. For GNT-2 to GNT-4 models, their triangle wave profiles of $s(y, t=0)$ have the same half period form as Eq. (5.9), but the respective g_{s} is increased to 2, 4 and 7 times $g_{\text{s}}^{\text{GNT-1}}$, and the respective λ is reduced to 1/2, 1/4 and 1/7 times $\lambda^{\text{GNT-1}}$.

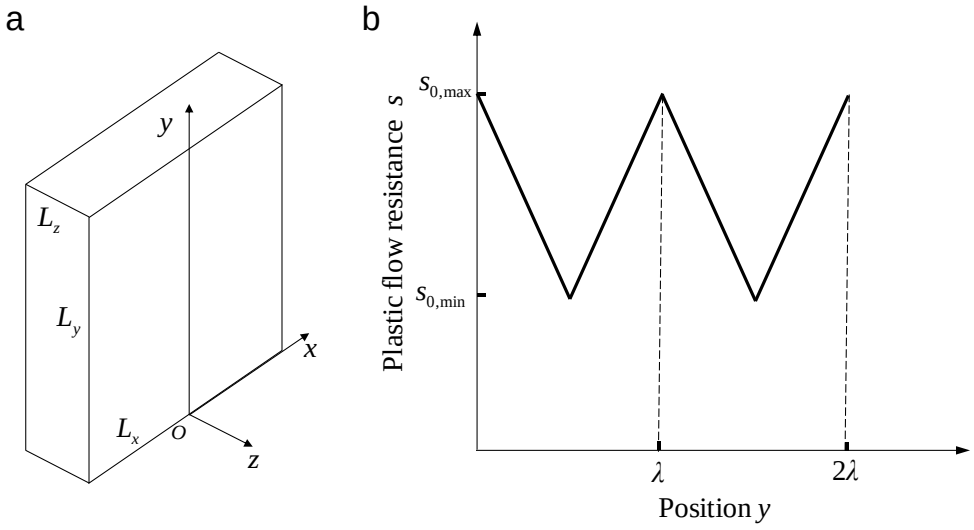

Figure 5.2 Schematics of GNT-1 to GNT-4 models. (a) A rectangular block is taken as a representative volume element of GNT Cu, with a gradient distribution of initial plastic flow resistance in the *x*-*y* cross section and under uniaxial tensile deformation along the *z*-axis. (b) A triangle wave profile of initial plastic flow resistance along *y*-axis, with the maximum resistance $s_{0,\max}$, minimum resistance $s_{0,\min}$ and wavelength λ.

5.4.2 1D Gradient Theory of Plasticity

Considering the fact that $s(y,t=0)$ for GNT-1 to GNT-4 models is only a function of coordinate *y*, we assumed all the stress and strain fields resulting from uniaxial tension depend only on coordinate *y* and time *t*. We further assumed that $\sigma_{zz}(y,t)$ is the only nonzero stress component. Compared to a full 3D stress analysis, this simplified 1D stress state facilitates a more physically transparent analysis of the primary strengthening effect of gradient plasticity. When a uniaxial stress state prevails, equilibrium is trivially satisfied. It follows that according to Eq. (5.4), the equivalent stress $\bar{\sigma}(y,t)$ is reduced to the axial stress $\sigma_{zz}(y,t)$; according to Eq. (5.3), the equivalent plastic strain rate $\dot{\bar{\varepsilon}}^{\mathrm{p}}(y,t)$ is reduced to the axial strain rate $\dot{\varepsilon}^{\mathrm{p}}_{zz}(y,t)$, such that the lateral strain rate is given by $\dot{\varepsilon}^{\mathrm{p}}_{xx}(y,t)=\dot{\varepsilon}^{\mathrm{p}}_{yy}(y,t)=-\dot{\bar{\varepsilon}}^{\mathrm{p}}(y,t)/2$. Once $\sigma_{zz}(y,t)$ is solved, the average axial stress $\sigma^{\mathrm{avg}}_{zz}(t)$ is obtained by

$$\sigma^{\mathrm{avg}}_{zz}(t)=\frac{1}{L_y}\int_0^{L_y}\sigma_{zz}(y',t)dy' \tag{5.10}$$

More specifically, to evaluate $\sigma^{\mathrm{avg}}_{zz}(t)$, we first solve for $\varepsilon^{\mathrm{p}}_{zz}(y,t)$, $s(y,t)$ and $\sigma_{zz}(y,t)$ by time integration of their respective rate equations. In the present 1D gradient theory, the plastic strain rate in Eq. (5.5) is reduced to

$$\dot{\varepsilon}^{\mathrm{p}}_{zz}(y,t)=\dot{\bar{\varepsilon}}^{\mathrm{p}}_0\left(\frac{\sigma_{zz}(y,t)}{s(y,t)}\right)^{1/m} \tag{5.11}$$

The accumulated equivalent plastic strain $\bar{\varepsilon}^{\mathrm{p}}(y,t)$ is given by $\bar{\varepsilon}^{\mathrm{p}}(y,t)=\varepsilon^{\mathrm{p}}_{zz}(y,t)=\int_0^t\dot{\varepsilon}^{\mathrm{p}}_{zz}(y,t')dt'$. The scale measure of the plastic strain gradient α in

Eq. (8) is reduced to $\alpha = \left|\partial \bar{\varepsilon}^{\mathrm{p}}(y,t)/\partial y\right|$. It follows that the hardening rate in Eq. (5.7) becomes

$$h(y,t) = \frac{h_0}{1+\left(\bar{\varepsilon}^{\mathrm{p}}/\varepsilon_1\right)^{n_1}}\left[1+\frac{\kappa\sqrt{\left|\partial \bar{\varepsilon}^{\mathrm{p}}/\partial y\right|}}{1+\left(\bar{\varepsilon}^{\mathrm{p}}/\varepsilon_2\right)^{n_2}}\right] \tag{5.12}$$

As discussed earlier, with an appropriate choice of material parameters, this hardening rate relation represents the two-stage hardening behavior of GNT Cu. That is, a high hardening rate on the order of $\kappa h_0\sqrt{\left|\partial \bar{\varepsilon}^{\mathrm{p}}/\partial y\right|}$ predominates when $\bar{\varepsilon}^{\mathrm{p}}$ is less than ε_2, while a low high hardening rate on the order of h_0 predominates when $\bar{\varepsilon}^{\mathrm{p}}$ is greater than ε_2. Once $\dot{\varepsilon}^{\mathrm{p}}_{zz}(y,t)$ and $h(y,t)$ are known, the hardening rate $\dot{s}(y,t)$ is determined by $\dot{s}(y,t) = h(y,t)\dot{\varepsilon}^{\mathrm{p}}_{zz}(y,t)$. Time integration of $\dot{s}(y,t)$ yields $s(y,t) = \int_0^t \dot{s}(y,t')dt'$. Suppose the *x*-*y* cross section in Figure 5.2a moves at a constant applied strain rate $\dot{\varepsilon}^{\mathrm{a}}_{zz}$. The elastic strain rate along the *z*-axis is

$$\dot{\varepsilon}^{\mathrm{e}}_{zz}(y,t) = \dot{\varepsilon}^{\mathrm{a}}_{zz} - \dot{\varepsilon}^{\mathrm{p}}_{zz}(y,t) \tag{5.13}$$

and the elastic strain rate in the lateral direction is $\dot{\varepsilon}^{\mathrm{e}}_{xx} = \dot{\varepsilon}^{\mathrm{e}}_{yy} = -\nu\dot{\varepsilon}^{\mathrm{e}}_{zz}$. The axial stress rate is

$$\dot{\sigma}_{zz}(y,t) = E\dot{\varepsilon}^{\mathrm{e}}_{zz}(y,t) \tag{5.14}$$

Time integration of $\dot{\sigma}_{zz}(y,t)$ yields $\sigma_{zz}(y,t) = \int_0^t \dot{\sigma}_{zz}(y,t')dt'$. Finally, the average axial stress $\sigma^{\mathrm{avg}}_{zz}(t)$ is obtained using Eq. (5.10).

5.4.3 Results

We numerically implemented the 1D gradient theory in section 5.4.2 to simulate the tensile response of GNT-1 to GNT-4 models. Suppose the *x*-*y* cross section of a GNT model moves at a constant applied strain rate $\dot{\varepsilon}_{zz}^{\mathrm{a}}$ of 1×10^{-3} s^{-1}. We obtained the average axial stress $\sigma_{zz}^{\mathrm{avg}}(t)$ versus applied tensile strain, $\varepsilon_{zz}^{\mathrm{a}}(t)=\dot{\varepsilon}_{zz}^{\mathrm{a}}t$, by explicit time integration of rate equations in section 5.4.2. The integration time step was taken as $1\times10^{-3}\mathrm{s}$. Eighty equally spaced integration points along the *y*-axis were used. The plastic strain gradient at each integration point was calculated by the central difference method. It should be emphasized that special care needs to be taken when calculating plastic strain gradients at both the free surface and at the end point of each half period. This is because, outside the free surface, the plastic strain does not exist; and at the end point of each half period, the plastic strain gradient flips sign when calculated from either side of the end point. We found that the forward or backward difference method can give a stable, physically-sound numerical solution. In other words, the plastic strain gradient at the material side of a free surface dictates local extra hardening; and the plastic strain gradient at one side of the end point of each half period controls local extra hardening. In contrast, the central difference method gives a zero-plastic strain gradient at the end point, resulting in an unable, oscillating solution around the end point. We further found that a similar treatment of plastic strain gradient is needed for the nonlinear wave profile of initial yield strength, as to be discussed in section 7. The material parameters used in numerical simulations are listed in Table 1. They were determined by fitting the experimentally measured stress-strain curves of GNT-1 to GNT-4 samples. Because of the small strain rate sensitivity *m* and low applied strain rate $\dot{\varepsilon}_{zz}^{\mathrm{a}}$ used, our numerical results represent the rate-independent responses under quasi-

static loading conditions. As such, the simulated stresses and strains are given as functions of applied tensile strain ε_{zz}^{a} without explicit time dependence.

Table 5.1 Parameters used in both 1D and 3D gradient plasticity simulations.

E (GPa)	ν	m	ε_0	h_0 (MPa)
124	0.3	0.001	0.001	2000
ε_1	n_1	ε_2	n_2	$\kappa\left(\sqrt{\mathrm{m}}\right)$
0.015	0.6	0.0001	2.0	1.65

Figure 5.3a shows the numerical results of average tensile (engineering) stress σ_{zz}^{avg} versus applied tensile (engineering) strain ε_{zz}^{a} for GNT-1 to GNT-4 models, which reasonably agree with the corresponding experimental results. Figure 3b shows the numerical results of the strain hardening rate $\mathrm{d}\sigma_{zz}^{avg}/\mathrm{d}\varepsilon_{zz}^{a}$ versus applied true strain for GNT-1 to GNT-4 models, which also reasonably agree with the corresponding experimental results. The experimental and simulated hardening rates clearly show the two-stage hardening behavior in GNT Cu, as discussed earlier in section 5.3. For each GNT model, the sample-average yield strength is defined as the average tensile stress σ_{zz}^{avg} at ε_{zz}^{a} = 1% and thus denoted as $\sigma_{1\%}$. In Figure 5.3c, the predicted $\sigma_{1\%}$ for GNT-1 to GNT-4 models (blue circles) are plotted as a function of hardness gradient g and they reasonably agree with the corresponding experimental results (red squares). It is seen that the predicted $\sigma_{1\%}$ for GNT-1 has a relatively large deviation from the corresponding

experimental data point. This difference is mainly caused by a constant strength gradient used in the GNT-1 model, while several hardness plateaus are present in the experimental GNT-1 sample (see Figure 5.1b). These plateaus arise due to non-gradient variations of nanotwin size [9]. It is noted that the yield strength gradients g_s were prescribed for GNT-1 to GNT-4 models, while the hardiness gradients g were measured for GNT-1 to GNT-4 samples in experiments. To compare the experimental and simulation results, we adopted the following scheme to convert g_s to g. That is, for GNT-1 to GNT-4 models, we used the experimental data of wavelength λ, maximum yield strength $s_{0,\max}$ and minimum yield strength $s_{0,\min}$; the latter two were measured from the nanotwinned samples without structural gradient [9]. As such, these parameters fix the respective g_s for GNT-1 to GNT-4 models. For example, the strength gradient for GNT-1 is a constant of $g_s^{\text{GNT-1}} = 0.56\ \text{GPa/mm}$. Since the tensile yield strength is approximately three times the corresponding indentation hardness [89], we assumed $g \approx 3g_s$ and thus obtained $g^{\text{GNT-1}} = 1.68\ \text{GPa/mm}$. As such, the simulation results of $\sigma_{1\%}$ versus g_s can be converted to $\sigma_{1\%}$ versus g, so as to compare with the corresponding experimental results.

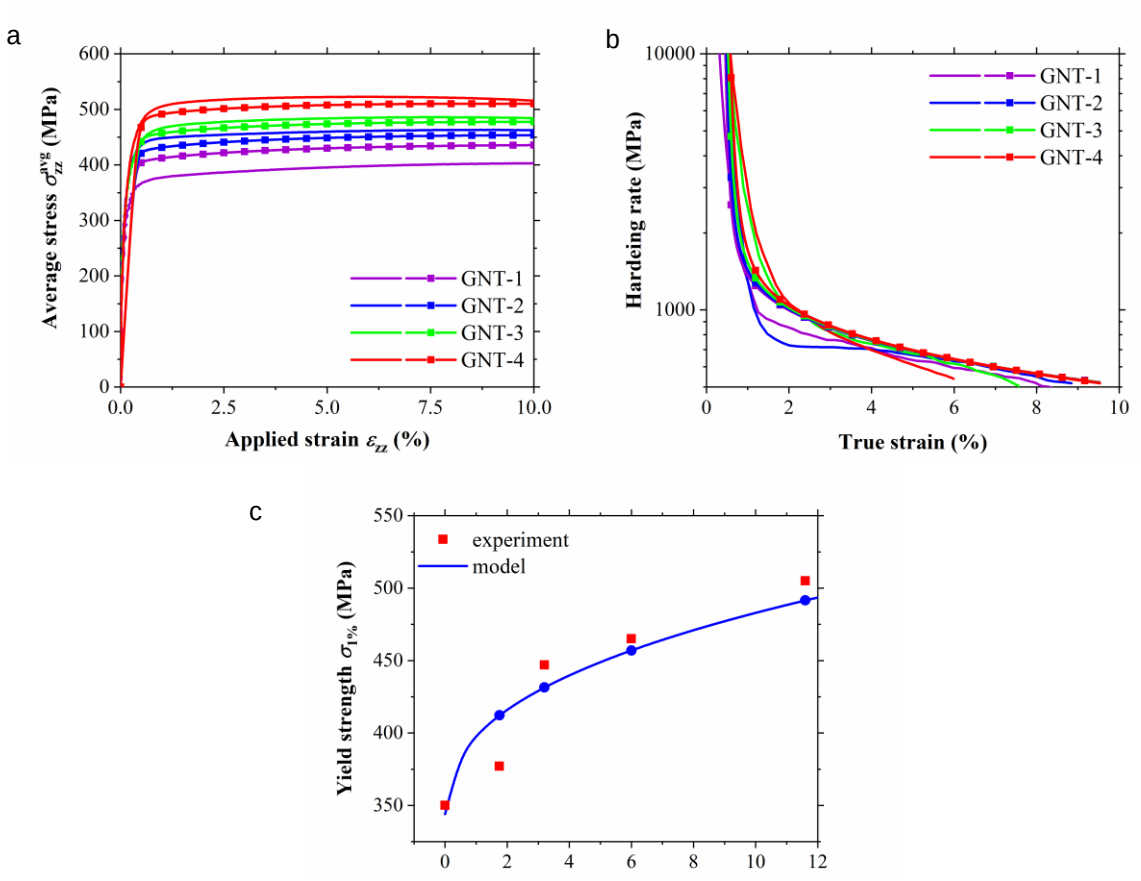

Figure 5.3 Comparison of experimental measurements [9] and simulation results of uniaxial tension from the 1D gradient theory of plasticity. (a) Tensile engineering stress σ_{zz}^{avg} versus engineering strain ε_{zz}^{a} for GNT-1 to GNT-4 from experiments (solid lines) and simulations (solid lines with symbols). (c) Strain hardening rate $\mathrm{d}\sigma_{zz}^{avg}/\mathrm{d}\varepsilon_{zz}^{a}$ versus true strain for GNT-1 to GNT-4 from experiments (solid lines) and simulations (solid lines with symbols). (c) Sample-average yield strength $\sigma_{1\%}$ versus hardness gradient g for GNT-1 to GNT-4 from experiments (red squares) and simulations (blue dots). Also plotted is the predicted average yield strength $\sigma_{1\%}$ versus hardness gradient (blue curve) from additional simulations of 25 GNT models with increasing hardness gradient from 0 to 12 GPa/mm (equal increment).

In addition, we estimated the sample-average yield strength at zero hardness gradient, $\sigma_{1\%,g=0}$, from a rule-of-mixture average of yield strengths measured from four nanotwinned samples without structural gradient, but with different uniform twin

thicknesses [9]. Then we calculated the extra strength of the GNT-1 model as $\Delta\sigma_{1\%} = \sigma_{1\%} - \sigma_{1\%,g=0}$. The extra strengths $\Delta\sigma_{1\%}$ for GNT-2 to GNT-4 models were calculated by the same procedure. To further characterize the non-linear functional dependence of $\sigma_{1\%}$ on g , we conducted additional simulations for 25 GNT models with increasing g from 0 to 12 GPa/mm by equal increment. The corresponding results of $\sigma_{1\%}$ versus g are plotted as the blue curve in Figure 5.3b. By least squares regression analysis of $\sigma_{1\%}$ versus g data points for these 25 GNT models, we found that the simulated extra strength $\Delta\sigma_{1\%}$ closely follows

$$\Delta\sigma_{1\%} = \beta\sqrt{g} \tag{5.15}$$

where the coefficient β was fitted as $41.7\sqrt{\text{MPa}\cdot\mu\text{m}}$. This functional relationship between the extra strength and hardness gradient is reasonably supported by the available experimental data (red squares) and warrants further validation by more GNT Cu samples with different structure gradients in the future. As to be discussed later, this relation between $\Delta\sigma_{1\%}$ and g originates from the hardening effect of the plastic strain gradient in GNT Cu.

Our detailed analysis of the numerical results for GNT-1 reveals several salient features in plastically deformed gradient structures, including progressive yielding, gradient distributions of plastic strain and extra plastic flow resistance. More specifically, Figure 4a shows the distributions of plastic flow resistance $s(\hat{y})$ along normalized $\hat{y}$ $(= y / L_y)$ at different applied strains ε_{zz}^{a} . The initial linear profile of $s(\hat{y})$ at $\varepsilon_{zz}^{a} = 0$ corresponds to Eq.

(5.9), with the maximum and minimum yield strength of 446 MPa and 223 MPa, respectively, giving a constant strength gradient $g_s = 0.56\ \text{GPa/mm}$. As ε_{zz}^{a} increases to 0.25%, the soft region at large $\hat{y}$ becomes plastically yielded, while the hard region at small $\hat{y}$ remains elastic. Due to the hardening effects of both plastic strain and plastic strain gradient, $s(\hat{y})$ increases in the plastic region and exhibits a nonlinear profile represented by a black curved segment. In contrast, $s(\hat{y})$ remains unchanged in the elastic region and maintains a linear profile represented by a black straight segment. The location where the black curved and straight segments meet is the boundary between the elastic and plastic regions.

Figure 5.4b shows the distribution of plastic strain $\varepsilon_{zz}^{p}(\hat{y})$ (the black curve) when $\varepsilon_{zz}^{a} = 0.25\%$. The plastic region with nonzero $\varepsilon_{zz}^{p}(\hat{y})$ can be readily identified. A gradient distribution of plastic strain develops within the plastic region, such that $\varepsilon_{zz}^{p}(\hat{y})$ has the largest value at $\hat{y} = 1$ and decreases to zero at the elastic-plastic boundary. It is interesting to observe that the plastic strain gradient $\alpha(\hat{y}) = \left|\partial \varepsilon_{zz}^{p} / \partial y\right|$ is close to a constant. To understand this result, we note that during the early stage of progressive yielding, the stress $\sigma_{zz}(\hat{y})$ and thus $s(\hat{y})$ at $\varepsilon_{zz}^{a} = 0.25\%$ is close to $s(\hat{y}, t = 0)$. Based on Eq. (5.13), a constant plastic strain gradient in the plastic region can be estimated as

$$\alpha(\hat{y}) \approx \left| \frac{\partial \left[\varepsilon_{zz}^{a} - s(y, t = 0)/E \right]}{\partial y} \right| = \frac{g_s}{E} \tag{5.16}$$

Equation (16) indicates that the plastic strain gradient $\alpha(\hat{y})$ is dictated by the built-in strength gradient g_s. But the calculated $\alpha(\hat{y})$ from the black curve in Figure 5.4b is only about 1/3 of g_s / E. This discrepancy is attributed to the nonlinear hardening responses at different $\hat{y}$ during the process of progressive yielding through the sample cross section.

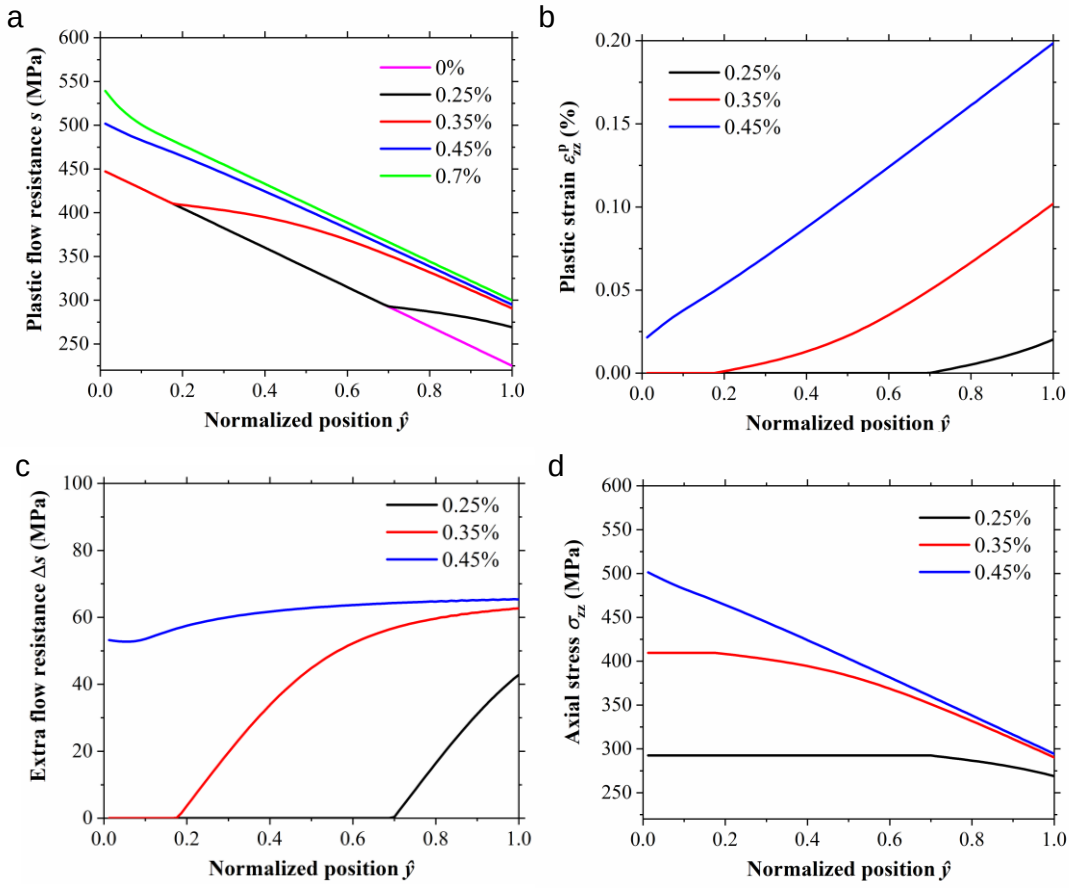

Figure 5.4 Simulation results of the GNT-1 model at different applied tensile strains ε_{zz}^{a} from the 1D gradient theory of plasticity, showing the distributions of (a) plastic flow resistance $s(\hat{y})$, (b) plastic strain $\varepsilon_{zz}^{p}(\hat{y})$, (c) extra flow resistance $\Delta s(\hat{y})$, and (d) axial stress $\sigma_{zz}(\hat{y})$.

Figure 5.4c shows the extra plastic flow resistance $\Delta s(\hat{y})$ defined as the difference of $s(\hat{y})$ with and without the hardening effect of plastic strain gradient, the latter of which is evaluated by setting $\kappa = 0$ in Eq. (5.12). Compared to the initial $s(\hat{y})$ at $\varepsilon_{zz}^{a} = 0$, $\Delta s(\hat{y})$ is substantial, reaching a maximum of about 40 MPa at $\varepsilon_{zz}^{a} = 0.25\%$. In addition, Figure 5.4d shows the distribution of axial stress $\sigma_{zz}(\hat{y})$ at $\varepsilon_{zz}^{a} = 0.25\%$. In the elastic region, $\sigma_{zz}(\hat{y})$ is constant, reflecting a uniform distribution of tensile elastic strain $\varepsilon_{zz}^{e}(\hat{y})$ equal to applied tensile strain ε_{zz}^{a}. In the plastic region, the non-linear profile of $\sigma_{zz}(\hat{y})$ closely matches that of $s(\hat{y})$; $\sigma_{zz}(\hat{y})$ decreases from the elastic-plastic boundary to $\hat{y} = 1$, due to the increased plastic strain and decreased elastic strain with increasing $\hat{y}$.

To reveal the effects of increasing load, Figure 5.4a shows that as ε_{zz}^{a} increases to 0.35%, $s(\hat{y})$ further increases in the plastic region and continues to exhibit a nonlinear profile as a red curved segment; $s(\hat{y})$ remains unchanged in the elastic region and thus maintains a linear profile as a red straight segment. Moreover, the plastic region expands, while the elastic region shrinks, such that the elastic-plastic boundary moves to a smaller $\hat{y}$. This progressive yielding response is also evident in Figure 5.4b, showing an increased plastic region with a concomitant increase of $\varepsilon_{zz}^{p}(\hat{y})$. As a result, the region with the gradient distribution of plastic strain expands. The plastic strain gradient $\alpha(\hat{y}) = \left|\partial \varepsilon_{zz}^{p} / \partial y\right|$ becomes close to g_s / E as estimated by Eq. (16). Figure 5.4c shows $\Delta s(\hat{y})$ at $\varepsilon_{zz}^{a} = 0.35\%$. Compared to $s(\hat{y})$ at $\varepsilon_{zz}^{a} = 0.25\%$, the increase of $s(\hat{y})$ is primarily caused by the extra hardening effect due to the plastic strain gradient. In addition, Figure 5.4d shows that in

the shrinking elastic region, the constant $\sigma_{zz}(\hat{y})$ is elevated due to an increase of elastic strain; in the expanding plastic region, the non-linear distribution of $\sigma_{zz}(\hat{y})$ follows that of $s(\hat{y})$ at $\varepsilon_{zz}^{a} = 0.35\%$.

When ε_{zz}^{a} reaches 0.45%, the progressive yielding process has completed, such that the entire cross section becomes plastically yielded. Figure 5.4a shows that similar to $s(\hat{y})$ at $\varepsilon_{zz}^{a} = 0$, the distribution of $s(\hat{y})$ at $\varepsilon_{zz}^{a} = 0.45\%$ becomes almost linear again. This arises from the saturation of the extra hardening effect due to the plastic strain gradient, as to be further discussed next. Figure 4b confirms that the plastic region occupies the entire cross section at $\varepsilon_{zz}^{a} = 0.45\%$; the plastic strain gradient $\alpha(\hat{y})$ is almost identical to g_s / E as estimated by Eq. (5.16). Figure 5.4c shows $\Delta s(\hat{y})$ that varies weakly between 55-65 MPa. This $\Delta s(\hat{y})$ represents the limit of the extra hardening effect due to the plastic strain gradient in GNT-1. To understand this limit, we note that Eq. (5.7) and accordingly Eq. (5.12) represent a two-stage hardening behavior. Namely, the hardening rate is dominated by the plastic strain gradient when $\bar{\varepsilon}^{p}$ is less than ε_2 (= 0.0001) and decays quickly as $\bar{\varepsilon}^{p}$ increases above ε_2, thereby giving rise to the limit of $\Delta s(\hat{y})$ due to plastic strain gradient. When $\bar{\varepsilon}^{p}$ increases above ε_2 at the hardest region ($\hat{y} = 0$), $\Delta s(\hat{y})$ becomes saturated in the entire cross section, resulting in the saturation of the overall extra strength $\Delta\sigma_{1\%}$ from the plastic strain gradient as ε_{zz}^{a} approaches about 0.5% and beyond. Hence, the extra strength $\Delta\sigma_{1\%}$ as defined earlier provides an effective measure of the sample-level extra strength. In addition, during progressive yielding, the limit of $\Delta s(\hat{y})$ at different $\hat{y}$ is attained at

different ε_{zz}^{a}, but the limit value of $\Delta s(\hat{y})$ depends weakly on $\hat{y}$, resulting in a linear profile of saturated $s(\hat{y})$. Figure 5.4d shows the nearly linear distribution of $\sigma_{zz}(\hat{y})$ at $\varepsilon_{zz}^{a} = 0.45\%$, which follows the corresponding $s(\hat{y})$.

Figure 5.4a also shows the representative distribution of $s(\hat{y})$ at a high load of $\varepsilon_{zz}^{a} = 0.7\%$. The overall linear profile (the green curve) is maintained with slight nonlinearity near $\hat{y} = 0$. As ε_{zz}^{a} increases from 0.45% to 0.7%, the weak increase of $s(\hat{y})$ is primarily caused by the hardening effect of plastic strain instead of plastic strain gradient. This result represents the saturated distribution of $s(\hat{y})$ that prevails under large tensile strains, e.g., in the range of 0.5% ~ 10% covered by the stress-strain curve in Figure 2a. In addition, the distributions of $\varepsilon_{zz}^{p}(\hat{y})$ and $\sigma_{zz}(\hat{y})$ are very close to the corresponding distributions at $\varepsilon_{zz}^{a} = 0.45\%$ with slight increase, while $\Delta s(\hat{y})$ remains unchanged. Similar to the case of $\varepsilon_{zz}^{a} = 0.45\%$, the sample average of $\Delta s(\hat{y})$ at $\varepsilon_{zz}^{a} = 0.7\%$ also approaches the extra strength $\Delta\sigma_{1\%}$.

For GNT-2 to GNT-4 models, the corresponding numerical results show that all the half-period profiles of plastic flow resistance $s(\hat{y})$, tensile plastic strain $\varepsilon_{zz}^{p}(\hat{y})$, extra flow resistance $\Delta s(\hat{y})$ and tensile stress $\sigma_{zz}(\hat{y})$ show qualitatively similar trends as GNT-1. However, due to the increasing strength gradient, the plastic strain gradient $\alpha(\hat{y})$ and extra flow resistance $\Delta s(\hat{y})$ become increasingly stronger from GNT-2 to GNT-4, leading to the increasing sample-level yield strength $\sigma_{1\%}$ and thus increasing sample-level extra strength $\Delta\sigma_{1\%}$.

5.5 Gradient Plasticity Finite Element (GPFE) Simulations

5.5.1 Method

To gain a complete understanding of the tensile responses of GNT-1 to GNT-4, we numerically implemented the 3D gradient plasticity theory in ABAQUS/Explicit and performed finite element simulations for 3D models of GNT-1 to GNT-4. We chose the classical rate-independent plasticity model with the Mises isotropic yield surface and associated plastic flow rule. Explicit time integration was used to simplify numerical calculations of plastic strain gradients and associated field variables. That is, the hardening rate relation of Eq. (5.12) was implemented by writing user subroutines VUSDFLD and VUHARD [39]. At the end of each time increment, VUSDFLD was used to calculate the gradient of equivalent plastic strain within each element with the finite-difference method; VUHARD was used to calculate the hardening response due to both plastic strain and plastic strain gradient; and then the updated yield strength s and hardening rate h were passed into ABAQUS/Explicit. The combined use of VUSDFLD and VUHARD provides a relatively simple method for 3D calculations of plastic strain gradients, as opposed to other VUMAT or UEL-based methods in ABAQUS [83, 84]. The 3D finite element models of GNT-1 to GNT-4 were constructed in ABAQUS/CAE [39]. Each GNT model has a thin-slice geometry of $400\ \mu m \times 400\ \mu m \times 50\ \mu m$ (corresponding to the schematic in Figure 5.2a) and contains 4096 brick elements with full integration (C3D8). Eight integration points in each brick element facilitate the direct finite-difference calculation of the plastic strain gradient within each element via VUSDFLD. To simulate uniaxial tension, we prescribed the following boundary conditions: the velocity along the *z*-

direction is 0.4 nm/s on the right side of the *x*-*y* surface; the displacement in the *z*-direction is fixed on the opposite side of the *x*-*y* surface; other surfaces are traction free. For the finite element GNT-1 to GNT-4 models, the initial distributions of yield strength were assigned according to the same triangle wave profiles as the corresponding 1D models in section 5.4. The material parameters listed in Table 5.1 were also used in GPFE simulations.

5.5.2 Results

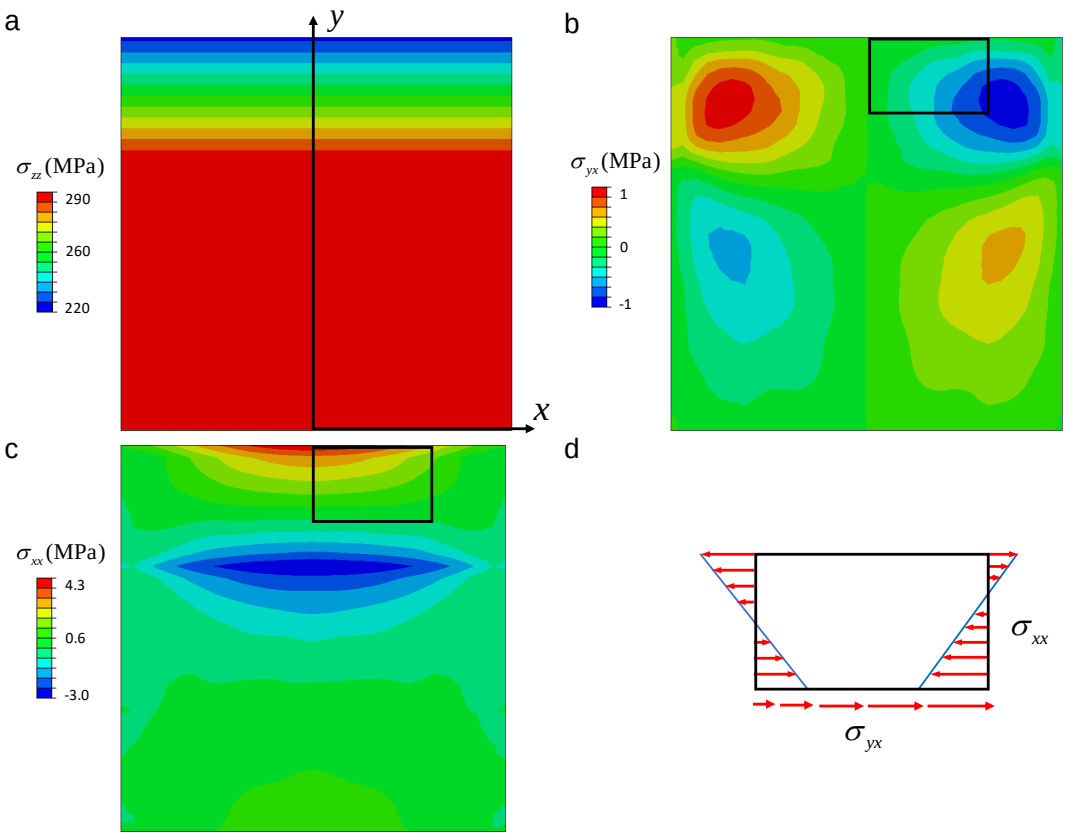

Figure 5.5 3D finite element simulation results of the GNT-1 model without accounting for the extra hardening effect of the plastic strain gradient. At the applied tensile strain of $\varepsilon_{zz}^{a} = 0.25\%$, plotted are the distributions of (a) axial stress $\sigma_{xx}(x, y)$, (b) lateral shear stress $\sigma_{yx}(x, y)$ and (c) lateral normal stress $\sigma_{xx}(x, y)$. (d) Equilibrium analysis of the non-uniform stresses $\sigma_{yx}(x, y)$ and $\sigma_{xx}(x, y)$ acting on a rectangle area in the *x*-*y* cross

section as marked in (b) and (c); only stress components relevant to the equilibrium in the *x*-direction are plotted as red arrows.

The GPFE simulation results of GNT-1 to GNT-4, including the overall tensile stress-strain curves and the axial stress and strain distributions in the cross section, agree closely with the corresponding 1D simulation results described in section 5.4.2. Next, we focus on the GPFE simulation results of stress components neglected in the 1D gradient theory and simulations.

Consider GNT-1 as an example. We first present the 3D finite element simulation results without considering the extra hardening effect of the plastic strain gradient. These results, as shown in Figure 5.5, were obtained by setting $\kappa = 0$ in Eq. (5.7). They serve to validate the simplification that we made to derive the 1D gradient theory, namely, stress components other than $\sigma_{zz}(x, y)$ are negligible. Figure 5.5a shows the contour plot of $\sigma_{zz}(x, y)$ in the *x*-*y* cross section at $\varepsilon_{zz}^{a} = 0.25\%$. The large red contour corresponds to constant tensile stress $\sigma_{zz}(x, y)$ arising from elastic deformation, while the contour with varying colors other than red shows a gradient distribution of tensile stress $\sigma_{zz}(x, y)$ due to progressive yielding. The elastic-plastic boundary is located at the transition layer between the red and yellow contours. These results are consistent with those from the 1D gradient theory, i.e., the black curve in Figure 5.4a. Figure 5.5b and 5.5c show the contour plots of shear stress $\sigma_{yx}(x, y)$ and normal stress $\sigma_{xx}(x, y)$ in the transverse direction at $\varepsilon_{zz}^{a} = 0.25\%$, respectively. First of all, it is seen that these stress components are much smaller than the corresponding axial stresses (Figure 5.5a), thus validating the 1D gradient

theory. Moreover, $\sigma_{yx}(x, y)$ and $\sigma_{xx}(x, y)$ exhibit non-uniform distributions in both *x* and *y* directions. These non-axial stresses originate from the gradient structure and associated gradient strength in the GNT-1 model. At any moment of a progressive yielding process, the axial stress and accordingly axial strain (including both its elastic and plastic components) vary along the *y*-direction, resulting in the varying lateral contraction ε_{xx} along the *y*-direction, irrespective of different Poisson's effects on the elastic and plastic parts of axial strain. Accommodation of the varying ε_{xx} (i.e., maintaining displacement continuity) along the *y*-direction gives rise to the non-zero shear stress $\sigma_{yx}(x, y)$. This further leads to other non-zero stress components such as $\sigma_{xx}(x, y)$, so as to maintain the stress equilibrium along the *x*-direction. It is interesting to note that while the axial stress σ_{zz} only varies along the *y*-direction, $\sigma_{xx}(x, y)$ varies along both *x* and *y* directions. This is because $\sigma_{xx}(x, y)$ must self-equilibrate within any *x*-*z* section, due to the absence of the applied load in the *x*-direction. The same reasoning is applicable to the cause of a non-uniform distribution of $\sigma_{yx}(x, y)$ in both *x* and *y* directions. As an illustration, Figure 5d shows the non-uniform $\sigma_{yx}(x, y)$ and $\sigma_{xx}(x, y)$ acting on the sides of a rectangular area in the *x*-*y* cross section (as marked in Figure 5.5b and 5.5c), and these non-uniform stresses

give zero resultant force and satisfy the equilibrium condition in the *x*-direction.

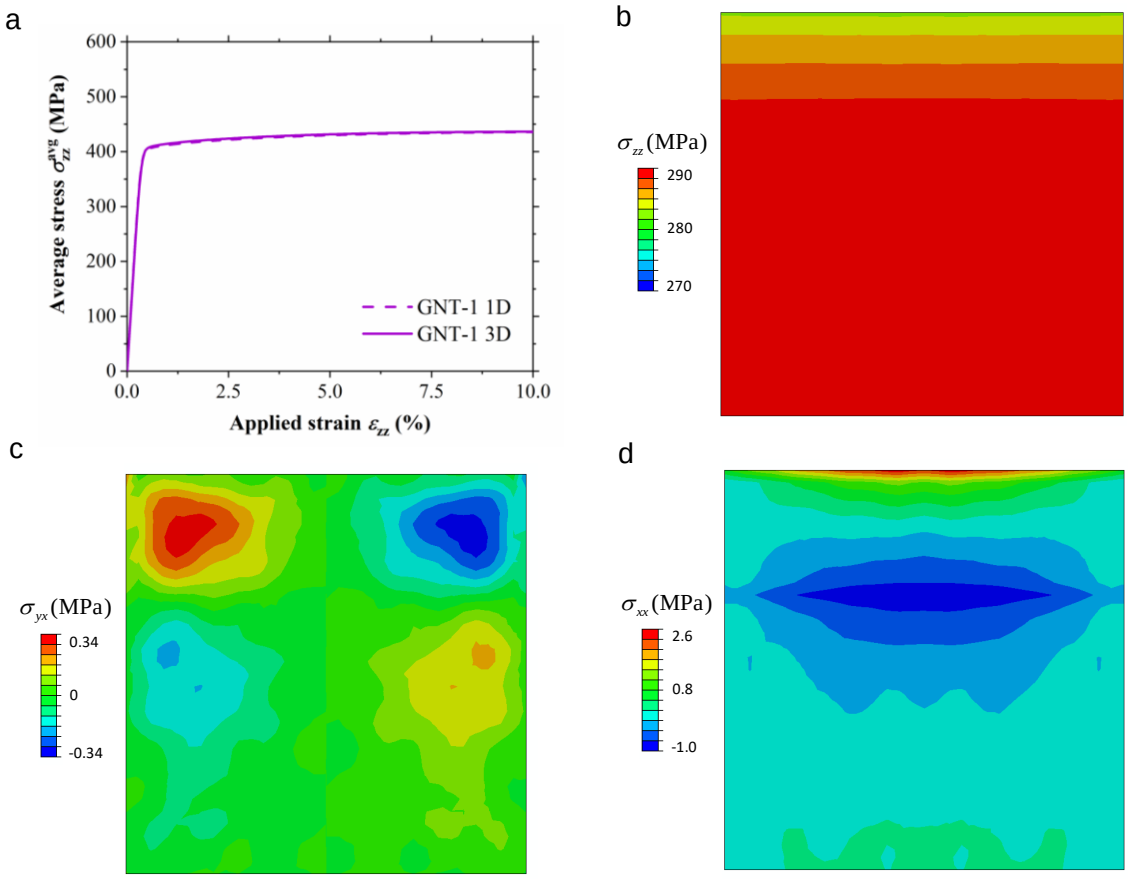

Figure 5.6 3D finite element simulation results of the GNT-1 model accounting for the extra hardening effect of the plastic strain gradient. (a) Comparison of the tensile stress-strain curves between 1D and 3D simulations. At the applied tensile strain of $\varepsilon_{zz}^{a} = 0.25\%$, plotted are the distributions of (b) axial stress $\sigma_{xx}(x, y)$, (c) lateral shear stress $\sigma_{yx}(x, y)$, and (d) lateral normal stress $\sigma_{xx}(x, y)$.

Next, we present the GPFE simulation results that account for the extra hardening effect of the plastic strain gradient by using the κ value in Table 5.1. As shown in Figure 5.6a, the predicted tensile stress-strain curves are nearly identical between 1D and 3D simulations for GNT-1. Figure 5.6b-d show the contour plots of $\sigma_{zz}(x, y)$, $\sigma_{yx}(x, y)$ and $\sigma_{xx}(x, y)$ in the *x*-*y* cross section of GNT-1 at $\varepsilon_{zz}^{a} = 0.25\%$. Compared to Figure 5.5a, Figure 5.6b shows that the extra hardening due to the plastic strain gradient causes an

increase of the lowest axial stress $\sigma_{zz}(x, y)$ by about 50 MPa. However, compared with Figure 5.5b-c, Figure 5.6b-d show that the extra hardening does not lead to significant changes of $\sigma_{yx}(x, y)$ and $\sigma_{xx}(x, y)$. As a result, $\sigma_{yx}(x, y)$ and $\sigma_{xx}(x, y)$ are still much lower than $\sigma_{zz}(x, y)$ when the extra hardening effect is accounted for. Hence, the combined 3D finite element simulation results in Figs. 5.5 and 5.6 quantitatively demonstrate that the axial stress dominates over other stress components in GNT Cu undergoing uniaxial tensile deformation.

5.6 Discussion

5.6.1 Optimization of Gradient Structure toward Maximum Strength

Insights from the above gradient plasticity simulations can be applied to optimize the gradient structures and associated gradient strengths in a GNT-D(esign) model toward achieving its maximum strength. For the GNT-D(esign) model, we considered a family of gradient strength distribution represented by the triangle wave shown in Figure 5.2b. Given the initial plastic flow resistance $s(y,t=0)$ of the GNT-D model, its sample-average plastic resistance s_{avg} at $\varepsilon_{zz}^{\text{a}}=1\%$ can be expressed as

$$s_{\text{avg}} = \bar{s} + \overline{\Delta s} \tag{5.17}$$

where $\bar{s}$ is the rule-of-mixture average of $s(y,t=0)$ through the cross section and becomes $\bar{s}=(s_{0,\max}+s_{0,\min})/2$ for the triangle wave profile of $s(y,t=0)$; $\overline{\Delta s}$ is the sample-average extra hardening arising from plastic strain gradient. In the current rate-independent model, s_{avg} corresponds to the sample-average yield strength $\sigma_{1\%}$. According

to Figure 5.3b and Eq. (5.15), $\overline{\Delta s}$ is approximately represented by $\overline{\Delta s} = \beta\sqrt{g} = \beta_s\sqrt{g_s}$, where g_s is the gradient of initial plastic flow resistance and given by $g_s = (s_{0,\max} - s_{0,\min})/(\lambda/2)$ for the triangle wave profile of $s(y, t=0)$; the coefficient β_s is given by $\beta_s = \sqrt{g/g_s}\beta = \sqrt{3}\beta = 72.2\sqrt{\text{MPa}\cdot\mu\text{m}}$. Thus, Eq. (5.17) becomes

$$s_{\text{avg}} = \frac{s_{0,\max} + s_{0,\min}}{2} + \beta_s\sqrt{\frac{s_{0,\max} - s_{0,\min}}{\lambda/2}} \tag{5.18}$$

Based on Eq. (5.18), the s_{avg} of the GNT-D model can be optimized in the parameter space of $\{s_{0,\max}, s_{0,\min}, \lambda\}$. Generally speaking, certain regions in the parameter space may not be accessible due to constraints from material processing; moreover, when certain parameters reach their accessible limits, s_{avg} has to be optimized in a reduced parameter space. Three scenarios of optimization can be considered under the aforementioned constraints. First, we note that s_{avg} increases monotonically with increasing $s_{0,\max}$, when both $s_{0,\min}$ and λ are fixed. This is because both $\bar{s}$ and $\overline{\Delta s}$ increase with $s_{0,\max}$. For nanotwinned Cu, reducing twin spacing can raise $s_{0,\max}$. However, it is difficult to keep reducing twin spacing by a specific processing method (e.g., electrodeposition [9]), such that s_{avg} is limited by accessible $s_{0,\max}$. Second, s_{avg} increases monotonically by reducing λ, when both $s_{0,\min}$ and $s_{0,\max}$ are fixed. In this case, as λ decreases, $\overline{\Delta s}$ increases, while $\bar{s}$ remains unchanged. Similarly, it is difficult to keep reducing λ by a specific processing method.

The third scenario involves a non-monotonic change of s_{avg}, thus requiring a search of the optimal parameter(s). For example. s_{avg} can be optimized by tuning $s_{0,min}$, when $s_{0,max}$ and λ are fixed. This is because increasing $s_{0,min}$ raises $\bar{s}$, but lowers $\overline{\Delta s}$ due to decreasing g_s. These two opposite effects can be optimized to achieve the maximum s_{avg}. As a more general example with two tunable parameters, Figure 5.7a shows the contour plot of $\sigma_{1\%}$ (equal to s_{avg}) for GNT-D in the parameter space of { $s_{0,min}$, $\lambda/2$ }, when $s_{0,max}$ is fixed at 446 MPa, which is the highest local yield strength in the GNT-4 model. Note that we used the model values of $s_{0,max}$ and $s_{0,min}$ instead of the experimental data since the statistical variation of the latter can obscure the trend. It is seen from Figure 5.7a that the maximum $\sigma_{1\%}$ occurs at the smallest $\lambda/2$ and intermediate $s_{0,min}$, consistent with the earlier discussion. From Figure 5.7a, the $\sigma_{1\%}$ versus $s_{0,min}$ curves are extracted for several representative $\lambda/2$, as shown in Figure 7b. In these curves, $\sigma_{1\%}$ invariably exceeds $s_{0,max}$, which is the strength of the strongest component of the GNT-D model; moreover, the non-monotonic change of $\sigma_{1\%}$ with $s_{0,min}$ becomes more pronounced as $\lambda/2$ is 100 μm or smaller. For $\lambda/2 = 50\ \mu m$ (as in the GNT-4 model), the corresponding peak value of $\sigma_{1\%}$ is 502 MPa when $s_{0,min} = 350$ MPa. This optimized strength for the GNT-D model exceeds $\sigma_{1\%} = 490$ MPa for the GNT-4 model with $s_{0,min} = 223$ MPa. This result indicates that the strength of the experimental GNT-4 sample [9] would become higher if its $s_{0,min} = 223$ MPa were to move to around $s_{0,min} = 350$ MPa.

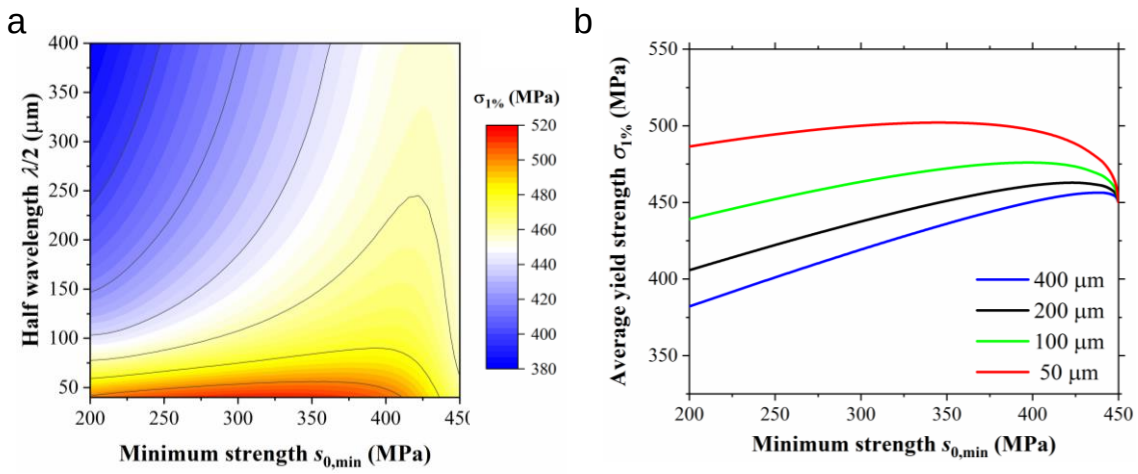

Figure 5.7 Optimization of the average plastic flow resistance s_{avg} by tuning $s_{0,min}$ and λ, while holding $s_{0,min}$ fixed. (a) Contour plot of $\sigma_{1\%}$ (equal to s_{avg}) for GNT-D in the parameter space of $\{s_{0,min}, \lambda/2\}$, when $s_{0,max}$ is fixed at 446 MPa. (b) $\sigma_{1\%}$ versus $s_{0,min}$ curves extracted from (a) for several representative half periods $\lambda/2$.

5.6.2 Plastic Strain Gradient

An important insight from the gradient plasticity simulation results in section 5.4.3 is that the plastic strain gradient $\alpha(\hat{y})$ in GNT Cu is dictated by the built-in structure and strength gradients, and the plastic strain gradient $\alpha(\hat{y})$ approaches a saturated value of about $g_s / E = g/3E$ throughout the sample cross section once progressive yielding is finished. This insight is further confirmed by Figure 5.8, where the blue line corresponds to the saturated plastic strain gradient $\alpha_{1\%}$ obtained from 25 GNT models with increasing hardness gradient g between 0 and 12 GPa/mm by equal increment. Also shown in Figure 5.8 is the theoretical prediction of $\alpha_{1\%} = g/3E$ (black line). A close agreement between the numerical result and theoretical prediction indicates that despite the extra hardening effect of plastic strain gradient, the saturated plastic strain gradient, $\alpha_{1\%}$, is still given

approximately by $g_s / E = g / 3E$. It follows that we can evaluate the density of geometrically necessary dislocations ρ_g in terms of the plastic strain gradient divided by the Burgers vector length *b* [78]. For example, from the simulation result of $\alpha_{1\%}$ in GNT Cu, we can estimate the corresponding $\rho_g = \alpha_{1\%} / b = g / (3bE)$. For GNT-4, $\alpha_{1\%}$ is about 27 /m (Figure 5.8). When *b* is taken as 2×10^{-10} m, ρ_g is estimated as $10^{11}/\mathrm{m}^2$. This ρ_g is much smaller than the measured extra dislocation density $\rho \sim 10^{14}/\mathrm{m}^2$ needed for providing the measured extra strength of GNT-4 [9]. This discrepancy implies that the ρ_g originating from gradient nanotwins must induce a significant number of additional dislocations during the tensile plastic deformation of GNT-4. Resolving this discrepancy requires a future study of how the geometrically necessary dislocations originating from gradient nanotwins impact the generation of the extra dislocations with different characters and distributions that can give rise to the extra strengths measured from GNT Cu.

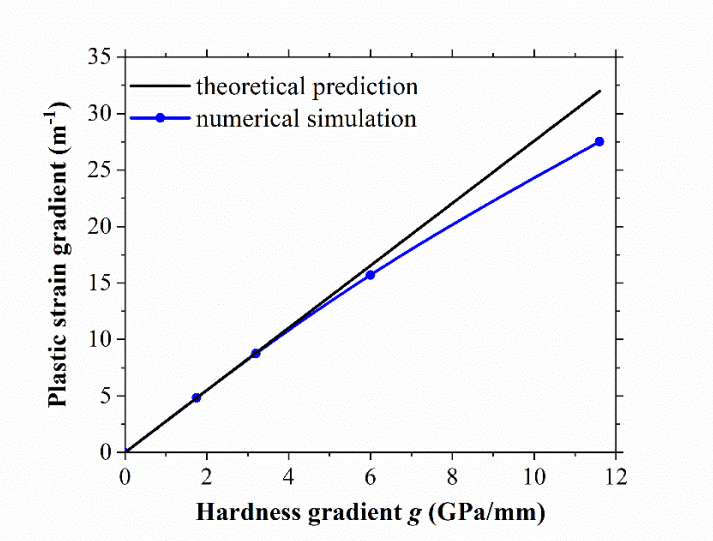

Figure 5.8 Simulation results of saturated plastic strain gradient $\alpha_{1\%}$ at $\varepsilon_{zz}^{a} = 1\%$ for 25 GNT models with increasing g from 0 to 12 GPa/mm (blue curve), as compared with the

theoretical prediction from $\alpha_{1\%} = g/3E$ (black line). Blue dots correspond to numerical simulation results of GNT-1 to GNT-4.

5.6.3 Nonlinear Strength Distribution

We also studied the effect of a non-linear distribution of initial plastic flow resistance on the tensile response of GNT Cu. To this end, we revised the GNT-1 and GNT-4 models by replacing their triangle wave profiles of $s(y, t=0)$ with sinusoidal wave profiles, while keeping the corresponding $s_{0,\max}$, $s_{0,\min}$ and λ unchanged. As a result, the strength gradient becomes a nonlinear function of position y in the sinusoidal wave profile, in contrast to a constant magnitude of strength gradient in the triangle wave profile. For example, the initial plastic flow resistance of the revised GNT-1 model is represented by the half period of a sinusoidal wave

$$s(y, t=0) = s_{0,\max} - (s_{0,\max} - s_{0,\min}) \sin\left(\frac{\pi}{\lambda} y\right) \tag{5.19}$$

where the wavelength λ is $2L_y$.

We numerically implemented the 1D gradient theory for the revised GNT-1 to GNT-4 models, with the same numerical procedure as for the triangle wave profiles of $s(y, t=0)$. As we mentioned earlier, special attention should be paid to the finite-difference calculation of the plastic strain gradient. For a non-linear sinusoidal wave profile, the plastic strain gradient is initially zero at the end point of a half period, but becomes non-zero with progressive yielding. As a result, the plastic strain gradient calculated from either side of the end point begins to flip sign as the integration time increases, leading to an unable, oscillating solution around the end point. We found that the forward or backward

difference method can give a stable, physically-sound numerical solution, similar to the cases of triangle wave profiles.

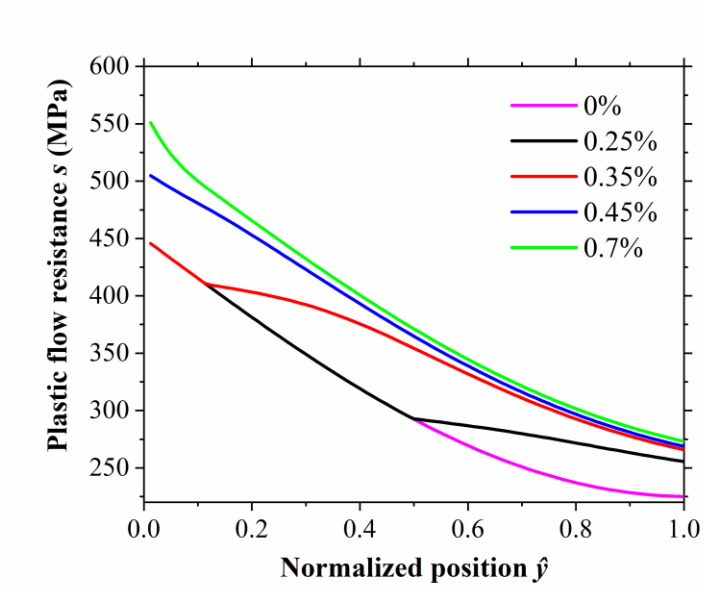

Figure 5.9 Simulation results of the revised GNT-1 model with a nonlinear sinusoidal wave profile of initial plastic flow resistance from the 1D gradient theory of plasticity, showing the cross-sectional distribution of plastic flow resistance $s(\hat{y})$ at different applied tensile strains ε_{zz}^{a}.

The numerical results of the revised GNT-1 to GNT-4 models are close to the corresponding GNT-1 to GNT-4 models with the triangle wave profiles of $s(y,t=0)$. As an example, Figure 5.9 shows the cross-sectional distributions of plastic flow resistance $s(\hat{y})$ at different applied tensile strains ε_{zz}^{a} for the revised GNT-1 model with $s(y,t=0)$ given by Eq. (5.19). Comparing with the results in Figure 5.4a, the difference in $s(\hat{y})$ at the same ε_{zz}^{a} is small between the linear and nonlinear distributions of $s(y,t=0)$. Overall, all the results obtained from the triangle wave profiles of $s(y,t=0)$ are close to those from the nonlinear sinusoidal wave profiles with identical $s_{0,\max}$, $s_{0,\max}$ and λ.

5.7 Summary

We have developed a 3D gradient theory of plasticity by incorporating the strengthening effect of plastic strain gradient into the classical J_2 flow theory. Numerical simulations based on a simplified 1D gradient theory show the dominant effects of gradient plasticity on GNT Cu under uniaxial tension, including progressive yielding, gradient distributions of plastic strain and extra flow resistance. We find that the extra strength depends on the hardness gradient g (being three times strength gradient g_s) through Eq. (5.15), and the saturated plastic strain gradient, $\alpha_{1\%}$, is given by $g_s / E = g / 3E$, as shown in Figure 5.8. Results from 3D gradient plasticity finite element simulations confirm 1D numerical results and further reveal the 3D distribution of non-axial stresses despite their negligible role in the overall tensile response of GNT Cu. Predictions of the optimal gradient structures and associated gradient strength distributions suggest possible routes for achieving the maximum strength of gradient nanostructures in GNT Cu.

While the present work has established a direct relationship between the built-in structure gradient and resultant plastic strain gradient in GNT Cu, future studies are needed to elucidate the mechanistic origin of the extra strength arising from plastic strain gradient. This requires a combined experimental and modeling effort to address several fundamental questions, including how geometrically necessary dislocations originate from built-in structure gradients and resulting plastic strain gradients, and how these geometrically necessary dislocations impact the generation of extra dislocations with different characters and distributions, leading to the extra strength in GNT Cu. In addition, the strengthening effect of the plastic strain gradient is characterized by a phenomenological relation of Eq.

(5.7) in this work. It remains to be established how the strengthening effect arises from the plastic strain gradient through a dislocation density-based model. Broadly, since GNT Cu represents a unique class of heterogeneous nanostructures with a high tunability of structure gradient, resolving the above issues may open opportunities for tailoring the structural heterogeneities in a variety of heterogeneous nanostructured materials [3] to obtain outstanding mechanical properties.

CHAPTER 6. MECHANISTICALLY-BASED THEORY OF STRAIN GRADIENT PLASTICITY

6.1 Introduction

The emergence of heterogeneous nanostructured metals offers great potential for achieving extraordinary mechanical properties such as ultra-high strength, ductility, toughness, and their combinations [8, 76, 86, 90-93]. The strengthening effects stemming from various types of heterogeneous nanostructures have been recently studied from different perspectives, including internal back and forward stresses [64, 94-98], Bauschinger effect [99, 100], plastic strain gradient [101-104], geometrically necessary dislocations (GNDs) [105-108], and among others [8, 92, 109, 110]. However, there is a critical lack of a general framework and associated exemplary study that unify these different perspectives. Such unification is essential to vastly accelerating efforts for understanding the origin of strengthening induced by heterogeneous nanostructures and therefore enabling more advanced development of heterogeneous nanostructured metals.

Recently, gradient nanotwinned (GNT) Cu has been fabricated by stacking four homogeneous nanotwinned (HNT) components with increasing twin thickness [91, 102]. By tuning the processing condition, GNT Cu exhibits a periodic variation of twin thickness through sample thickness. As a result, its overall yield strength surpasses the rule-of-mixture average of yield strengths of four HNT components, giving a substantial extra strength of GNT Cu. An increase of twin thickness gradient (hereafter referred to as structural gradient) can result in a marked increase of extra strength. Given the excellent

control of structural gradient and the resultant tunability of extra strength, GNT Cu can serve as a prototypical heterogeneous nanostructured material to unravel the origin of extra strengthening in heterogeneous nanostructures.

Figure 6.1 presents a general framework for understanding the mechanics of heterogeneous nanostructures with GNT Cu as an example. Here it is important to take into consideration the size of a selected representative volume element (RVE) relative to the characteristic length scales of GNT Cu, which feature the wavelength of periodically varying twin thickness (on the order of hundreds of micrometers) as well as nanotwin thickness (on the order of tens of nanometers). As shown in the red panel of Figure 6.1, when the entire sample of GNT Cu is taken as a "large" RVE, the strengthening effect of structural gradient inside the RVE can be characterized by partitioning the overall stress into back and effective stresses based on the plasticity model of kinematic hardening[5-7]. The back stress reflects the strengthening contribution from the directional, long-range internal stress arising from plastically inhomogeneous deformation in gradient structures, while the effective stress represents the strengthening contribution from the non-directional, short-range resistance to gliding dislocations from lattice friction and local pinning obstacles [64]. In contrast, the blue panel of Figure 6.1 shows an alternative approach of choosing a "small" RVE that contains twin lamellae with a uniform thickness. Suppose a "small" RVE represents a "soft" region containing uniformly-thick twin lamellae, while an adjacent "small" RVE represents a "hard" region containing uniformly-thin twin lamellae. A structural gradient across the two RVEs results in a gradient of plastic strain, whose strengthening effect can be characterized by the constitutive model of strain gradient plasticity [102]. Note that such "small" RVEs with uniform twin thickness also

contain structural heterogeneity due to the presence of twin boundaries (TBs) and twin lamellae with different orientations. The strengthening effect of such kind of structural heterogeneity at the "small" RVE level can be characterized by the corresponding back and effective stresses [111]. Therefore, the strengthening effects of nanotwin gradients and uniform nanotwins are separated in the "small-RVE" approach, while these two strengthening effects are combined in the "large-RVE" approach.

In this Chapter, we first measured the back stress and effective stress of four freestanding HNT Cu samples with different average twin thicknesses, and each HNT Cu sample is treated as a "small" RVE. Then we measured the sample-level back stress and effective stress of four GNT Cu samples with different structural gradients, and each GNT Cu sample is considered as a "large" RVE. The results from the two RVE approaches allow us to identify the extra back and effective stresses arising from structural gradients, thereby providing a deeper mechanistic understanding of the extra strengthening effect of heterogeneous nanostructures.

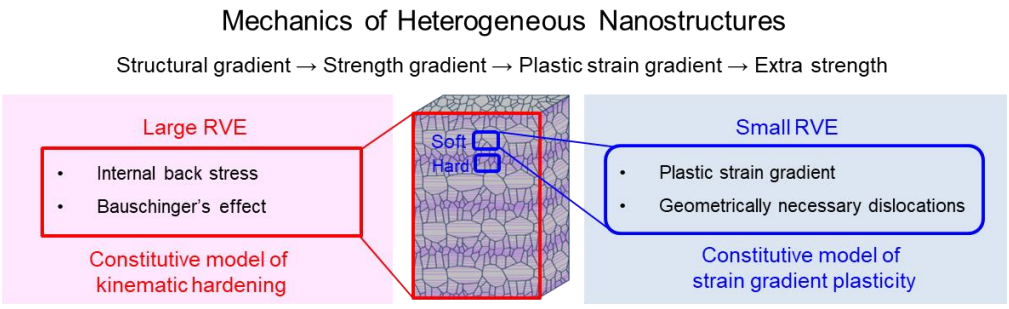

Figure 6.1 A general framework for understanding the mechanics of heterogeneous nanostructures with GNT Cu as an example in terms of representative volume elements (RVEs) at different scales.

6.2 Experiment

Specifically, four HNT Cu samples, referred to as HNT-Ⓐ, HNT-Ⓑ, HNT-Ⓒ and HNT-Ⓓ, respectively, were prepared by direct-current electrodeposition. From HNT-Ⓐ to HNT-Ⓓ, the average twin thickness increases from 28, 37, 50 to 70 nm, respectively. These HNT Cu samples consist of columnar-shaped grains along their growth direction. Inside these grains, most of nanotwins are preferentially oriented with TBs perpendicular to the growth direction, as shown by the schematic illustration, scanning electron microscope (SEM) and transmission electron microscope (TEM) images for HNT-Ⓐ as an example (Figure 2a-c), respectively.

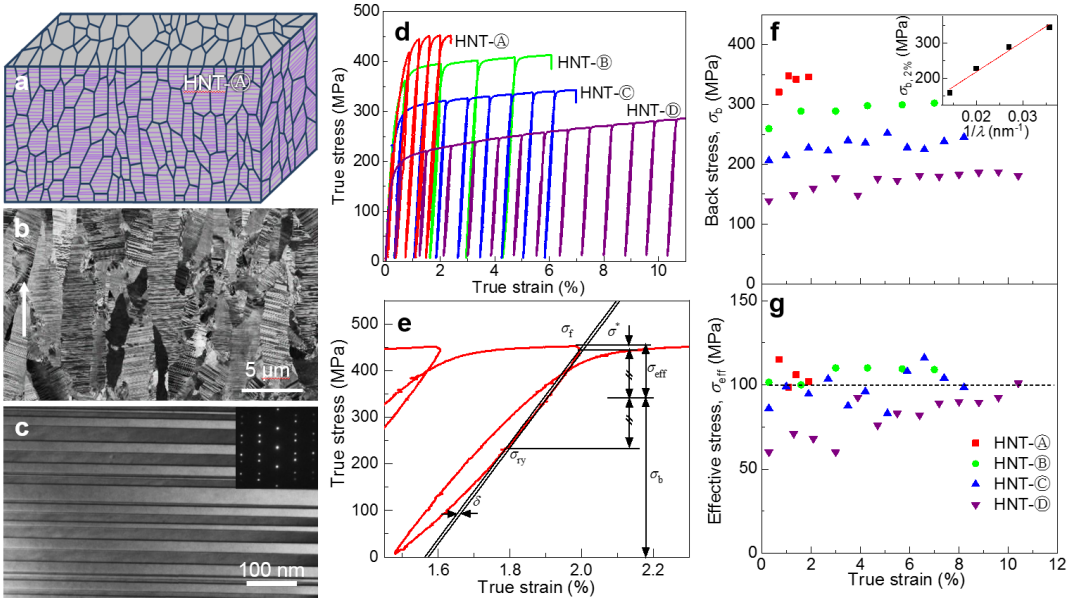

Figure 6.2 Microstructure, back stress and effective stress of HNT Cu samples. a-c, Schematic, SEM image and TEM image of HNT-Ⓐ sample. The white arrow in **b** indicates the growth direction of HNT Cu. **d**, Loading-unloading tensile true stress-strain curves of four HNT Cu samples. **e,** Definition of back stress σ_b and effective stress σ_{eff} based on Dickson's method in a magnified unloading-reloading branch of the stress-strain curve of HNT-Ⓐ sample. σ_f, flow stress; σ_{ry}, reverse yield stress; σ^*, stress interval past the peak

stress; δ, offset stain; E, elastic modulus. **f**, Back stress σ_b against tensile strain for four HNT Cu samples. Insert shows that the back stress of HNT Cu samples at ε = 2%, denoted as $\sigma_{b,\,2\%}$, follows a linear relationship with the reciprocal of twin thickness. **g**, Same as **f** except for effective stress σ_{eff}.

Figure 6.2d shows tensile true stress-strain curves with multiple unloading-reloading branches for four HNT Cu samples. The tensile stress σ exhibits rapid increase at small strains and then switches to slow increase beyond the tensile strain ε of about 2%. A similar two-stage hardening response is also measured for GNT Cu, as to be shown. Hence, the tensile stress σ at ε = 2%, denoted as $\sigma_{2\%}$, is taken as an approximate measure of yield strength for both HNT and GNT Cu. From HNT-Ⓐ to HNT-Ⓓ, $\sigma_{2\%}$ decreases from 448, 392, 320 to 228 MPa, showing a strong dependence on twin thickness in HNT Cu.

Figure 6.2e shows a representative unloading-reloading branch of HNT-Ⓐ, where the Dickson's method [112] is applied to partition the tensile stress into its components of back stress σ_b and effective stress σ_{eff}. Once unloading begins at ε = 2%, the unloading curve deviates markedly from the reference curve of linear elastic unloading. Notably, reverse plastic yielding occurs while stress is still tensile, indicative of a strong Bauschinger effect associated with a high back stress and low effective stress.

From multiple unloading-reloading branches (Figure 6.2d), σ_b and σ_{eff} were determined as a function of ε for four types of HNT Cu (Figs. 6.2f and 6.2g). From HNT-Ⓓ to HNT-Ⓐ, σ_b increases markedly with decreasing twin thickness λ. For example, σ_b at ε = 2%, denoted as $\sigma_{b,\,2\%}$, reaches 160 MPa in the softest HNT-Ⓓ with the largest λ of

70 nm, as compared with 346 MPa in the strongest HNT-Ⓐ with the smallest λ of 28 nm. The inset of Figure 6.2f shows that $\sigma_{b,\,2\%}$ follows approximately a linear relationship with $1/\lambda$. σ_{eff} exhibits a weak dependence on λ at low ε and approaches a saturated value close to 100 MPa, as shown in Figure 6.2g. There is no significant increase in σ_{eff} with increasing ε, except for HNT-Ⓓ whose σ_{eff} increases from ~60 MPa at small ε to the saturated value close to 100 MPa at ε ~ 8%. Altogether, the above results indicate that the back stress of HNT Cu at ε = 2% is much higher than the corresponding effective stress and accounts for about 70% of the overall tensile stress. The twin thickness dependence of the tensile stress is caused almost entirely by that of the back stress, while the effective stress depends weakly on twin thickness.

Taking HNT-Ⓐ, HNT-Ⓑ, HNT-Ⓒ and HNT-Ⓓ as building blocks, four types of GNT Cu were fabricated with the stacking sequence of ⒶⒷⒸⒹ, ⒶⒷⒸⒹⒹⒸⒷⒶ, 2×ⒶⒷⒸⒹⒹⒸⒷⒶ and 4×ⒶⒷⒸⒹⒹⒸⒷⒶ, referred to as GNT-1, GNT-2, GNT-3 and GNT-4, respectively. Taking GNT-3 as an example, we show the schematic illustration (Figure 6.3a) and SEM image (Figure 6.3b) of its microstructure with gradient twin thickness. A series of micro-hardness measurements were conducted through sample thickness. The measured hardness gradient, denoted as *s*, increases from 1.75 to 11.6 GPa/mm for GNT-1 to GNT-4. For clarity of discussion, hereafter these hardness gradient values will be used to represent both structural and strength gradients in GNT Cu.

Figure 6.3c shows tensile true stress-strain curves of four types of GNT Cu. From GNT-1 to GNT-4, the sample-level tensile stress at the tensile strain of 2%, denoted as $\bar{\sigma}_{2\%}$,

increases from 358, 406, 420 to 460 MPa, showing a strong dependence on structural gradient. Note that the sample-level stress and strain in GNT Cu are different from their local counterparts in sample's cross section. Hence, we add an overbar to each sample-level quantity for GNT Cu. It should be noted that each GNT Cu has the same volume fraction (~25%) of four homogeneous components of HNT-Ⓐ to HNT-Ⓓ. Based on the $\sigma_{2\%}$ of these four HNT components, a simple rule-of-mixture estimate of the $\bar{\sigma}_{2\%}$ of GNT Cu gives 348 MPa. However, the measured $\bar{\sigma}_{2\%}$ of all four GNT Cu samples surpasses the rule-of-mixture value, giving the respective extra strength of 10, 58, 70, 112 MPa from GNT-1 to GNT-4. These results clearly demonstrate the extra strengthening effects of structural gradients in GNT Cu.

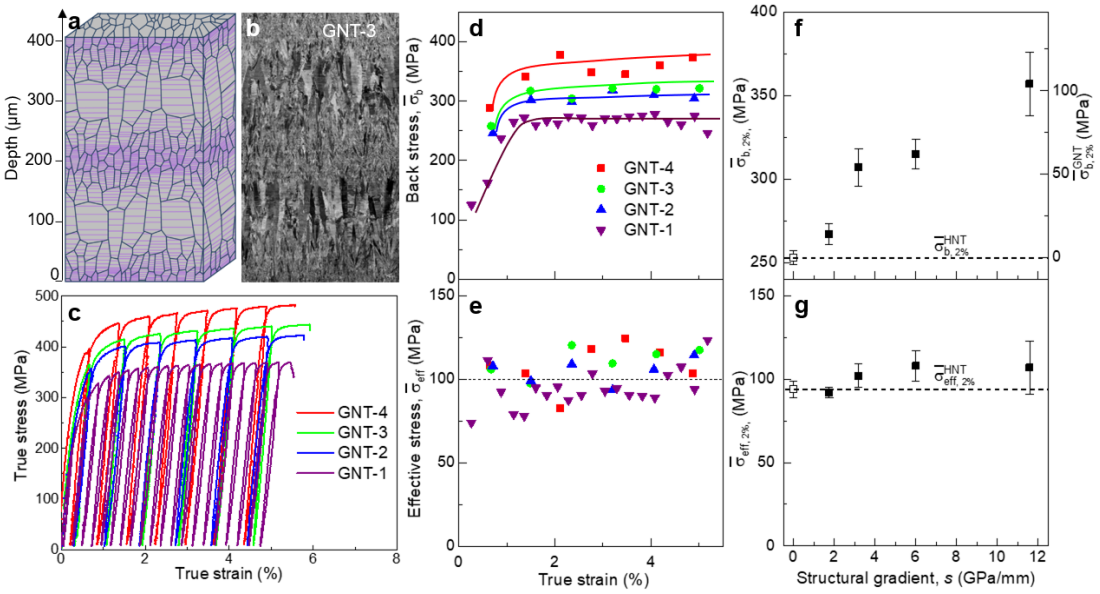

Figure 6.3 Microstructure, back stress and effective stress of GNT Cu samples. **a**, Schematic of microstructure in GNT-3. **b**, Corresponding SEM image. **c**, Loading-unloading tensile true stress-strain curves. **d**, Back stress $\bar{\sigma}_b$ against true strain. **e**, Same as **d** except for effective stress $\bar{\sigma}_{eff}$. **f**, Back stress at ε = 2%, denoted as $\bar{\sigma}_{b,2\%}$ (y axis on the left), against structural gradient s induced back stress, along with $\bar{\sigma}^{GNT}_{b,2\%}$ (y axis on the

right)$\bar{\sigma}_b^{GNT}$. The open symbol and the horizontal dashed line represent the HNT-induced back stress $\bar{\sigma}_{b,\,2\%}^{HNT}$, which is estimated by the rule of mixture in terms of back stresses of four HNT Cu samples. $\bar{\sigma}_{b,\,2\%}^{GNT}$ $\bar{\sigma}_b^{GNT}$is the difference between $\bar{\sigma}_{b,\,2\%}$ and $\bar{\sigma}_{b,\,2\%}^{HNT}$. The error bars are evaluated from 3~5 measured values around ε = 2%. **g**, Same as **f** except for effective stress at ε = 2%, denoted as $\bar{\sigma}_{eff,\,2\%}$.

6.3 Mechanistic-Based Strain Gradient Plasticity

To determine dislocation mechanisms responsible for the extra back stress, we conducted TEM analysis of deformed HNT and GNT samples, and identified an unusual type of dislocation structure, called bundles of concentrated dislocations (BCDs), that only forms in GNT Cu, but not in HNT Cu. These BCDs facilitate the accumulation of GNDs for accommodating the gradients of plastic strain in GNT Cu that give rise to the extra strengthening effect. For example, Figure 4a shows the BCDs inside columnar grains in GNT-4 deformed to ε = 1%. These BCDs appear as long contrast strips (indicated by red arrows) aligned with the direction of twin thickness gradient. The BCD width along the horizontal direction increases from component Ⓐ to Ⓓ, ranging from 0.3 to 1.5 μm. The number fraction of grains with BCDs increases from 15% to 45%, indicating the variation of BCD morphology with gradient twin structure.

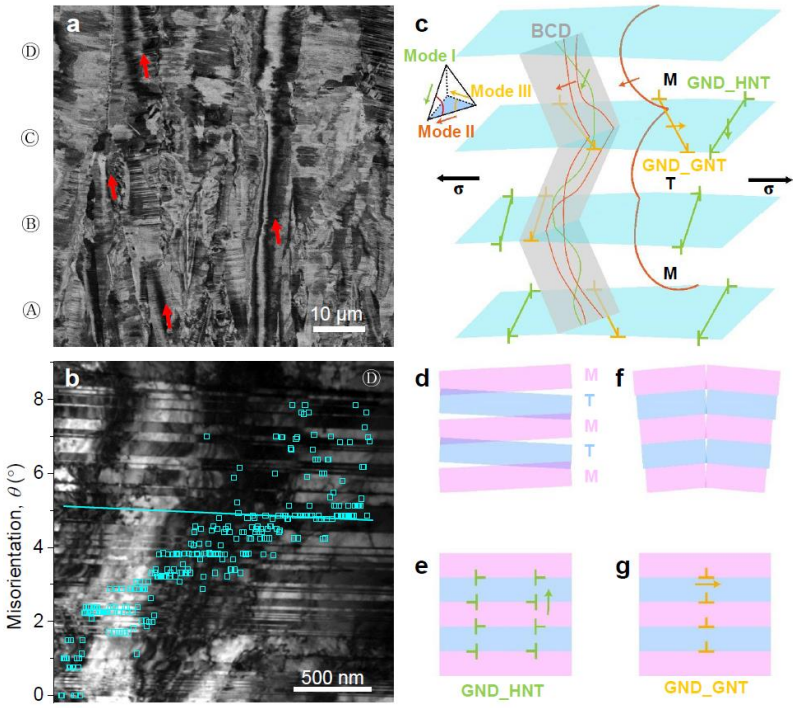

Figure 6.4 Deformation mechanisms in GNT Cu. **a**, Bundles of concentrated dislocations (BCDs) (indicated by the red arrows) in the SEM image of a GNT-4 sample at tensile strain of 1%. **b**, TEM image of a BCD in component Ⓓ of GNT-4, with misorientation mapping along a twin lamella as indicated by a solid line. **c**, Schematic illustration of dislocation structures in twin (T) and matrix (M) developed under applied stress □, based on TEM results. Dislocations of Mode I, II and III are represented by green, brown and orange lines, respectively, and the corresponding Burgers vectors are shown on the Thompson tetrahedron. **d**, Incompatible deformation between twin (T) and matrix (M) in HNT structure, and **e**, resulting accumulation of geometrically necessary dislocations (denoted as GND_HNT). **f**, Incompatible deformation induced by sample-level plastic strain gradient stemming from structural gradient in GNT structure, and **e**, resulting accumulation of geometrically necessary dislocations (denoted as GND_GNT).

To reveal the effect of BCDs on GNDs, Figure 6.4b shows the magnified TEM image of a BCD in the component Ⓓ of GNT-4. Across this BCD, the local contrast changes along the direction parallel to TBs. The orientation mapping technique [113] in TEM was used to characterize the variation of local contrast in terms of lattice misorientation $\Delta\theta$, which reaches ~8° across the BCD. It follows that the local density of GNDs associated with this BCD ρ_G^{BCD} was estimated as 3.6×10^{14} m^{-2}, and the corresponding average

density of GNDs inside grain ρ_G^{GNT} is 6.5×10^{11} m^{-2}, which is consistent with an estimate from the gradient of plastic strain in GNT-4. Hence, these GNDs associated with BCDs serve to accommodate gradients of plastic strain generated from structural gradients in GNT Cu. In addition, the dislocation types inside BCDs were analyzed using a two-beam diffraction technique in TEM [114, 115]. As illustrated in Figure 6.4c, we identified glide dislocation lines traversing several twin lamellae as Mode II dislocations (with slip plane inclined to TBs and Burgers vector parallel to TBs) [114-116]; we also observed BCDs consisting of tangled dislocation lines that can be Mode II or Mode I (with both the slip plane and Burgers vector inclined to TBs); many dislocation segments near TBs were also observed, and they are either Mode II or Mode III (with both slip plane and Burgers vector parallel to TBs).

Based on the above results, we rationalize the strengthening effects in GNT Cu from various types of dislocation indicated in Figure 6.4c. First, the effective stress is likely controlled by the glide dislocations of Mode II traversing several twin lamellae. As discussed earlier, we measured the effective stresses that are almost independent of twin thickness and approach similar saturated values around 100 MPa in both HNT and GNT Cu. From Taylor's hardening law [117, 118], the characteristic length scale associated with the effective stress of about 100 MPa can be estimated as ~100 nm, which is two and five times the twin thickness of NT-Ⓓ and NT-Ⓐ, respectively. Hence, the Mode II dislocation should have a characteristic length of ~100 nm between pinning points and thus consist of several connected segments, which traverse nanotwin lamellae and move concertedly as a continuous line on the corrugated {111} glide plane in the matrix and nanotwins [119, 120].

6.3.1 Intergranular Internal Stresses from Gradient Structures

Next, we consider dislocations underlying the back stress associated with HNT Cu that exhibits a strong dependence on twin thickness. This type of back stress can stem from the directional, long-range internal stress of GNDs accumulated at TBs. During plastic deformation, glide dislocations on geometrically different slip systems in the matrix and nanotwins produce deformation incompatibility at TBs [105, 106]. Such incompatibility would lead to overlap or opening if the matrix and nanotwins were allowed to deform independently (Figure 6.4d). To accommodate the incompatibility, GNDs of Mode I should be accumulated at TBs (Figure 6.4e). Their density $\rho_{\mathrm{G}}^{\mathrm{HNT}}$ will scale with $\Delta\gamma^{p}/(\lambda b)$, where $\Delta\gamma^{p}$ is the local incompatible strain at a TB. Hence, the back stress associated with $\rho_{\mathrm{G}}^{\mathrm{HNT}}$ in HNT components will increase with decreasing twin thickness.

6.3.2 Intragranular Internal Stresses from Nanotwins

Finally, we consider dislocations providing the extra back stress that increases with structural gradient. In GNT Cu, BCDs belong to a new type dislocation structure consisting of tangled dislocation lines traversing several twin lamellae (Figure 6.4c). These BCDs can consist of sessile dislocation lines of Mode I and II. More importantly, these dislocations can act as forest obstacles [121-123] to facilitate the accumulation of Mode III dislocations at BCDs, which serve as GNDs to produce the misorientation across the BCD, as illustrated in Figs. 6.4f and 6.4g. These GNDs produce extra back stresses through long-range internal stresses to hinder dislocation glide in between BCDs [97, 124, 125]. Moreover, the

measured effective density of these GNDs inside grains, denoted as $\rho_{\mathrm{G}}^{\mathrm{GNT}}$, matches the gradient of plastic strain arising from the structural gradient in GNT Cu.

6.4 Strain Gradient Plasticity Modeling of GNT Cu

To investigate the origin of strengthening effects in GNT Cu, we developed a three-dimensional strain gradient plasticity model that accounts for the back and effective stresses arising from structural gradient. In the following, we present the one-dimensional formulation of this model used in this work.

The strain gradient plasticity model is formulated based on the classical J_2 rate-dependent plasticity theory [102]. The total tensile strain rate $\dot{\varepsilon}$ is decomposed into elastic and plastic parts,

$$\dot{\varepsilon} = \dot{\varepsilon}^{\mathrm{e}} + \dot{\varepsilon}^{\mathrm{p}} \tag{6.1}$$

In Eq. (6.1), the elastic strain rate $\dot{\varepsilon}^{\mathrm{e}}$ is related to the tensile stress rate $\dot{\sigma}$ by Hooke's law

$$\dot{\varepsilon}^{\mathrm{e}} = \dot{\sigma} / E \tag{6.2}$$

where E is Young's modulus. The plastic strain rate $\dot{\varepsilon}^{\mathrm{p}}$ is given by a viscoplastic relation

$$\dot{\varepsilon}^{\mathrm{p}} = \dot{\varepsilon}_0^{\mathrm{p}} \left(\frac{\left| \sigma - \sigma_{\mathrm{b}} \right|}{S} \right)^m \operatorname{sgn}\left(\sigma - \sigma_{\mathrm{b}} \right) \tag{6.3}$$

where $\dot{\varepsilon}_0^{\mathrm{p}}$ is the reference plastic strain rate, σ_{b} is the back stress, and S is the isotropic plastic flow resistance dictating the effective stress. We assume that S arises from the Taylor hardening [64], as given by

$$S = M\alpha\mu b\sqrt{\rho_S} \tag{6.4}$$

where M is the Taylor factor, α is the Taylor constant, μ is the shear modulus of Cu, b is the Burgers vector length, and ρ_S is the density of statistically stored dislocations (SSDs). According to the Kocks-Mecking model [118], the rate of ρ_S is expressed as

$$\dot{\rho}_{\mathrm{S}} = \left(k_1\sqrt{\rho_{\mathrm{S}}} - k_2\rho_{\mathrm{S}} + k_3\rho_{\mathrm{G}}^{\mathrm{GNT}}\right)\dot{\varepsilon}^{\mathrm{p}} \tag{6.5}$$

Within the parenthesis on the right hand side of Eq. (6.5), the first two terms represent the effect of multiplication and annihilation of SSD, respectively, while the third term represents the effect of GND arising from GNT on SSD; k_1, k_2 and k_3 are the constant coefficient associated with these three terms, respectively.

The total back stress is decomposed as

$$\sigma_{\mathrm{b}} = \sigma_{\mathrm{b}}^{\mathrm{HNT}} + \sigma_{\mathrm{b}}^{\mathrm{GNT}} \tag{6.6}$$

where $\sigma_{\mathrm{b}}^{\mathrm{HNT}}$ is the HNT-induced back stress and $\sigma_{\mathrm{b}}^{\mathrm{GNT}}$ is the extra back stress arising from structural gradient. Note that $\sigma_{\mathrm{b}}^{\mathrm{HNT}}$ originates from incompatible plastic deformation between the matrix and nanotwins, which produces GNDs on twin boundaries. The rate of $\sigma_{\mathrm{b}}^{\mathrm{HNT}}$ is expressed as [126]

$$\dot{\sigma}_{\mathrm{b}}^{\mathrm{HNT}} = c^{\mathrm{HNT}} \left(\sigma_{\mathrm{sat}}^{\mathrm{HNT}} - \sigma_{\mathrm{b}}^{\mathrm{HNT}} \right) \dot{\varepsilon}^{\mathrm{p}} \tag{6.7}$$

where $\sigma_{\mathrm{sat}}^{\mathrm{HNT}}$ is the saturated value of the HNT-induced back stress and c^{HNT} is the constant coefficient. According to our experimental measurements, $\sigma_{\mathrm{sat}}^{\mathrm{HNT}}$ is proportional to the inverse of twin thickness λ. Hence, $\sigma_{\mathrm{sat}}^{\mathrm{HNT}}$ is expressed as

$$\sigma_{\mathrm{sat}}^{\mathrm{HNT}} = \beta \frac{\mu b}{\lambda} \tag{6.8}$$

where β is the constant coefficient. Likewise, $\sigma_{\mathrm{b}}^{\mathrm{GNT}}$ obeys a similar rate relation

$$\dot{\sigma}_{\mathrm{b}}^{\mathrm{GNT}} = c^{\mathrm{GNT}} \left(\sigma_{\mathrm{sat}}^{\mathrm{GNT}} - \sigma_{\mathrm{b}}^{\mathrm{GNT}} \right) \dot{\varepsilon}^{\mathrm{p}} \tag{6.9}$$

where $\sigma_{\mathrm{sat}}^{\mathrm{GNT}}$ is the saturated value of the extra back stress arising from structural gradient and c^{GNT} is the constant coefficient. We assume that $\sigma_{\mathrm{sat}}^{\mathrm{HNT}}$ is proportional to the extra GNDs associated with BCDs resulting from structural gradient and express $\sigma_{\mathrm{sat}}^{\mathrm{HNT}}$ as

$$\sigma_{\mathrm{sat}}^{\mathrm{GNT}} = \mu b L \rho_{\mathrm{G}}^{\mathrm{GNT}} \tag{6.10}$$

where L is the characteristic length of GNDs induced by structural gradient, and $\rho_{\mathrm{G}}^{\mathrm{GNT}}$ is the density of the extra GNDs resulting from the structural gradient and resultant plastic strain gradient. We express $\rho_{\mathrm{G}}^{\mathrm{GNT}}$ as [105]

$$\rho_{\mathrm{G}}^{\mathrm{GNT}} = \frac{\left| \nabla \varepsilon^{\mathrm{p}} \right|}{b} \tag{6.11}$$

where $\left|\nabla \varepsilon^{p}\right|$ represents the magnitude of the gradient of tensile plastic strain $\varepsilon^{p} = \int_0^t \dot{\varepsilon}^{p} dt'$

In a typical numerical simulation, the GNT Cu sample was subjected to uniaxial tension with a constant strain rate of 0.001 s^{-1}. The finite difference method was used with the integration time step of 0.001 s. Given the periodicity of strength distribution in the cross section, we considered one period of the triangular wave of saturated HNT-induced back stress given by 346-160 MPa. Within this period, the normalized *y*-axis along the gradient direction was divided into 100 equally spaced sections. In the middle of the period, the central difference scheme is used to calculate the plastic strain gradient for ensuring numerical stability [102], and the skew difference is used at two ends of the period. The material parameters used in our simulations are listed in Table 6.1, which are determined by fitting model predictions to experimental results.

Table 6.1 Parameters used in strain gradient plasticity simulations.

Symbol (unit)	Magnitude
E (GPa)	115
μ (GPa)	42
m	500
$\dot{\varepsilon}_0^{p}$ (s^{-1})	0.001
M	3.0
α	0.3
b (nm)	0.255

Table 6.1 continued

$k_1(\mathrm{m}^{-1})$	5e9
k_2	5e2
k_3	8.5e4
c^{HNT}	1e4
c^{GNT}	5e2
$L(\mu\mathrm{m})$	90

Figure 6.5a shows the simulated tensile stress-strain curves for GNT-1 to GNT-4, which agree with the experimental results in Figure 6.3c. Taking GNT-2 as an example, Figure 6.5b shows the SGP results of the sample-level tensile stress $\bar{\sigma}$ along with its components of effective stress $\bar{\sigma}_{\mathrm{eff}}$, back stress associated with HNT $\bar{\sigma}_{\mathrm{b}}^{\mathrm{HNT}}$, and extra back stress arising from structural gradient $\bar{\sigma}_{\mathrm{b}}^{\mathrm{GNT}}$. It is seen that $\bar{\sigma}_{\mathrm{b}}^{\mathrm{HNT}}$ provides a stronger strengthening effect than both $\bar{\sigma}_{\mathrm{eff}}$ and $\bar{\sigma}_{\mathrm{b}}^{\mathrm{GNT}}$ in GNT-2. However, it should be emphasized that $\bar{\sigma}_{\mathrm{b}}^{\mathrm{GNT}}$ increases substantially with structural gradient, while $\bar{\sigma}_{\mathrm{b}}^{\mathrm{HNT}}$ and $\bar{\sigma}_{\mathrm{eff}}$ do not, as shown in Figs. 6.5e and 6.5f. For GNT-2, Figure 6.5c shows the SGP results of cross-sectional distributions of plastic strain $\varepsilon^{\mathrm{p}}(y)$ at different $\bar{\varepsilon}$, which directly reveal the evolution of plastic strain gradient associated with progressive yielding in the cross section. Namely, since the local yield strength decreases from component Ⓐ to Ⓓ, component Ⓓ first yields; and the plastic region with non-zero $\varepsilon^{\mathrm{p}}(y)$ expands gradually to component Ⓐ with increasing $\bar{\varepsilon}$. Such progressive yielding is completed around

$\bar{\varepsilon} = 0.3\%$. After that, a nearly linear distribution of $\varepsilon^{\mathrm{p}}(y)$ with a constant plastic strain gradient is maintained with increasing $\bar{\varepsilon}$. The SGP result regarding the constant saturated gradient of plastic strain can be also be verified through a scaling analysis of plastic strain gradient.

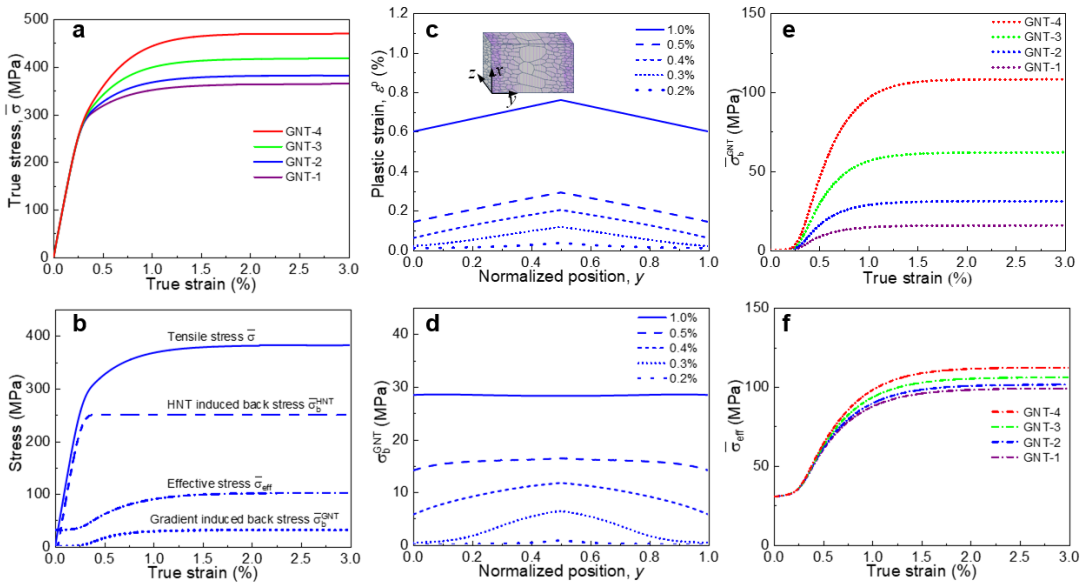

Figure 6.5 Numerical results of strain gradient plasticity modeling of GNT Cu, showing the spatiotemporal evolution of back stress and effective stress**.** **a**, Sample-level stress-strain curves of GNT-1 to GNT-4. **b**, Sample-level tensile stress $\bar{\sigma}$ for GNT-2, along with its components of effective stress $\bar{\sigma}_{\mathrm{eff}}$, back stress associated with HNT $\bar{\sigma}_{\mathrm{b}}^{\mathrm{HNT}}$, and extra back stress arising from structural gradient $\bar{\sigma}_{\mathrm{b}}^{\mathrm{GNT}}$. **c**, Distribution of plastic strain ε^{p} as a function of position *y* (defined in inset and normalized by sample thickness) in the cross section of GNT-2 at different tensile strains. **d**, Same as **c** except for the local extra back stress $\sigma_{\mathrm{b}}^{\mathrm{GNT}}$ arising from structural gradient. **e,** Sample-level extra back stress arising from structural gradient $\bar{\sigma}_{\mathrm{b}}^{\mathrm{GNT}}$ against tensile strain for GNT-1 to GNT-4. **f,** Same as **e** except for sample-level effective back stress $\bar{\sigma}_{\mathrm{eff}}$. The effective stresses in **b** and **f** are evaluated from the isotropic flow resistance *S*.

The saturated gradient of plastic strain after progressive yielding can understandably result in a saturated extra strength at the sample level. However, the saturation of extra strength is achieved until $\bar{\varepsilon}$ reaches about 1%, which is larger than the characteristic strain of $\bar{\varepsilon} = 0.3\%$ to complete progressive yielding. To understand this delayed response, Figure 6.5d shows that $\sigma_{\mathrm{b}}^{\mathrm{GNT}}(y)$ is not statured immediately after the entire cross section becomes plastically yielded; the nonlinear hardening causes a further increase of $\sigma_{\mathrm{b}}^{\mathrm{GNT}}(y)$, such that a uniform distribution of saturated $\sigma_{\mathrm{b}}^{\mathrm{GNT}}(y)$ is achieved until $\bar{\varepsilon} = 1\%$, giving the saturated extra strength at the sample level. Moreover, Figure 6.5e shows that the increasing structural gradient from GNT-1 to GNT-4 raises substantially the extra back stress $\bar{\sigma}_{\mathrm{b}}^{\mathrm{GNT}}$ at the sample level. In contrast, Figure 6.5f shows that the increasing structural gradient from GNT-1 to GNT-4 has negligible effects on both their effective stress $\bar{\sigma}_{\mathrm{eff}}$ and back stress associated with HNT $\bar{\sigma}_{\mathrm{b}}^{\mathrm{HNT}}$ at the sample level. These results underscore the predominant role of structural gradient and associated plastic strain gradient in the extra back stress $\bar{\sigma}_{\mathrm{b}}^{\mathrm{GNT}}$ and resultant extra strength of GNT Cu.

6.5 Summary

In summary, our combined experimental and modeling results have identified the primary source of extra strengthening in GNT Cu as the extra back stress arising from nanotwin structure gradient. The extra back stress is induced by the GNDs associated with BCDs that only form in gradient nanotwin structures. An increase in nanotwin structure gradient can lead to a substantial increase in plastic strain gradient giving rise to a high extra strength. In contrast, the strengthening effect of HNT Cu largely comes from a

different type of back stress originated from incompatible deformation between the matrix and nanotwins. Such back stress is enhanced with decreasing twin thickness. The effective stress is much less sensitive to the geometry of nanotwins in both GNT and HNT Cu. Altogether, these results underscore the predominant strengthening effect of the extra back stress arising from gradient structure, and thus point to a "going for nano" strategy for further enhancing the strength of GNT Cu by a simultaneous decrease of nanotwin thickness and increase of nanotwin gradient. This strategy requires innovations in material processing to push the limit of attainable nanostructure geometry in the future.

Broadly, this work exemplifies a general mechanistic approach to unravel the strengthening mechanism in heterogeneous nanostructures. We demonstrate that in a material with hierarchical nanostructures such as GNT Cu, there generally exist multiple sources of back and effective stresses, due to different levels of structural heterogeneity with distinct characteristic length scales. A combined use of the "large RVE" and "small RVE" approaches enable us to decouple various sources of strengthening stemming from different types of structural heterogeneity. Future mechanistic studies along this line can provide deep insights and may pave the way for a rational development of heterogeneous nanostructured metals with outstanding mechanical performance.

Part III: Nanoscale Heterogeneities in Nanocrystalline Metals and Composites

CHAPTER 7. GRAIN GROWTH IN NANOCRYSTALLINE AL

7.1 Introduction

Decades of research have advanced our fundamental understanding of the role GBs have in the deformation process of nc metals. However, significant challenges remain toward quantitative characterization of GB-mediated deformation processes within real GB networks of nc metals as well as quantitative correlation between these processes and bulk mechanical properties. One of the limitations to widespread use of nc metals is the notable loss of ductility due to a lack of strain hardening which leads to localized deformation [1] and limited uniform elongation [127]. The combination of high flow stress and low work hardening in nc metals promotes neck formation, resulting in 'unusable' elongation and reduced tensile ductility. During the neck formation processes, the role of nano-grain coarsening on this behavior is not well understood. The abovementioned studies provide valuable insight into the mechanisms of deformation induced grain growth, but the techniques used are limited in the ability to measure the far-field applied stress while observing deformation processes, and thus cannot accurately correlate the GB-mediated processes with the mechanical properties.

In this work, we investigate the active deformation mechanisms during tensile loading of nc Al thin films using two quantitative MEMS-based *in situ* TEM nanomechanical testing platforms. This approach allows us to measure far field stress values and correlate them with the active GB and dislocation-based deformation mechanisms with the goal of better understanding the deformation processes that dictate the onset of plastic instability and ultimately the mechanical properties of nc Al thin films. To better understand the

atomic-scale mechanisms underpinning GB migration, we conduct MD simulations, using a novel coloring scheme to track GB migration over time. The combined *in situ* observation and MD simulation results underscore the important role of grain growth in plastically deforming nc Al.

7.2 Microstructures

Nc Al thin film specimens of 200 nm thickness were fabricated via electron beam evaporation of Al (99.99% purity) onto a Si substrate, at a pressure of ~10^{-6} Torr and deposition rate of 0.5 Å/s. The specimens were fabricated using the same batch fabrication technique previously used to fabricate Au specimens. The technique involves optical lithography and a lift-off procedure to define rows of dog-bone shaped specimens, with a gauge section of width ~1.5 μm and length ~20 μm shown in Figure 7.1a. The specimens become free-standing after XeF_2 etching of the Si substrate (see Figure 7.1b). Following fabrication, the films were annealed at 400 °C for 2 hours in a high vacuum oven. Using a micromanipulator, the specimens were detached from the row of specimens, placed onto the MEMS device, and clamped using UV-curable glue (Figure 7.1c). Note that the image in Figure 7.1c shows a fractured specimen captured post-deformation. Figure 7.1d is a pre-deformation orientation map showing that the initial microstructure has no strong out-of-plane texture with most GBs being of the random high-angle type (Figure 7.1f). The films have a general columnar grain structure with an average grain size of 57 ± 30 nm. The grain size distribution is shown in Figure 7.1e.

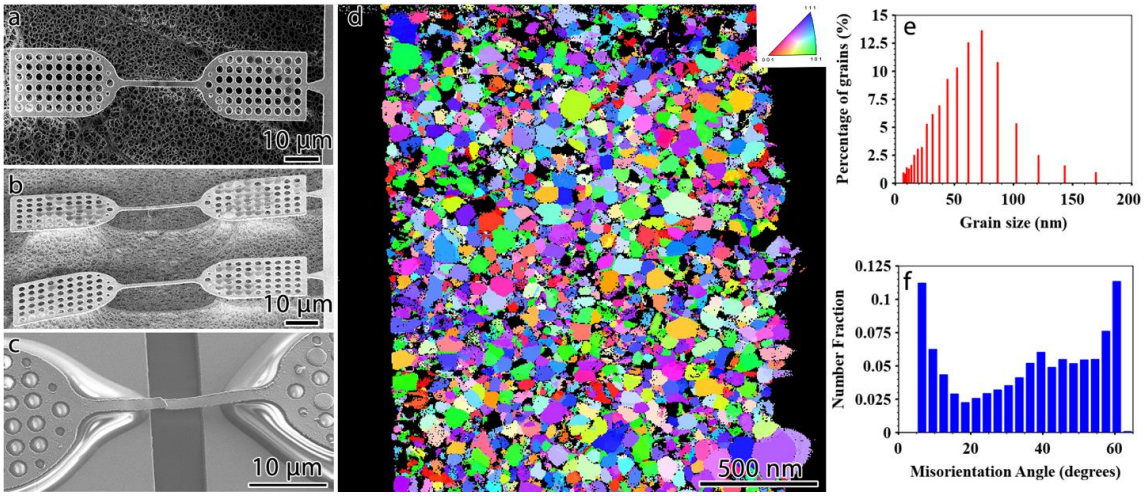

Figure 7.1 Sample fabrication and initial microstructure of Al thin film. (a) SEM image of free-standing specimen. (b) Tilted view to show free-standing specimen. (c) SEM image of specimen clamped to MEMS-device using UV-curable epoxy glue. Image is taken at a tilt in order to capture the amount of gauge length that is supported by glue. (d) Orientation map showing no out-of-plane texture, (e) corresponding grain size distribution and (f) GB misorientation distribution taken from ACOM data.

7.3 Grain Growth under Tensile Deformation

Figure 7.2 is an example of the ability of the MEMS-based platform to capture real-time deformation while reliably measuring far-field stress and strain values. The specimen was strained at $\dot{\varepsilon} \sim 3 \times 10^{-4}$ s^{-1} until failure with roughly 45% of the specimen gauge in the view frame. Figure 7.2a-f are TEM micrographs that track the deformation and formation of a neck. The view frame is moved towards the end to capture the neck, with the arrowhead marking the same location in each figure (Figure 7.2 d-f). The far-field engineering stress and strain values for each figure are marked in the accompanying stress-strain curve shown in Figure 7.2g. From the data, the yield point and Young's modulus were determined to be 380 MPa and 8.9 GPa, respectively. The offset of the initial stress

from a zero value results from residual tensile stress developing when the glue shrinks after curing. The low Young's modulus value stems from the approximate calculation of strain based on crosshead displacement values. The compliance of the glue leads to finite deformation of the thin film specimen along both the fillet region and the gauge section that is in contact with the glue. These sections of the specimen are not included in the free-standing gauge length used to calculate strain, and therefore lead to an underestimate of Young's modulus. While the measured value of Young's modulus is highly sensitive to the accuracy of small strain measurement, this issue does not affect the ability of the technique to measure relatively large plastic strains, as has been previously demonstrated [128, 129]. The loading was paused twice in order to capture the neck formation in more detail, which resulted in the stress relaxation/drop seen prior to Figure 7.2d and after Figure 7.2e. From the pre-test Figure 7.2a to b, only minor contrast changes can be seen accompanied by a uniform reduction in width, with some contrast variations attributed to eliminating any film bending that might be present due to specimen manipulation. Continued width reduction is seen in the progression from Figure 7.2b to c, however slight localized width reduction can be seen near the top of the micrograph. As deformation unfolds to Figure 7.2d, localized reduction continues and leads to the development of a necked region. The neck further develops in Figure 7.2e and f where failure eventually occurs. Within this region, pronounced visible grain growth is observed, with grain sizes exceeding 250 nm.

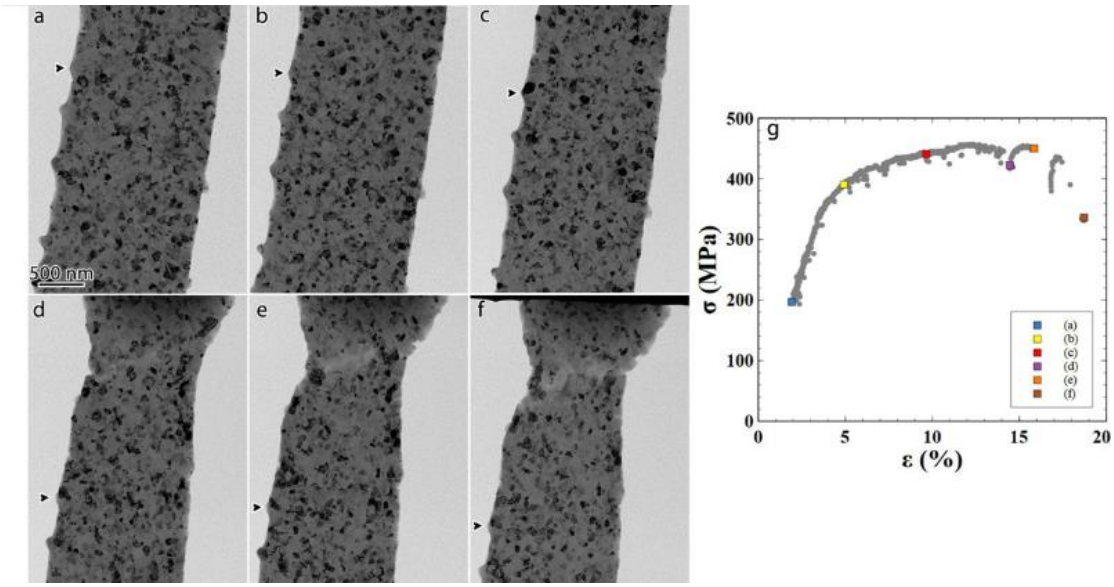

Figure 7.2 Low magnification TEM images showing microstructure evolution at different strain values. The frames are taken at (a) 1.9%, (b) 4.9%, (c) 10%, (d) 14.5%, (d) 16.5% and (f) 18.7% total strain. Arrowhead in each designating the same feature. (g) Engineering stress-strain curve with the total strain of (a-f) indicated by the colored squares.

As deformation progresses and a neck develops, fast GB motion was observed within the necked region, with an example shown in Figure 7.3. Figure 7.3a shows that a neck has developed, and the corresponding stress has dropped below the ultimate tensile strength in Figure 7.3e. Resetting the TEM time t = 0, the vertical dimension of the grain marked by an arrowhead in Figure 7.3b is measured at 115 nm. After 78 seconds, only a slight decrease to 112 nm occurs. However, from Figure 7.3c to d, the bottom boundary migrates 12 nm in 5 seconds, resulting in a migration rate of 2.4 nm s^{-1}. This indicates that within the necked region where the stresses are higher, boundary migration occurs at an increased speed resulting in the rapid collapsing of grains and by geometrical necessity, the rapid growth of neighboring grains. Within this region, the local gauge width is decreased from 1700 nm to 1190 nm. For a simple lower-bound estimate, this indicates that the local stress is increased by a factor of 1.4, resulting in a local stress of at least 630 MPa. This value is not

accounting for any decrease in local film thickness that would also contribute to a further increase in stress. To better visualize the different migration rates, the grains traced in Figure 7.3b-d have been isolated and shown in Figure 7.3f-g and h-i, respectively. It is clear that the grain within the necked region experiences a larger change in grain size over the course of the 5 seconds separating Figure 7.3h and i due to the faster GB migration speed of 2.4 nm s^{-1}. This is another example of 'jerky' type boundary motion, with limited motion for over a minute and then rapid boundary motion.

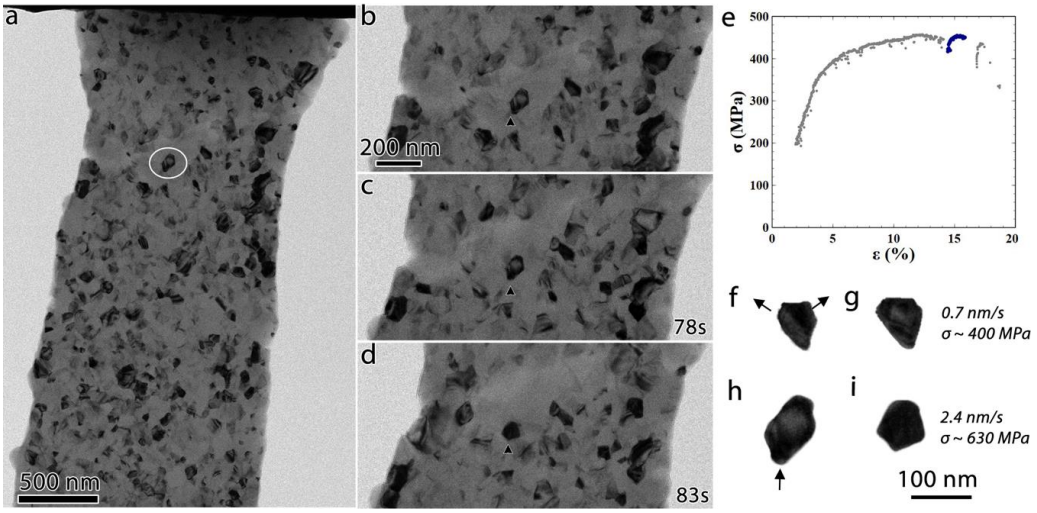

Figure 7.3 Fast GB migration after neck develops. (a) Low magnification TEM image showing developed neck near top of snapshot. White circle indicates location of highlighted grain in (b-d). (e) Stress-strain curve with highlighted region corresponding to when snapshots (a-d) were recorded. Change in grain size as a function of time for (f,g) a grain in uniform region and (h,i) necked region (from b-d). Arrows indicate direction of boundary migration. Both (g) and (i) are taken 5 seconds after (f) and (h), respectively. The size scale for both grains is the same and the respective GB migration velocities and estimated local stress are given.

7.4 Atomistic Modeling of Grain Growth

MD simulations of uniaxial tension of a nc Al thin film were performed using LAMMPS [47]. The initial thin film structure was constructed by a Voronoi tessellation

procedure that generated 32 grains with sizes of about 10 nm, nearly equiaxed shape, and random crystallographic orientations. The thin film structure has dimensions of 32.4 nm × 32.4 nm × 32.4 nm and contains a total of 1,996,000 atoms. Periodic boundary conditions were imposed in the tensile loading direction, while other side surfaces are traction free. The interactions between Al atoms were modeled by an embedded atom method (EAM) potential [130]. To relax the GB structures, the system was annealed under zero stress by first heating to 900 K for 100 ps, then cooling to 300 K, and finally equilibrating at 300 K for 10 ps. Uniaxial tensile strain up to 100% was applied with a strain rate of 10^9 s^{-1} at 300 K. A novel atom coloring scheme is developed and used to visualize both the initial GBs ($t = 0$) and current GBs (time t) in the same atomic configuration at time t. As a result, the morphological evolution of grains and GBs, particularly GB migration, can be traced clearly and continuously during tensile deformation of the nanocrystalline thin film. Specifically, the color of atom i is rendered based on a time-dependent parameter $\Delta c_i(t)$, which is defined as the difference of the centrosymmetry parameter of atom i at time t, denoted as $c_i(t)$, and that at $t = 0$, denoted as $c_i(0)$, such that $\Delta c_i(t) = c_i(t) - c_i(0)$. To understand how $\Delta c_i(t)$ works, we first explain the meaning of c_i. Let us consider atom i in a perfect face-centered cubic lattice. In this case, the neighboring atoms around atom i obey the centrosymmetry, thus giving $c_i = 0$. In contrast, when atom I sits in a stacking fault or a GB, the local centrosymmetry is broken, giving a positive c_i that typically falls in the range of 10~20. A larger c_i reflects a stronger deviation from the local centrosymmetry. Next, we explain the meaning of $\Delta c_i(t)$. Suppose atom i sits at a GB at $t = 0$, giving $c_i(0) > 0$; and atom j resides in the grain interior at $t = 0$, giving $c_j(0) = 0$. Due to GB migration, atom i resides in the grain interior at time t, giving $c_i(t) = 0$ and thus $\Delta c_i(t) < 0$; atom j

sits at a GB at time *t*, giving $c_j(t) > 0$ and thus $\Delta c_j(t) > 0$. Hence, $\Delta c_i(t)$ is *negative* for atom *i* that initially sits at a GB at $t = 0$, but has left the GB at time *t*; and $\Delta c_j(t)$ is *positive* for atom *j* that initially resides in the grain interior at $t = 0$, but has joined a GB at time *t*. In addition, $\Delta c_k(t)$ is zero for atom *k* that resides in the grain interior at both $t = 0$ and time *t*. Using OVITO [131], we render atoms with three colors of red, blue and light gray for positive, negative and zero values of $\Delta c_i(t)$, respectively, so as to simultaneously visualize both the initial GBs ($t = 0$) and current GBs (time *t*) at the same time t. Since the parameter $\Delta c_i(t)$ is computed according to the unique number assigned to each atom throughout the whole MD simulation, the rigid-body displacement, elastic deformation and plastic deformation are automatically filtered out. Hence, the time-dependent morphological evolution of grains and GBs, particularly GB migration, can be visualized clearly and continuously.

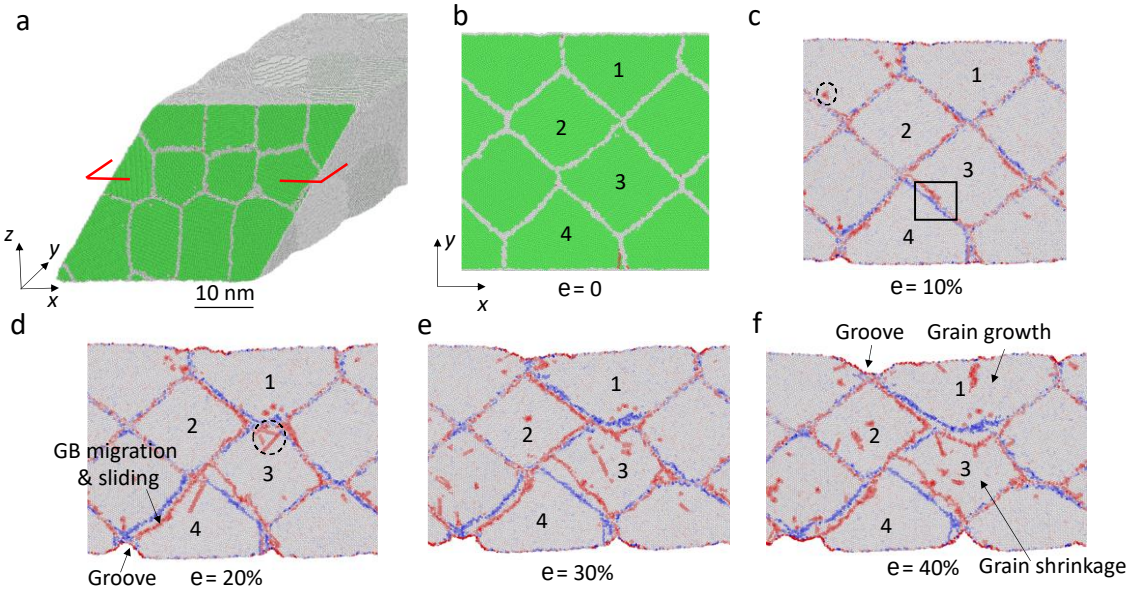

Figure 7.4 MD simulation setup and results of small and modest plastic deformation during uniaxial tension of a nc Al thin film. (a) Three-dimensional view of the nc structure after

annealing. Red segments indicate the cutting plane for exposing the x-y section of the film in (b). (b) Two-dimensional view of the x-y section of the film in (a). Atoms in (a-b) are colored by the common neighbor analysis in OVITO [131], showing atoms in GBs (light gray) and grain interiors (green). (c-f) MD snapshots at different applied tensile strains ε from 0 to 40%, showing the dislocation emission and absorption at GBs, GB migration and sliding, and grain growth and shrinkage. Atoms in (c-f) are colored by a novel scheme explained in the Section 7.4 such that both the initial GBs (at $t = 0$; with the constituent atoms colored in blue) and the current GBs (at time t; with the constituent atoms colored in red) are displayed in the same structure at time t; atoms in the stacking faults are colored in red; and other atoms are colored in light-gray.

Our MD simulations support *in situ* TEM observations of grain growth and further uncover the underlying atomic processes that are not directly visible through TEM. Figure 7.4a and b show two views of the three-dimensional simulated nc Al thin film before tensile loading. In the x-y plane view, Figure 7.4b, four grains are labelled. These 4 grains and the associated GBs were traced during the MD simulation of tensile deformation. In Figure 7.4a and b, the atomic configurations are colored by the common neighbor analysis in OVITO, so that the initial grain geometry and GB structures can be clearly visualized. Figure 7.4c-f present a series of MD images at different tensile strains ε. In this work, a novel atom coloring scheme is developed and used to visualize both the initial GBs ($t = 0$) and current GBs (time t) in the same atomic configuration at time t. As described in detail above, this atom coloring scheme enables us to continuously trace the morphological evolution of grains and GBs, particularly GB migration, during tensile deformation of the nc thin film.

Close examination of the MD results (Figure 7.4c-f) reveals the active mechanisms underlying our *in situ* TEM observations of plastic deformation and fracture in nc Al thin films. Throughout the MD simulations, dislocation activity is observed frequently. These dislocations usually emit from one side of GBs, traverse the grains, and are absorbed into

the opposite side of GBs. Full dislocations of the $1/2\langle 110\rangle\{111\}$ type, which dissociate into leading and trailing partial dislocations of the $1/6\langle 110\rangle\{112\}$ type separated by narrow stacking fault regions, are the majority of intragranular lattice defects, consistent with the high stacking fault energy of Al. As these dislocations glide inside grains, Lomer-Cottrell locks (see circled examples in Figure 7.4c and d) occasionally form, due to the intersection of two dislocations on different slip systems. These locks are disrupted as the applied load increases. The unlocked dislocations further glide inside grains and are eventually absorbed into GBs. Occasionally, only a leading partial is emitted from a GB, leaving behind a long stacking fault; the subsequent emission of a trailing partial occurs with increased load. For grains near the free surface, nucleation of surface dislocations is frequently observed, as the energy barrier of dislocation nucleation at the free surface is often lower than that in the bulk [132]. These MD results of deformation-induced dislocations of different types and on different slip systems complement our *in situ* TEM imaging that was taken along a specific orientation and thus revealed the activity of dislocations on certain slip systems.

In addition to dislocation activity, MD simulations reveal the active processes of GB migration and sliding. Because of random grain orientations, most GBs are of the mixed tilt and twist type. At ε = 10% (Figure 7.4c), GB migration is clearly visible thanks to the aforementioned novel coloring scheme, which enables the display of both the initial and current GBs at the same time. It is seen from Figure 7.4c that GB migration typically occurs at certain boundary segments and thus serves to accommodate local deformation incompatibilities between adjoining grains. GB migration is broadly distributed in different grains, thus facilitating an overall uniform elongation of the thin film. Coupled GB sliding

and migration are often reported in previous MD simulations of sheared bicrystals [133]. However, our MD simulations reveal less active GB sliding than GB migration at small tensile strains (e.g., Figure 7.4c at ε = 10%), largely because of the geometrical constraints of grain triple junctions. We note that while the novel atom coloring scheme is effective for displaying GB migration, GB sliding is less obvious from the colored GBs, but can be determined by movements of grain triple junctions and GB intersections at the free surface.

As the applied tensile strain ε increases from 20% to 40% (Figure 7.4d to f), GB migration gradually increases and also becomes increasingly non-uniform, resulting in large migration of several GBs. Compared to the triple junctions associated with interior GBs, the junctions between GBs and free surface are more prone to local reconstruction because of less surface constraints. As a result, the GBs intersecting the free surface often migrate much faster than the interior GBs. Migration of these near-surface GBs is often coupled with pronounced GB sliding, also because of the lack of surface constraints. Such GB sliding is evidenced by the formation of surface grooves, as seen in Figure 7.4d to f. These MD results suggest that GB migration in the TEM thin film samples likely initiated from the film surface. As the applied tensile strain increases, the interior triple junctions are reconstructed, resulting in coupled GB sliding and migration. These highly active processes of GB migration and sliding result in drastic grain morphology changes, as evidenced by the growth of grain 1 and 4, and the concurrent shrinkage of grain 3 accompanied with a large shape change. The common occurrence of grain growth and shrinkage during MD is consistent with our *in situ* TEM observations. The change of grain 2 is relatively small, confirming the common occurrence of non-uniform grain deformation in polycrystalline materials, as revealed in the experimental data of grain size statistics in

Figure 7.4a. Incidentally, our MD simulations further reveal that coupled GB sliding and migration are primarily caused by glide of GB disconnections (to be discussed later), instead of less frequent dislocation emission and absorption at GBs that mainly serve to accommodate local deformation incompatibilities during GB migration.

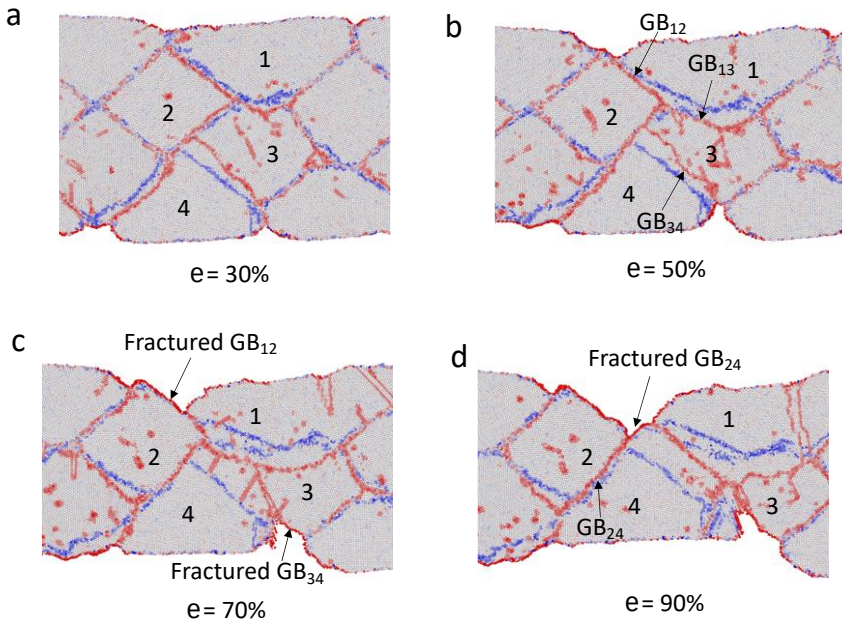

Figure 7.5 MD simulation results of large plastic deformation and intergranular fracture during uniaxial tension of a nc Al thin film. (a-d) MD snapshots at different applied tensile strains ε from 30% to 90%, showing the drastic grain growth and shrinkage through large GB migration and sliding, as well as intergranular fracture via sliding-off of GBs. The same atom coloring scheme is used as in Figure 7.4c-f.

The MD simulations further reveal the highly localized plastic deformation and final intergranular fracture in the nc Al thin film at large applied tensile strains. From a series of MD snapshots in Figure 7.5, it is seen that plastic deformation becomes increasingly localized in the region containing grains 1-4. Large migration of GB_{13} and GB_{34} causes drastic growth of grains 1 and 4 and shrinkage of grain 3, eventually resulting in direct contact between grains 1 and 4. Meanwhile, large sliding of GB_{12} and GB_{34} occurs, leading

to growth of surface grooves associated with GB_{12} and GB_{34} (Figure 7.5b). The increased stress concentrations in these deep grooves cause the continued slide-off of GB_{12} and GB_{34}, thereby producing the fractured surfaces of GB_{12} and GB_{34} (Figure 7.5c). As the sliding-off of GB_{12} completes, the local fracture process switches to the sliding-off of GB_{34}. These processes clearly demonstrate a predominant intergranular fracture mode through large GB sliding, which is consistent with that observed during our *in situ* TEM testing of Al thin film samples.

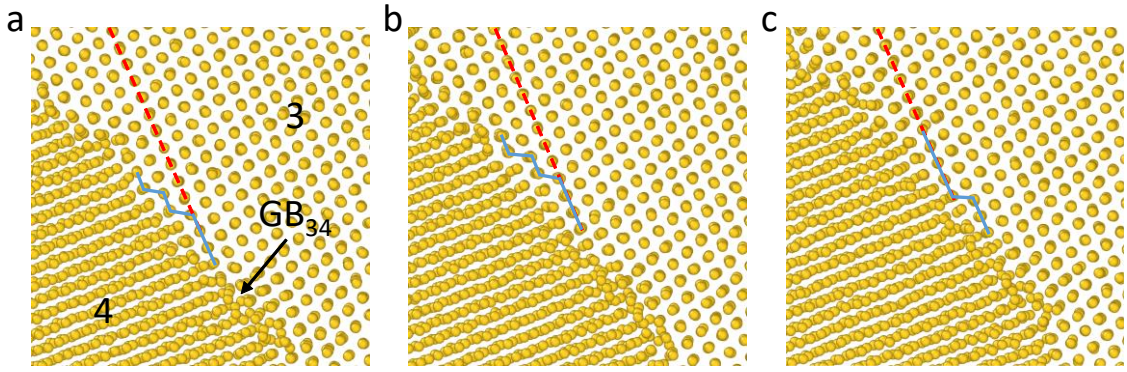

Figure 7.6 MD results showing atomic-scale processes of migration of a general GB of mixed tilt and twist type in nc Al. (a-c) MD snapshots of migration of GB_{34} toward grain 3 through the glide of GB steps (indicated by blue lines), signaling the glide of corresponding GB disconnections. This GB corresponds to the boxed region of GB_{34} in Fig 7.4c at 10% strain. The atomic configuration is viewed along the $\langle 110 \rangle$ direction of grain 3. The red dashed line indicates the edge-on $\{111\}$ plane in grain 3.

The general GBs in the current study are mostly of mixed tilt and twist type with high angle misorientation. As such, it is difficult to resolve the exact atomic mechanisms of GB migration through *in situ* TEM observations. However, our MD simulations offer atomistic insight into GB migration. Figure 7.6 shows a representative example of stress-driven migration of a general GB between grain 3 and 4, denoted as GB_{34}, at the applied tensile strain ε = 10%; this GB segment is boxed in Figure 7.4c. The atomic structure of GB_{34} is

viewed along the ⟨110⟩ direction of grain 3, thereby showing a clear image of projected ⟨110⟩ atomic columns inside this grain. Since GB_{34} is of mixed tilt and twist type, grain 4 is not aligned with a specific crystallographic direction, such that the projected atomic columns overlap with each other in grain 4. The contrast of projected atomic columns in the adjoining grain 3 and 4 facilitates our tracking of the atomically sharp GB_{34} during its migration. Note that GB_{34} consists of atomic-sized boundary steps on the edge-on {111} planes in grain 3. By comparing local GB steps (marked by blue lines) relative to a reference {111} plane marked by the red dashed line, it is seen from Figure 7.6a-c that migration of GB_{34} towards grain 3 occurs through glide of GB steps. In general, a GB disconnection consists of both a GB step and a GB dislocation component. For a GB of mixed tilt and twist type, the observed gliding of a GB step signals the movement of a corresponding GB disconnection, while the GB dislocation component cannot be easily visualized due to complex lattice geometry but usually moves simultaneously with the GB step. Hence, MD results in Figure 7.6 complement our *in situ* TEM observations by revealing the representative atomic-scale processes of coupled GB sliding and migration through gliding of disconnections on a general GB in nc Al.

Despite differences in strain rate, grain morphology and film dimensions between MD simulations and experiments, qualitative agreement was found in the GB migration and fracture behavior, which was found most pronounced in areas with localized necking deformation. Both simulations and experimental results point to GB migration leading to grain growth as a dominant deformation mechanism. The MD simulations suggest that dislocation emission and absorption are not a major contributor to the migration and sliding but do play a role in accommodating deformation incompatibility at GBs. This is consistent

with experimental findings that showed *in situ* evidence of bend contours (suggestive of dislocation activity) and post-mortem observations of dislocation structures, but that GB migration was also observed to occur separate from dislocation evidence. Both simulations and experiments also show that GB migration begins early in deformation and is further promoted by increased stress due to localized deformation (necking or surface grooves). As with the experimental results, the simulations also show inhomogeneous grain growth with certain grains growing at the expense of other. Additionally, MD simulations reveal the atomic-scale processes of coupled GB sliding and migration through gliding of GB disconnections. Finally, large GB sliding is observed by both simulations and experiments (especially near fracture surface) and in both cases, leading to intergranular fracture as the observed failure mechanism.

7.5 Summary

Using *in situ* TEM MEMS-based straining combined with MD simulations, we have studied deformation-induced grain growth while investigating how the local stress imposed by necking promotes GB migration. The results of these experiments indicate that GB migration is primarily stress-induced, as opposed to thermally-driven GB migration during high temperature annealing or creep. The local increase in stress (either due to necking or a crack tip) drives faster GB migration. Measured GB migration speeds ranged from 0.2 – 0.7 nm s^{-1} when the applied tensile stresses were close to the ultimate tensile strength of 450 MPa, increased up to 2.5 nm s^{-1} for grains within the necked region where the local tensile stresses were elevated to around 630 MPa, and even rose to 6 nm s^{-1} for GB migration that occurred ahead of crack tip. MD simulations utilized a novel coloring scheme to easily track GB motion over time, which yielded qualitative agreement with

experimental observations that significant GB migration leads to grain growth. MD simulations further complement *in situ* experiments by uncovering the underlying atomic processes of grain growth and GB migration that are not directly visible through TEM. Altogether, these results underscore the important role of stress-driven grain growth in plastically deforming nanocrystalline metals, particularly in regions with large localized deformation.

CHAPTER 8. PLASTIC DEFORMATION KINETICS IN FCC NANOCRYSTALLINE METALS

8.1 Introduction

Many inelastic deformation processes in metallic systems, including dislocation glide, deformation twining, phase transformation, grain boundary sliding, occur by stress-driven, thermally-activated atomic rearrangement. The rate of a stress-driven, thermally-activated process can be estimated based on transition-state theory (TST) [134],

$$v = v_0 \exp\left(-\frac{\Delta G(\sigma, T)}{k_B T}\right) \tag{8.1}$$

where v_0 is the trial frequency, k_B is the Boltzmann constant, ΔG is the activation free energy of the transition state, σ is the applied stress, T is the temperature. The trial frequency v_0 is on the order of 10^{11} s^{-1}, as dictated by atomic vibration. In order for a unit process observable in a typical laboratory strain rate such as 10^{-2} s^{-1}, the activation energy needs to be around $30k_BT$, which is about 0.7 eV at room temperature. Hence, the activation energy, as a function of stress, is an important quantity that determines the kinetic rate within the transition-state theory. To a first approximation, the stress-dependent activation energy can be calculated from the nudged elastic band (NEB) method [132], as to be discussed in Section 8.3.1. The NEB method bridges the unit defect process to the macroscopic strain rate sensitivity that characterizes plastic deformation kinetics.

On the experimental side, stress relaxation and measurements of associated activation volume represent one of the most effective ways of elucidating the strength/rate-controlling mechanisms governing the plastic deformation kinetics of polycrystalline metals and alloys. This approach has been well established in the study of conventional coarse-grained materials [135, 136], and it has been recently extended to study ultrafine-grained (ufg) and nanocrystalline (nc) metals [129, 137, 138]. However, the currently available results of activation volumes for ufg and nc metals are limited and, more importantly, puzzling, as to be discussed below.

8.2 *In Situ* TEM Measurements of Activation Volume

This study investigates the plastic deformation kinetics of two different metal thin films: 200-nm thick nc Al and 100-nm thick ufg Au. Both specimens were fabricated following similar procedures involving optical lithography, electron beam evaporation of high purity Au or Al onto a Si substrate and a lift-off technique to reveal dog-bone shaped specimens with gauge dimensions of width 1.5 μm and length 20 μm. The nc Al specimens have an average grain size of 57 nm and a random out-of-plane texture while the Au specimens have an average grain size of 150 nm and exhibit <111> out-of-plane texturing. Bright-field TEM images of undeformed specimens for Al and Au are shown in Figure 8.1, respectively.

The MEMS device is used to perform both *in situ* monotonic and stress-relaxation experiments. By performing consecutive stress-relaxations segments, the true activation volume V^* is determined using the equation below

$$V^* = \sqrt{3}kT \frac{\ln\left(\dot{\varepsilon}_{i2} / \dot{\varepsilon}_{f1}\right)}{\Delta\sigma_{12}} \tag{8.2}$$

where k is Boltzmann's constant, T is temperature, $\Delta\sigma_{12}$ is the stress increase during the elastic reloading, $\dot{\varepsilon}_{i2}$ is the initial plastic strain rate of the second relaxation and $\dot{\varepsilon}_{f1}$ is the final plastic strain rate of the first relaxation segment. The plastic strain rate $\dot{\varepsilon}_p$ is determined by

$$\dot{\varepsilon}_p = -\dot{\sigma} / M \tag{8.3}$$

where $\dot{\sigma}$ is stress rate obtained by fitting the stress relaxation data with logarithmic fit and M is the machine-specimen modulus. By combining Eq. (8.2) and Eq. (8.3), the true activation volume V^* can be obtained from

$$V^* = \sqrt{3}kT \frac{\ln\left(\dot{\sigma}_{i2} / \dot{\sigma}_{f1}\right)}{\Delta\sigma_{12}} \tag{8.4}$$

Using Eq. (8.4) eliminates the dependency of V^* on the strain rate and instead implies that the accuracy of V^* depends on the stress rate, which is independent of gauge length and is more accurately determined using this technique. The accuracy of the determined stress rate depends on the signal-to-noise ratio (SNR) of the measurement. Previous work has shown that a SNR > 5 requires logarithmic fits with R^2 > 0.9, which is used as a criterion for accurate V^* measurements. The apparent activation volume V_a can also be obtained by fitting the stress-relaxation data with a logarithmic variation in time *t*, following

$$\Delta\sigma = \frac{\sqrt{3}kT \ln\left(1 + t / c_r\right)}{V_a} \tag{8.5}$$

where $\Delta\sigma$ is the stress drop, and c_r and V_a are the fitting parameters. The above equation can be rearranged to solve for the apparent activation volume V_a, which is considered because it avoids the implicit assumption of constant dislocation density ρ_m that is required in the true activation volume derivation. In this work, we determine both the apparent and true activation volumes, however, we primarily focus on true activation volume measurements as it is more characteristic of the rate-controlling deformation mechanisms and directly represents the dislocation velocity dependence on stress.

Figure 8.1 shows V^* measurements for relaxation segments of different Au and Al specimens with different sample thickness. The measured activation volume for Au is ranged from $5b^3$ to $25b^3$. For the Al, one group of activation volumes are larger than $15b^3$ (with b being the Burgers vector length), while another group are between $1b^3$ to $10b^3$. This puzzle further motivates us to determine the rate-limiting process by the atomistic nudged elastic band calculations.

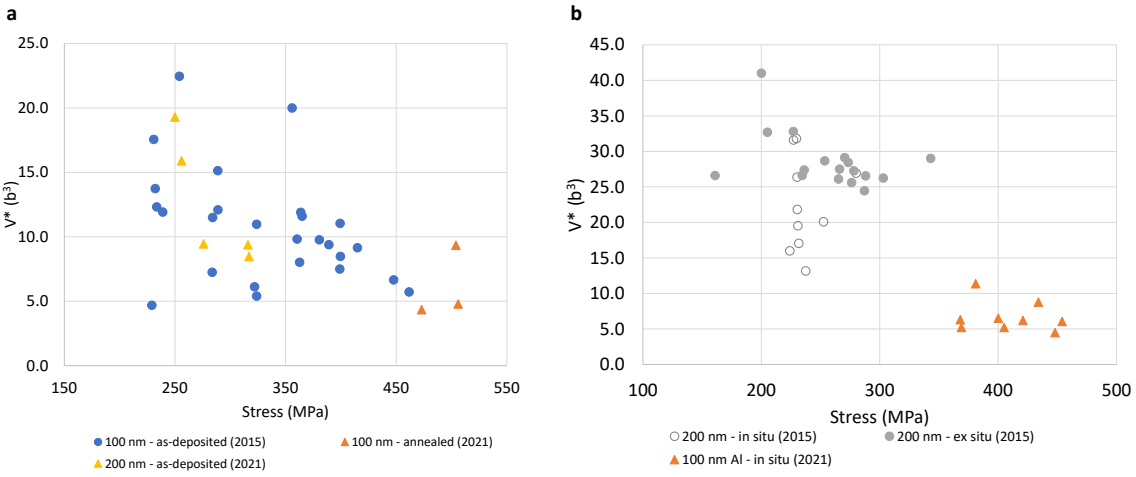

Figure 8.1 True activation volume measurements for Au and Al. (a) Au specimens with thickness of 100 nm and 200 nm. (b) Al specimens with thickness of 100 nm and 200 nm.

8.3 Atomistic Modeling

8.3.1 Nudged Elastic Band (NEB) Method

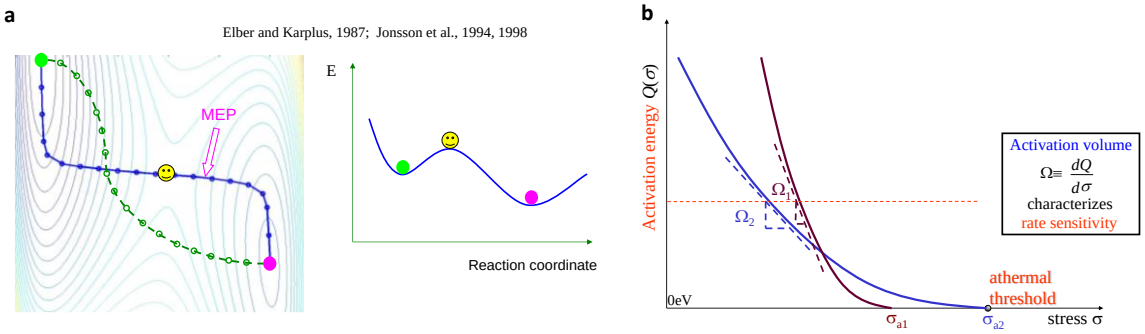

Figure 8.2 Schematic illustration of nudged elastic band method and activation. (a) An illustration of the NEB method and MEP in a model system. (b) Definition of activation volume.

The NEB method is a chain-of-states approach to find the minimum energy path (MEP) on the potential energy surface (PES). In the coordinate configuration space of N atoms, the potential energy is a function of $3N$ degrees of freedom of atoms; that is each point in the PES corresponds to one configuration of atoms in the system, as shown in Figure 8.1. In general, there are local minimum, local maximum and saddle point on the PES. The MEP is the lowest energy path connecting two neighboring local minimum configurations. The maximum on the MEP is the saddle point which gives the activation energy barrier, that is the ΔG in Eq. (8.1). The derivative of activation energy with respect to stress gives us the activation volume, which characterizes the strain-rate sensitivity as shown in Figure 8.2.

In an NEB calculation, one should first obtain the initial and final configurations in two neighboring basins on the PES by using energy minimization. Then, multiple replicas are generated by linear interpolation of the coordinate of each atom between the initial and final states. Every two adjacent replicas are connected by a spring mimicking an elastic band of beads and spring. With proper relaxation, the internal replicas will converge to the MEP as shown in Figure 8.2a, while the initial state and final state are kept fixed. Let us denote $\mathbf{R}_i$ as the atomic coordinate of the replica *i* and estimate the unit tangent at each replica as $\mathbf{t}_i$. The configuration force (3*N* dimensional vector) contains both the perpendicular component of the potential force and the parallel component of the spring force with respect to the tangent vector.

$$\mathbf{F}_i = -\nabla E\left(\mathbf{R}_i\right)_\perp + \mathbf{F}_i^{\text{spring}}{}_\parallel \tag{8.6}$$

where $\nabla E\left(\mathbf{R}_i\right)$ is the gradient of the potential energy with respect to the atomic coordinate for replica *i*. In the above equation, $\mathbf{F}_i^{\text{spring}}$ is the spring force acting on replica *i* with a spring constant of *k*.

$$\mathbf{F}_i^{\text{spring}} = k\left(\left|\mathbf{R}_{i+1} - \mathbf{R}_i\right| - \left|\mathbf{R}_i - \mathbf{R}_{i-1}\right|\right)\mathbf{t}_i \tag{8.7}$$

Henkelman [139] also discussed in details how to estimate the tangent vector, force and other techniques to find the saddle point. The converged MEP is usually plotted as the energy versus the reaction coordinate. The reaction coordinate is defined as the relative arc length in the 3*N* hyperspace. For each replica, the arc length to the initial configuration is defined as,

$$l \equiv \int_{\mathbf{R}_0^{3N}}^{\mathbf{R}_i^{3N}} \sqrt{d\mathbf{R}^{3N} \cdot d\mathbf{R}^{3N}} \tag{8.8}$$

The normalized reaction coordinate *s* can be calculated according to $s = l / l_0$, where l_0 is the hyperspace arc length between the initial and final state.

The NEB method presented above is effective in finding the MEP of a highly localized activation process where the initial state and final state are relatively close to each other on the hyperspace. However, this method is inefficient to sample the MEP for extend defect nucleation such as dislocation nucleation, where the final local minimum is far away from the initial state. In order to capture the long MEP associated with extended defects, a large number of replicas are needed. This issue is more pronounced at the higher stress level, where the saddle point is near the initial configuration. To improve this computational inefficacy, a free-end NEB (FENEB) method has been developed by Zhu and coworkers [140]. The idea of the FENEB method is to reduce the MEP length. This is realized by removing the constraint of the final state as the local minimum. The final state is allowed to move freely on an energy iso-surface close to the initial state. In addition to the perpendicular component of potential force, a spring force is added to the last replica to keep the energy close to the energy of the initial state. Using this FENEB method, one could use much fewer replica to model extended defect such as dislocation nucleation, where the last replica is kept close to the saddle point and initial state thus significantly improving the computational efficiency.

For our 3D atomistic simulations, we mainly focus on the dislocation nucleation from surfaces or grain boundaries. We first set up a bi-crystal containing a tilt symmetrical grain

boundary with the tilt axis of [111] and grain boundary plane of [213], as shown in Figure 8.3. This [111] tilt grain boundary is a representative grain boundary in the [111]-textured Au sample as observed in the experiment. The bi-crystal has the dimension of 16.3 nm × 32.8 nm × 20.6 nm and contains 226,260 Au atoms. The periodic boundary condition is imposed in the X-[415] direction. A partial dislocation is embedded in grain #2 through molecular dynamics simulations of uniaxial tension along X axis. We use the defect-free configuration as the initial state and the configuration with a fully-developed partial dislocation as the final state in a fixed-end NEB calculation. After this fixed-end NEB calculation, we locate the replica whose energy is close to the energy of the first replica, and use that configuration as the final configuration in an FENEB calculation. Then a series of FENEB simulations with different applied strains are calculated. We also simulate a similar process of dislocation nucleation from the free surface in Au and Al.

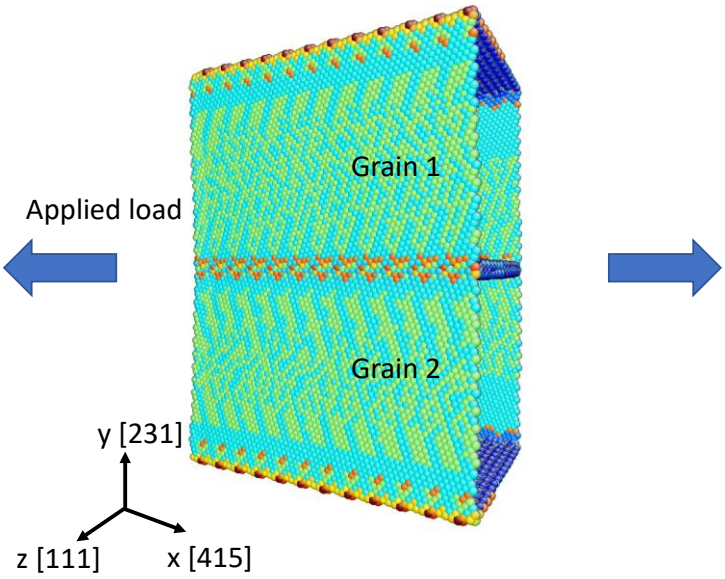

Figure 8.3 Atomistic simulation setup for grain boundary dislocation nucleation.

8.3.2 Displacive Process – Partial Dislocation Nucleation

We first examine the dislocation nucleation process from grain boundaries in Au. Our FENEB results in Figure 8.4 show partial dislocation nucleation from the intersection of the tilt grain boundary and free surface. Figure 8.4a shows the converged MEPs of dislocation nucleation, when the free-end energy has the same energy as the initial state. The initial dislocation-free configuration is shown in Figure 8.4b. The configuration in Figure 8.4c contains a grain boundary defect that facilitates the subsequent nucleation of a dislocation loop. The energy of this particular configuration is relatively insensitive to resolved shear stress since it is a local grain boundary defect and does not produce significant plastic deformation. The configuration in Figure 8.4e is the saddle-point state, where two adjacent patches of atoms are sheared relative to each other to form the partial dislocation core. This saddle-point state gives the corresponding activation energy of dislocation nucleation. We also calculate the stress-dependent activation energy and the results will be discussed later.

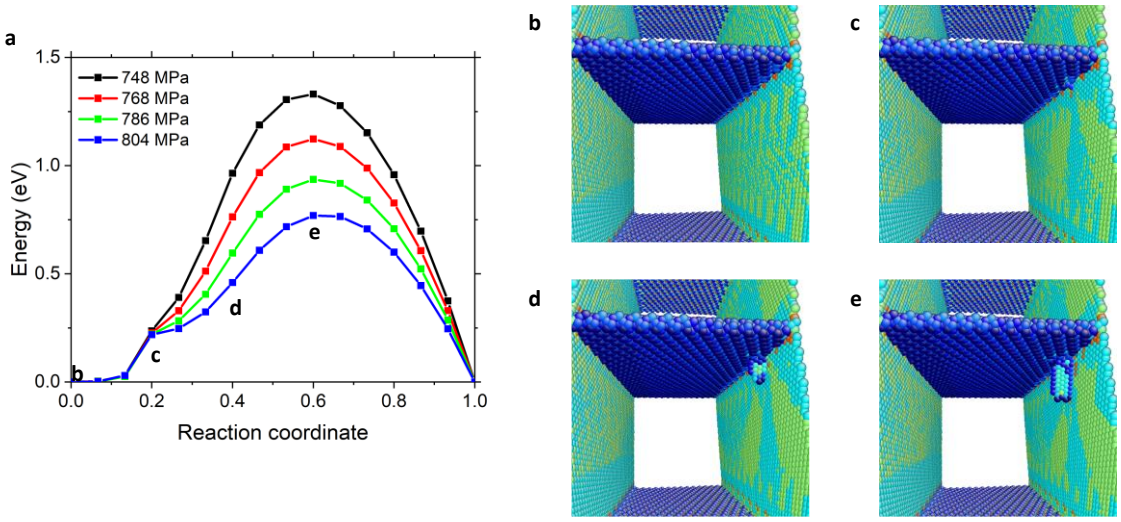

Figure 8.4 FENEB results of the partial dislocation nucleation at the grain boundary and free surface corner in Au. (a) Stress dependent minimum energy path for different resolved shear stresses. (b-e) Atomistic configuration on the MEP of 804 MPa resolved shear stress, (e) correspond to the saddle point.

We perform similar FENEB simulations for dislocation nucleation from free surfaces in Au. Figure 8.5 shows partial dislocation nucleation from free surface. Figure 8.5a shows the converged MEPs of dislocation nucleation. Notice that there is no metastable state of local defect creation, as shown in Figure 8.4c. As the partial dislocation is emitted from the free surface, only a surface step is created and no other stress-insensitive defect is needed. The configuration in Figure 8.5e is the saddle point, where two adjacent patches of atoms are sheared relative to each other to form the partial dislocation core. The shape of the dislocation loop is close to a quarter of a circle, due to a symmetrical constraint from two free surfaces, while the dislocation loop nucleated from the grain boundary is elongated. We also calculate stress-dependent activation energy, as shown in Figure 8.6.

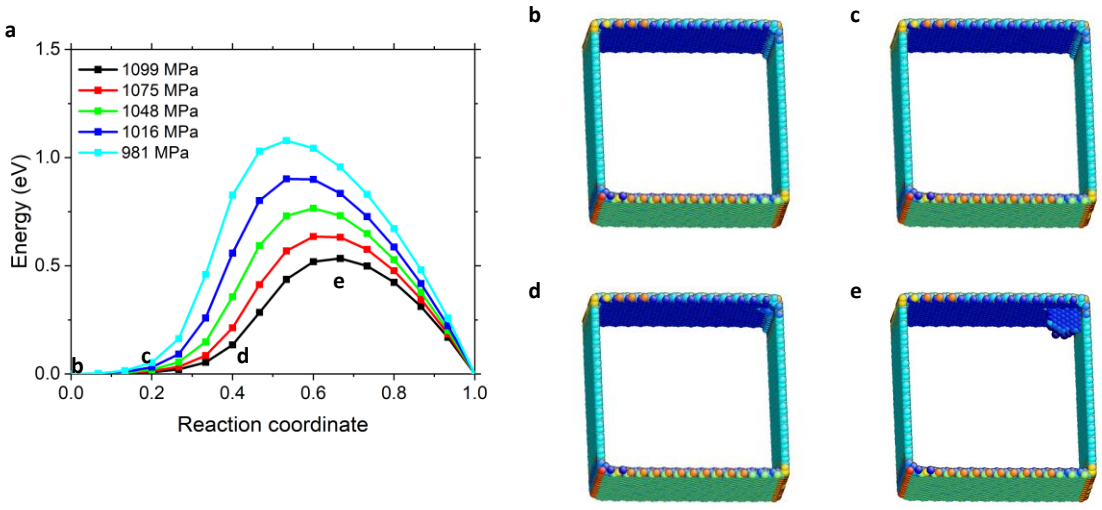

Figure 8.5 FENEB results of the partial dislocation nucleation at free-surface corners in Au. (a) Stress dependent minimum energy path for different resolved shear stresses. (b-e) Atomistic configuration on the MEP of 1099 MPa resolved shear stress, (e) correspond to the saddle point.

We compare the activation energy versus the resolved shear stresses in Figure 8.6. The derivative of the energy barrier with respect to resolved shear stress gives the activation volume, which is closely related to the number of atoms in the dislocation loop at its saddle-point state. As shown in Figure 8.6, the activation volume of surface nucleation is about $31b^3$, while the activation volume of grain boundary nucleation is higher, around $52b^3$. This can be understood as follows. Similar activation processes usually have close zero-stress activation energies. If we approximate the activation curves as a straight line, then the activation volume can be estimated as $V^* = \frac{G_0}{\tau_a}$, where G_0 is the zero-stress activation energy, τ_a is the athermal stress of this process. Therefore, the heterogeneous nucleation with a lower athermal stress needs a higher activation volume, as shown in Figure 8.6. Thus, the grain boundary nucleation has a higher activation volume than surface

nucleation. However, the activation volumes of both mechanisms are higher than the experimentally measured activation volumes. To understand this discrepancy, we further explore other possible deformation mechanisms. Our preliminary results indicate that the displacive deformation mechanisms such as, disconnection nucleation, slip transmission across grain boundary, and cross slip usually have similar activation volumes larger than $10b^3$.

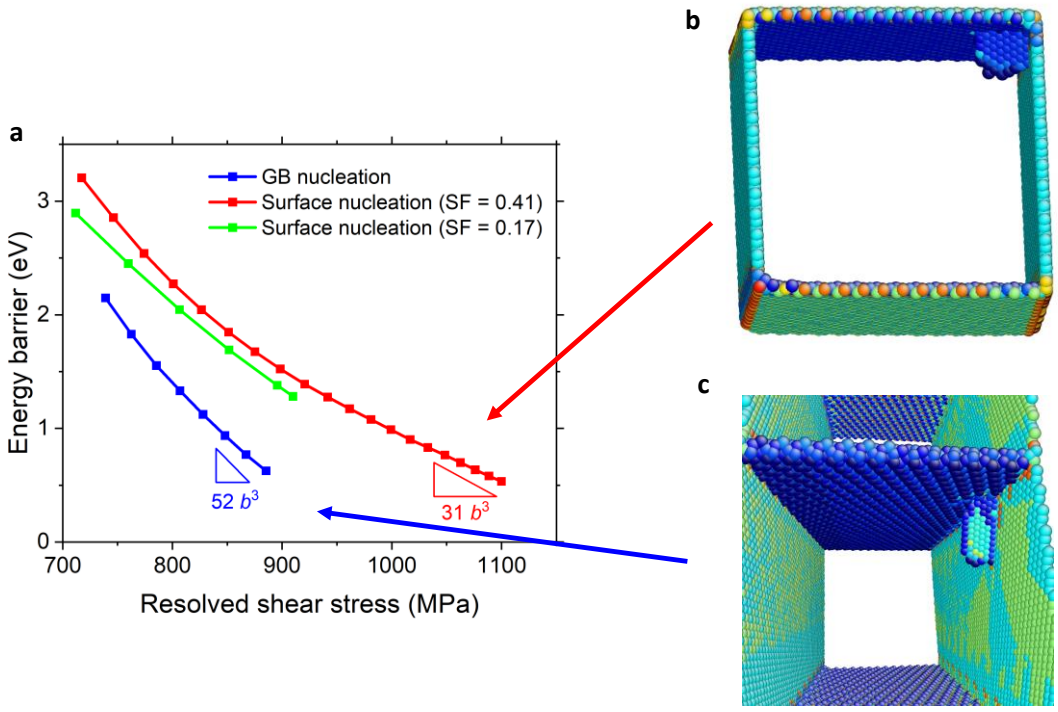

Figure 8.6 Activation volume of partial dislocation nucleation in Au. (a) Stress-dependent activation energy of partial dislocation nucleation in Au. The negative of the slope of the curve is defined as activation volume. (b) Saddle-point configuration of surface nucleation when the activation energy is around 0.7 eV. (c) Saddle-point configuration of grain boundary (GB) nucleation when the activation energy is around 0.7 eV.

We also perform the FENEB calculations for Al with a similar setup. Al has a higher shear modulus than Au, and Al also has a higher ideal shear strength than Au [141]. The

high stacking fault energy of Al further increases the stress needed to nucleation a partial dislocation. Figure 8.7 shows the stress-dependent energy barrier of surface dislocation nucleation in Al. The corresponding activation volume of Al is $16b^3$, which is higher than $5b^3$ measured from 100 nm specimen and lower than $35b^3$ from 200 nm specimen.

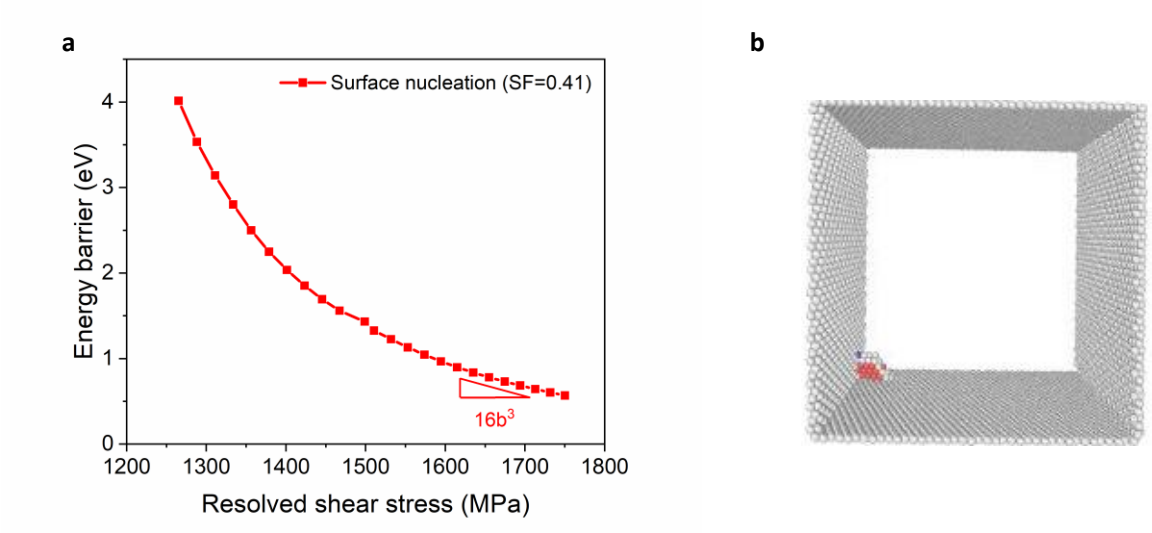

Figure 8.7 Activation volume of partial dislocation nucleation in Al. (a) Stress-dependent activation energy of partial dislocation nucleation in Al. The negative of the slope of the curves is defined as activation volume. (b) Saddle-point configuration of surface nucleation when the activation energy is around 0.7 eV.

8.3.3 Diffusive Process – Grain Boundary Dislocation Climb

To identify GB processes underlying the group of large activation volumes, our FENEB calculations for various displacive processes associated with the motion, absorption, desorption, transmission of dislocations and disconnections at Au and Al GBs give the activation volumes larger than $20b^3$. To identify GB processes underlying the group of small activation volumes less than $10b^3$, it has been suggested that they might correspond to either shearing of a patch of GB atoms or atomic diffusion [129, 137, 138].

However, our FENEB calculations indicate that neither process could give activation volumes in the range of $1b^3$ to $10b^3$. This is because shearing of a patch of GB atoms gives large activation volumes greater than $20b^3$, while atomic diffusion gives small activation volumes on the order of $0.1b^3$.

To solve the aforementioned puzzle, we made a hypothesis that the diffusive process associated with the non-conservative motion of GB dislocations/disconnections, such as their climb, in ultrafine-grained and nanocrystalline metals could be the controlling process giving activation volume in the range of $1b^3$ to $10b^3$. Our recent study provides direct evidence of GB dislocation climb under applied high stresses and room temperature from atomic resolution in situ HRTEM observation, as shown in Figure 8.8, where multiple grain boundary dislocations climb to accommodate the applied bending deformation. Inspired by this HRTEM result, we performed FENEB calculations of climb of a GB dislocation through double-jog formation and migration at the core of this GB dislocation, involving a series of unit processes of insertion of vacancies (equivalent to the removal of atoms) at the dislocation jogs.

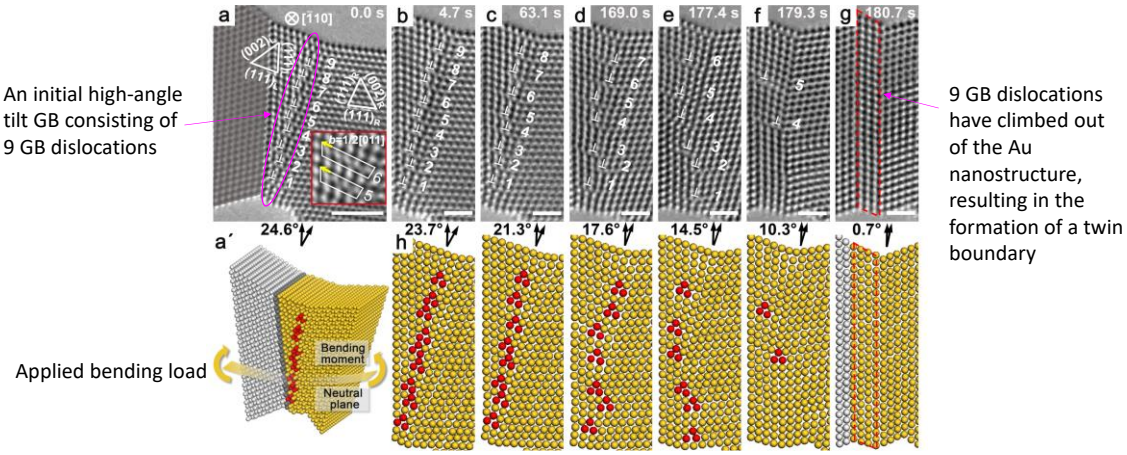

Figure 8.8 GB dislocation climb mediated by diffusive processes of point defects at the dislocation core.

Figure 8.9 shows the results of climb of a grain boundary dislocation through double-jog nucleation and migration. The grain boundary shown in Figure 8.9 is a [110] ∑3 tilt twin boundary. A pre-existing dislocation is embedded by introducing a small misorientation between the two grains. The minimum energy path is calculated by adding vacancies to the dislocation core. After three vacancies are added to the dislocation core, a pair of double-jogs is fully developed. Figure 8.9e shows the corresponding saddle-point configuration with three atoms removed at the dislocation core. We also calculated the stress-dependent energy barriers and obtained the corresponding activation volume of $1.5b^3$, as shown in Figure 8.10b.

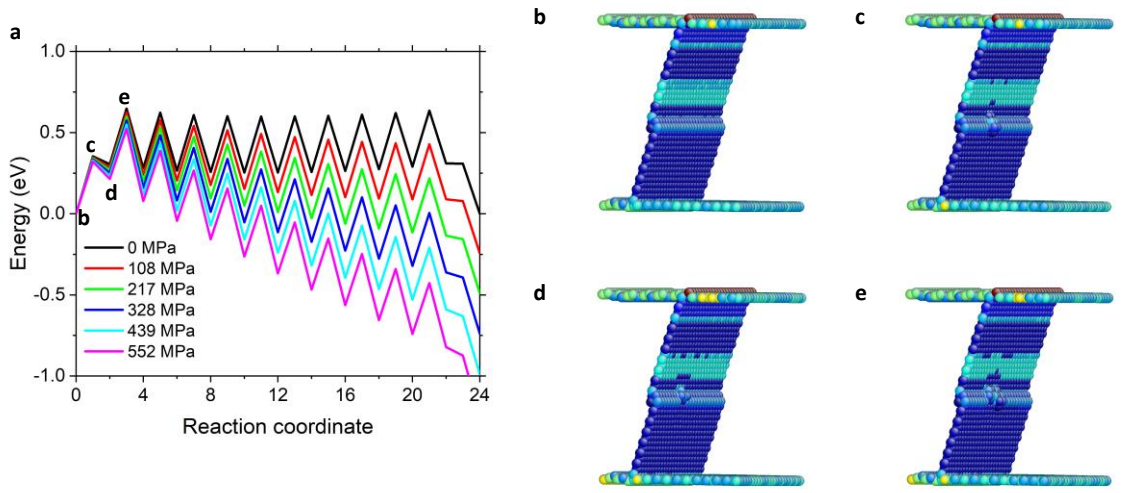

Figure 8.9 MEP of the grain boundary climb in Au. (a) Stress dependent minimum energy path for different resolved shear stresses. (b-e) Atomistic configuration on the MEP of 552 MPa resolved shear stress, (c) correspond to the saddle point.

The above diffusive process associated with GB dislocation climb was traditionally considered to prevail during creep deformation at high temperatures and low stresses. However, our FENEB calculations of double-jog motion give activation volumes in the range of $1b^3$ to $10b^3$ that match experimental measurements for ultrafine-grained and nanocrystalline metals from our and other groups [129, 137, 138].

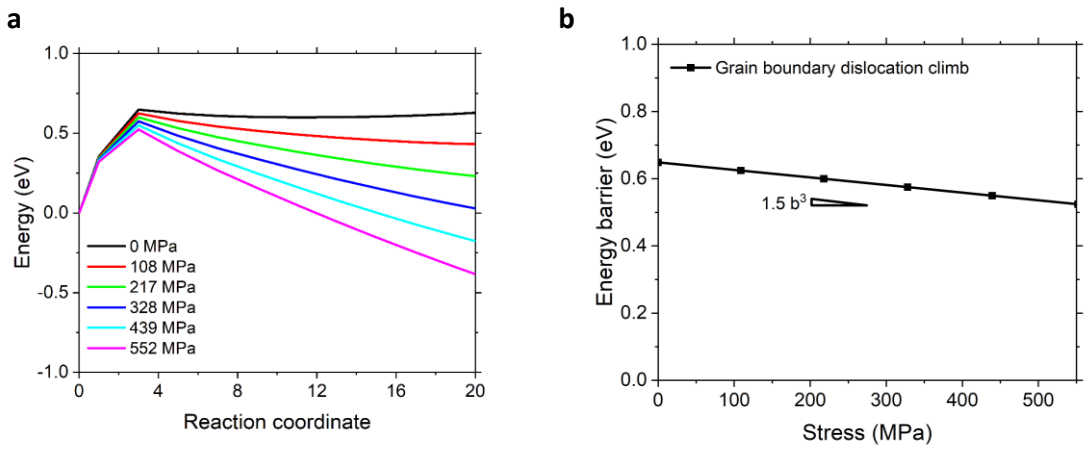

Figure 8.10 MEP and activation volume of grain boundary climb in Au. (a) Stress dependent minimum energy paths for different stresses. (b) Energy barrier versus applied stress, giving the corresponding activation volume of $1.5b^3$.

8.4 Discussion

To understand the above results, we note that Conrad [137] has developed an illuminating theoretical framework on the grain size dependence of activation volume, which gives a remarkable scaling relation similar to the classical Hall-Petch relationship for the grain size dependence of yield strength. To account for the grain size effect, Conrad used a dislocation pile-up model to connect the applied stress to a polycrystal with the local stress triggering a strength/rate-controlling process at the grain boundary (GB). He showed that the following Hall-Petch-type relation [137]

$$\frac{1}{V*} = \frac{1}{V_0^*} + \frac{M^2 \mu b}{V_{GB}^* K_{GB} d^{1/2}} \tag{8.9}$$

where $V*$ denotes the measured activation volume of a polycrystal; V_0^* represents the activation volume of an intragranular process such as the stress-driven, thermally activated cutting of forest dislocations inside grains; V_{GB}^* represents the activation volume of an

intergranular process associated with GB sliding. In Eq. (8.9), M is the Taylor factor, μ is the shear modulus, b is the Burgers vector length, K_{GB} is the same Hall-Petch coefficient in the Hall-Petch relation of grain size-dependent yield strength and it is known to be dictated by the critical local stress at the GB for triggering the strength/rate-controlling process associated with GB deformation. The above Hall-Petch-type relation of grain size-dependent activation volume in Eq. (8.9) has been verified by previous experimental studies such as nanotwinned and nanocrystalline Cu [142]. However, the measured activation volumes of ultra-fine-grained Al and Au, as discussed earlier, fall into two different characteristic groups. Namely, one group of activation volumes are larger than $15b^3$ and mostly between $20b^3$ to $30b^3$ (e.g., ultrafine-grained Al with the average grain size of 74 nm), while another group of activation volumes are between $1b^3$ to $10b^3$ (e.g., ultrafine-grained Al with the average grain size of 47 nm). These differences cannot be simply attributed to the effect of grain sizes that only have relatively small changes in our ultra-fine-grained samples

To resolve the above puzzle and based on our FENEB calculations of activation volumes of GB-mediated processes, we generalize the Conrad's relation in Eq. (8.9) to incorporate two competing rate-controlling processes at the GB.

$$\frac{1}{V*} = \frac{1}{V_0^*} + \frac{M^2 \mu b}{V_{\text{GB-I}}^* K_{\text{GB-I}} d^{1/2}} + \frac{M^2 \mu b}{V_{\text{GB-II}}^* K_{\text{GB-II}} d^{1/2}} \tag{8.10}$$

where $V_{\text{GB-I}}^*$ and $V_{\text{GB-II}}^*$ represent the activation volume of two different types of intergranular process, respectively; $K_{\text{GB-I}}$ and $K_{\text{GB-II}}$ are the respective Hall-Petch coefficient that depends on the critical local stress at the GB for triggering the respective strength/rate-

controlling process associated with GB deformation. For ultrafine-grained and nanocrystalline samples with the same grain size, the change of operating flow stresses (along with the corresponding change of strain rate) can lead to activation of the rate/strength-controlling processes with different activation volumes. Equation (8.10) can capture this effect because $K_{\text{GB-I}}$ and $K_{\text{GB-II}}$ have characteristically different values due to their dependence on the critical local stress to trigger the corresponding GB process.

8.5 Summary

Our *in situ* TEM/MEMS-based measurements and FENEB calculations have revealed two characteristic groups of activation volume ($V^* > 15b^3$ and $1b^3 < V^* < 10b^3$), which signify an active competition between the displacive and diffusive types of rate-controlling GB mechanism in ultra-fine grained and nanocrystalline metals. The most important finding is that the diffusive type of rate-controlling GB mechanism can operate at room temperature in ultrafine-grained and nanocrystalline metals, due to their prevailing high stresses. This key finding is supported by in situ HRTEM observations.

CHAPTER 9. EXTRA HARDENING IN NANOGRAINED METAL COMPOSITES

9.1 Introduction

High-performance materials with high strength and ductility are desirable for promoting weight saving and energy efficiency, but may unavoidably suffer from harsh environment such as high loads and high temperatures [143-145]. The strengthening mechanisms in structural metals and alloys are built on a fundamental principle of hindering dislocation slip through the introduction of different types of obstacles, e.g., precipitates and grain boundaries [146]. However, these dislocation obstacles are energetically unfavorable that can be merged or recovered at elevated temperatures, leading to serious property degradation [147, 148]. Nanograined metals, for example, have been extensively investigated for high strength. However, they exhibit limited hardening ability and low thermal stability, bottlenecking the development and applications of this new materials family. The alloying approach by one [149] or multiple [150-152] elements has been proven effective to address the "strength-stability" trade-off limitations, but often comes with high cost and faces challenges of recyclability and sustainability [153]. Moreover, the alloying-based approach is principally difficult to change the brittle nature of nanocrystalline metals. A concurrent attainment of high strength, large tensile ductility and good thermal stability in metallic materials presently seems impossible.

Nanotwinning is a promising way of achieving a combined increase of strength and ductility [154, 155]. However, the applicability of the twinning strategy is limited to

specific metallic systems with low stacking-fault energy (e.g., Cu[156], Ag[157]), and may be insufficient for general applications. Incorporation of e second phases into metal matrix, forming the so-called metal matrix composite (MMC), provides a feasible approach for strengthening and stabilizing nanostructured metals [158-160]. Nevertheless, particles are generally agglomerated and distributed along grain boundaries, which aggravate stress concentrations leading to premature failure [159, 161]. Therefore, the tensile properties of nanocrystalline composites obtained so far have been disappointing, as the high tensile strength at the gigapascal level is inevitably accompanied by a lower ductility.

Here we report a general approach to overcome the above dilemma. Our design concept aims to create high-density intragranularly dispersed nanoparticles in nanograins for work hardening and microstructural stabilization. Numerous intragranular interfaces, with strong interfacial bonding, enable us not only to fully harness the strengthening effect of nanograins but also to activate multiple hardening mechanisms via dislocation-interface interactions leading to improved tensile ductility in nanograined metals. We show that this nanodispersion strategy is able to push the limit of strength-ductility trade-offs. We prepared the nanocrystalline copper (nc-Cu) and nickel (nc-Ni) matrix composites with ultra-dense (5.6×10^{23} m^{-3}) nanocarbon (2.6±1.2 nm) embedded inside nanograins. In contrast to traditional precipitate/dispersion strengthening strategies, we find that strong carbon-metal bonding is generated due to the defective nature of nanocarbon. Such strong interfacial bonding enables a unique two-stage hardening mechanism in nanograined metals, leading to enhanced tensile ductility. The dense nanocarbon dispersion also exerts a strong pinning effect on grain coarsening. The resultant nc-Cu composites (0.8 vol.% C) exhibit an exceptional combination of high tensile strength (1252±22 MPa), uniform

elongation (13.3±0.9%), and thermal stability (stable up to $0.72T_m$, where T_m is the melting temperature of Cu). The present "nanodispersion-in-nanograins" strategy is applicable for other metals, offering a new pathway to develop engineering materials with ultra-high strength and stability.

9.2 Experiment

We developed a process to achieve a uniformly dense dispersion of carbon nanoparticles in nanograined metals using reduced graphene oxide (RGO) flakes as a precursor. This process involves high-energy ball milling of metal nanoflakes with RGO flakes uniformly distributed on powder surfaces. The ball milling process is particularly effective for fragmenting RGO sheets and then mixing them with the metallic matrix, leading to a highly uniform dispersion of carbon nanoparticles inside the resultant nanocrystalline metals. Microstructure characterization by transmission electron microscopy (TEM) in Figure 1a-c indicates that as-synthesized nc-Cu is dispersed with carbon nanoparticles. The average grain size of nc-Cu is 63 ± 16 nm, Figure 1a. A high density of uniformly distributed carbon nanoparticles, up to a carbon concentration of 0.8 vol.%, is shown by a high-angle annular dark-field scanning transmission electron microscopy (HAADF-STEM) image in Figure 1b and electron energy loss spectroscopy (EELS) C imaging map in Figure 1c. The statistical histogram in Figure 1d indicates that the carbon nanoparticles have an average diameter of 2.6 ± 1.2 nm and a number fraction of ~92% inside grains as opposed to at grain boundaries. Because of their extremely small sizes, we refer to these carbon nanoparticles as ultra-nano-carbon (unc).

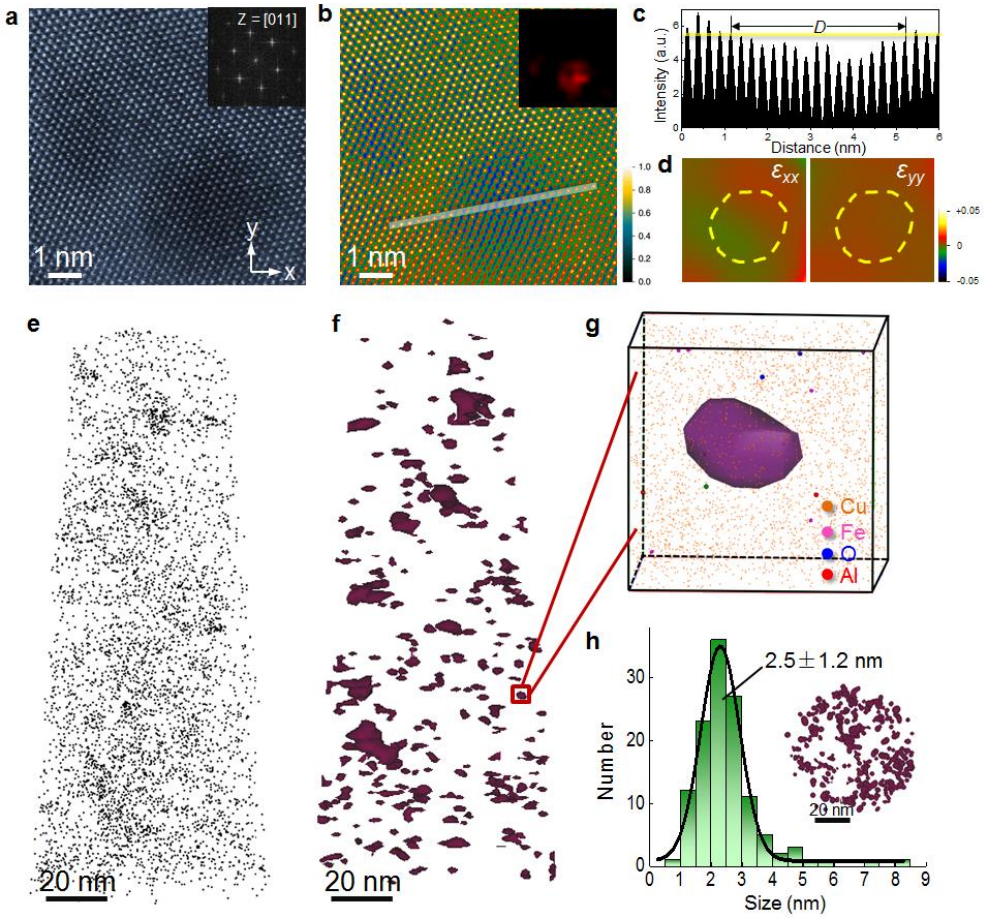

Figure 9.1 High-resolution TEM and APT characterization of nc-Cu composites (0.8 vol.% C). **a,** High-resolution HAADF-STEM image of the local atomic structure near unc particles taken along the [011] zone axis, as confirmed by the fast Fourier transformation (FFT) pattern in the inset. **b,** FFT-filtered image of **a.** Variation of color from black to yellow indicates intensities from low to high. Inset is the C imaging map for this region, showing that the low-intensity regions correspond to unc (due to the sensitivity of STEM image to atomic number Z). Inset shows two unc particles determined from their FFT image (see **C** for clarity). **c,** Intensity profile along the line in **b,** where the decrease of atom intensity in the unc-contained region is observed. The yellow line, which represents 90% of the averaged atom intensity of the Cu matrix, is taken as the cutoff intensity to estimate the diameter (4.1 nm) of the unc particle. **d,** Strain maps of ε_{xx} and ε_{yy} in the unc-contained region in **a**. The reference zero strain region is chosen from the dislocation free region (the upper-left corner of **a**). No obvious strain concentration is observed near the unc particle (marked by a dashed-line circle). **e-f,** Side-view APT images of C background and unc particles reconstructed with the threshold iso-composition surface below and above 0.25 at.% C, respectively. **g,** Enlarged region in **f**, showing a representative unc particle, along with atomic distributions of Cu (10% of Cu atoms are shown to reduce the background intensity) and other detected impurities, including Al, Fe and O. **h,** Statistical histograms showing the size distributions of unc particles (124 counts). The average particle size is 2.5

± 1.2 nm. Inset shows a top-view APT image of unc particles, indicating their nearly spherical shapes.

High-resolution TEM and atom probe tomography (APT) were used to characterize unc particles (Figure 9.1). The HAADF-STEM image in Figure 9.1a indicates that the Cu-C interface is coherent and no significant lattice distortion is present surrounding unc particles. The individual particle size can be determined under HAADF-STEM by combining the fast Fourier transformation (FFT) filtered image and the intensity variation of lattice fringes, Figure 9.1b and c. This is due to the sensitivity of STEM image to the atomic number (Z). Geometrical phase analysis (GPA) strain mapping further indicates the coherency of Cu-C interface as the atomic strains around C nanoparticles exhibit nearly uniform distributions, Figure 9.1d. APT measurements (Figure 9.1e-h) show that the number density of unc particles reaches a high mean value of ~5.6×10^{23} m^{-3}. Most unc particles are nearly spherical in shape and show random distributions, as revealed by the side-view (Figure 9.1f) and top-view APT images (inset of Figure 9.1h). The average size of unc particles from APT probe is 2.5 ± 1.2 nm (Figure 9.1h), in agreement with TEM measurements. Some trace amounts of impurities (i.e., Fe, Al, O) are detectable but no large clusters are found (Figure 9.1g); few carbon atoms are dissolved in Cu matrix (0.01 at.%, Figure 9.1e), due to a highly limited solubility of carbon in Cu.

We conducted *in situ* scanning electron microscope (SEM) micro-tensile tests to measure the mechanical properties of nc-Cu composites. As-prepared tensile samples have a sufficiently large number of Cu nanograins (~200) through the cross section (1.3 μm × 1.3 μm), thus minimizing the sample size effect on measured mechanical properties [162,

163]. Two methods, namely elastic strain calibration and dynamic image tracking, were employed to ensure the validity of strain measurement during tensile testing. Five samples of each type were used to ensure the reproducibility of measurements. Figure 9.2a shows the representative tensile stress-strain curves of pure nc-Cu (with the average grain size of 73 ± 16 nm), and two nc-Cu composites reinforced by 0.4 vol.% and 0.8 vol.% of unc particles, respectively. The reference nc-Cu has a yield strength (σ_y) of 660 ± 28 MPa, ultimate tensile strength (σ_u) of 776 ± 21 MPa, and elongation to failure (ε_f) of 6.3% ± 0.4%, which are consistent with those reported for bulk Cu samples with similar grain sizes [164]. For our nc-Cu composites, σ_y increases to 765 ± 32 MPa and 890 ± 21 MPa for the carbon volume fraction of 0.4% and 0.8%, respectively. Beyond plastic yielding, nc-Cu composites are further work-hardened until failure, giving the large σ_u of 995 ± 11 MPa and 1252 ± 22 MPa for 0.4 vol.% and 0.8 vol.% of unc, respectively, with the corresponding large uniform elongation (UE, ε_u) of 10.6% ± 0.8% and 13.3% ± 0.9%. The σ_y of 0.8 vol.% of this unc sample is ~92% higher than that predicted from the Hall-Petch relation for Cu [165], and its σ_u approaches the strength limit of nanocrystalline/nanotwinned Cu [166] when the grain size/twin spacing is extremely small (~10 nm) [167, 168].

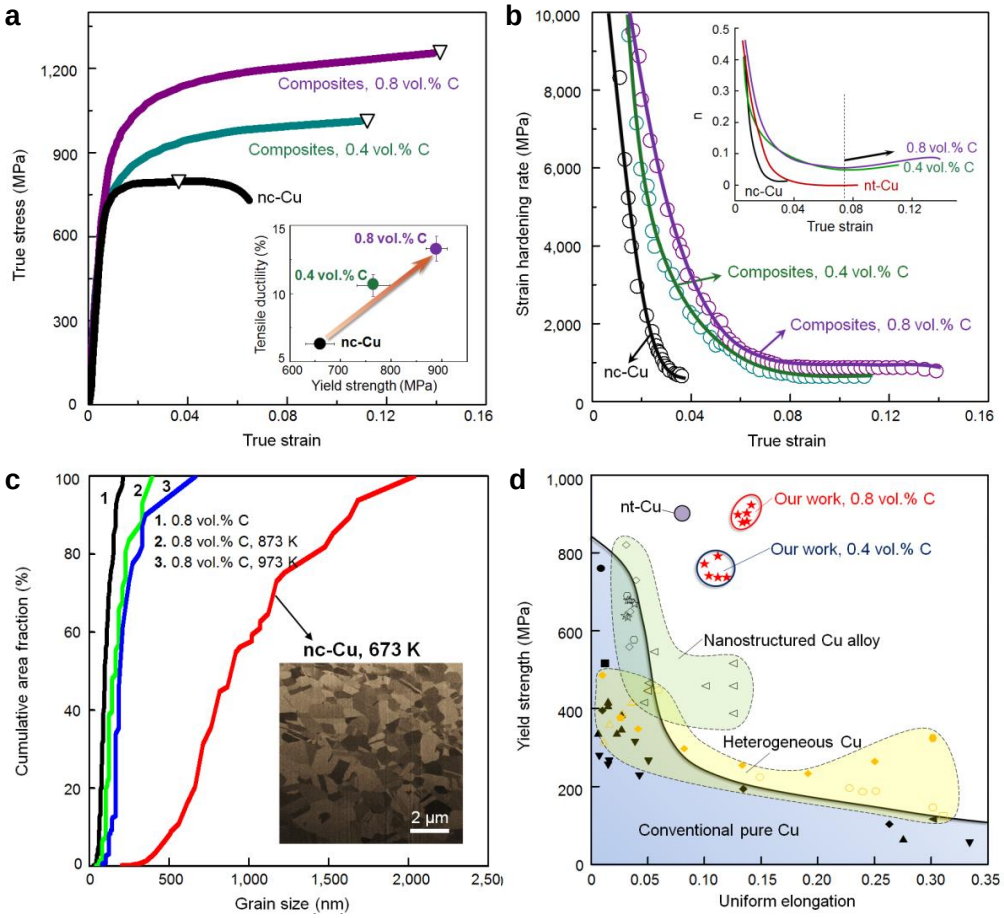

Figure 9.2 Tensile and thermal properties of nc-Cu composites. **a,** Representative tensile true stress-strain curves for pure nc-Cu and nc-Cu composites (with 0.4 vol.% and 0.8 vol.% C, respectively). All tensile tests were performed at a strain rate of 5×10^{-4} s^{-1} and room temperature. The strains at which necking occurs were identified during the *in situ* scanning electron microscopy (SEM) deformation processes and marked with an open triangle on each curve. The inset shows the remarkable improvement of yield strength and electrical conductivity of nc-Cu composites over pure nc-Cu. **b,** Experimentally measured strain hardening rate $d\sigma/d\varepsilon$ (with σ and ε being the true stress and true strain, respectively) for nc-Cu composites and nc-Cu. Inset shows the strain hardening exponent (n = $d(\ln\sigma)/d(\ln\varepsilon)$) as a function of strain. **c,** Thermal stability of nc-Cu composites: cumulative area fraction of grain size of the nc-Cu composite (0.8 vol.% C) annealed at various temperatures (873 K and 973 K) for 1h, in comparison with that of the reference nc-Cu annealed at 673 K for 1h. Inset shows pronounced grain growth in nc-Cu, as indicated by the ion-channeling cross-sectional image. In contrast, no grain growth was observed in nc-Cu composites after annealing at 973 K for 1h. **d,** Yield strength versus uniform elongation of nc-Cu composites as compared with those of other Cu-based materials, including heterogeneous Cu, nanostructured Cu alloys and nanotwinned (nt) Cu. Superior properties

are observed for nc-Cu composites. Sources of the references are cited in the supplementary materials.

9.3 Atomistic Modeling

We used LAMMPS [169] to perform molecular dynamics simulations for studying interactions between dislocations and unc particles. The atomic interactions in the Cu-C system were modelled by combining the embedded atom method (EAM) potential [130] for Cu-Cu interaction, the Tersoff potential [170] for C-C interaction, and the Lennard-Jones potential [171] for Cu-C interaction. A slab of face-centred cubic Cu single crystal was constructed with the dimension of 46.3 nm × 63.2 nm × 10.7 nm. The corresponding crystal orientation was X-$[110]$, Y-$[001]$, and Z-$[1\bar{1}0]$. Periodic boundary conditions were imposed in both the X and Z directions, while the Y surface of the slab was free to relax. A spherical C particle with a diameter d of 2.5 nm was embedded in the simulation cell, representing a periodic array of C particles with a spacing of 10.7 nm along the Z direction due to the periodic boundary condition imposed. This setup represents an equivalent C concentration of 0.8% as studied in our experiment. Both the crystalline C particle with a diamond cubic lattice structure and the amorphous C particle with a disordered atomic structure were modelled. Different C particle sizes and the effect of misfit strains between the C particle and Cu matrix were studied. Either one or two 60° dislocations of the $1/2\langle 110\rangle\{111\}$ type were embedded in the simulation cell; the dislocation line was aligned along the Z-direction of $[1\bar{1}0]$ and located on a $\{111\}$ slip plane intersecting the C particle. To control the position and character of a dislocation embedded in the simulation cell, we first imposed the atomic displacements of this dislocation according to its elastic

solution and then relaxed the simulation cell to obtain a dissociated full dislocation consisting of a pair of leading and trailing partials with a stacking fault in between. The simulation cell was subjected to an imposed tensile strain up to 0.1% along the X-direction, which was sufficient to drive the dislocation(s) to bypass the periodic array of C particles. We obtained similar results by both molecular statics simulations (i.e., a sequence of energy minimization by the conjugate gradient method) and molecular dynamics simulations at low temperatures. The von Mises equivalent atomic strain field in Figure 9.3d-g was produced by OVITO [131].

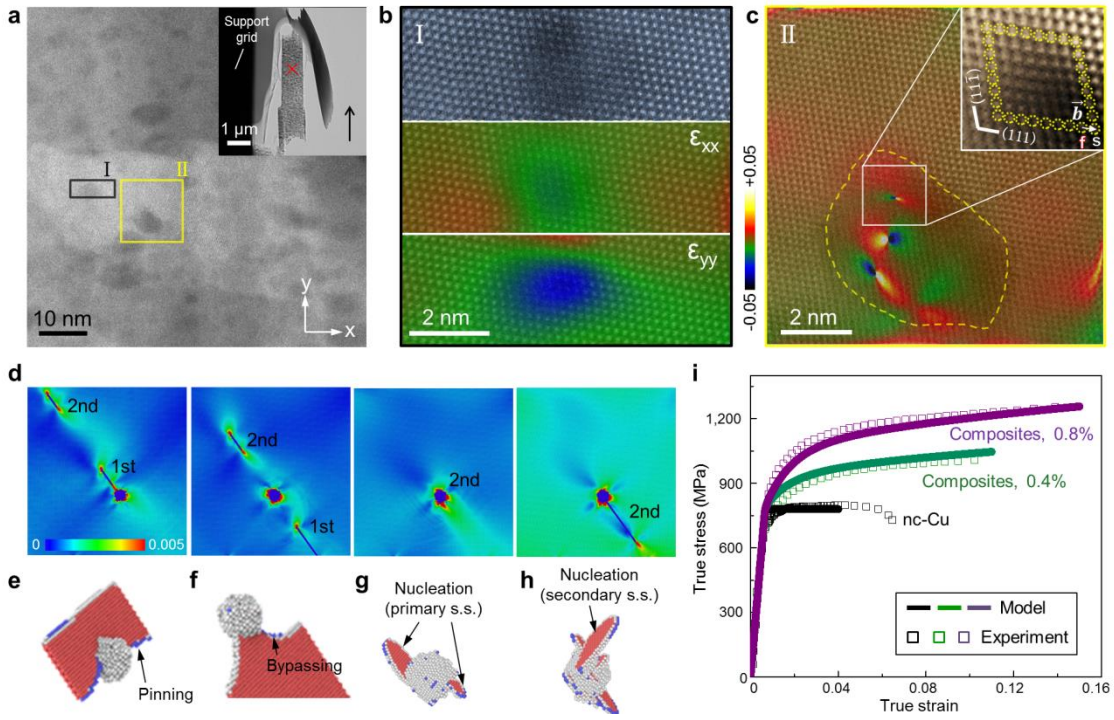

Figure 9.3 Hardening mechanisms in nc-Cu composites. **a,** HAADF-STEM image of the gauge region (marked with an "X" in the inset image) of a deformed nc-Cu composite (0.8 vol.% C) after tensile straining. Two representative regions (I and II) containing a small and large unc particle, respectively, are chosen for microstructural analysis. **b,** HAADF-STEM image of region I and corresponding strain maps (ε_{xx} and ε_{yy}). The zero-strain reference was chosen in the lower-left corner of this image. Residual compressive strain is found around the C particle. **c,** A high-resolution HAADF-STEM image shows atomic structure of region II, superimposed with the dilatation strain (ε_{xx}) map of the same region.

Three dislocation cores can be clearly identified at the C nanoparticle region (indicated by the yellow dashed circle), suggestive of a particle blockage mechanism. The Burgers circuit analysis (inset) of one dislocation indicates a Burgers vector of 1/2[011] (i.e., a full dislocation). **d,** Snapshots of MD simulations for the successive dislocation bypassing across a periodic array of unc particles aligned in the out-of-plane direction. The particle size is 2.5 nm and the particle spacing is 10.7 nm. Each dislocation dissociates into a pair of leading and trailing partials with a stacking fault in between. Atomic Mises strain maps in **d** reveal the local strain fields around dislocations and unc particles as well as long-range elastic interactions between dislocations. **e-h,** Magnified MD snapshots showing the three-dimensional dislocation structure near a unc particle during the pinning of the leading partial (**e**), and the denning of the trailing partial (**f**). **g,** Nucleation of a dislocation loop from the unc particle on the primary slip system (s. s.) with the largest resolved shear stress. The two half loops form on parallel {111} slip planes. **h**, Nucleation of a dislocation loop on the secondary slip system with a lower resolved shear stress. Atoms in **e-h** are colored through common neighbor analysis, so that atoms in the perfect lattice are invisible. **i,** Stress-strain responses obtained from the two-stage hardening model, in comparison with the corresponding experimental results.

Because of strong covalent C-C bonding, unc particles possess high resistance to plastic shear, thus inhibiting direct cutting of these particles by dislocations. Moreover, they can strongly hinder dislocation bypassing between them, due to the considerably small spacing of ~10 nm between unc particles. To reveal these effects, MD results in Figure 9.3d show the dynamic processes of two $1/2\langle 110\rangle\{111\}$ full dislocations (marked as 1st and 2nd) that sequentially bypass a periodic array of unc particles embedded in a Cu matrix. The spherical unc particles have a diameter d of 2.5 nm and a spacing l of 10.7 nm, giving an equivalent C concentration of about 0.8 vol.%, as studied in our experiment. Atomic strain maps in Figure 9.3d reveal the strong pinning effects of unc particles on the two dislocations. Specifically, it shows that the obstructed 1st dislocation exerts a strong back stress to the 2nd dislocation, due to their long-range elastic interaction manifested as interconnected light-green strain contours. This back stress opposes the motion of the 2nd dislocation, giving rise to a strong back-stress hardening effect arising from unc particles [172]. Figure 9.3e-f present the corresponding three-dimensional process where the 1st

dislocation bypasses a representative unc particle via the Orowan mechanism [136]. After bypassing, an interface dislocation loop is left around the unc particle, producing a shell of high strain contour (in red). Similar MD results were obtained for both amorphous and diamond-cubic unc particles, as well as for random distributions of unc particles. These Orowan loops are geometrically necessary dislocations (GNDs) for accommodating the local deformation incompatibility around unc particles [173, 174]. An increase of applied load raises the density of GNDs, thereby increasing the local stress concentration around unc particles. To release these stresses, additional GND loops nucleate on other primary slip planes (Figure 9.3g) as well as on secondary slip planes (Figure 9.3h). These GND loops tend to spread out between unc particles with increasing load and thus impede the movement of dislocations on primary planes [173, 174], contributing to the strong work hardening of nc composites.

9.4 Work Hardening Model

Based on the above experimental and MD results, we developed a two-stage work hardening model to analyze the experimental stress-strain responses, in order to determine the major sources of extra work hardening of nc-Cu composites relative to nc-Cu.

We used a classical rate-dependent plasticity model to analyze the experimental stress-strain response. The strain rate $\dot{\varepsilon} = \dot{\varepsilon}^e + \dot{\varepsilon}^p$ is decomposed into elastic strain rate $\dot{\varepsilon}^e$ and plastic strain rate $\dot{\varepsilon}^p$. The stress rate can be calculated from Young's modulus E and elastic strain rate $\dot{\sigma} = E\dot{\varepsilon}^e$. The normal stress/strain and the shear stress/strain are related through

the Taylor factor M, $\sigma = M\tau$ and $\dot{\gamma}^p = M\dot{\varepsilon}$. The density of geometrically necessary dislocations from dispersed particles is $\rho^{\mathrm{G}} = \dfrac{f\gamma^p}{bd}$, where f is the volume fraction of unc particles, b is the Burgers vector length, and d is the unc particle size.

The plastic shear rate $\dot{\gamma}^p$ is determined by the resolved shear stress τ and the total slip resistance τ_{T}.

$$\dot{\gamma}^p = \dot{\gamma}_0^p \left(\frac{\tau}{\tau_{\mathrm{T}}} \right)^{\frac{1}{m}}$$

The total slip resistance can be expressed as $\tau_{\mathrm{T}} = \tau_{\mathrm{y}} + \tau_{\mathrm{I}}^{\mathrm{UNC}} + \tau_{\mathrm{II}}^{\mathrm{UNC}}$, where τ_{y} is the shear resistance for pure nc-Cu. The rapidly growing back stress $\tau_{\mathrm{I}}^{\mathrm{UNC}}$ due to the GNDs is expressed as,

$$\dot{\tau}_{\mathrm{I}}^{\mathrm{UNC}} = k\left(\tau_{\mathrm{I,sat}}^{\mathrm{UNC}} - \tau_{\mathrm{I}}^{\mathrm{UNC}} \right) \dot{\gamma}^p$$

where k characterizes the back stress hardening rate and $\tau_{\mathrm{I,sat}}^{\mathrm{UNC}} = \beta_1 \mu b \rho_{4\%}^{\mathrm{G}} D$ is the saturated back stress value at 4% plastic strain. The resistance from stage II hardening $\tau_{\mathrm{II}}^{\mathrm{UNC}}$ is estimated as $\tau_{\mathrm{II}}^{\mathrm{UNC}} = \beta_2 \mu b \sqrt{\rho^{\mathrm{G}}}$. The stress strain curves were calculated under the applied strain rate $1\times10^{-3}\ \mathrm{s}^{-1}$ and the integration increment is 0.001 s. The parameter used in this model are listed below.

Table 9.1 Parameters used in the two-stage hardening model.

M	$\dot{\gamma}_0^p$	m	k	β_1	β_2	σ_y
2.7	1×10^{-3} s^{-1}	0.06	74 MPa	0.6	0.35	780 MPa

During stage I hardening at small strains, nc-Cu composites exhibit markedly higher hardening rates (Figure 9.2b), quickly raising yield strengths by significant amounts relative to nc-Cu. According to Ashby [173], the density of GNDs from dispersed particles, ρ^G, increases with plastic shear strain γ by $\rho^G \sim f\gamma/(bd)$, where f is the volume fraction of unc particles, b is the Burgers vector length, and d is the unc particle size. Strong bonding at Cu-C interfaces hinders the relaxation of GNDs around unc particles. As a result, the partially relaxed GNDs collectively exert a large long-range back stress to the strength-limiting process, which could involve the activation of dislocation sources near GBs [175]. To account for this strong hardening effect, the total slip resistance on the primary slip plane τ_{T} is expressed as $\tau_{\mathrm{T}} = \tau_{\mathrm{y}} + \tau_{\mathrm{I}}^{\mathrm{UNC}}$, where τ_{y} is the shear resistance of the strength-limiting process for pure nc-Cu; $\tau_{\mathrm{I}}^{\mathrm{UNC}}$ is the back stress from the GNDs on the primary slip planes arising from unc particles. $\tau_{\mathrm{I}}^{\mathrm{UNC}}$ rises quickly with increasing ρ^G in a strong nonlinear manner, and becomes saturated at the tensile strain of a few percent. Afterwards, stage II hardening sets in, due to nucleation and spread of additional GNDs on secondary slip planes. To accounts for this additional GNDs hardening effect, the total slip resistance is expressed as $\tau_{\mathrm{T}} = \tau_{\mathrm{y}} + \tau_{\mathrm{I}}^{\mathrm{UNC}} + \tau_{\mathrm{II}}^{\mathrm{UNC}}$, where $\tau_{\mathrm{I}}^{\mathrm{UNC}}$ has become saturated; $\tau_{\mathrm{II}}^{\mathrm{UNC}}$ is the slip resistance from additional GNDs and increases with a lower rate than stage I due to the spread of these additional GNDs around unc particles [173]. As shown in Figure 9.3i,

the numerical results from the above two-stage hardening model agree closely with the experimentally measured stress-strain responses of nc-Cu composites and nc-Cu. Hence, $\tau_{\mathrm{I}}^{\mathrm{UNC}}$ and $\tau_{\mathrm{II}}^{\mathrm{UNC}}$ reflect the major sources of extra work hardening in nc-Cu composites relative to pure nc-Cu.

9.5 Summary

By harnessing the ultra-dense and strong metal-carbon interfaces, we show that the incorporation of unc into nanocrystalline metals is an effective approach to achieve exceptional work hardening and high ductility, in conjunction with improved thermal stability. These combined properties are superior to those from other nanostructuring strategies including GB engineering [74], hierarchical microstructuring [3], and nanotwinning [176, 177]. Hence, nanodispersion of unc in nanograins represents a novel nanostructuring strategy that may be widely applicable to make ultrastrong and stable metallic materials, which would improve energy savings and system performance in engineering applications.

CHAPTER 10. CONCLUSION

Heterogeneous metallic systems often exhibit exceptional combinations of strength and ductility. To understand the mechanics of heterogeneous metallic systems, we have developed a unified framework in this thesis to elucidate the effects of mechanical heterogeneities arising from structural heterogeneities. This framework resides on (i) the large RVE method, which is centered on the evolution of back-stresses and forward-stresses, and (ii) the small RVE method, which is focused on the effect of strain gradient on extra hardening. We applied this unified framework to the heterogeneities of different length scales: microscale, macroscale and nanoscale heterogeneities.

We have investigated the microscale heterogeneities in AM alloys in terms of two types of internal stresses, i.e., type-II intergranular internal stresses and type-III intragranular internal stresses. The effect of type-II intergranular internal stresses is shown to arise from the elastic anisotropy of grain crystals and is understood by a micromechanics model. In particular, we have derived a general analytic solution of grain-level lattice strains and diffraction elastic constants for an elastically isotropic polycrystal using a self-consistent micromechanics model. This solution is applicable to a broad class of "texture-free" polycrystals with cubic crystal symmetry and only requires an input of the three independent elastic constants of a cubic crystal.

We have combined experimental and modelling studies to analyze the microscale residual stresses in AM 316L steels, which have profound impacts on the yielding and strain hardening behavior of as-printed stainless steel. *In situ* SXRD experiments provide a powerful approach to unravel the residual lattice strains and associated Type II

intergranular residual stresses for individual grain families in as-printed stainless steel as well as their evolution under applied loads. The combined SXRD and modeling results elucidate the effects of elastic anisotropy, progressive yielding and strain hardening on the evolution of lattice strains and associated Type II intergranular residual stresses in different grain families. On the other hand, a pronounced tension-compression asymmetry of yield strength is observed from as-printed stainless steel, together with an asymmetric work hardening behavior. Such tension-compression asymmetries are shown to be governed by the back stresses and associated Type III intragranular residual stresses, which arise from heterogeneous dislocation distributions that can be strongly influenced by both L-PBF processing and mechanical loading. Our CPFE simulations show that the former dictates the tension-compression asymmetry of yield strength in as-printed samples, while the latter can quickly build up during loading and thereby affect both the yield strength and strain hardening responses. Altogether, our results demonstrate the quantitative and mechanistic connections between the microscale residual stresses and mechanical behavior of AM stainless steel.

We have extended the micromechanics model and CPFE model to another AM metallic system of dual-phase eutectic high-entropy alloy. The micromechanics model is used to inversely determine the elastic constants of the FCC and BCC nanolamellae in the eutectic high-entropy alloy, on the basis of lattice strain data from neutron diffraction experiments. A dual-phase CPFE is developed to capture the stress partition and work hardening behaviors of the dual phase materials. It is shown that both BCC and FCC nanolamellae exhibit high strain hardening for a fairly large range of tensile strains, but BCC nanolamellae make greater contributions to the overall high strain hardening responses than

FCC nanolamellae, thereby promoting the overall high tensile ductility of the present EHEA. Hence, the AM dual-phase eutectic high-entropy alloy enables the high strain hardening behavior in its constituent BCC nanolamellae that is hitherto difficult to achieve in single-phase BCC nanostructures.

For the macroscale heterogeneities, we have chosen the gradient nanotwinned Cu as the model system to study the effect of structural gradient on its extra hardening response. We have developed a 3D gradient theory of plasticity by incorporating the strengthening effect of plastic strain gradient into the classical J_2 flow theory. Numerical simulations based on a simplified 1D gradient theory show the dominant effects of gradient plasticity on GNT Cu under uniaxial tension, including progressive yielding, gradient distributions of plastic strain and extra flow resistance. We find that the extra strength depends on the hardness gradient g (being three times strength gradient g_s) through Eq. (5.15). Results from 3D gradient plasticity finite element simulations confirm 1D numerical results and further reveal the 3D distribution of non-axial stresses despite their negligible role in the overall tensile response of GNT Cu. Predictions of the optimal gradient structures and associated gradient strength distributions suggest possible routes for achieving the maximum strength of gradient nanostructures in GNT Cu.

We have developed a mechanistically-based theory of strain gradient plasticity. Our combined experimental and modeling results have identified the primary source of extra strengthening in GNT Cu as the extra back stress arising from nanotwin structure gradient. The extra back stress is induced by the GNDs associated with BCDs that only form in gradient nanotwin structures. An increase in nanotwin structure gradient can lead to a

substantial increase in plastic strain gradient giving rise to a high extra strength. In contrast, the strengthening effect of HNT Cu largely comes from a different type of back stress originated from incompatible deformation between the matrix and nanotwins. Such back stress is enhanced with decreasing twin thickness. The effective stress is much less sensitive to the geometry of nanotwins in both GNT and HNT Cu. Altogether, these results underscore the predominant strengthening effect of the extra back stress arising from gradient structure, and thus point to a "going for nano" strategy for further enhancing the strength of GNT Cu by a simultaneous decrease of nanotwin thickness and increase of nanotwin gradient. This strategy requires innovations in material processing to push the limit of attainable nanostructure geometry in the future.

For the nanoscale heterogeneities, we have used *in situ* TEM MEMS-based straining experiments, combined with MD simulations, to study deformation-induced grain growth while also investigating how the local stress induced by necking promotes GB migration. The results of these experiments indicate that GB migration is primarily stress-induced, as opposed to thermally-driven GB migration during high temperature annealing or creep. MD simulations utilized a novel coloring scheme to track GB motion over time, which yielded qualitative agreement with experimental observations of significant GB migration leading to grain growth. MD simulations further complement *in situ* experiments by uncovering the underlying atomic processes of grain growth and GB migration that are not directly visible through TEM. Altogether, these results underscore the important role of stress-driven grain growth in plastically deforming nanocrystalline metals, particularly in regions with large localized deformation.

We have combined *in situ* TEM/MEMS-based measurements and FENEB calculations to reveal two characteristic groups of activation volume ($V^* > 15b^3$ and $1b^3 < V^* < 10b^3$), which signify an active competition between the displacive and diffusive types of rate-controlling GB mechanism in ultrafine-grained and nanocrystalline metals. The most important finding is that the diffusive type of rate-controlling GB mechanism can operate at room temperature in ultrafine-grained and nanocrystalline metals, due to their prevailing high stresses.

Lastly, we have investigated the monodispersed carbon nanoparticles in nanograined Cu. We show that the incorporation of carbon nanoparticles into nanocrystalline metals is an effective approach to achieve exceptional work hardening leading to high ductility, in conjunction with improved thermal stability. These combined properties are superior to other nanostructuring strategies including GB engineering, hierarchical microstructuring, and nanotwinning. Hence, nanodispersion of carbon nanoparticles in nanograins represents a novel nanostructuring strategy that may be widely applicable to make materials with ultrahigh strength and stable nanostructures, which would improve energy savings and system performance in engineering applications.

Overall, this thesis research provides a new framework to bridge structural heterogeneities and mechanical heterogeneities in several emergent heterogeneous material systems through constitutive modeling and atomistic simulations. Coupled with novel material processing, characterization, and testing, the modeling and simulation results offer quantitative predictions and mechanistic insights toward the design of heterogeneous metallic materials with improved combinations of strength and ductility. This framework could be further applied to other heterogeneous metallic systems, such as gradient

nanograins, transmodal grains and other nanoprecipitate-hardened materials. A fundamental understanding of mechanics of heterogeneous metallic systems can open up opportunities of harnessing structural and mechanical heterogeneities for achieving outstanding mechanical properties of engineering materials.

APPENDIX A. ELASTIC PROPERTIES OF REPRESENTATIVE CUBIC POLYCRYSTALS

Table A1. Elastic properties of representative cubic polycrystals. The single-crystal elastic constants of C_{11}, C_{12} and C_{44} are taken from Simmons and Wang [38], except for those of stainless steel (SS) 316L from Clausen *et al*. [15]; the effective elastic consonants $\overline{K}$ and $\overline{\mu}$ for elastically isotropic polycrystals are calculated from Eq. (2.17) and Eq. (2.18), respectively.

Material	Structure	C_{11} (GPa)	C_{12} (GPa)	C_{44} (GPa)	$\bar{K}$ (GPa)	$\bar{\mu}$ (GPa)	A
Ag	FCC	124.00	93.40	46.10	103.60	30.20	3.01
Al	FCC	107.30	60.90	28.30	76.37	26.15	1.22
Au	FCC	192.90	163.80	41.50	173.50	27.89	2.85
Cu	FCC	168.40	121.40	75.40	137.07	48.17	3.21
Ir	FCC	580.00	242.00	256.00	354.67	216.97	1.51
Ni	FCC	246.50	147.30	124.70	180.37	86.90	2.51
Pb	FCC	49.50	42.30	14.90	44.70	8.79	4.14
Pd	FCC	227.10	176.00	71.70	193.03	48.28	2.81
Pt	FCC	346.70	250.70	76.50	282.70	63.69	1.59
Cr	BCC	339.80	58.60	99.00	152.33	113.89	0.70
Fe	BCC	231.40	134.70	116.40	166.93	82.45	2.41
K	BCC	4.14	3.31	2.63	3.59	1.33	6.34

Table A1 continued

Li	BCC	13.50	11.44	8.78	12.13	4.05	8.52
Mo	BCC	440.80	172.40	121.70	261.87	126.56	0.91
Na	BCC	6.15	4.96	5.92	5.36	2.56	9.95
Nb	BCC	240.20	125.60	28.20	163.80	37.64	0.49
Ta	BCC	260.20	154.50	82.60	189.73	69.23	1.56
V	BCC	228.00	118.70	42.60	155.13	47.09	0.78
W	BCC	522.40	204.40	160.80	310.40	160.08	1.01
C	DC	949.00	151.00	521.00	417.00	468.14	1.31
Ge	DC	128.40	48.20	66.70	74.93	54.45	1.66
Si	DC	166.70	64.40	79.80	98.50	66.83	1.56
CuZn	FCC	129.04	109.56	82.45	116.05	38.16	8.47
Cu_3Au	FCC	190.69	138.30	66.31	155.76	46.29	2.53
NiAl	BCC	211.55	143.23	112.11	166.00	70.83	3.28
SS 316L	FCC	204.60	137.70	126.20	160.00	75.64	3.77

REFERENCES

[1]. M.A. Meyers, A. Mishra, and D.J. Benson, Mechanical Properties of Nanocrystalline Materials. *Progress in Materials Science*, 2006. **51**(4): 427-556.

[2]. R. Valiev, Nanostructuring of Metals by Severe Plastic Deformation for Advanced Properties. *Nature Materials*, 2004. **3**(8): 511-516.

[3]. E. Ma and T. Zhu, Towards Strength–Ductility Synergy through the Design of Heterogeneous Nanostructures in Metals. *Materials Today*, 2017. **20**: 323-331.

[4]. D. Dye, H.J. Stone, and R.C. Reed, Intergranular and Interphase Microstresses. *Current Opinion in Solid State & Materials Science*, 2001. **5**(1): 31-37.

[5]. C.J. Bayley, W.a.M. Brekelmans, and M.G.D. Geers, A Comparison of Dislocation Induced Back Stress Formulations in Strain Gradient Crystal Plasticity. *International Journal of Solids and Structures*, 2006. **43**(24): 7268-7286.

[6]. N. Fleck, M. Ashby, and J. Hutchinson, The Role of Geometrically Necessary Dislocations in Giving Material Strengthening. *Scripta Materialia*, 2003. **48**(2): 179-183.

[7]. H. Mughrabi, Deformation-Induced Long-Range Internal Stresses and Lattice Plane Misorientations and the Role of Geometrically Necessary Dislocations. *Philosophical Magazine*, 2006. **86**(25-26): 4037-4054.

[8]. Y.M. Wang, T. Voisin, J.T. Mckeown, J. Ye, N.P. Calta, Z. Li, Z. Zeng, Y. Zhang, W. Chen, T.T. Roehling, R.T. Ott, M.K. Santala, Philip j. Depond, M.J. Matthews, A.V. Hamza, and T. Zhu, Additively Manufactured Hierarchical Stainless Steels with High Strength and Ductility. *Nature Materials*, 2018. **17**(1): 63-71.

[9]. Z. Cheng, H. Zhou, Q. Lu, H. Gao, and L. Lu, Extra Strengthening and Work Hardening in Gradient Nanotwinned Metals. 2018. **362**(6414): eaau1925.

[10]. J.L. Bassani, Incompatibility and a Simple Gradient Theory of Plasticity. *Journal of the Mechanics and Physics of Solids*, 2001. **49**(9): 1983-1996.

[11]. Z. Cheng, H.F. Zhou, Q.H. Lu, H.J. Gao, and L. Lu, Extra Strengthening and Work Hardening in Gradient Nanotwinned Metals. *Science*, 2018. **362**(6414): 559.

[12]. S. Plimpton, Fast Parallel Algorithms for Short-Range Molecular-Dynamics. *Journal of Computational Physics*, 1995. **117**(1): 1-19.

[13]. G.E. Ice, J.D. Budai, and J.W.L. Pang, The Race to X-Ray Microbeam and Nanobeam Science. *Science*, 2011. **334**(6060): 1234-1239.

[14]. A.J. Allen, M.T. Hutchings, C.G. Windsor, and C. Andreani, Neutron Diffraction Methods for the Study of Residual Stress Fields. *Advances in Physics*, 1985. **34**(4): 445-473.

[15]. B. Clausen, T. Lorentzen, and T. Leffers, Self-Consistent Modelling of the Plastic Deformation of Fcc Polycrystals and Its Implications for Diffraction Measurements of Internal Stresses. *Acta Materialia*, 1998. **46**(9): 3087-3098.

[16]. B. Clausen, T. Lorentzen, M.a.M. Bourke, and M.R. Daymond, Lattice Strain Evolution During Uniaxial Tensile Loading of Stainless Steel. *Materials Science and Engineering A*, 1999. **259**(1): 17-24.

[17]. M.R. Daymond, M.a.M. Bourke, R.B. Vondreele, B. Clausen, and T. Lorentzen, Use of Rietveld Refinement for Elastic Macrostrain Determination and for Evaluation of Plastic Strain History from Diffraction Spectra. *Journal of Applied Physics*, 1997. **82**(4): 1554-1562.

[18]. M.R. Daymond, C.N. Tome, and M.a.M. Bourke, Measured and Predicted Intergranular Strains in Textured Austenitic Steel. *Acta Materialia*, 2000. **48**(2): 553-564.

[19]. J.W.L. Pang, T.M. Holden, and T.E. Mason, The Development of Intergranular Strains in a High-Strength Steel. *Journal of Strain Analysis for Engineering Design*, 1998. **33**(5): 373-383.

[20]. J.W.L. Pang, T.M. Holden, J.S. Wright, and T.E. Mason, The Generation of Intergranular Strains in 309h Stainless Steel under Uniaxial Loading. *Acta Materialia*, 2000. **48**(5): 1131-1140.

[21]. T.M. Holden, A.P. Clarke, and R.A. Holt, Neutron Diffraction Measurements of Intergranular Strains in Monel-400. *Metallurgical and Materials Transactions A*, 1997. **28**(12): 2565-2576.

[22]. T.M. Holden, R.A. Holt, and A.P. Clarke, Intergranular Strains in Inconel-600 and the Impact on Interpreting Stress Fields in Beat Steam-Generator Tubing. *Materials Science and Engineering A*, 1998. **246**(1-2): 180-198.

[23]. Y.M. Wang, T. Voisin, J.T. Mckeown, J.C. Ye, N.P. Calta, Z. Li, Z. Zeng, Y. Zhang, W. Chen, T.T. Roehling, R.T. Ott, M.K. Santala, P.J. Depond, M.J. Matthews, A.V. Hamza, and T. Zhu, Additively Manufactured Hierarchical Stainless Steels with High Strength and Ductility. *Nature Materials*, 2018. **17**(1): 63-70.

[24]. W. Chen, T. Voisin, Y. Zhang, J.-B. Florien, C.M. Spadaccini, D.L. Mcdowell, T. Zhu, and Y.M. Wang, Microscale Residual Stresses in Additively Manufactured Stainless Steel. *Nature Communications*, 2019. **10**(1): 4338.

[25]. F. Bollenrath, V. Hauk, and E.H. Muller, On the Calculation of Polycrystalline Elasticity Constants from Single Crystal Data. *Zeitschrift Fur Metallkunde*, 1967. **58**(1): 76-82.

[26]. H. Behnken and V. Hauk, Calculation of the X-Ray Elasticity Constants (Xec) of the Polycrystal from the Elastic Data of the Single-Crystal for Arbitrary Crystal Symmetry. *Zeitschrift Fur Metallkunde*, 1986. **77**(9): 620-626.

[27]. R. Dewit, Diffraction Elastic Constants of a Cubic Polycrystal. *Journal of Applied Crystallography*, 1997. **30**: 510-511.

[28]. T. Gnaupel-Herold, P.C. Brand, and H.J. Prask, Calculation of Single-Crystal Elastic Constants for Cubic Crystal Symmetry from Powder Diffraction Data. *Journal of Applied Crystallography*, 1998. **31**: 929-935.

[29]. J.N. Hu, B. Chen, D.J. Smith, P.E.J. Flewitt, and A.C.F. Cocks, On the Evaluation of the Bauschinger Effect in an Austenitic Stainless Steel-the Role of Multi-Scale Residual Stresses. *International Journal of Plasticity*, 2016. **84**: 203-223.

[30]. Y. Wu, W.H. Liu, X.L. Wang, D. Ma, A.D. Stoica, T.G. Nieh, Z.B. He, and Z.P. Lu, In-Situ Neutron Diffraction Study of Deformation Behavior of a Multi-Component High-Entropy Alloy. *Applied Physics Letters*, 2014. **104**(5): 051910.

[31]. R. Li, Q. Xie, Y.-D. Wang, W. Liu, M. Wang, G. Wu, X. Li, M. Zhang, Z. Lu, C. Geng, and T. Zhu, Unraveling Submicron-Scale Mechanical Heterogeneity by Three-Dimensional X-Ray Microdiffraction. *Proceedings of the National Academy of Sciences of the United States of America*, 2018. **115**(3): 483-488.

[32]. J.D. Eshelby, The Determination of the Elastic Field of an Ellipsoidal Inclusion, and Related Problems. *Proceedings of the Royal Society of London Series A*, 1957. **241**(1226): 376-396.

[33]. J. Qu and M. Cherkaoui, Fundamentals of Micromechanics of Solids. 2006: Wiley.

[34]. E. Kroner, Allgemeine Kontinuumstheorie Der Versetzungen Und Eigenspannungen. *Archive for Rational Mechanics and Analysis*, 1960. **4**(4): 273-334.

[35]. D.-F. Li and N.P. O'dowd, On the Evolution of Lattice Deformation in Austenitic Stainless Steels—the Role of Work Hardening at Finite Strains. *Journal of the Mechanics and Physics of Solids*, 2011. **59**(12): 2421-2441.

[36]. L. Margulies, G. Winther, and H.F. Poulsen, In Situ Measurement of Grain Rotation During Deformation of Polycrystals. *Science*, 2001. **291**(5512): 2392-2394.

[37]. J.W. Hutchinson, Elastic-Plastic Behaviour of Polycrystalline Metals and Composites. *Proceedings of the Royal Society of London Series A*, 1970. **319**(1537): 247-272.

[38]. G. Simmons and H. Wang, Single Crystal Elastic Constants and Calculated Aggregate Properties: A Handbook. 2nd ed. 1971, Cambridge, Mass.: Cambridge, Mass., M.I.T. Press.

[39]. Abaqus 6.14, User's Manual. *SIMULIA, Providence, R.I.*, 2016.

[40]. W.E. Frazier, Metal Additive Manufacturing: A Review. *Journal of Materials Engineering and performance*, 2014. **23**(6): 1917-1928.

[41]. J.H. Martin, B.D. Yahata, J.M. Hundley, J.A. Mayer, T.A. Schaedler, and T.M. Pollock, 3d Printing of High-Strength Aluminium Alloys. *Nature*, 2017. **549**: 365-369.

[42]. D. Herzog, V. Seyda, E. Wycisk, and C. Emmelmann, Additive Manufacturing of Metals. *Acta Materialia*, 2016. **117**: 371-392.

[43]. T. Debroy, H. Wei, J. Zuback, T. Mukherjee, J. Elmer, J. Milewski, A. Beese, A. Wilson-Heid, A. De, and W. Zhang, Additive Manufacturing of Metallic Components–Process, Structure and Properties. *Progress in Materials Science*, 2017. **92**: 112-224.

[44]. P.J. Withers and H.K.D.H. Bhadeshia, Residual Stress. Part 1 – Measurement Techniques. *Materials Science and Technology*, 2001. **17**(4): 355-365.

[45]. Y.M. Wang, R.T. Ott, A.V. Hamza, M.F. Besser, J. Almer, and M.J. Kramer, Achieving Large Uniform Tensile Ductility in Nanocrystalline Metals. *Physical Review Letters*, 2010. **105**(21): 215502.

[46]. J. Hu and A.C.F. Cocks, A Multi-Scale Self-Consistent Model Describing the Lattice Deformation in Austenitic Stainless Steels. *International Journal of Solids and Structures*, 2016. **78-79**: 21-37.

[47]. R.G. Li, Q.G. Xie, Y.D. Wang, W.J. Liu, M.G. Wang, G.L. Wu, X.W. Li, M.H. Zhang, Z.P. Lu, C. Geng, and T. Zhu, Unraveling Submicron-Scale Mechanical Heterogeneity by Three-Dimensional X-Ray Microdiffraction. *Proceedings of the National Academy of Sciences of the United States of America*, 2018. **115**(3): 483-488.

[48]. M.A. Kumar, B. Clausen, L. Capolungo, R.J. Mccabe, W. Liu, J.Z. Tischler, and C.N. Tome, Deformation Twinning and Grain Partitioning in a Hexagonal Close-Packed Magnesium Alloy. *Nature Communications*, 2018. **9**: 4761.

[49]. C.L.A. Leung, S. Marussi, R.C. Atwood, M. Towrie, P.J. Withers, and P.D. Lee, In Situ X-Ray Imaging of Defect and Molten Pool Dynamics in Laser Additive Manufacturing. *Nature Communications*, 2018. **9**(1): 1355.

[50]. L.F. Liu, Q.Q. Ding, Y. Zhong, J. Zou, J. Wu, Y.L. Chiu, J.X. Li, Z. Zhang, Q. Yu, and Z.J. Shen, Dislocation Network in Additive Manufactured Steel Breaks Strength-Ductility Trade-Off. *Materials Today*, 2018. **21**(4): 354-361.

[51]. Z. Sun, X. Tan, S.B. Tor, and C.K. Chua, Simultaneously Enhanced Strength and Ductility for 3d-Printed Stainless Steel 316l by Selective Laser Melting. *NPG Asia Materials*, 2018. **10**: 127-136.

[52]. P. Mercelis and J.-P. Kruth, Residual Stresses in Selective Laser Sintering and Selective Laser Melting. *Rapid prototyping journal*, 2006. **12**(5): 254-265.

[53]. D.W. Brown, D.P. Adams, L. Balogh, J.S. Carpenter, B. Clausen, G. King, B. Reedlunn, T.A. Palmer, M.C. Maguire, and S.C. Vogel, In Situ Neutron Diffraction Study of the Influence of Microstructure on the Mechanical Response of Additively Manufactured 304l Stainless Steel. *Metallurgical and Materials Transactions a-Physical Metallurgy and Materials Science*, 2017. **48A**(12): 6055-6069.

[54]. A.S. Wu, D.W. Brown, M. Kumar, G.F. Gallegos, and W.E. King, An Experimental Investigation into Additive Manufacturing-Induced Residual Stresses in 316l Stainless Steel. *Metallurgical and Materials Transactions a-Physical Metallurgy and Materials Science*, 2014. **45A**(13): 6260-6270.

[55]. M. Shamsujjoha, S.R. Agnew, J.M. Fitz-Gerald, W.R. Moore, and T.A. Newman, High Strength and Ductility of Additively Manufactured 316l Stainless Steel Explained. *Metallurgical and Materials Transactions a-Physical Metallurgy and Materials Science*, 2018. **49A**(7): 3011-3027.

[56]. L. Thijs, F. Verhaeghe, T. Craeghs, J. Van Humbeeck, and J.-P. Kruth, A Study of the Microstructural Evolution During Selective Laser Melting of Ti–6al–4v. *Acta Materialia*, 2010. **58**(9): 3303-3312.

[57]. Y. Lu, S. Wu, Y. Gan, T. Huang, C. Yang, L. Junjie, and J. Lin, Study on the Microstructure, Mechanical Property and Residual Stress of Slm Inconel-718 Alloy Manufactured by Differing Island Scanning Strategy. *Optics & Laser Technology*, 2015. **75**: 197-206.

[58]. Y. Zhong, L.F. Liu, S. Wikman, D.Q. Cui, and Z.J. Shen, Intragranular Cellular Segregation Network Structure Strengthening 316l Stainless Steel Prepared by Selective Laser Melting. *Journal of Nuclear Materials*, 2016. **470**: 170-178.

[59]. J.R. Trelewicz, G.P. Halada, O.K. Donaldson, and G. Manogharan, Microstructure and Corrosion Resistance of Laser Additively Manufactured 316l Stainless Steel. *Jom*, 2016. **68**(3): 850-859.

[60]. Z. Sun, X. Tan, S.B. Tor, and W.Y. Yeong, Selective Laser Melting of Stainless Steel 316l with Low Porosity and High Build Rates. *Materials & Design*, 2016. **104**: 197-204.

[61]. A.C. Lund, T.G. Nieh, and C.A. Schuh, Tension/Compression Strength Asymmetry in a Simulated Nanocrystalline Metal. *Physical Review B*, 2004. **69**(1): 012101.

[62]. M. Daymond, C. Tomé, and M. Bourke, Measured and Predicted Intergranular Strains in Textured Austenitic Steel. *Acta Materialia*, 2000. **48**(2): 553-564.

[63]. S.R. Kalidindi, C.A. Bronkhorst, and L. Anand, Crystallographic Texture Evolution in Bulk Deformation Processing of Fcc Metals. *Journal of the Mechanics and Physics of Solids*, 1992. **40**(3): 537-569.

[64]. X. Feaugas, On the Origin of the Tensile Flow Stress in the Stainless Steel Aisi 316l at 300 K: Back Stress and Effective Stress. *Acta Materialia*, 1999. **47**(13): 3617-3632.

[65]. M.S. Pham, S.R. Holdsworth, K.G.F. Janssens, and E. Mazza, Cyclic Deformation Response of Aisi 316l at Room Temperature: Mechanical Behaviour, Microstructural Evolution, Physically-Based Evolutionary Constitutive Modelling. *International Journal of Plasticity*, 2013. **47**: 143-164.

[66]. S. Zheng, I.J. Beyerlein, J.S. Carpenter, K. Kang, J. Wang, W. Han, and N.A. Mara, High-Strength and Thermally Stable Bulk Nanolayered Composites Due to Twin-Induced Interfaces. *Nature Communications*, 2013. **4**(1): 1696.

[67]. Y.T. Zhu and X. Liao, Retaining Ductility. *Nature Materials*, 2004. **3**(6): 351-352.

[68]. B. Cantor, I.T.H. Chang, P. Knight, and A.J.B. Vincent, Microstructural Development in Equiatomic Multicomponent Alloys. *Materials Science and Engineering: A*, 2004. **375-377**: 213-218.

[69]. L. Fan, T. Yang, Y. Zhao, J. Luan, G. Zhou, H. Wang, Z. Jiao, and C.-T. Liu, Ultrahigh Strength and Ductility in Newly Developed Materials with Coherent Nanolamellar Architectures. *Nature Communications*, 2020. **11**(1): 6240.

[70]. J.W. Yeh, S.K. Chen, S.J. Lin, J.Y. Gan, T.S. Chin, T.T. Shun, C.H. Tsau, and S.Y. Chang, Nanostructured High-Entropy Alloys with Multiple Principal Elements: Novel Alloy Design Concepts and Outcomes. *Advanced Engineering Materials*, 2004. **6**(5): 299-303.

[71]. D. Zhang, W. Niu, X. Cao, and Z. Liu, Effect of Standard Heat Treatment on the Microstructure and Mechanical Properties of Selective Laser Melting Manufactured Inconel 718 Superalloy. *Materials Science and Engineering: A*, 2015. **644**: 32-40.

[72]. J.H. Martin, B.D. Yahata, J.M. Hundley, J.A. Mayer, T.A. Schaedler, and T.M. Pollock, 3d Printing of High-Strength Aluminium Alloys. *Nature*, 2017. **549**(7672): 365-369.

[73]. Y. Zhang, W. Chen, D.L. Mcdowell, Y.M. Wang, and T. Zhu, Lattice Strains and Diffraction Elastic Constants of Cubic Polycrystals. *Journal of the Mechanics and Physics of Solids*, 2020. **138**: 103899.

[74]. K. Lu, Stabilizing Nanostructures in Metals Using Grain and Twin Boundary Architectures. *Nature Reviews Materials*, 2016. **1**(5): 16019.

[75]. X. Wu and Y. Zhu, Heterogeneous Materials: A New Class of Materials with Unprecedented Mechanical Properties. *Materials Research Letters*, 2017. **5**(8): 527-532.

[76]. T.H. Fang, W.L. Li, N.R. Tao, and K. Lu, Revealing Extraordinary Intrinsic Tensile Plasticity in Gradient Nano-Grained Copper. *Science*, 2011. **331**(6024): 1587-1590.

[77]. X. Wu, P. Jiang, L. Chen, F. Yuan, and Y.T. Zhu, Extraordinary Strain Hardening by Gradient Structure. *Proceedings of the National Academy of Sciences of the United States of America*, 2014. **111**(20): 7197-7201.

[78]. M.F. Ashby, Deformation of Plastically Non-Homogenous Materials *Philosophical Magazine*, 1970. **21**(170): 399-424.

[79]. E.C. Aifantis, On the Microstructural Origin of Certain Inelastic Models. *Journal of Engineering Materials and Technology-Transactions of the Asme*, 1984. **106**(4): 326-330.

[80]. N.A. Fleck, G.M. Muller, M.F. Ashby, and J.W. Hutchinson, Strain Graident Plasticity - Theory and Experiment. *Acta Metallurgica et Materialia*, 1994. **42**(2): 475-487.

[81]. W.D. Nix and H.J. Gao, Indentation Size Effects in Crystalline Materials: A Law for Strain Gradient Plasticity. *Journal of the Mechanics and Physics of Solids*, 1998. **46**(3): 411-425.

[82]. A.G. Evans and J.W. Hutchinson, A Critical Assessment of Theories of Strain Gradient Plasticity. *Acta Materialia*, 2009. **57**(5): 1675-1688.

[83]. S.P. Lele and L. Anand, A Large-Deformation Strain-Gradient Theory for Isotropic Viscoplastic Materials. *International Journal of Plasticity*, 2009. **25**(3): 420-453.

[84]. S.P. Lele and L. Anand, A Small-Deformation Strain-Gradient Theory for Isotropic Viscoplastic Materials. *Philosophical Magazine*, 2008. **88**(30-32): 3655-3689.

[85]. J. Li and A.K. Soh, Modeling of the Plastic Deformation of Nanostructured Materials with Grain Size Gradient. *International Journal of Plasticity*, 2012. **39**: 88-102.

[86]. Y. Wei, Y. Li, L. Zhu, Y. Liu, X. Lei, G. Wang, Y. Wu, Z. Mi, J. Liu, H. Wang, and H. Gao, Evading the Strength-Ductility Trade-Off Dilemma in Steel through Gradient Hierarchical Nanotwins. *Nature Communications*, 2014. **5**: 3580.

[87]. Z. Zeng, X. Li, D. Xu, L. Lu, H. Gao, and T. Zhu, Gradient Plasticity in Graident Nano-Grained Metals. *Extreme Mechanics Letters*, 2016. **8**: 213-219.

[88]. J. Li, G.J. Weng, S. Chen, and X. Wu, On Strain Hardening Mechanism in Gradient Nanostructures. *International Journal of Plasticity*, 2017. **88**: 89-107.

[89]. M.F. Ashby and D.R.H. Jones, Engineering Materials 1. 2012, Oxford, UK: Butterworth-Heinemann.

[90]. X. Li, L. Lu, J. Li, X. Zhang, and H. Gao, Mechanical Properties and Deformation Mechanisms of Gradient Nanostructured Metals and Alloys. *Nature Reviews Materials*, 2020. **5**(9): 706-723.

[91]. Z. Cheng, H. Zhou, Q. Lu, H. Gao, and L. Lu, Extra Strengthening and Work Hardening in Gradient Nanotwinned Metals. *Science*, 2018. **362**(6414): eaau1925.

[92]. R.O. Ritchie, The Conflicts between Strength and Toughness. *Nature Materials*, 2011. **10**(11): 817-822.

[93]. O. Bouaziz, Y. Brechet, and J.D. Embury, Heterogeneous and Architectured Materials: A Possible Strategy for Design of Structural Materials. *Advanced Engineering Materials*, 2008. **10**(1-2): 24-36.

[94]. X. Wu, M. Yang, F. Yuan, G. Wu, Y. Wei, X. Huang, and Y. Zhu, Heterogeneous Lamella Structure Unites Ultrafine-Grain Strength with Coarse-Grain Ductility. *Proceedings of the National Academy of Sciences of the United States of America*, 2015. **112**(47): 14501-5.

[95]. M. Yang, Y. Pan, F. Yuan, Y. Zhu, and X. Wu, Back Stress Strengthening and Strain Hardening in Gradient Structure. *Materials Research Letters*, 2016. **4**(3): 145-151.

[96]. C.X. Huang, Y.F. Wang, X.L. Ma, S. Yin, H.W. Höppel, M. Göken, X.L. Wu, H.J. Gao, and Y.T. Zhu, Interface Affected Zone for Optimal Strength and Ductility in Heterogeneous Laminate. *Materials Today*, 2018. **21**(7): 713-719.

[97]. H. Mughrabi, On the Role of Strain Gradients and Long-Range Internal Stresses in the Composite Model of Crystal Plasticity. *Materials Science and Engineering: A*, 2001. **317**(1-2): 171-180.

[98]. W.D. Nix and H. Gao, Indentation Size Effects in Crystalline Materials: A Law for Strain Gradient Plasticity. *Journal of the Mechanics and Physics of Solids*, 1998. **46**(3): 411-425.

[99]. X. Hu, S. Jin, H. Zhou, Z. Yin, J. Yang, Y. Gong, Y. Zhu, G. Sha, and X. Zhu, Bauschinger Effect and Back Stress in Gradient Cu-Ge Alloy. *Metallurgical and Materials Transactions A*, 2017. **48**(9): 3943-3950.

[100]. O.B. Pedersen, L.M. Brown, and W.M. Stobbs, The Bauschinger Effect in Copper. *Acta Metallurgica*, 1981. **29**(11): 1843-1850.

[101]. Z. Zeng, X. Li, D. Xu, L. Lu, H. Gao, and T. Zhu, Gradient Plasticity in Gradient Nano-Grained Metals. *Extreme Mechanics Letters*, 2016. **8**: 213-219.

[102]. Y. Zhang, Z. Cheng, L. Lu, and T. Zhu, Strain Gradient Plasticity in Gradient Structured Metals. *Journal of the Mechanics and Physics of Solids*, 2020. **140**: 103946.

[103]. Y. Wang, G. Yang, W. Wang, X. Wang, Q. Li, and Y. Wei, Optimal Stress and Deformation Partition in Gradient Materials for Better Strength and Tensile Ductility: A Numerical Investigation. *Sci. Rep.*, 2017. **7**(1): 10954.

[104]. Y. Huang, H. Gao, W. Nix, and J. Hutchinson, Mechanism-Based Strain Gradient Plasticity—Ii. Analysis. *Journal of the Mechanics and Physics of Solids*, 2000. **48**(1): 99-128.

[105]. M.F. Ashby, The Deformation of Plastically Non-Homogeneous Materials. *Philosophical Magazine*, 1970. **21**(170): 399-424.

[106]. N. Fleck, G. Muller, M.F. Ashby, and J.W. Hutchinson, Strain Gradient Plasticity: Theory and Experiment. *Acta Metallurgica et Materialia*, 1994. **42**(2): 475-487.

[107]. X. Ma, C. Huang, J. Moering, M. Ruppert, H.W. Höppel, M. Göken, J. Narayan, and Y. Zhu, Mechanical Properties of Copper/Bronze Laminates: Role of Interfaces. *Acta Materialia*, 2016. **116**: 43-52.

[108]. H. Gao, Y. Huang, W. Nix, and J. Hutchinson, Mechanism-Based Strain Gradient Plasticity—I. Theory. *Journal of the Mechanics and Physics of Solids*, 1999. **47**(6): 1239-1263.

[109]. K. Tai, M. Dao, S. Suresh, A. Palazoglu, and C. Ortiz, Nanoscale Heterogeneity Promotes Energy Dissipation in Bone. *Nature Materials*, 2007. **6**(6): 454-462.

[110]. T. Yang, Y.L. Zhao, Y. Tong, Z.B. Jiao, J. Wei, J.X. Cai, X.D. Han, D. Chen, A. Hu, J.J. Kai, K. Lu, Y. Liu, and C.T. Liu, Multicomponent Intermetallic Nanoparticles and Superb Mechanical Behaviors of Complex Alloys. *Science*, 2018. **362**(6417): 933-7.

[111]. H. Wang, Z. You, and L. Lu, Kinematic and Isotropic Strain Hardening in Copper with Highly Aligned Nanoscale Twins. *Materials Research Letters*, 2018. **6**(6): 333-338.

[112]. J. Dickson, J. Boutin, and L. Handfield, A Comparison of Two Simple Methods for Measuring Cyclic Internal and Effective Stresses. *Materials Science and Engineering*, 1984. **64**(1): L7-L11.

[113]. D. Viladot, M. Veron, M. Gemmi, F. Peiro, J. Portillo, S. Estrade, J. Mendoza, N. Llorca-Isern, and S. Nicolopoulos, Orientation and Phase Mapping in the Transmission Electron Microscope Using Precession-Assisted Diffraction Spot Recognition: State-of-the-Art Results. *Journal of Microscopy*, 2013. **252**(1): 23-34.

[114]. Z. You, X. Li, L. Gui, Q. Lu, T. Zhu, H. Gao, and L. Lu, Plastic Anisotropy and Associated Deformation Mechanisms in Nanotwinned Metals. *Acta Materialia*, 2013. **61**(1): 217-227.

[115]. Q. Lu, Z. You, X. Huang, N. Hansen, and L. Lu, Dependence of Dislocation Structure on Orientation and Slip Systems in Highly Oriented Nanotwinned Cu. *Acta Materialia*, 2017. **127**: 85-97.

[116]. T. Zhu and H. Gao, Plastic Deformation Mechanism in Nanotwinned Metals: An Insight from Molecular Dynamics and Mechanistic Modeling. *Scripta Materialia*, 2012. **66**(11): 843-848.

[117]. G.I. Taylor, The Mechanism of Plastic Deformation of Crystals. Part I.—Theoretical. *Proceedings of the Royal Society of London, Series A*, 1934. **145**(855): 362-387.

[118]. U. Kocks and H. Mecking, Physics and Phenomenology of Strain Hardening: The Fcc Case. *Progress in Materials Science*, 2003. **48**(3): 171-273.

[119]. H. Zhou, X. Li, S. Qu, W. Yang, and H. Gao, A Jogged Dislocation Governed Strengthening Mechanism in Nanotwinned Metals. *Nano Lett.*, 2014. **14**(9): 5075-80.

[120]. Q. Pan, H. Zhou, Q. Lu, H. Gao, and L. Lu, History-Independent Cyclic Response of Nanotwinned Metals. *Nature*, 2017. **551**(7679): 214-217.

[121]. X. Huang and G. Winther, Dislocation Structures. Part I. Grain Orientation Dependence. *Philosophical Magazine*, 2007. **87**(33): 5189-5214.

[122]. N. Hansen, R.F. Mehl, and A. Medalist, New Discoveries in Deformed Metals. *Metallurgical and Materials Transactions A*, 2001. **32**(12): 2917-2935.

[123]. T. Ungár, L.S. Tóth, J. Illy, and I. Kovács, Dislocation Structure and Work Hardening in Polycrystalline Ofhc Copper Rods Deformed by Torsion and Tension. *Acta Metallurgica*, 1986. **34**(7): 1257-1267.

[124]. C.W. Sinclair, W.J. Poole, and Y. Bréchet, A Model for the Grain Size Dependent Work Hardening of Copper. *Scripta Materialia*, 2006. **55**(8): 739-742.

[125]. H. Mughrabi, Dislocation Wall and Cell Structures and Long-Range Internal-Stresses in Deformed Metal Crystals. *Acta Metallurgica*, 1983. **31**(9): 1367-1379.

[126]. J.L. Chaboche, Time-Independent Constitutive Theories for Cyclic Plasticity. *International Journal of Plasticity*, 1986. **2**(2): 149-188.

[127]. N. Tsuji, Y. Ito, Y. Saito, and Y. Minamino, Strength and Ductility of Ultrafine Grained Aluminum and Iron Produced by Arb and Annealing. *Scripta Materialia*, 2002. **47**(12): 893-899.

[128]. S. Gupta and O.N. Pierron, A Mems Tensile Testing Technique for Measuring True Activation Volume and Effective Stress in Nanocrystalline Ultrathin Microbeams. *Journal of Microelectromechanical Systems*, 2017. **26**(5): 1082-1092.

[129]. S. Gupta, S. Stangebye, K. Jungjohann, B. Boyce, T. Zhu, J. Kacher, and O.N. Pierron, In Situ Tem Measurement of Activation Volume in Ultrafine Grained Gold. *Nanoscale*, 2020. **12**(13): 7146-7158.

[130]. Y. Mishin, M. Mehl, D. Papaconstantopoulos, A.F. Voter, and J. Kress, Structural Stability and Lattice Defects in Copper: Ab Initio, Tight-Binding, and Embedded-Atom Calculations. *Physical Review B*, 2001. **63**(22): 224106.

[131]. A. Stukowski, Visualization and Analysis of Atomistic Simulation Data with Ovito–the Open Visualization Tool. *Modelling and Simulation in Materials Science and Engineering*, 2009. **18**(1): 015012.

[132]. T. Zhu, J. Li, A. Samanta, A. Leach, and K. Gall, Temperature and Strain-Rate Dependence of Surface Dislocation Nucleation. *Physical Review Letters*, 2008. **100**(2): 025502.

[133]. J.W. Cahn, Y. Mishin, and A. Suzuki, Coupling Grain Boundary Motion to Shear Deformation. *Acta Materialia*, 2006. **54**(19): 4953-4975.

[134]. P. Hänggi, P. Talkner, and M. Borkovec, Reaction-Rate Theory: Fifty Years after Kramers. *Reviews of Modern Physics*, 1990. **62**(2): 251-341.

[135]. G. Caillard and J.L. Martin, Thermally Activated Mechanisms in Crystal Plasticity. 2003: Pergamon.

[136]. A.S. Argon, Strengthening Mechanisms in Crystal Plasticity. 2008, New York: Oxford Unversity Press Inc.

[137]. H. Conrad, Plastic Deformation Kinetics in Nanocrystalline Fcc Metals Based on the Pile-up of Dislocations. *Nanotechnology*, 2007. **18**(32): 325701.

[138]. N.J. Karanjgaokar, C.S. Oh, J. Lambros, and I. Chasiotis, Inelastic Deformation of Nanocrystalline Au Thin Films as a Function of Temperature and Strain Rate. *Acta Materialia*, 2012. **60**(13): 5352-5361.

[139]. G. Henkelman, B.P. Uberuaga, and H. Jónsson, A Climbing Image Nudged Elastic Band Method for Finding Saddle Points and Minimum Energy Paths. *The Journal of Chemical Physics*, 2000. **113**(22): 9901-9904.

[140]. T. Zhu, J. Li, A. Samanta, H.G. Kim, and S. Suresh, Interfacial Plasticity Governs Strain Rate Sensitivity and Ductility in Nanostructured Metals. *Proceedings of the National Academy of Sciences*, 2007. **104**(9): 3031.

[141]. S. Ogata, J. Li, N. Hirosaki, Y. Shibutani, and S. Yip, Ideal Shear Strain of Metals and Ceramics. *Physical Review B*, 2004. **70**(10): 104104.

[142]. L. Lu, M. Dao, T. Zhu, and J. Li, Size Dependence of Rate-Controlling Deformation Mechanisms in Nanotwinned Copper. *Scripta Materialia*, 2009. **60**(12): 1062-1066.

[143]. K. Lu, The Future of Metals. *Science*, 2010. **328**(5976): 319-320.

[144]. G.Y. Lai, High-Temperature Corrosion and Materials Applications. 2007: ASM international.

[145]. M. Yamaguchi, H. Inui, and K. Ito, High-Temperature Structural Intermetallics. *Acta Materialia*, 2000. **48**(1): 307-322.

[146]. A. Argon, Strengthening Mechanisms in Crystal Plasticity. Vol. 4. 2008: Oxford University Press on Demand.

[147]. S. Ringer, W. Yeung, B. Muddle, and I. Polmear, Precipitate Stability in Al · Cu · Mg · Ag Alloys Aged at High Temperatures. *Acta Metallurgica et Materialia*, 1994. **42**(5): 1715-1725.

[148]. X. Zhou, X. Li, and K. Lu, Enhanced Thermal Stability of Nanograined Metals Below a Critical Grain Size. *Science*, 2018. **360**(6388): 526-530.

[149]. T. Chookajorn, H.A. Murdoch, and C.A. Schuh, Design of Stable Nanocrystalline Alloys. *Science*, 2012. **337**(6097): 951.

[150]. T. Yang, Y.L. Zhao, Y. Tong, Z.B. Jiao, J. Wei, J.X. Cai, X.D. Han, D. Chen, A. Hu, J.J. Kai, K. Lu, Y. Liu, and C.T. Liu, Multicomponent Intermetallic Nanoparticles and Superb Mechanical Behaviors of Complex Alloys. *Science*, 2018. **362**(6417): 933.

[151]. Z. Li, K.G. Pradeep, Y. Deng, D. Raabe, and C.C. Tasan, Metastable High-Entropy Dual-Phase Alloys Overcome the Strength-Ductility Trade-Off. *Nature*, 2016. **534**(7606): 227-230.

[152]. Q.Q. Ding, Y. Zhang, X. Chen, X.Q. Fu, D.K. Chen, S.J. Chen, L. Gu, F. Wei, H.B. Bei, Y.F. Gao, M.R. Wen, J.X. Li, Z. Zhang, T. Zhu, R.O. Ritchie, and Q. Yu,

Tuning Element Distribution, Structure and Properties by Composition in High-Entropy Alloys. *Nature*, 2019. **574**(7777): 223-227.

[153]. D. Raabe, C.C. Tasan, and E.A. Olivetti, Strategies for Improving the Sustainability of Structural Metals. *Nature*, 2019. **575**(7781): 64-74.

[154]. K. Lu, L. Lu, and S. Suresh, Strengthening Materials by Engineering Coherent Internal Boundaries at the Nanoscale. *Science*, 2009. **324**(5925): 349-352.

[155]. T. Lagrange, B.W. Reed, M. Wall, J. Mason, T. Barbee, and M. Kumar, Topological View of the Thermal Stability of Nanotwinned Copper. *Applied Physics Letters*, 2013. **102**(1): 011905.

[156]. Z. Cheng, H. Zhou, Q. Lu, H. Gao, and L. Lu, Extra Strengthening and Work Hardening in Gradient Nanotwinned Metals. *Science*, 2018. **362**(6414).

[157]. X. Ke, J. Ye, Z. Pan, J. Geng, M.F. Besser, D. Qu, A. Caro, J. Marian, R.T. Ott, and Y.M. Wang, Ideal Maximum Strengths and Defect-Induced Softening in Nanocrystalline-Nanotwinned Metals. *Nature Materials*, 2019. **18**(11): 1207-1214.

[158]. S.P. Rawal, Metal-Matrix Composites for Space Applications. *Jom*, 2001. **53**(4): 14-17.

[159]. C. Du, S. Jin, Y. Fang, J. Li, S. Hu, T. Yang, Y. Zhang, J. Huang, G. Sha, and Y. Wang, Ultrastrong Nanocrystalline Steel with Exceptional Thermal Stability and Radiation Tolerance. *Nature Communications*, 2018. **9**(1): 1-9.

[160]. A. Mortensen and J. Llorca, Metal Matrix Composites. *Annual review of materials research*, 2010. **40**: 243-270.

[161]. L. Jiang, H. Yang, J.K. Yee, X. Mo, T. Topping, E.J. Lavernia, and J.M. Schoenung, Toughening of Aluminum Matrix Nanocomposites Via Spatial Arrays of Boron Carbide Spherical Nanoparticles. *Acta Materialia*, 2016. **103**: 128-140.

[162]. Y. Hu, Q. Guo, L. Zhao, Z. Li, G. Fan, Z. Li, D.-B. Xiong, Y. Su, and D. Zhang, Correlating Micro-Pillar Compression Behavior with Bulk Mechanical Properties: Nanolaminated Graphene-Al Composite as a Case Study. *Scripta Materialia*, 2018. **146**: 236-240.

[163]. D. Jang and J.R. Greer, Size-Induced Weakening and Grain Boundary-Assisted Deformation in 60 Nm Grained Ni Nanopillars. *Scripta Materialia*, 2011. **64**(1): 77-80.

[164]. S. Cheng, E. Ma, Y. Wang, L. Kecskes, K. Youssef, C. Koch, U. Trociewitz, and K. Han, Tensile Properties of in Situ Consolidated Nanocrystalline Cu. *Acta Materialia*, 2005. **53**(5): 1521-1533.

[165]. Y.M. Wang, R.T. Ott, T. Van Buuren, T.M. Willey, M.M. Biener, and A.V. Hamza, Controlling Factors in Tensile Deformation of Nanocrystalline Cobalt and Nickel. *Physical Review B*, 2012. **85**(1): 014101.

[166]. G. Wu, K.-C. Chan, L. Zhu, L. Sun, and J. Lu, Dual-Phase Nanostructuring as a Route to High-Strength Magnesium Alloys. *Nature*, 2017. **545**(7652): 80-83.

[167]. J. Schiøtz and K.W. Jacobsen, A Maximum in the Strength of Nanocrystalline Copper. *Science*, 2003. **301**(5638): 1357-1359.

[168]. L. Lu, X. Chen, X. Huang, and K. Lu, Revealing the Maximum Strength in Nanotwinned Copper. *Science*, 2009. **323**(5914): 607-610.

[169]. S. Plimpton, Fast Parallel Algorithms for Short-Range Molecular Dynamics. *Journal of Computational Physics*, 1995. **117**(1): 1-19.

[170]. P. Erhart and K. Albe, Analytical Potential for Atomistic Simulations of Silicon, Carbon, and Silicon Carbide. *Physical Review B*, 2005. **71**(3): 035211.

[171]. S. Dorfman, K.C. Mundim, D. Fuks, A. Berner, D.E. Ellis, and J. Van Humbeeck, Atomistic Study of Interaction Zone at Copper–Carbon Interfaces. *Materials Science and Engineering: C*, 2001. **15**(1-2): 191-193.

[172]. J.C. Fisher, E.W. Hart, and R.H. Pry, The Hardening of Metal Crystals by Precipitate Particles. *Acta Metallurgica*, 1953. **1**(3): 336-339.

[173]. M.F. Ashby, Deformation of Plastically Non-Homogeneous Materials *Philosophical Magazine*, 1970. **21**(170): 399-424.

[174]. M.F. Ashby, Work Hardening of Dispersion-Hardened Crystals. *Philosophical Magazine*, 1966. **14**(132): 1157-1178.

[175]. A.S. Argon and S. Yip, The Strongest Size. *Philosophical Magazine Letters*, 2006. **86**(11): 713-720.

[176]. L. Lu, Y. Shen, X. Chen, L. Qian, and K. Lu, Ultrahigh Strength and High Electrical Conductivity in Copper. *Science*, 2004. **304**(5669): 422-426.

[177]. X. Ke, J. Ye, Z. Pan, J. Geng, M.F. Besser, D. Qu, A. Caro, J. Marian, R.T. Ott, Y.M. Wang, and F. Sansoz, Ideal Maximum Strengths and Defect-Induced Softening in Nanocrystalline-Nanotwinned Metals. *Nature Materials*, 2019. **18**(11): 1207-1214.